Fabrication and characterisation of KNN-based multifunctional ceramics for hybrid energy harvesters

By

Guoyang Ye

A thesis submitted to the University of Birmingham for the degree of

DOCTOR OF PHILOSOPHY

UNIVERSITY OF BIRMINGHAM

School of Metallurgy and Materials

College of Engineering and Physical Sciences

The University of Birmingham

Birmingham, United Kingdom

July 2020

Acknowledgements

First and foremost, I wish to express my gratitude to my primary supervisors Prof Jon Binner and Prof Tim Button for offering me the opportunity to do this research work and all their support through my PhD study. They always kept me motivated when I was frustrated and stressed. Their invaluable guidance and suggestions on my work and personal development make me become Dr. Ye from someone who doesn't know what research is. I feel lucky and forever grateful to be guided by them!

Secondly, I wish to acknowledge the kind help and support provided by my second supervisors Dr. Daniel Reed, Dr. James Wade-Zhu and Dr. Ji Zou. And I also want to express my appreciation to Mr. Paul Stanley, Mr. Carl Meggs, Mrs. Theresa Morris and Miss Amy Newell for their technical training and assistance on laboratory equipment and practical suggestions. Furthermore, I would also like to extend my special thanks to my team colleagues and friends, Benjamin Baker, Tailin Zhang, Matthew Porter, Vinothini Venkatachalam, Erin Valenzuela, Qingbin Liu, Ye Zhang, Bai Yang, Chang Shu, Martin Safar and Arjin Boonruang for their valuable advice, the help of addressing technical problems and obtaining data, and support in my research.

Thirdly, I must acknowledge the experimental facilities and financial support provided by School of Metallurgy and Materials of the University of Birmingham. Also, I gratefully thank Qinetiq lab (UK), University of Bath, University of Edinburg, St Andrews University, National University of Singapore, Queen Mary University of London and Imperial College of London for technique supports. Massive thanks are also given to MISE (EPSRC) to provide financial support during my PhD study in University of Birmingham.

Finally, my greatest thanks go to my parents Mr. BangLiang Ye and Mrs. Xiuzhen Qiu for their endless support, their love, understanding and encouragement throughout my study. They are the reason why I am able to be pursuing my dreams and living a meaningful life.

Synopsis

There is an increasing demand for transforming from traditional energy resources into renewable, environmental energies. Owing to the excellent coupling of mechanical – electrical effect, piezoelectric ceramics have devoted considerable attention as a promising candidate for use in energy harvester by converting mechanical energy into electricity. Ferroelectric materials are the subset of piezoelectric materials due to switchable polarisation direction. Recently, the built-in field in ferroelectric ceramics can promote the separation of photo-induced charges and produces voltages higher than its bandgap (bulk photovoltaic effect), exceeding the Shockley-Queisser limit. Hence, it is possible to produce photovoltaic-ferroelectric hybrid energy harvesters with improved performance and applicability by using photovoltaic-ferroelectrics. For many years, $Pb(Zr_{1-x}Ti_x)O_3$ (PZT) have been identified as a leading ferroelectric ceramic. However, due to concerns from lead pollution, the development of lead-free alternatives is required. Sodium potassium niobate ($K_xNa_{1-x}NbO_3$, KNN)-based ceramics is one of the leading replacements for PZT ceramics being large owing to their high Curie temperature (410°C) and outstanding piezoelectric properties (465 pC/N). However, the KNN usually possess poor light absorb ability due to wide bandgap. Thus, this aim of this project is to explore a way to enhance the light absorbing ability and avoid the decreasing of polarisation of 5KNN and investigate the effect of multifunctional materials on the performance of hybrid prepared energy harvester.

This dissertation includes three parts. As KNN-based ceramics always suffer poor sinterability and exhibit poor piezoelectric properties, in the first part, the research of this project is mainly concentrated on the fabrication of 5KNN ($K_{0.5}Na_{0.5}NbO_3$) ceramics. In this study, a new sintering method, two-step sintering (TSS), was adopted to improve the sinterability by suppressing the grain growth and improving the density. The maximum density achieved by optimised TSS conditions was 95% of theoretical. This compared favourably, however, to the 91% achieved by single-step sintering (SSS). 5KNN ceramics densified by optimised TSS exhibited enhanced piezoelectric, dielectric properties, energy conversion efficiency and energy density. The typical dielectric, piezoelectric and ferroelectric property values of $\varepsilon_r \approx 294$, d_{33}=101 pC/N, k_p=0.33, P_r=9.8 μC/cm^2 and $\varepsilon_r \approx 337$, d_{33}=122 pC/N, k_p=0.36, P_r=12 μC/cm^2 have been observed for the 5KNN ceramics densified by SSS and TSS, respectively. Moreover, the correlation between grain size, density and functional properties were also studied.

In the second part, the dependence of sintering mechanism, phase structure and functional properties of the 5KNN ceramics on BNNO addition were investigated. The doping with Ba and Ni creates an oxygen-deficient environment, which caused the ex-solution of Ni at high sintering temperature even after a short soak time. Compared with 5KNN ceramics, all doped 5KNN ceramics exhibited denser, finer and more homogenous microstructures. The phase transition diagrams of (1-y) 5KNN - y BNNO ($y \leq 0.10$) have been successfully established by employing Raman spectroscopy and X-ray diffraction. It revealed that the (1-y) 5KNN - y BNNO systems evolved from orthorhombic (y=0, 5KNN) phase to tetragonal phase with a raise in y. At elevated temperatures up to 500°C, the KNN-based ceramics underwent an additional phase transition from orthorhombic→tetragonal→cubic phase, and the Curie temperature decreased from ~415°C in y=0 composition (5KNN) to ~168°C in y=0.10 composition (5KNN-10BNNO). The highest room temperature functional properties have been detected for y=0.02 compositions. The typical dielectric, piezoelectric and ferroelectric property values of $\varepsilon_r \approx 742$, d_{33}=132 pC/N, k_p=0.42, P_r=14 μC/cm^2 and $\varepsilon_r \approx 337$, d_{33}=122 pC/N, k_p=0.36, P_r=12 μC/cm^2 were observed for the 5KNN-2BNNO and 5KNN composition, respectively. However, with further increases in the dopant level, the 5KNN-based ceramics exhibited enhanced conductivity, relaxing dielectric properties and degraded piezoelectric properties on account of the high concentration of oxygen-vacancy and phase transition that developed. Moreover, a continuous bandgap reduction was also found in all doped compositions.

In the third part, energy harvesters were designed, prepared and tested using 5KNN and 5KNN-2BNNO piezoelectric elements. The performance comparison of the energy harvesters suggested that functional elements with higher electromechanical coupling coefficient and energy density may be preferred for the selection of piezoelectric materials, while higher polarisation and narrower bandgap may be preferred for the selection of multifunctional materials. The highest open-circuit voltage (1.77 V) and power density (268 μW/cm^3) were observed on 5KNN-2BNNO hybrid energy harvester under vibration at 10 Hz, combined with illumination. Results from the prepared 5KNN-2BNNO hybrid energy harvester indicated the potential of the novel 5KNN-2BNNO multifunctional materials for energy harvesting applications.

Contents

Index of figures

Index of tables

List of abbreviations and acronyms

Materials

KNN $(K, Na)NbO_3$	Sodium potassium niobate
KN $KNbO_3$	Potassium niobate
NN $NaNbO_3$	Sodium niobate
5KNN $(K_{0.5}Na_{0.5})NbO_3$	Sodium potassium niobate in 50/50 composition
$Ba(Ni_{0.5}Nb_{0.5})O_{3-\delta}$	Barium nickel niobate in 50/50 composition, BNNO
5KNN-2BNNO	$0.98(K_{0.5}Na_{0.5})NbO_3$-0.02 $Ba(Ni_{0.5}Nb_{0.5})O_{3-\delta}$
5KNN-4BNNO	$0.96(K_{0.5}Na_{0.5})NbO_3$-0.04 $Ba(Ni_{0.5}Nb_{0.5})O_{3-\delta}$
5KNN-6BNNO	$0.94(K_{0.5}Na_{0.5})NbO_3$-0.06 $Ba(Ni_{0.5}Nb_{0.5})O_{3-\delta}$
5KNN-8BNNO	$0.92(K_{0.5}Na_{0.5})NbO_3$-0.08 $Ba(Ni_{0.5}Nb_{0.5})O_{3-\delta}$
5KNN-10BNNO	$0.90(K_{0.5}Na_{0.5})NbO_3$-0.10 $Ba(Ni_{0.5}Nb_{0.5})O_{3-\delta}$
BTO $BaTiO_3$	Barium titanate
PZT $Pb(Zr_xTi_{1-x})O_3$	Lead zirconate titanate
BCZT	Barium zirconate titanate
MPB	Morphotropic phase boundary
PPT	Polymorphism phase transition
FPOs	Ferroelectric perovskite oxides
PFs	Photovoltaic ferroelectrics
PVA	Polyvinyl alcohol binder
FTO	Fluorine doped thin oxide coated glass
TSS	Two-step sintering
SSS	Single-step sintering

Devices

EH	Energy harvesting
EHers	Energy harvesters
EEHers	Electrostatic energy harvesters
PEEHers	Piezoelectric energy harvesters
PV-PEEHer	Photovoltaic-piezoelectric energy harvesters
KEHers	Kinetic energy harvesters
HEH	Hybrid energy harvesting

PV-FEEHers	Photovoltaic-ferroelectric energy harvesters
HEHers	Hybrid energy harvesters
WSNs	Wireless sensor networks
EMEHers	Electromagnetic energy harvesters
ESEHers	Electrostatic energy harvesters
MEMS	Microelectromechanical systems
RF	Radio frequency
PCs	Photovoltaic cells
IDE	Interdigitated electrode
PPE	Parallel plate electrode

Equipment

SEM	Scanning electron microscope
DSC	Differential scanning calorimetry
TGA	Thermal gravimetric analysis
STA	Simultaneous thermal analyser
XRD	X-ray diffraction or X-ray diffractometer
BSE	Back scattering electron
CCD	Charge coupled device
EDS	Electron dispersive X-Ray spectroscopy
UV-vis-NIR	Ultraviolet-visible-Near Infrared spectrophotometer

Parameters

T	Temperature
T_c	Curie temperature (ferroelectric-paraferroelectric phases transition temperature)
$T_{R\text{-}C}/T_{C\text{-}R}$	Rhombohedral - cubic phases transition temperature
$T_{T\text{-}C}/T_{C\text{-}T}$	Tetragonal - cubic phases transition temperature
$T_{R\text{-}O}/T_{O\text{-}R}$	Rhombohedral - orthorhombic phase transition temperature
$T_{O\text{-}T}/T_{T\text{-}O}$	Orthorhombic - tetragonal phases transition temperature
A	Area
$tol.$	tolerance factor
r	Ionic radii
s^{E}	Compliance constant

D	Electric displacement
E	Electric field
T	Mechanical stress
S	Mechanical strain
C	Capacitance
f_0	fundamental resonant frequency,
f	overall natural resonant frequency
λ_0	function of fundamental resonant boundary condition
ρ	density
L, l	length
w	width
t	thickness
F	applied force
m	mass
d	diameter
d_{hkl}	Lattice spacing
θ	Incident angle of X-ray beam
m_{pul}	mass per unit length
I	moment of inertia
y	distance
i	Mode index of vibration
ε	permittivity
ε_r	relative permittivity
ε_0	vacuum permittivity of free space
$tan\delta$	dissipation factor or dielectric loss factor
ω	Frequency in angular
Z'	Real part of impedance
Z''	Imaginary part of impedance
d_{15}, d_{33}, d_{31}	Piezoelectric charge coefficient
g_{33}	Piezoelectric voltage coefficient
k_p, k_{eff}	Electromechanical coupling coefficient
Q_{m}	mechanical quality factor
f_r	resonant frequency (piezoelectric)
f_a	anti-resonant frequency (piezoelectric)

h	Planck constant
v	Photon's frequency
R_∞	Reflectance
E_c	Coercive field
P_r	Remanent polarisation
P_s	Spontaneous polarisation
E_g	Bandgap
E_{pi}	Polarisation-induced internal electric field
E_d	Depolarisation field
E	Modulus of elasticity
I	Moment of inertia
U	Electric energy
u	Energy per unit volume
I_{sc}	Short-circuit current
V_{oc}	Open-circuit voltage
V_R	Voltage across the resistor
P	Power
P_d	Power density
P_{RMS}	Root mean square of power in 30 cycles
FF	Fill factor
η	Energy conversion efficiency
a, b, c	Lattice constant length
DFOM	Dimensionless figure of merit
QPA	Quantitative phase analysis
Γ FWHM	Full width at half maximum
$n\lambda$	Multiple of incident wavelength
k_β	Boltzmann constant
R	Universal gas constant
R_{wp}	Weighted profile R-factor
V	Unit cell volume
y	$Ba(Ni_{0.5}Nb_{0.5})O_{3-\delta}$ content
α, β, γ	Lattice constant angle
Φ_B	Schottky barrier height
Φ	Work function

Chapter 1. Introduction

Piezoelectric materials have been widely applied in sensors, actuators and transducers owing to their excellent capability of energy converting between electricity and mechanical vibrations[1–4]. Energy harvesting (EH) technology has been proposed and studied since 2000's[5,6], which is the process to convert environmental energy, for example, wind, sea wave and solar energy into useful electricity by using piezoelectric material. The development of piezoelectric materials and EH technology helps to relieve the pressure of energy utilisation and to address the issues of frequently replacing/recharging batteries and supplying efficient power[7]. Ferroelectric materials are the subset of piezoelectric materials owing to their switchable polarisation direction and strong build-in electric field. Recently, it is proved that the build-in filed in ferroelectric materials can be employed to separate the photo-induced carriers and enable to coupling the photovoltaic properties in ferroelectric materials, and this designed multifunctional materials (photovoltaic-piezoelectric-ferroelectric properties) can be used to prepare the synergistic energy harvesters (EHers) to improve the efficiency of energy conversion[8]. Hence, this project aims to develop a new multifunctional material to improve the efficiency of energy harvester prepared by piezoelectric materials.

Although piezoelectric materials are considered to be superior to other vibrational energy harvesters (EHers) on the micro/mesoscale, the output of these is still low and cannot completely fulfil the power requirements of electrical appliances[9]. Also, most widely used piezoelectric energy harvesters (PEHers) are made using lead-based materials, which is harmful for the environment and human health because of the toxicity of lead[10]. Furthermore, because of the limitations caused by the materials, most PEHers are only designed for harvesting kinetic energy[11,12]. In reality, this energy source is not always stable or continuously available. For example, a kinetic energy harvester (KEHers) is usually designed to harvest the vibration of machines or of humans walking[11,12]. However, machines do not run constantly and humans need to have a rest. Thus, the input energy can be highly variable. It is also essential to consider that most energy sources are coexistent. For instance, solar energy can simply be divided into light energy and thermal energy, also, kinetic energy and thermal energy usually coexist in both machines and human bodies.

Thus, a single-energy source induced energy harvester will waste a significant amount of harvestable energy which hinders the harvesting capability. Consequently, the development of multifunctional materials with a lead-free composition is required for the future manufacture of hybrid energy harvesters (HEHers)[13].

The coupling of photovoltaics and ferroelectric has attracted a great amount of interest in the hybrid energy harvesting (HEH) area. This is resulting in the assembly of multiple ideal properties in a single device to yield highly integrated energy harvesting[13]. In past decades, it was reported that the strong internal electric field in ferroelectrics can promote the separation of the light-induced carriers to enhance the conversion efficiency of the EHers[8]. However, it is difficult to obtain two excellent properties (photovoltaic properties and ferroelectric properties) in a single material on account of their fundamentally different mechanisms. Ferroelectric materials usually exhibit wide bandgaps (3-5 eV) due to the large electronegativity differences between its oxygen-atom and the metal-atom[14]. Therefore, the ferroelectric can only absorb <20% of the solar spectrum. It has been found that the lowering bandgaps is largely reliant on the presence of a high concentration of oxygen-vacancy[15]. Too many oxygen vacancies, however, will increase the conductivity and degrade the polarisation switching and thus will weaken the ferroelectric properties[16]. Hence, oxygen vacancies are a key factor of ferroelectric and photovoltaic properties[16].

The aim of this project was to combine the ferroelectric and photovoltaic properties in a single material to prepare a hybrid energy harvester. Therefore, the fabrication of 5KNN ferroelectric materials with lower bandgaps whilst keeping as large a spontaneous polarisation as possible is needed. It has been reported that two different metal cations (heterovalent ions) occupied the perovskite B-site can contribute to produce ferroelectric oxides with low bandgap, with one cation driving ferroelectricity and the other one generate a narrower bandgap in the visible range[14]. In this project, $(K_{0.5}Na_{0.5})NbO_3$ (5KNN) ferroelectric materials were selected as the ferroelectric hosts due to its lead-free composition, good piezoelectric properties and ferroelectric properties[17]. Considering the charge compensation and ionic radius, $Ba(Ni_{0.5}Nb_{0.5})O_{3-\delta}$ (BNNO) materials were introduced into 5KNN to tune the bandgap. The substitution of Ni ions in the Nb-site generated the oxygen vacancies for maintain charge neutrality in the 5KNN system. The combination of Ni^{2+} and oxygen vacancies could increase the electronic states of the host 5KNN materials, moreover, the large sizes of K^{+} and Ba^{2+} would help to maintain the stability of the perovskite structure[14,18].

This project contains broad but systematic studies, consisting of powder synthesis, ceramic fabrication and material characterisation, hybrid energy harvester preparation and dynamic vibration-illumination testing of hybrid energy harvesting devices. Furthermore, it displays the practicality of adopting KNN-based ferroelectric materials for the preparation of hybrid energy harvesting devices, giving a generic view of lead-free hybrid energy harvesting, creating relevant background and forming an initial data base in KNN-based hybrid energy harvester group.

Thesis overview

The thesis structure is as follows:

Chapter 2: The background of multifunctional materials, from their fundamentals and mechanisms of work principles to the corresponding fabrication processes are comprehensively reviewed.

Chapter 3: An introduction to the energy harvesting topic including the energy situation, basic structure, structure coupling and optimisation of the hybrid energy harvester and requirements of multifunctional materials.

Chapter 4: The aims and objectives of this project are summarised.

Chapter 5: The experimental approach used to fabricate and characterise the multifunctional materials and subsequently fabricate and test the hybrid vibration-light energy harvesters are described.

Chapter 6: The optimisation of the synthesis and sintering of pure $(K_{0.5}Na_{0.5})Nb_3$ (5KNN) ceramics and the sintering mechanism of pure KNN are discussed. In addition, the properties of pure 5KNN are characterised and the dependence of functional properties on density and grain size are also provided.

Chapter 7: The (1-y) $(K_{0.5}Na_{0.5})Nb_3$-y $Ba(Ni_{0.5}Nb_{0.5})O_{3-\delta}$ (y=0.00, 0.02, 0.04, 0.06, 0.08, 0.10) systems are investigated from the perspective of powder synthesis, ceramics processing and the characterisation of structural, dielectric, ferroelectric, piezoelectric and optical properties. The functional properties with respect to the doping amount are also discussed.

Chapter 8: The prototype hybrid energy harvesters were designed, prepared and tested. The effects of material properties and devices structure on the performance of prepared energy harvester are also discussed.

Chapter 9: The main conclusions of this research work and opportunities for future studies in this field are given.

Chapter 2. Multifunctional materials

2.1 Introduction

In recent years, ferroelectric perovskite oxides (FPOs) have aroused great interest for use in the manufacture of hybrid energy harvesters (HEHers) due to their three-way coupling among mechanical, optical and electrical properties in a single material[14,18]. This chapter will introduce the fundamentals of piezoelectricity and photovoltaics, and the mechanism of the coupling effect between them.

2.2 Piezoelectricity

2.2.1 Phenomenology

Piezoelectricity comes from the Greek word *piezein*[19]. In 1880, the phenomenon of piezoelectricity was first discovered by brothers Pierre and Jacques Curie, from quartz (SiO_2), Rochelle salt (potassium sodium tartrate, $KNaC_4H_4O_6{\cdot}4H_2O$) and tourmaline[20]. Following that, the technical term was put forward by W. G. Hankel in 1881[21]. The Piezoelectric Effect literally means to generate electric power via the stressing (by pressing or squeezing) of those materials that demonstrate 'piezoelectricity'. This is defined as coupling between mechanical properties and electricity in a crystalline material. The piezoelectric effect can be simply divided into the direct piezoelectric effect and the converse piezoelectric effect[22]. The direct piezoelectric effect (figure 2.1 a) means that potential difference will be produced across the crystalline material when it is under strain. The converse piezoelectric effect, however, (figure 2.1 b) defines that the deformation will be generated when the crystalline material is applied by an external electric field. Because of the coupling of mechanical force (or displacement) and electricity, the piezoelectric effect is widely utilised as sensors, actuators and energy harvesters in the aerospace field[23], traffic integration field[24], the medical industries (ultrasound transducer application)[25]. For example, the usage of piezoelectric materials for energy harvesting applications has the potential to be the replacement of hazardous electrochemical battery as a permanent power source for sensor systems[26]. Thus, the progress of piezoelectric material research and even efficiency improvement of energy harvesting devices will make everyday life become more convenient, greener, and leaving clean air as well as plentiful energy resources for our descendants.

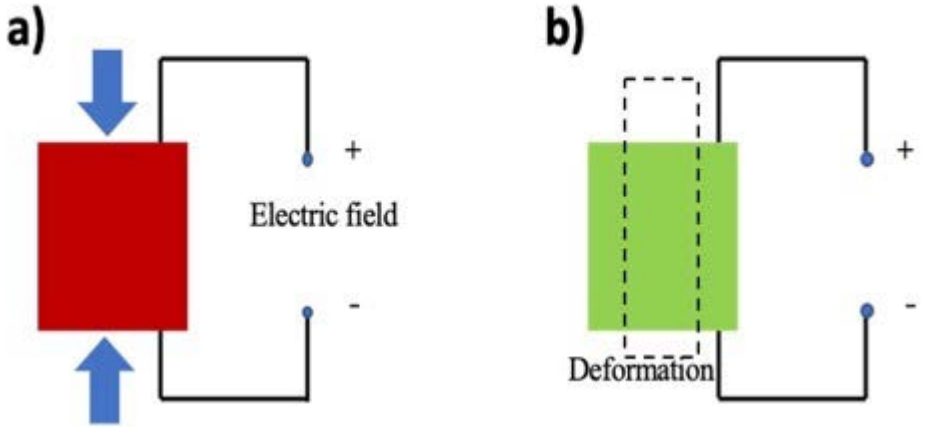

Figure 2.1 Schematic explanation of a) direct piezoelectric effect and b) converse piezoelectric effect

2.2.2 Fundamentals

2.2.2.1 Crystallographic structure

Piezoelectricity is derived from the asymmetric structure within the crystal. In a non-centrosymmetric crystal, the positive ions centre and negative ions centre is not coincident, thus a dipole moment with a built-in electric field generates, its direction is opposite to the dipole orientation, leading to a charged state on the boundary of the unit cell[22]. For a centrosymmetric crystal, however, the centre of the positive and negative charges is not separated, leading to a zero-net charge in the crystal unit cell (no piezoelectric properties)[22].

According to the Crystallographic Theory, 32 crystal point groups exist of which only 20 do not possess a centre of symmetry and can thus generate a piezoelectric effect[22]. Amongst the 20 crystal point groups without a centrosymmetric unit cell structure, only 10 can be said to have a ferroelectric structure. The crystallographic classification is shown in figure 2.2. In principle, the ferroelectric structure is used to describe the units that allow more than two spontaneous polarisation orientation states under no external electric field[27]. If the spontaneous polarisations can be shifted by changes of temperature, the crystals are identified as pyroelectric material. If they can be reoriented by an applied electric field permanently, the crystals are known as ferroelectric material. Therefore, it is easy to understand that the ferroelectric material is a subset of the set of pyroelectric and piezoelectric material, because they are polar material in which the spontaneous polarisation direction can be changed by the application of an electric field and temperature[28]. For example, $Pb(Zr_xTi_{1-x})O_3$ (PZT) in perovskite structure is ferroelectric because it exhibits polarisation switching characteristics under electric fields. ZnO (Wurtzite structure), however, is pyroelectric because the dipole moment of ZnO

is aligned with the crystal orientations, influenced by the applied temperature and is non-switchable[29]. SiO_2 crystals (diamond structure) are solely piezoelectric materials, because they can only generate the dipole moment under stress or an electric field and do not exhibit a net dipole moment under static conditions[30].

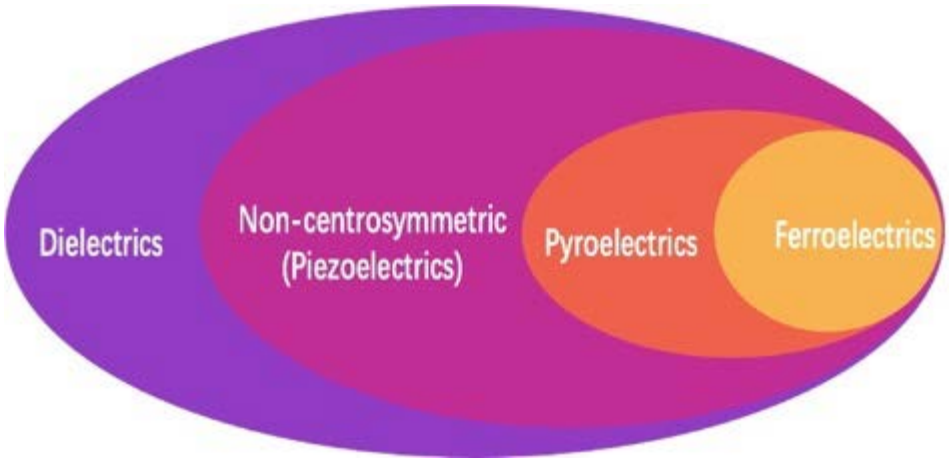

Figure 2.2 Crystallographic classification

2.2.2.2 Perovskite structure

Piezoelectric materials were not widely studied until barium titanate ($BaTiO_3$, BTO) ceramics were investigated. The unit cell of these types of materials is the perovskite structure (ABO_3). In the formula of ABO_3, "A", atoms occupy the corners (eight positions) of a cube, known as an "A site", the "O" atoms occupy the face centre (six positions) and the "B" atoms occupy the body centre (one position), known as the "B" site. For example, the $KNbO_3$ (KN) piezoelectric material is one of the promising lead-free piezoelectric materials. Eight potassium ions (K^+) occupy the A site, six oxygen ions (O^{2-}) take up the face centre positions as well as one niobium ion (such as Nb^{5+}) occupies the body centre of the $KNbO_3$ cube. A schematic diagram of KN crystal is clearly shown in figure 2.3.

The perovskite structure is extremely sensitive to temperature, *i.e.* changes in temperature can distort it, leading to a change in the piezoelectric properties. Figure 2.4[31] demonstrates the changing of the crystallographic structures of PZT, the most commonly used piezoelectric material of the last 50 years. When temperature is higher than the Curie temperature (T_c), PZT ($PbZr_xTi_{1-x}O_3$), a solid solution of $PbTiO_3$ and $PbZrO_3$, shows cubic symmetry with no piezoelectricity as the centres of the positive and negative charges overlap, which means that no dipole-moment can be existed. When the temperature is decreased (below T_c), the lattice structure of $PbZr_xTi_{1-x}O_3$ becomes distorted along the <100>, <110>

or <111> directions and an extremely active phase transformation exists. The oxygen ions (O^{2-} octahedra), the lead ions (Pb^{2+}), zirconium ions (Zr^{4+}) and titanium ions (Ti^{4+}) produce a relative shift, resulting in the development of the net dipoles, which is indicated by the arrows in figure 2.4.

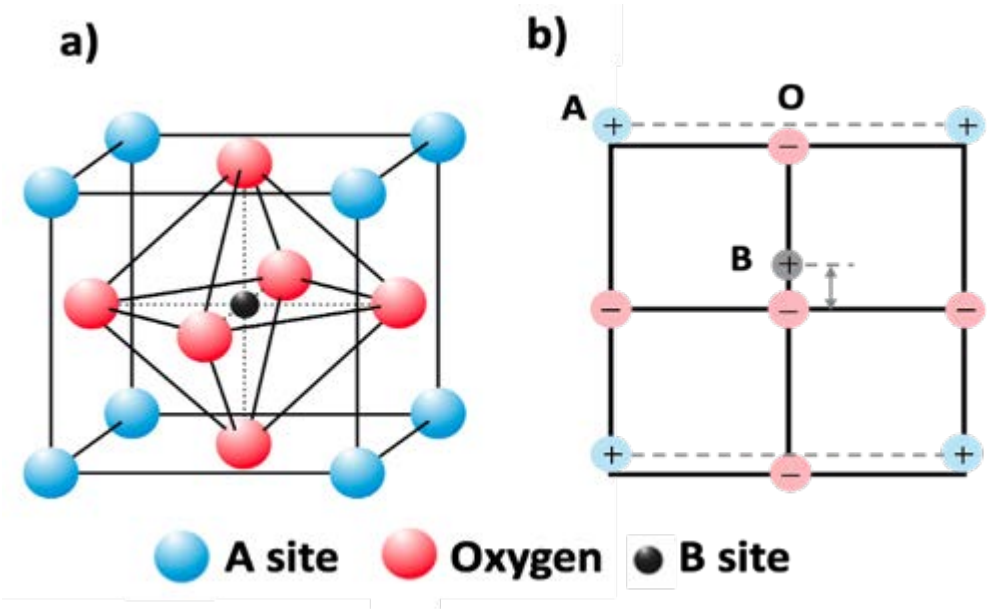

Figure 2.3 Schematic diagram of a) the perovskite crystal structure and b) side view of the tetragonal structure

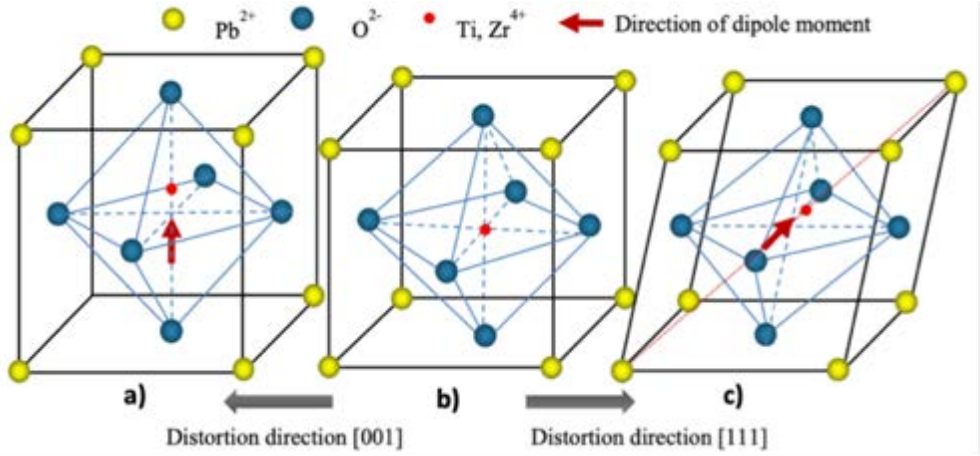

Figure 2.4 The different structures of $PbZr_xTi_{1-x}O_3$, a) tetragonal phase, b) cubic phase and c) rhombohedral phases[31]

The perovskite structure is also very sensitive to the composition, as such the mole ratio of Zr and Ti in $Pb(Zr_xTi_{1-x})O_3$ or Na and K in $K_{1-x}Na_xNbO_3$. The composition-temperature-phase diagram of PZT is exhibited in figure 2.5[32]. With the increasing of $PbTiO_3$ addition, the phase of PZT gradually transforms from a rhombohedral to a tetragonal phase. It can be seen from figure 2.5 that the rhombohedral –

tetragonal phases transition boundary, well-known as the morphotropic phases boundary (MPB, x=0.52 at room temperature for $PbZr_xTi_{1-x}O_3$ system), is almost independent of temperature. It is well known that PZT ceramics possess the best piezoelectric properties when the composition close to the MPB since two ferroelectric phases co-exist, allowing more polarisation directions[32,33].

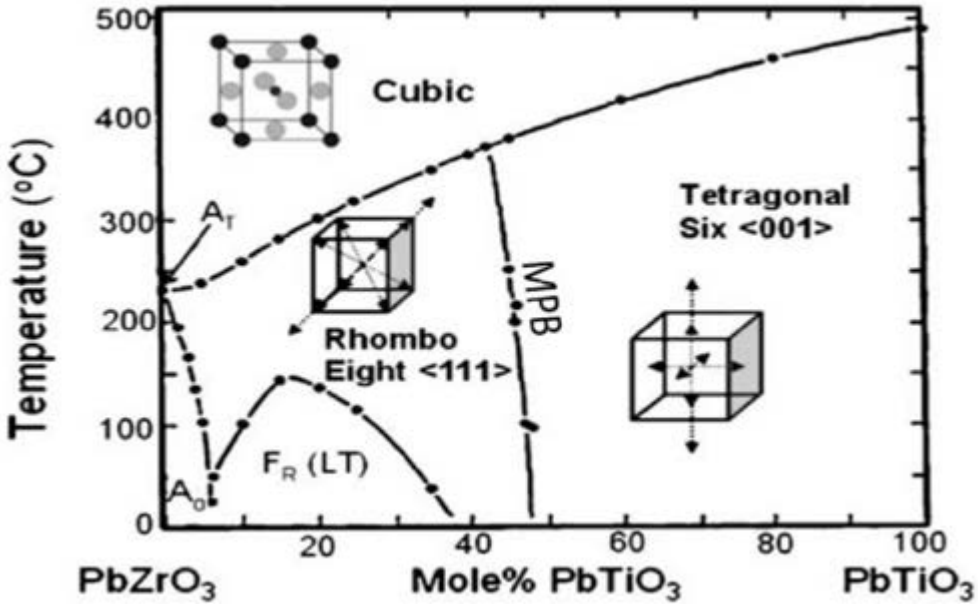

Figure 2.5 Phase diagram of the $PbZrO_3$- $PbTiO_3$ system[34]

Piezoelectricity originates from the asymmetric structure. To maintain the perovskite structure stability, the Goldschmidt tolerance factor ($t.$), which is an indicator for predicting the stability and distortion of crystal structures based only on the chemical formula[35], ABO_3, and the ionic radius of A-site ions, B-site ions and oxygen ions[35]. The mathematical expression of the tolerance factor is given in Equation 2-1[35,36]:

$$t. = \frac{r_A + r_O}{\sqrt{2} \cdot (r_B + r_O)} \qquad 2\text{-}1$$

Where r_A, r_B and r_O are the ionic radii of A/B-site ion and oxygen ions, respectively. For the cubic perovskite phase, 0.9<$t.$<1.0; for the tetragonal/hexagonal perovskite phase, $t.$>1.0; and for the orthorhombic/rhombohedral perovskite phase, 0.71<$t.$<0.9. In order to retain the stability of other non-cubic perovskite phases, $t.$ needs to be considered[33,37].

2.2.3 Domains and poling process

As mentioned previously, because of the non-coincidence of the positive and negative ion centre, piezoelectric materials possess a dipole moment and generate a charged state on the boundary of the

crystal unit cell[22], *i.e.* every unit cell in a piezoelectric material presents its own spontaneous polarisation direction. If the spontaneous polarisations are aligned along the same direction in crystal regions which are defined as a "domain", the interface between the two domains is defined as the "domain wall" [38]. Figure 2.6 a)[39] illustrates the domain configurations of a polycrystalline ferroelectric ceramic material in which the orientations of grains are usually random, the different orientation of domains will offset the polarisation of the other, resulting in a weak or zero piezoelectric effect. Therefore, in order to reorient all domains to the same or similar direction, a high electric field needs to be applied. This high electric field treatment process is called poling, illustrated in figure 2.6 b) and c), and is usually carried out at a high temperature (below T_c) for increasing domain wall mobility. During poling, the domains with randomly oriented directions are forced to align along the applied electric field direction (figure 2.6 b). After poling, the direction of domains is along or close to the direction of applied electric field, generating a net dipole in the poling direction.

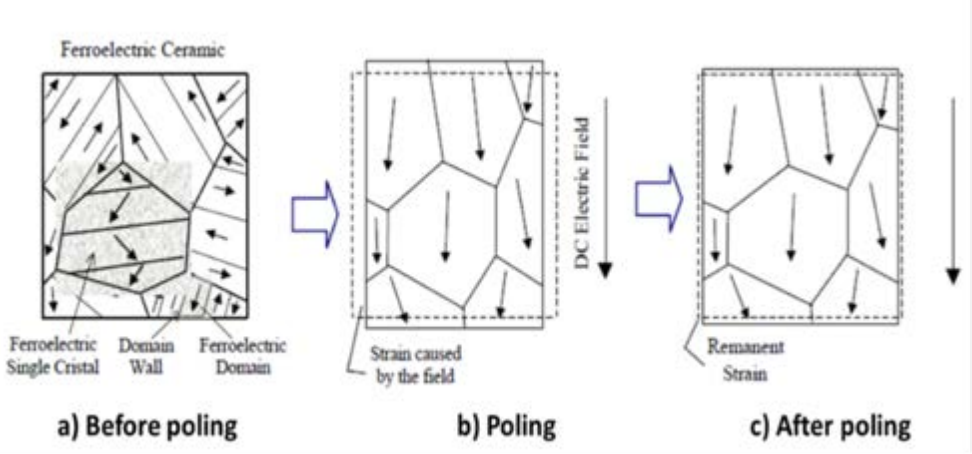

Figure 2.6 Domain configurations a) before poling, b) during poling and c) after poling[39]

2.2.4 Properties and related parameters of the piezoelectric ceramic materials

Because the performance of polarised piezoelectric materials is different from anisotropic and isotropic structures. Therefore, the notations of axis are required to describe piezoelectric behaviour along different directions. Figure 2.7 presents the widely accepted convention of piezoelectric ceramic materials.

The directions of the piezoelectric effect can be clearly seen in figure 2.7. Normally, the poling directions are defined as "3(z)" and the "1(x)" and "2(y)" are orthogonal in the axis "3(z)" (such as a space rectangular coordinate system). The three rotational directions marked as "4" direction (around

"1" direction), "5" direction (around "2" direction) and "6" direction (around "3" direction) are the shear piezoelectric directions regarding to the direction "1(x)", "2(y)" and "3(z)", respectively.

As reviewed in section 2.2.1, the piezoelectricity describes the conversion of mechanical force/displacement and electricity. Thus, one of them is input power and the other one is output power. For example, the vibration (mechanical force) can be converted to electricity by a vibrational energy harvester. Because both force and voltage are vectors, the direction of input and output need to be defined and are inserted as subscripts to certain parameters (figure 2.7 b). The first number represents the input direction (electric field or stress), and the second number represents the responding directions (electric field or displacement). For example, A_{31} is described by the piezoelectric effect A of materials being stimulated by the "3(z)" direction and acted on the "1(x)" direction. To be specific, the d_{31} coefficient (*d* represents the piezoelectric charge constants) relates the input energy (stress) along the polar axis (direction "3") and the output energy (potential difference/strain) along direction "1", and the d_{33} coefficient represents the input energy (stress/electric field) along the polar axis (direction "3") and output energy (potential difference/strain) acts on direction "3".

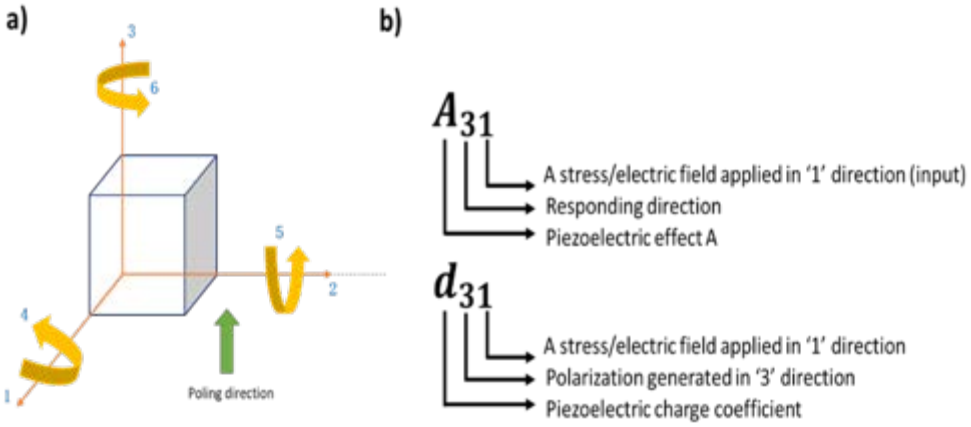

Figure 2.7 a) Notations of axes for the poled ceramic elements and b) Defined properties[22]

2.2.4.1 Dielectricity

Dielectric materials are well-known as electrical insulators that can store charges (polarised) by applying an electric field (*E*) and, as shown in Figure 2.2, piezoelectric, pyroelectric and ferroelectric material are all subsets of this classification. Permittivity (denoted by ε) is used to evaluate the electric polarizability of dielectrics[40]. A dielectric material with a high permittivity represents high polarization

(the ferroelectric hysteresis loop could make this visible[41] in section 2.2.4.3), *i.e.* storing more charges. Permittivity can be affected by a change of temperature and transition of the phase structure. The change of permittivity with temperature for a single BTO crystal is demonstrated in figure 2.8[42]. It can be clearly observe from figure 2.8 that above the Curie temperature (T_C), the dielectric permittivity falls off with temperature. Relative permittivity (ε_r), the ratio of the permittivity and the vacuum permittivity, can be calculated using the equation 2-2:

$$\varepsilon_r = \frac{\varepsilon}{\varepsilon_0} \qquad 2\text{-}2$$

where ε_0 is the permittivity of free space in a vacuum, ε_r can be interpreted as the relative permittivity.

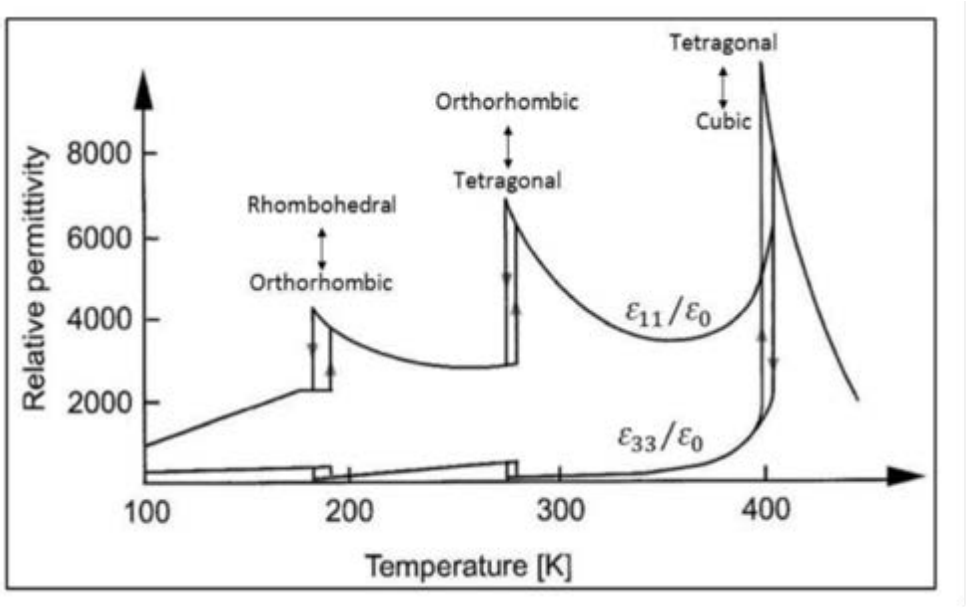

Figure 2.8 Relative permittivity as a function of temperature of single crystal $BaTiO_3$[42]

In anisotropic materials, the dielectric properties can be represented by ε_{11} and ε_{33} (using the subscript notation described in Section 2.2.4).

Dielectric loss is also an important parameter of dielectric properties. When the material is under a varying electric field, there is some additional dissipation of energy induced within the dielectric material itself. This is because the phase of electric field and the phase of electric field induced dipole rotations and oscillations is different[43]. The term dissipation factor ($tan\delta$) is usually adopted to represent the dielectric loss level and the phase difference δ is called the loss angle. A higher $tan\delta$ indicates a larger dielectric loss.

2.2.4.2 Piezoelectricity

As previously mentioned, piezoelectricity means that certain crystals can generate an electric potential when force is applied or can generate deformation when placed in an external electric field.[5] The piezoelectric effect can be easily expressed by the following constitutive equations[5,38]:

$$D = dT + \varepsilon^T E \qquad 2\text{-}3$$

$$S = s^E T + dE \qquad 2\text{-}4$$

Where D, T, E, S are the electric displacement, mechanical stress, electric field and mechanical strain, respectively. s^E, d and ε^T represent the elastic compliance coefficient, piezoelectric charge constants and permittivity of the piezoelectric materials under constant stress.

For piezoelectricity, the conversion efficiency between mechanical energy and electric energy is very important; this is indicated by the coupling coefficient, k. Generally, the effective electromechanical coupling coefficient k_{eff} is expressed by Equation 2-5[44]. Due to the different vibration modes possible with different geometries (figure 2.9), the coupling coefficients also include k_p (planar mode), k_{31}(transverse mode), k_{33}(longitudinal mode), k_{15}(shear mode) and k_t(thickness mode), etc[45].

$$k_{eff}^2 = \frac{Mechanical\ energy\ converted\ to\ electric\ energy}{Input\ mechanical\ energy} \qquad 2\text{-}5$$

$$= \frac{Electrical\ energy\ converted\ to\ mechanical\ energy}{Input\ mechanical\ energy}$$

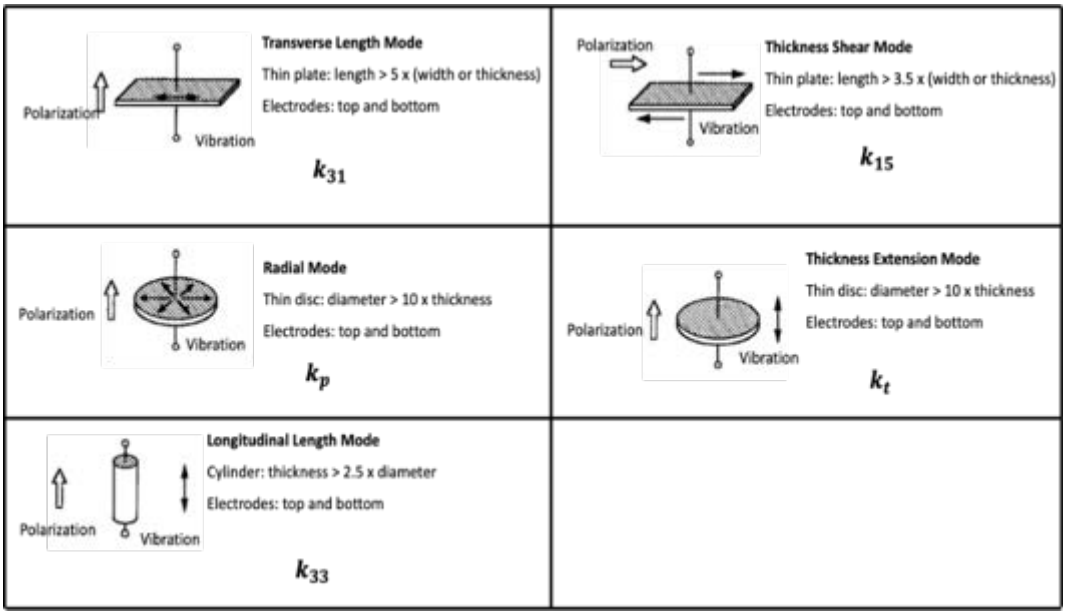

Figure 2.9 Vibration modes and standard sample shapes[46,47]

The mechanical quality Q_m is a dimensionless measure of the mechanical losses of piezoelectric resonators, describing the "sharpness of the resonance" of a piezoelectric resonator[47]. Q_m is the ratio of the energy stored in the oscillating resonator to the energy dissipated in each cycle during the damping; thus higher Q_m means lower mechanical loss[48]. This effect is explained by the following equation (2-6).

$$Q_m = 2\pi \cdot \frac{Stored\ Mechanical\ Energy}{Dissipated\ Energy\ per\ Cycle} = \frac{1}{2\pi f_m |Z| C^T k_{eff}^2} \qquad 2\text{-}6$$

2.2.4.3 Ferroelectricity

The polarisation directions of piezoelectric materials are switchable after induced an applied electric field (E), defined as ferroelectric materials[49]. Because the polarisation of ferroelectric varies with the E, the ferroelectricity can be simply demonstrated by an electrical-hysteresis loop exhibited in figure 2.10[50].

Hysteresis is the dependence of the state of a system on its history. As illustrated in figure 2.10[50], when the E increases from 0, the orientations of ferroelectric domains are forced to align in the direction of E and the polarisation rises until it arrives at the largest value (nearly all domains are aligned along the direction of E), known as the saturation polarisation. However, when the electric field decreases to 0, the polarisation is reduced to a value, called the remanent polarisation, rather than 0. Similarly, when the electric field increases in the reverse direction, the polarisation continues to decrease to 0 and increases in the reverse direction until the value of saturation. As the electric field is reversed again through zero to a positive value the second part of the hysteresis loop is defined. Thus, the remanent polarisation (P_r) and coercive field (E_c) are utilised to explain ferroelectric behaviour. P_r represents the trapped dipole amount after removing E. And E_c represents the critical electric field values, when the E beyond E_c, a permanent dipole-moment can be generated[51]. The higher P_r is, the better the piezoelectric effect is after poling and the lower E_c is, the easier the ferroelectric domains can be reoriented.

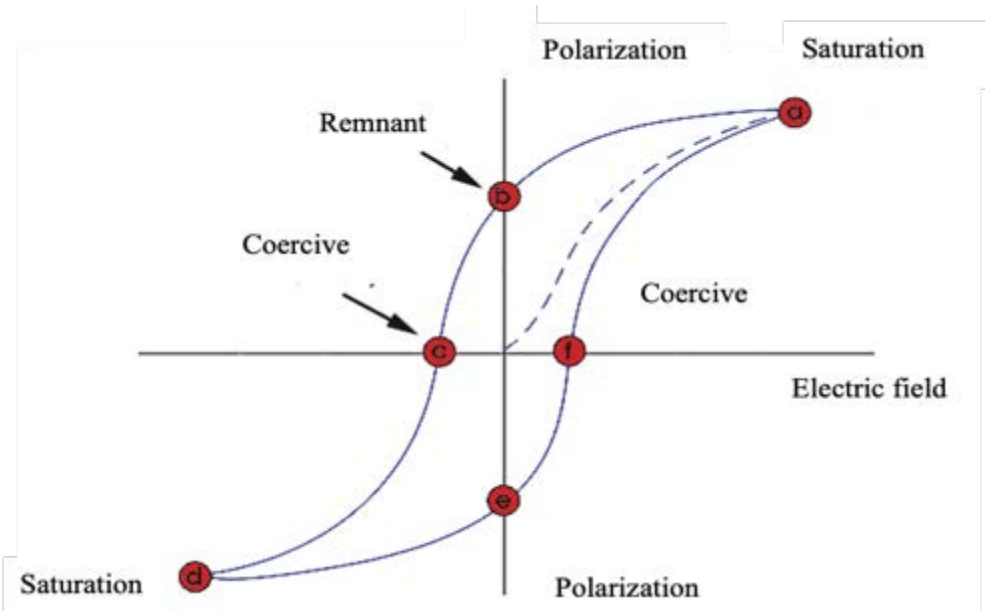

Figure 2.10 P-E hysteresis loop for a ferroelectric material[52]

2.3 Ferroelectric-photovoltaic

2.3.1 Photovoltaic phenomenology

The photovoltaic effect is regarded as the generation of voltage and electric current in a material after the illumination of light[53]. The photovoltaic effect was first observed in 1839 by Edmund[54]. Until the late 1880s, this theory was applied to build solid photovoltaic cells made of selenium. The efficiency of the selenium photovoltaic cells (PCs) was only 1-2% in converting light to electricity[55,56]. A milestone leap forward took place in 1954. Scientists working at the Bell Telephone Laboratories used silicon to produce PCs which improved the efficiency from 1% to 6% and then to 11%[55,56]. This improvement opened up the new photovoltaic era.

The photovoltaic mechanism can be simply described as follows. When sunlight enters into matter, the valence electrons (the electrons in the outermost orbit) can harness the solar energy and be excited from valence band (VB) to the conduction band (VB). This process creates a number of holes in the VB (positive) and free electrons in the CB (negative), thus, an asymmetric electric potential occurs across the materials (photocurrent)[56,57]. Electrons and holes generated in this manner are known as light-generated electron-hole pairs. Figure 2.11[56] exhibits an explanation of the electron-hole pairs in silicon generated by sunlight striking. However, these light-induced carriers will back to the ground-state due to the energy being given off as emission of the light or heat and the photovoltaic-effect is lost[56]. To avoid the recombination of electrons and holes, an asymmetric

potential, named P-N junction[58,59], was built in. This potential barrier can separate the light-generated electrons and holes selectively, sending more holes to one side and more electrons to the other side[56]. This barrier (P-N junction) is established by acceptor doping (positive, p-type dopant) and donor doping (negative, n-type dopant) depending on accepting an electron or donating the electrons[56,60]. Let's take silicon material as an example, when a silicon atom (Si, 4 valence electrons) doped with a phosphorus atom (P, 5 valence electrons), each P atom can generate 4 covalent bonds with a Si atom and the fifth electron of P is 'single' which brings in an electron (Figure 2.12 a). On the contrary, the substitution of a boron atom (B, 3 valence electrons) can form 3 covalent bonds with a Si atom and the fourth electron of Si is un-bonding which introduces a hole to make the fourth electron 'married' (Figure 2.12 b). The P-N junction is formed by p-type silicon (boron doped) with excess holes and n-type silicon (phosphorus doped) with excess electrons (Figure 2.12 c). A line separating the two different kinds of silicon sets up the position of a potential barrier to make the electric current pass through the junction only in one direction by means of an external circuit. However, the crossed carriers will also build an electric force (electric field) to impede the further flow of the free carriers (Figure 2.12 d and e). After equilibrium is established, no more electrons or holes can switch sides. [56,60] Moreover, the open-circuit voltage generated by P-N junction type solar cells is limited by the energy band of the p-type layer and the n-type layer and the matching state of the junction bandgap[61].

PCs are commonly made with semiconductor materials. Semiconductors with a larger bandgap[13](the width between the conduction band and valance band) will reduce the capability of the photovoltaic devices because the electrons require substantial amounts of energy for excitation from the VB to the CB. If the bandgap is too narrow, however, most protons will have more energy than necessary to excite electrons across the bandgap resulting in the return of electrons. Hence, bandgap is an important factor that affects photovoltaic efficiency. This limitation can be explained by the Shockley-Queisser limit[62], *i.e.* the maximum solar conversion efficiency of a single p-n junction PCs. The highest efficiency of 33.7% can be obtained at a bandgap of 1.34 eV.

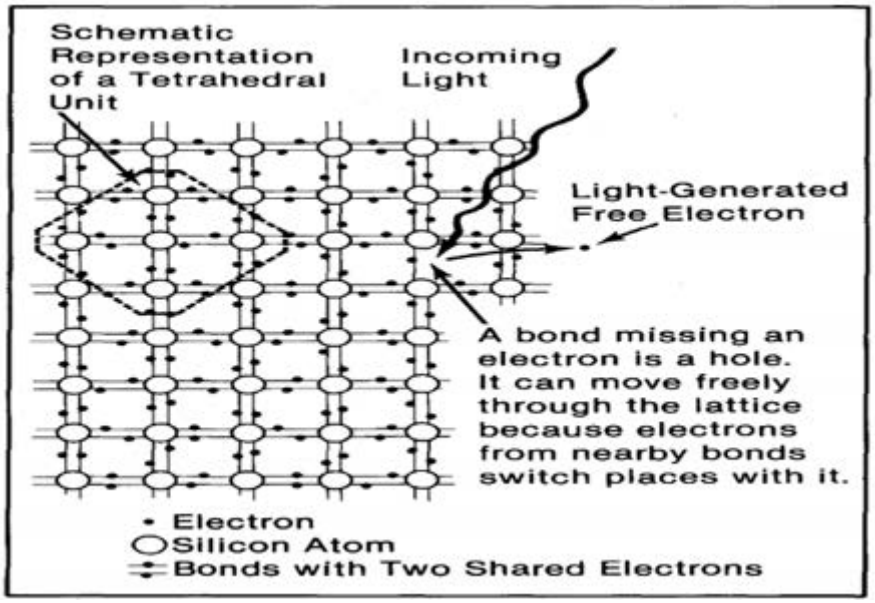

Figure 2.11 Schematic diagram of the electron-hole pairs in silicon generated by sunlight[56]

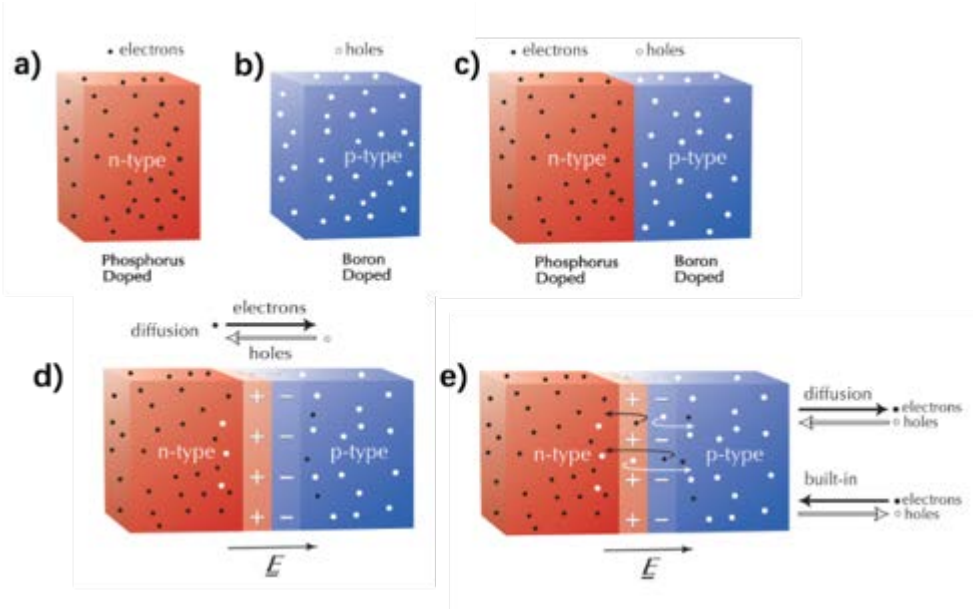

Figure 2.12 Schematic representation of (a) Donor doping, (b) acceptor doping of Silicon, (c) n-type and p-type silicon conjunction, (d) 'built-in' electric field established by diffusion and (e) movement of free electrons and holes because of the diffusion and the 'built-in' electric field[52]

2.3.2 Fundamentals of the photovoltaic effect in ferroelectrics

Photovoltaic effects in ferroelectrics were first reported in the 1950s[63] and are now gaining increasing attention due to the generation of high photo-voltages far beyond the bandgap and a steady photocurrent[64–66]. In contrast to conventional solar cells, the separation of charges in photovoltaic-ferroelectrics can be driven by the built-in potential[65] provided by the spontaneous polarisation.

Consequently, the Shockley-Queisser limitations (η<33.7%) are not predicted to apply to the photovoltaic-ferroelectric energy harvesters (PV-FEEHers)[67–71]. The working principles of P-N junction based solar cells and PV-FEEHers are demonstrated in figure 2.13[72].

The photovoltaic effect involves two processes which are the generation and separation of the light induced electron-hole pairs. As reviewed previously, ferroelectric materials can exhibit, over a range of temperature, spontaneous electric polarisations that can be reoriented by an external electric field. Thus, ferroelectrics can generate permanent built-in electric fields which can induce polarisation of the dipole and further adjust the polarised electric field, *i.e.* the internal electric field generated by polarisation can promote carrier separation resulting in a photocurrent. A explanation of this process is presented in figure 2.14[73,74]. Ferroelectric materials are employed to generate photo-excited electron-hole pairs and provide the polarisation-induced internal electric field (E_d) to enhance the separation rate of the photo-excited electron-hole pairs. Then the top/bottom electrodes can form the two Schottky barriers, leading to the depletion of the ferroelectric layer via built-in fields (E_d), at the interfaces between the photovoltaic-ferroelectrics and the electrode. Hence, it is concluded that the high open-circuit voltage generated by photovoltaic-ferroelectrics is due to the built-in potential. However, there are big controversies on the origin of this built-in field, since it is affected by several factors[75], such as the magnitude and direction of polarisation[70,76–78], domain walls[70,79] and depolarisation field[80]. Due to these multiple factors, it is difficult to understand the nature of the ferroelectric-photovoltaic effects. Therefore, in order to be able to further enhance the properties of multifunctional materials and the performance of the related devices, the mechanisms that drive the photovoltaic effect in ferroelectrics will be discussed below.

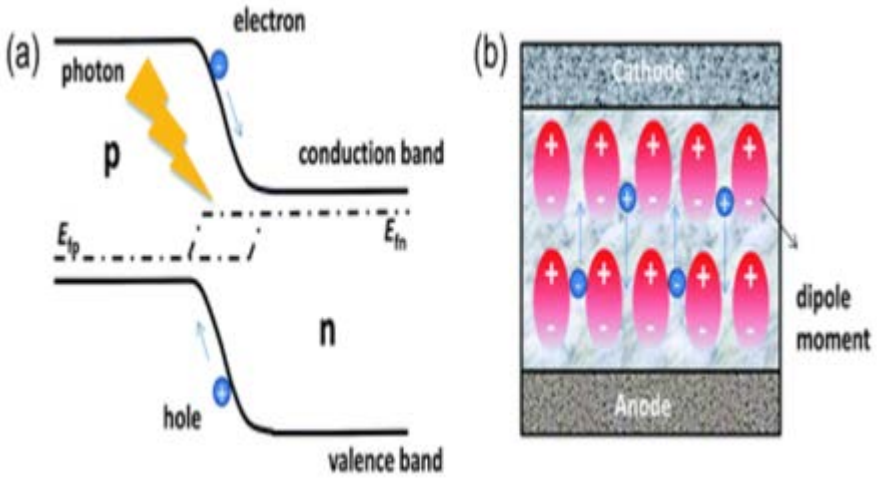

Figure 2.13 The working principles of a) P-N junction solar cell, b) ferroelectric-photovoltaic solar cell[72]

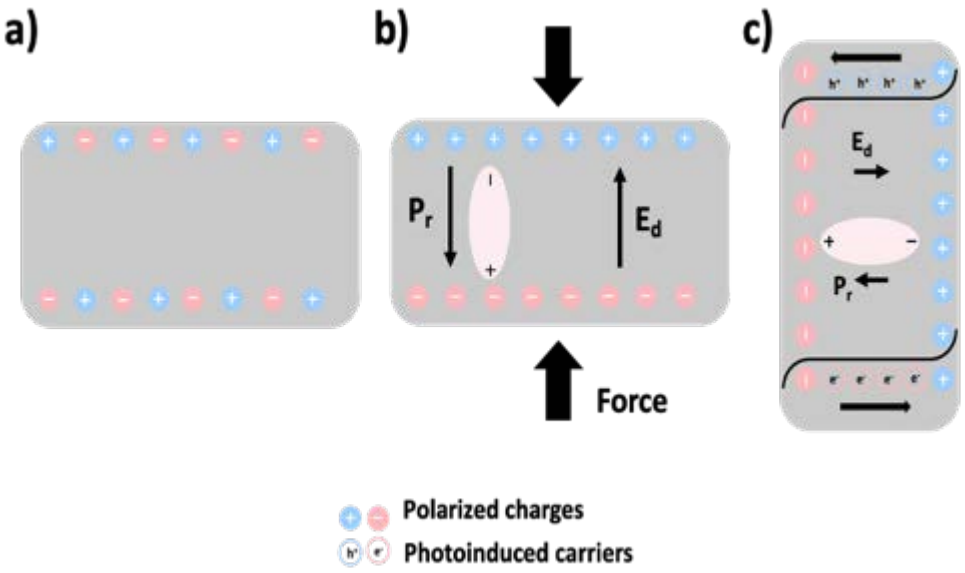

Figure 2.14 Explanation the photovoltaic effect in ferroelectric materials. a) piezoelectric-semiconductors without strain, b) piezoelectric semiconductors under force and c) separation of photo-generated charge carriers enhanced by the built-in electric field[73,74]

2.3.3 Mechanisms

Depolarisation field (E_d)

A photocurrent with a direction antiparallel to the polarisation was observed by Chen[81] and then it was hypothesised that the generation of the photocurrent was caused by an internal electric field opposite to the polarisation. This internal field was later identified as the depolarisation field E_d[82–84] (figure 2.14). As it is commonly known, a charge distributed at two separate surfaces of the ferroelectric material will produce a depolarisation field (E_d) with the direction opposite to the polarisation due to the incomplete screening of the ferroelectric polarisation charges[65,82]. For bulk ferroelectric materials, the effect of E_d can be ignored because the distances of the two charged surfaces of ferroelectrics are too large. For ferroelectric thin films, however, the effect of E_d cannot be ignored because the thickness of the thin film is usually below a few hundred nanometers[65]. The existence of E_d results in unstable polarisation and even the disappearance of ferroelectricity in ultrathin films[85–87]. Thus, ferroelectric polarisation in thin films can become stable only when the polarisation charges are screened by the charge carriers from the ferroelectrics themselves or from the electrodes. Moreover, the polarisation charges are normally partially compensated[65]. The residual E_d can thus act as a driving force to separate and transport photo-excited charge carriers. Because E_d exists over the whole thickness of the film, the photocurrent driven by E_d is uniformly distributed

within this region[65]. The E_d driven-photovoltaic model is the most straightforward way to explain the switchable photovoltaic response by manipulation of the ferroelectric polarisation[78,80].

Bulk photovoltaic effect

The bulk photovoltaic effect (BPVE), also called the photogalvanic effect or non-linear photonics, was driven by the non-centrosymmetric structure and proposed by Glass *et al*[66]. From a microscopic level, BPVE can be understood by using the ''ballistic'' and ''shift current'' models[71,75,88], a schematic diagram of which is represented in figure 2.15[73,89].

Due to the asymmetric structure, the electrostatic potential is also asymmetric. Hence, there exists anisotropy in the potential at an absorbing centre owing to the crystal polarisation[66]. Under the appropriate illumination, the thermalised carriers located at the valence band are excited by illumination to the conduction band, *i.e.* thermalised carriers are jumped from the state E_0 to an energy E (figure 2.15 a) [73,89]. If E is smaller than V_1 (potential energy), the excited electrons cannot across the energy barriers and remain trapped in the potential well[73,89]. If E is larger than V_2, the excited carriers can pass the V_1 barriers. If $V_1<E<V_2$, the carriers are partially scattered by the potential barriers and a net flow of carriers is established[73,89]. Also, in a non-centrosymmetric structure, the momentum of the carriers is asymmetric. From figure 2.15 b), the momentum is symmetric in a centrosymmetric structure. Therefore, no net flow of current can be built up. However, in an asymmetric structure, the momentum of the carriers in the conduction band is unevenly distributed. In order to equilibrate the asymmetric momentum, the carrier loses its energy and settles at the bottom of the CB by suffering a inter-band transition or a shift by distance l_0, hence generating an additional photocurrent leading to BPVE[88,90]. From the above discussion it can be concluded that the 'ballistic model' is built from the movement of charge carriers in the band[73,89]. The 'shift current model', however, is of a quantum-mechanical nature[89]. It is obtained by considering the asymmetry of electron density[89]. The BPVE in the ''shift'' model is caused by the virtual shift of carriers in the real space followed by the inter-band transition. After excitation, the behaviour of the carriers is dominated by coherent excitation, allowing the net current flow from the potential asymmetry[75,91–93]. This model is verified by the studies on $BaTiO_3$, $PbTiO_3$ ferroelectric[91,94] and $BiFeO_3$ multiferroic (the materials can also exhibit ferromagnetism properties)[94].

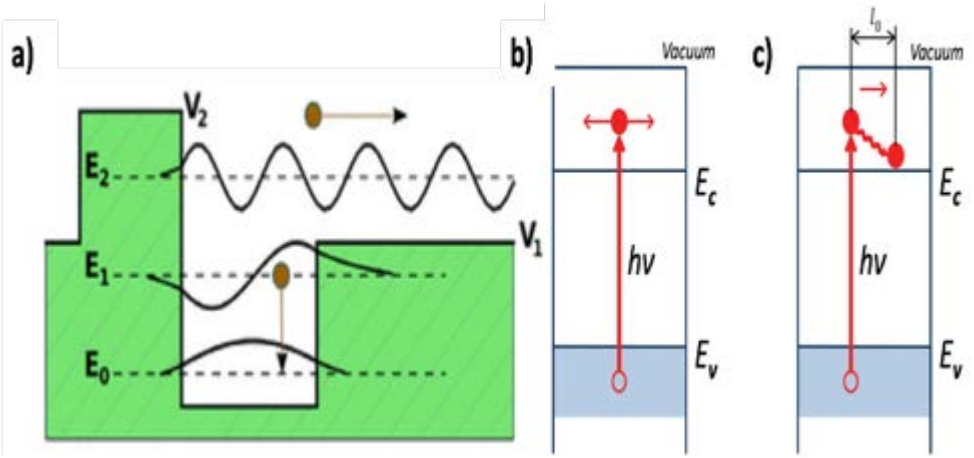

Figure 2.15 a) Asymmetric potential well at a carrier generation centre in non-centrosymmetric structures; b) photoelectrons in centrosymmetric crystals with isotropic non-equilibrium momentum distribution and c) photoelectrons in non-centrosymmetric crystals with anisotropic non-equilibrium momentum distribution, respectively[73,89]

Domain wall

Yang *et al*[70]. observed an interesting phenomenon (illustrated in figure 2.16[70]), a large photo-voltage (up to 16 V) can be obtained in the $BiFeO_3$ (BFO) with in-plane electrodes positioned parallel to the domain walls. However, no photovoltaic effect could be found in the BFO with in-plane electrodes positioned perpendicular to the domain walls. Therefore, the authors[65,70] proposed the domain wall theory to study the nature of the photovoltaic effect in ferroelectrics, *i.e.* the separation of photo-induced charges is driven by the electrostatic potential steps at the nanoscale domain walls (figure 2.17 a))[65,70].

Previous studies have calculated the existence of built-in potential steps at domain walls, generated from the component of polarisation perpendicular to the domain wall. The potential step offsets the conduction and valence bands and then leads to a zigzag band shape (figure 2.15 b)). Under illumination, charge carriers excited in the domain walls are more effectively separated by the built-in potential and easily drift to the other side of the domain wall. The photo-induced carriers within the domains, however, are highly localised, tightly bound and tend to recombine quickly[65,70]. Hence, in the area near the domain wall, a net imbalance of charge carriers and tilted band-structure are created (figure 2.15 c), d))[65,70]. Overall photo-voltage, the cumulative effect of potential steps across each domain wall, is then generated. Although the domain wall theory can answer many questions, such as the linear increase of the output photo-voltage with the electrode spacing[40], there are some experimental phenomena that still cannot be explained. For example, why can a BFO single-domain-

structured thin film still show above-bandgap photovoltage?[95]. Alexe *et al.*[96,97] demonstrated that the generation of non-equilibrium photo-excited charge carriers were uniform and were not significantly different between the domain and the domain walls. Alexe *et al.*[98] have also proposed that the origin of the analogous FPOs is BPVE rather than the domain wall effect. The domain walls only play the role of providing a higher density of non-equilibrium photo-excited charge carriers due to the higher photoconductivity of the domain walls[65].

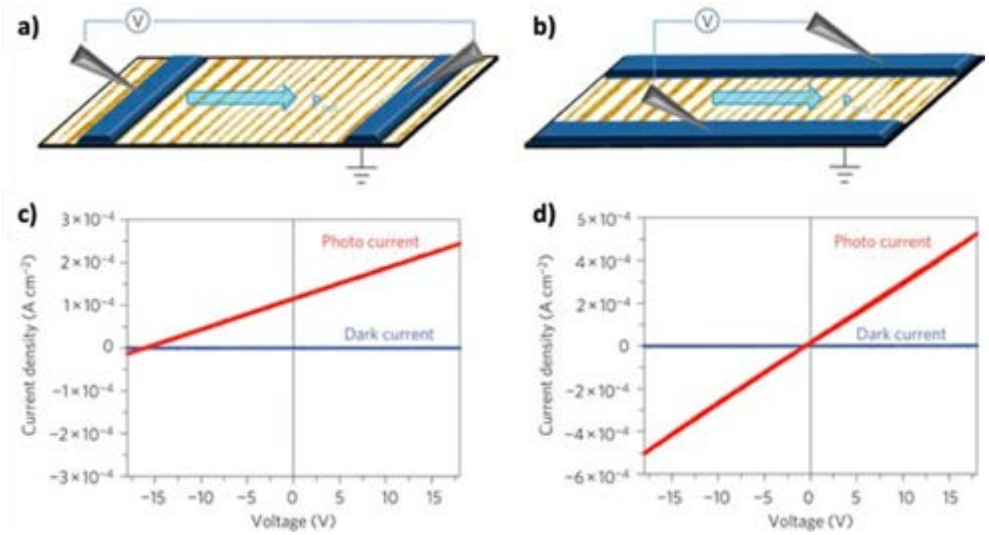

Figure 2.16 Schematic diagram of orientation of electrodes a) parallel and b) perpendicular to the domain walls. Corresponding I-V curves of devices with c) parallel and d) perpendicular electrode configurationns[70]

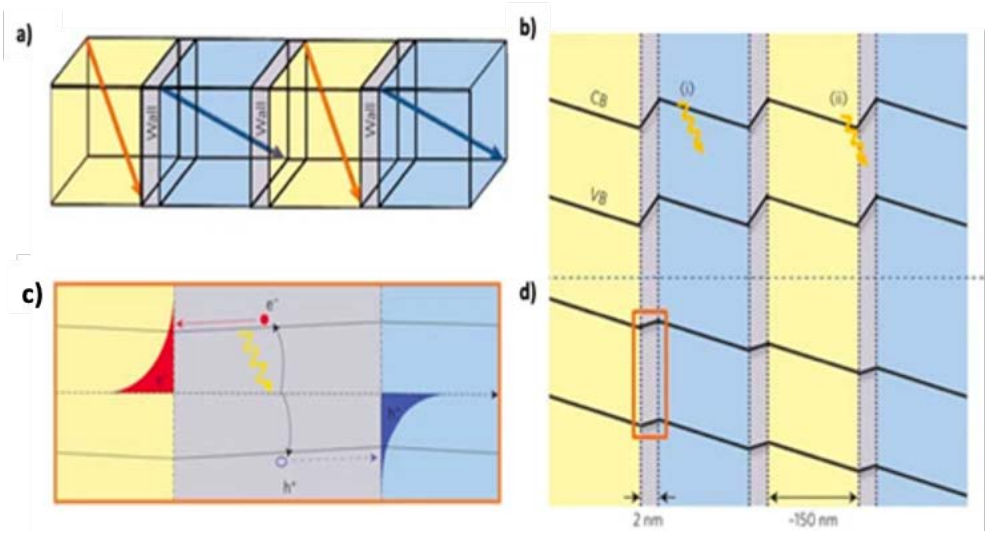

Figure 2.17 a) Schematic diagram of four domains (71° domain walls), b) band-transition presenting the valence band (VB) and conduction band (CB) across these domains and domain walls in the dark, c) evolution of band structure under illumination, d) detailed picture of the build-up photo excited charges at a domain wall[70]

Schottky-junction effect

A Schottky-barrier is another factor that may cause the photovoltaic effect in ferroelectric materials. Schottky-barriers, an interfacial energy barrier, are constructed at the interface between ferroelectric material and metal electrode owing to the differences in the work function, leading to the generation of a local electric field (E_{bi}, expressed in equation 2-7) at the depletion region near the interface of the ferroelectrics and electrodes. E_{bi} drives the separation of photo-excited electron-hole pairs, thus, the barrier height determines the output photo-voltage. Considering the thickness of the Schottky contact depletion layer (the thickness of the electrodes) is very small (<200 nm), the influence of E_{bi} is less significant than E_d. in bulk ferroelectrics. However, if the PV-FE layer is thin film, the higher the internal net potential E_{bi} is, the wider the depletion layer is, which would degrade the output of the solar cell[65].

$$\Delta\phi(E_{bi}) = \phi_{electrode} - \phi_{ferroelectrics} \quad 2\text{-}7$$

Where $\Delta\phi(E_{bi})$ is the local electric field induced by a Schottky-barrier. $\phi_{electrode}$ and $\phi_{ferroelectrics}$ are the work function of electrodes and ferroelectrics, respectively.

The total internal electric field (E_{total}) in photovoltaic-ferroelectrics is the difference between the depolarisation field induced by ferroelectric polarisation and the local electric field driven by the Schottky barriers (equation 2-8). The barrier height at the metal and ITO sides can be expressed by equations 2-9 and 2-10, respectively. Hence, it is easy to understand that the metal with lower work function can construct smaller barrier height. When illuminated by the photon energy higher than $\Delta\phi$, metal electrons could be emitted from the electrode surface and oriented by the E_d to participate in the separation process of photo-induced charge pairs. The effect of the Schottky-junction can be graphically represented as shown in figure 2.18[99]. Before poling, there is no internal built-in field in the ferroelectrics, hence, no band tilting occurs (figure 2.18 a). After negative poling (figure 2.18 b), a depolarisation field (E_d) is built in, the total internal field can be expressed in equation 2-11. In this case, the metal electrodes with higher work function can create higher internal field. However, after positive poling (figure 2.18 c), an internal field with reversed direction is built in, the total internal field can be written as equation 2-12. In this case, the lower the work function of metal electrodes is, the higher the internal field is.

$$E_{total} = E_d - \Delta E_{bi} \quad 2\text{-}8$$

$$E_{bi1} = \phi_{metal} - \phi_{ferroelectrics} \quad 2\text{-}9$$

$$E_{bi2} = \phi_{ITO} - \phi_{ferroelectrics} \quad 2\text{-}10$$

$$E_{total} = E_d + E_{bi1} - E_{bi2} \quad 2\text{-}11$$

$$E_{total} = E_d - E_{bi1} + E_{bi2} \quad \text{2-12}$$

where E_d is the depolarisation field of ferroelectrics, ΔE_{bi} is the local electric field; E_{bi1}, E_{bi2} and E_{total} are the local electric field in metal side, ITO side and the total internal electric field, respectively; $\phi_{electrode}$, ϕ_{ITO} and $\phi_{ferroelectrics}$ are the work function of metal electrode, ITO electrode and ferroelectrics, respectively.

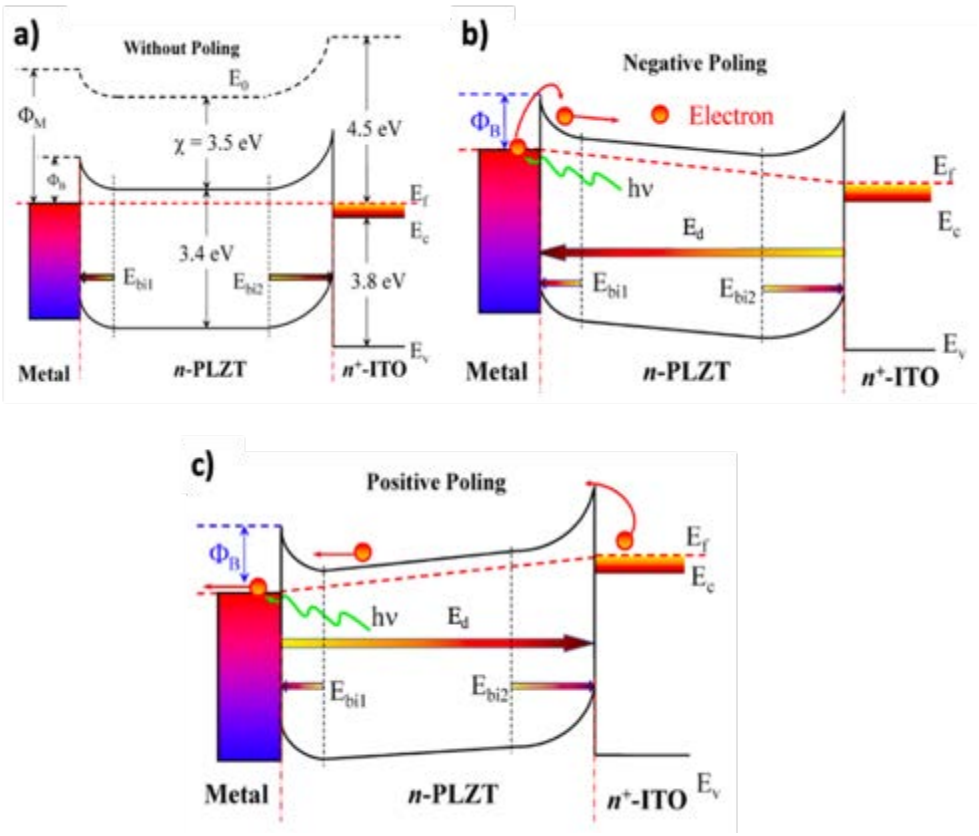

Figure 2.18 The energy band structure of metal/PLZT/ITO structure, where E_0 represents the vacuum energy band, E_c represents the conduction band, E_v represents the valance band, E_f represents the Fermi level, E_d is the depolarisation field: (a) Before poling, (b) after negative poling and (c) after positive poling (the e-h pairs photo-generated in PLZT are not showed in figure)[99]

Although PFs can provide such promising features as stable photocurrent, high voltage, etc[61]., there are still some drawbacks that need to be overcome. Ferroelectrics, as such KNN, PZT or BFO, usually have a relatively high bandgap (>3 eV) because the electrons need to travel from the valence band edge dominated by oxygen *2p* orbitals to the *d* orbitals of transition metals, such as Nb, Ti or Fe[14]. The wide bandgap limits the conversion efficiency resulted from low absorption in the solar spectrum and leads to poor charge transport properties because of the short-carrier diffusion lengths and lifetimes[65,72,75]. Several attempts have been made to narrow the bandgap via chemical replacement

and/or generating cation ordering. The detailed doping strategy used in this work will be introduced in section 2.4.1.2.

2.4 KNN-based ceramics

2.4.1 KNN-based piezoelectric materials

2.4.1.1 Crystal structure and phase diagram of pure $(K_{1-x}Na_x)NbO_3$

Potassium sodium niobate (KNN, $K_{1-x}Na_xNbO_3$) ceramics are pseudo-binary solid solutions formed by ferroelectric $KNbO_3$ and anti-ferroelectric $NaNbO_3$ (the properties are shown in Table 2-1)[100] and the studies of it for piezoelectric materials, can be traced back to as early as the 1950s[101]. Amongst the lead-free piezoelectric ceramics available, KNN is one of the most promising alternatives to replace lead-based piezoelectric materials owing to its excellent functional properties, such as a high T_C (~415°C), low relative permittivity and acceptable piezoelectric charge coefficient (*e.g.* d_{33}~160 pC N^{-1}, ε_r~586)[18,32,102,103].

Table 2.1 Some properties of KN and NN[100,104–107]

Property	KN ($KNbO_3$)	NN ($NaNbO_3$)
ε_r	430	160
ρ (g/cm^3)	4.15~4.20	4.38~4.40
d_{33} (pc/N)	91.7	63
k_p	0.19	0.24
P_r (μC/cm^2)	18	10.7

From the phase diagram of KNN presented in figure 2.19[33], it can be seen that, regardless of the doping amount of $NaNbO_3$ (NN), $(K_{1-x}Na_x)NbO_3$ can form perovskite-structure solid solutions but with different symmetries[17]. Pure $KNbO_3$ (KN) forms rhombohedral phase at < -10°C, an orthorhombic phase at room temperature, a tetragonal phase between 225°C to 435°C as well as a cubic phase at > 435°C[108]. The phase transitions of pure NN are far more complicated than KN due to the tilting nature of oxygen octahedral in NN and the relatively non-ideal perovskite structure resulting from a smaller ion radii (Na^+) which cannot fill the 12-coordinated cavity[17]. Generally, $NaNbO_3$ possesses orthorhombic and antiferroelectric structures at room temperature[109]. The phase transition order of $NaNbO_3$ and $KNbO_3$ is presented in figure 2.20. From figure 2.19, with increasing temperature, $(K_{1-x}Na_x)NbO_3$ (x=0.5) materials experience the following phase transitions: a rhombohedral phase at around -123°C, an

orthorhombic phase at room temperature, a tetragonal phase at approximately 200°C and a cubic phase at ~410°C[110].

KNN piezoelectric material exhibits a complex perovskite structure since the A-site of perovskites is took up by more than one type of ion (K^+ and Na^+)[17]. Figure 2.21[17] illustrates the KNN structure at room temperature. From figure 2.21, at room temperature KNN would be expected to have an orthorhombic structure with Amm2/Bmm2 space-group. However, the relationship of KNN lattice parameters is $a = c > b$, and b is perpendicular to the a, c plane as well as the inter-axial angle β is larger than 90°, meaning KNN lattice presents monoclinic symmetry at room temperature (shown in figure 2.21 b and c)[17,111]. Figure 2.18 d)[17] illustrates the four adjacent monoclinic KNN primary cells. Due to the length equality of a and c, the diagonals form a rectangle in the ac plane, which could be viewed as the projection of the KNN unit cell along the b axis. Therefore, it can be understood that the KNN unit cell exhibits orthorhombic-symmetry but its primary cell is monoclinic at room temperature[112,113].

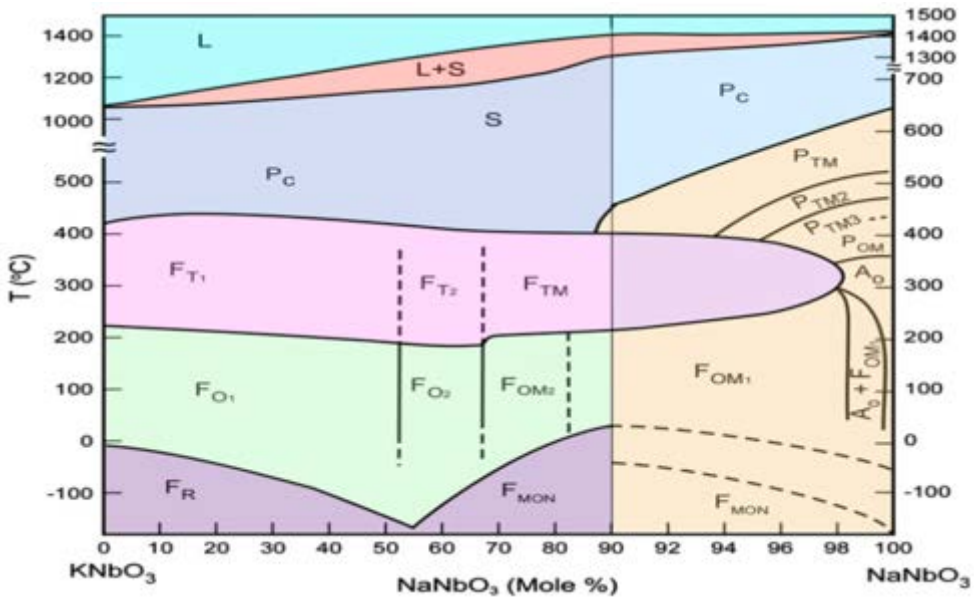

Figure 2.19 Phase diagram of the $KNbO_3$-$NaNbO_3$ system[114]. Note the uneven scale of the composition axis

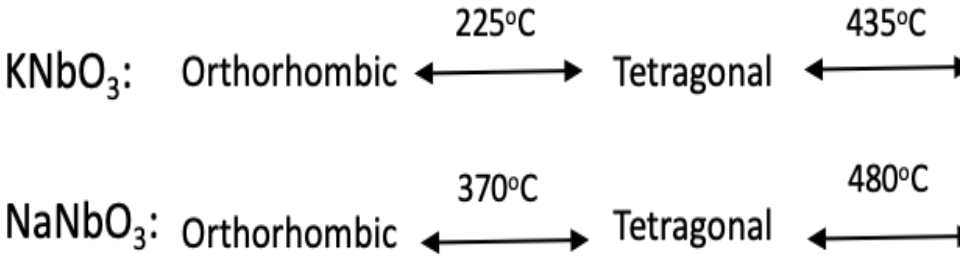

Figure 2.20 Phase transition order of $NaNbO_3$ and $KNbO_3$

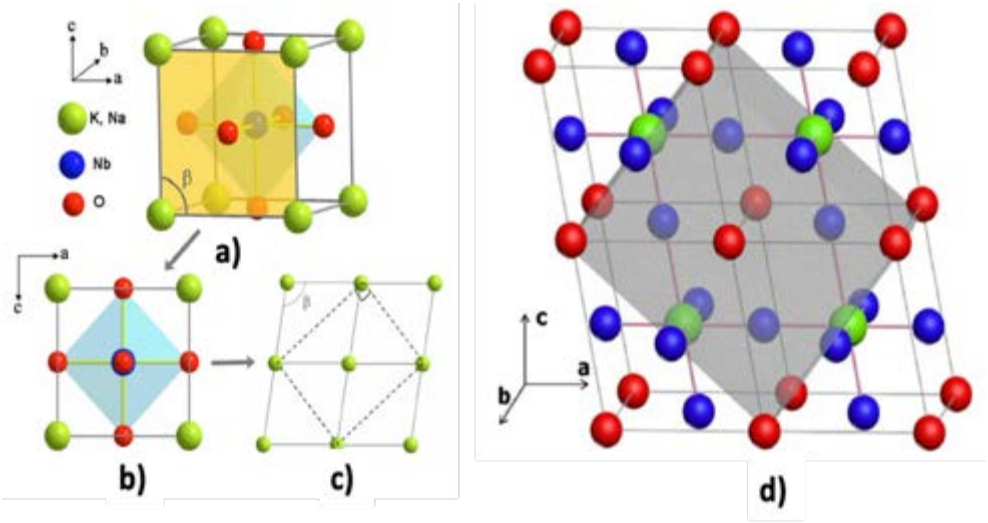

Figure 2.21 Lattice structure of $(K_{0.5}Na_{0.5})NbO_3$ at room temperature in a), b), c) and d) Schematic diagram of four adjacent KNN primary cells. The balls with red, green and blue colours are A-sites, B-sites, and oxygen atoms, respectively[17,113]

Generally, PZT ceramics shows outstanding functional properties at the MPB (as reviewed in chapter 2)[111]. However, the property boosting mechanism of KNN-based system is more complex and involves both PPT (polymorphism phase transition, representing the transition of tetragonal – orthorhombic phases T_{O-T}) and MPB[111]. For the PPT mechanism, the phase transition temperature point can be decreased to room temperature from ~200°C by chemical doping[111,115,116]. The shifting of T_{O-T} can enhance the piezoelectric properties of KNN. For KNN-based piezoelectric ceramics, PPT can be characterised via XRD by the splitting of the (222) peaks and intensity changes in the (002)/(200) and (004)/(400) peaks[111,116]. For the MPB mechanism, it is interesting to note that only a small amount of K (2%) doping is able to change the structure from that of NN to KN[17,117]. The octahedral tilting, however, remains until the K/Na ratio is ~1:1, at which the best functional properties can be achieved for KNN ceramics. It is clearly observed from figure 2.19 that KNN exists in two different orthorhombic

phases (F_{O1} and F_{O2}) around $(K_{0.5}Na_{0.5})NbO_3$ at room temperature, forming a MPB, thus the x=0.5 composition can exhibit outstanding functional properties[111].

2.4.1.2 Properties and doping of KNN-based materials

KNN piezoelectric ceramics exhibit moderate piezoelectric constant d_{33} (~80 pC N^{-1})[101]. Compared with PZT ceramics, this value is much lower. However, chemical modification and grain alignment can significantly enhance the properties of KNN-based materials. For example, $LiTaO_3$ and $LiSbO_3$ co-doped KNN ceramics with textured structure were prepared by Saito *et al.*[118] in 2004, and reported d_{33} values up to 416 pC N^{-1}, and for un-textured KNN prepared by Wu *et al.*[119] d_{33} values of 306 pC N^{-1} were reached. In general, the piezoelectric properties of ferroelectric ceramics are dominated by the combination of the intrinsic and extrinsic contributions[119]. For intrinsic contributions, there is a linear relationship between the lattice displacement and the piezoelectric effect. The extrinsic contributions, however, mainly depend on the movement of the domain walls[119]. The linear function is proportional to the values of spontaneous polarisation, in other word, the piezoelectric ceramics with higher P_s can possess higher piezoelectric coefficient. Normally, the range of spontaneous polarisation of KNN is 15~25 μC cm^{-2} which is comparable to those of PZT material. Thus, the reason why the properties between KNN and PZT differ so much may result from the differences in extrinsic contributions, which means that preferable domain wall movement along the MPB/PPT can significantly enhance the properties[120]. The control of MPB or PPT is usually linked to the compositional modification, *i.e.* doping[33].

The effect of doping can be simply classified as donor doping, acceptor doping and isovalent doping of A and /or B site ions[44]. For the donor doped KNN, K^+, Na^+ in KNN are replaced by Mn^{2+}, Ba^{2+}, Bi^{3+}, Cu^{2+}, Zn^{2+} or some rare earth metal ions (La^{3+}, Eu^{3+}, etc.) , and the cation vacancies will be generated to keep neutrality[121], the donor dopants and cation vacancies are formed as dipolar pairs, resulting in more active domain. This tends to enhance the permittivity and dielectric loss[121,122]. Also, since the mobility of the domains becomes more active, a larger piezoelectric effect (larger coupling coefficient and piezoelectric coefficient) and ferroelectric properties are observed (higher remanent polarisation P_r and smaller coercive field E_c)[123]. Donor doping amounts usually controlled within 5 at. %[33]. For the acceptor doped KNN, Nb^{5+} ions are substituted by Ni^{2+}, Fe^{3+}, Co^{3+}, Cr^{3+}, Ti^{4+}, etc[44]., and oxygen vacancies are created for charge compensation. The oxygen vacancies tend to combine with acceptor dopants to form the defect dipoles and the absence of oxygen causes the lattice shrinkage and distortion of KNN unit cells[44]. Differently from the donor doping, the oxygen-vacancy defect dipoles have the

capability to generate a field to stabilise the domain structures of KNN ceramics (domain walls pinning effect), leading to the difficulties of domain reorientation during the poling process[44]. Therefore, a reduced permittivity, piezoelectric effect (lower coupling coefficients and piezoelectric coefficient) and ferroelectric properties (lower P_r and higher E_c) are obtained[124]. In addition, the existence of oxygen vacancies results in a high leakage current and dielectric loss[123]. Finally, for the iso-valent doped KNN, Li^+, Ag^+ ions and/or Ta^{5+}, Sb^{5+} ions are able to replace Na^+/K^+ in A-site and/or Nb^{5+} in B-site, respectively[44]. This substitution tends to merge rhombohedral phase and tetragonal phase to create morphotropic phase boundary at room temperature by increasing transition temperature of rhombohedral – orthorhombic phase transition (T_{R-O}) and decreasing the transition temperature of orthorhombic – tetragonal phase (T_{O-T}) transition[125]. Therefore, an enhanced permittivity, coupling coefficient, piezoelectric coefficient, mechanical quality effect (Q_m) at room temperature but lower Curie temperature (T_C) can be obtained[126]. The proper amount of iso-valent doping is up to 10 at. %[33]. The functional property of pure KNN as well as doped-KNN ceramics are summarised in Table 2-2.

Table 2.2 Piezoelectric and dielectric properties of KNN-based ceramics (Ac: acceptor doping; D: donor doping; I: isovalent doping and -: unavailable)

Materials	Doping strategy	d_{33} (pC/N)	k_p	ε_r	$tan\delta$	Q_m	T_c(℃)	T_{O-T}(℃)	c/a
KNN[17,101]	-	80	0.36	290	0.04	130	415	-	-
KNN-Zr[127]	Ac to B-site	134	0.35	402	0.04	-	370	190	-
KNN-Ni[124]	Ac to B-site	87	0.32	-	0.11	249	-	-	-
KNN-Mn[124]	Ac to B-site	39	0.17	-	0.02	317			
KNN-Er[128]	D to A-site	133	0.44	-	0.03	-	-	-	-
KNN-La[122]	D to B-site	118	0.34	693	0.07		370	170	-
KNN-Li[129]	I to A-site	235	0.44	534	0.04	-	465	75	1.021
KNN-Sb[130]	I to B-site	204	0.47	850	0.02	150	300	130	1.006
KNN-Li, Ta, Sb[118]	I to A/B-site	416	0.61	1570	-	-	253	-	1.013
KNN-$AgNbO_3$[131]	I to A/B-site	186	0.42	495	-	-	355	165	-
KNNLT-$AgSbO_3$[132]	I to A/B-site	265	-	1000	-	-	235	40	1.009

It can be seen from the table 2-2 that most of the dopants except lithium (KNN-Li) present lower Curie temperature[133]. Although the piezoelectric properties of KNN can be effectively raised by chemical substitution through shifting the T_{O-T} to room temperature to produce a co-existence of two phases, KNN-based materials may suffer from problems of temperature instability[115,134–140], *i.e.* the enhanced functional properties can only exist within a narrow temperature range[115,140], some discontinuity in

piezoelectric properties[141], or lower T_c and poor thermal fatigue properties will result[139]. Thus, a suitable dopant and doping amount need to be considered.

To improve the practicality of KNN for hybrid energy harvesters (HEHers), the photovoltaic properties also need to be considered. As reviewed previously, the general photovoltaic process is that the KNN-based material absorbs the light and generates photo-induced carriers which can then be separated by the built-in potential to generate the photocurrent. Due to quite large differences in electronegativity between O and Nb, KNN ceramics possess a wide bandgap (>3 eV), resulting in a relatively poor ability of light absorption. Thus, the main strategy for improving the photovoltaic properties of ferroelectric oxides has been to narrow the bandgap while maintaining or even enhancing the polarisation.

Bennett *et al.*[15] have used first-principle calculations to predict that the doping of oxygen vacancy stabilized d^8 M^{2+} in $PbTiO_3$ may help to lower the bandgap to below 2.0 eV. However, as mentioned previously, the acceptor doping will degrade the piezoelectric properties, such as polarisations and temperature stability, etc. The other route is to introduce d^n MO_{6-x} (x being 1 or 2, *i.e.* FeO_5 or FeO_4) networks into ferroelectrics to reduce oxygen coordination and hence reduce the bandgap[142]. $KBiFe_2O_5$ with 1.59 eV bandgap (the bandgap of BFO is 2.6 eV) was proposed by Zhang *et al.*[142], but the spontaneous polarisations of $KBiF_2O_5$ dropped dramatically, from 30 μC cm^{-2} to 3.3 μC cm^{-2} due to the unstable perovskite structure[142,143]. Therefore, the bandgap reduction of ferroelectric oxides without sacrifice the ferroelectric properties is an instructional concept to enhance the practicality of the hybrid energy harvester[144], but perhaps more difficult to achieve in practice.

Thus the strategy involves a combination of B-site doping by one transition-metal cation for introducing M^{2+}-oxygen vacancies in the oxygen octahedra and A-site doping to maintain the stability of the perovskite structure[14,18]. $LaCoO_3$ doped $Bi_4Ti_3O_{12}$ films have confirmed that this strategy can tune the bandgap without affecting ferroelectricity[145]. Also, the bandgap of doped-Bi_2FeCrO_6 can be altered to 1.4 eV via adjusting the ordering of Fe/Cr cation and the ordered domain size[144]. Following this method, Grinberg[14] and his co-works use $BaNi_{0.5}Nb_{0.5}O_{3-\delta}$ (BNNO) to dope $KNbO_3$ (KN) to tune the bandgap of KN from around 1.3 eV to 2.0 eV and maintain its polarisation. The Ba ions are doped onto the A-site to maintain the stability of the perovskite structure and the Ni ions are added onto the B-site to form the Ni-O vacancy-pairs which can lower the bandgap of the parent KN ceramic due to the higher electronic states[14]. Moreover, Ba^{2+}, which carry a higher charge than K^+, enable to compensate the oxygen vacancies to reduce the impact of oxygen vacancies upon the functional properties.

Compared with KN, $(K_{0.5}Na_{0.5})NbO_3$(5KNN) possesses better piezoelectric properties and similar structure. Hence, it is possible to use BNNO to reduce the bandgap of 5KNN and to maintain or even enhance the polarisation[14,18].

2.4.2 Fabrication of KNN-based ceramics

The fabrication of KNN-based ceramics is similar to other ceramics, including the synthesis of the KNN-based ceramic powder, the shaping of the KNN-based powder compacts and the sintering of the KNN-based ceramics. To achieve the piezoelectric properties in KNN-based ceramics, the electroding and poling process are also required.

2.4.2.1 KNN powder

For the powder synthesis, the raw inorganic powders with high-purity (>99 %), such as metal oxides, alkaline earth-carbonate, etc.[33], are mixed and milled to obtain the powder-mix with stoichiometric proportions, homogenous particle size and size distribution before calcination. The aim of calcination is to pre-form the desired ceramic phase, enhance the powder homogeneity as well as reduce volume shrinkage at high-temperature treatment step[33]. Therefore, the selection of the calcination temperature needs to satisfy the following requirements: driving the appropriate reactions to obtain the desired phase and to suppress chemical loss[33,44]. After calcination, the as-prepared powder needs to be milled again to break the agglomerate particles to reach the homogenous particle size and the required size distribution. For KNN ceramics, because of the low melting temperature of K_2CO_3 (891°C) and Na_2CO_3 (851°C), the evaporation of sodium and potassium during calcination can be observed[133]. It can be found that the perovskite phase can be obtained at around 600°C, however, broad X-ray diffraction peaks without obvious orthorhombic splitting revealed the absence of compositional homogeneity[133,146]. Therefore, the calcination temperature of 5KNN needs to be carefully controlled.

2.4.2.2 Shaping

Before sintering, the as-prepared powders need to be shaped into a specific shape which is similar to the final product shape. Dry pressing is the most widely employed method to prepare bulk ceramics with a simple shape as well as constant cross-sectional areas[44,147]. However, dry pressing may cause some issues, such as stress concentration or larger variation in density[44,147,148]. To solve these issues, hot pressing and /or isostatic pressing are used in the laboratory and industry[44,147,148].

2.4.2.3 Sintering

Sintering is the thermodynamic process where ceramic powder compacts after shaping are consolidated into dense and robust ceramics after high-temperature heat treatment at the temperature below the melting point of the materials[149,150]. The main driving force of sintering is known as the reduction of the surface free energy of an assembly of particles, and this surface free energy can be enhanced by reducing the particle size[150]. The quality of sintering will significantly affect the properties and qualities of the ceramics because the sintering process determines the density and grain size of as-prepared ceramics. Sintering is an interplay between compact densification and grain growth. It can be divided into three overlapping stages[150]. At the first stage, the particles start to connect via sintering necks to produce a porous network of interconnected particles. At this stage, the surface roughness of particles decreases and a 60%-70% of relative density can be obtained. The second stage can be characterised by rapid shrinkage resulting from the raised densification rate with a relative density. In the final stage, the densification rate decreases dramatically and grain growth occurs[150].

Although ceramics with high density and small, uniform grain size (nm) tend to have excellent mechanical properties, piezoelectric ceramics are commonly engineered to exhibit relatively larger grains (μm) since the higher piezoelectric properties can be observed with grain sizes above a critical grain size[151,152]. For example, the piezoelectric properties of BTO piezoelectric ceramics are increased with an increased grain size up to approximately 1 μm[153]. Consequently, a suitable sintering temperature and time are very important for fabricating ceramics with a high density and an appropriate grain size.

Owing to the low melting temperature of KNN and the evaporation of alkaline components, the sintering of KNN-based ceramics is very complex[150]. The initial stage involves the fusing of the characteristically faceted powder particles of KNN to form stacks of plate-type particles[154]. This is achieved through inter-particle neck growth via the mechanisms of diffusion, vapour transport or viscous flow. At the intermediate stage, high temperatures lead to the evaporation of Na (as well as some K) at the grain boundary and the creation of a K-rich liquid phase that bridges residual pores present at grain boundary junctions[155]. This liquid phase provides a transport path for the rearrangement of particles resulting in a reduced surface area and improved packing[156]. The final stage is dominated by liquid phase-induced rapid and abnormal grain growth via diffusion-controlled coarsening mechanisms[154,157]. Here, limited densification occurs.

There are many reasons causing abnormal grain growth of KNN ceramics. Firstly, KNN powder particles possess faceted features in which oriented grain boundaries move faster than disoriented ones, leading to discontinuities in terms of particle orientation. As a result, some particles will be well-oriented and have a grain boundary of high mobility, whilst others will be disoriented and have a grain boundary of low mobility. Secondly, the grain boundary energies of pure KNN are intrinsically anisotropic, leading to local differences in the mobility of the grain boundary during sintering[150,158]. Lastly, in an oxidising environment, the evaporation of Na will lead to K and Nb segregation, generating sites that are K-rich and Nb-rich at the grain boundaries. At the K-rich sites, a K-rich liquid-solid phase mixture forms preferentially, which, as described above, reduces the energy for grain boundary migration, causing the grains to expand rapidly[159–161]. Meanwhile, Nb-rich grain boundaries remain in a state of solid-phase sintering and, thus, continue to grow at a normal rate. Differences in the migration rate of the grain boundaries leads to abnormal grain growth[162] and contribute significantly to the wide grain size distributions. It is important to note that the higher vapour pressure of K (8×10^{-3} pa) means that, as a whole, it evaporates more than Na (3×10^{-3} pa) during sintering[130,163–167]. However, K-rich sites have been shown to form in local areas[168], especially grain boundaries. From the KNN phase diagram, Na_2O evaporation will cause a compositional shift to the K-rich side to form a Na-deficient liquid phase during sintering and a K-rich secondary phase ($K_2Nb_4O_{11}$) during cooling[154,155].

One simple and cheaper route to increase the density whilst suppressing grain growth of KNN-based materials is two-step sintering (TSS)[169]. This is achieved by first densifying the ceramic to an intermediate density at a high initial temperature, T_1, over a short period of time. The ceramic is then cooled rapidly to a lower temperature, T_2, typically 50 – 100°C below T_1 and densified over a much longer period of time. The TSS method exploits the higher activation energy of grain boundary migration at triple-points, which form during the first stage of sintering and are immobilised by the rapid cooling of the ceramic. Subsequent densification to final density occurs by grain boundary diffusion[169]. For the sintering of KNN specifically, the use of a lower dwelling temperature at high temperature in TSS has the added benefit of reducing the evaporation of Na and K, enabling better stoichiometric control, the retention of a higher liquid content during sintering and improved piezoelectric performance[150,154,155]. The detailed sintering work will be discussed in chapters 5 and 6.

2.4.2.4 Electroding and poling

It is well known that the piezoelectric ceramic is an insulator. Thus, in order to exploit the electrical properties, a thin layer of conductive material needs to be coated into their surfaces perpendicular to the intended polarisation direction[33]. Generally, any metal could be utilised as an electrode, such as silver, gold, Nickel, copper or platinum, etc., of which silver and gold electrodes are more widely adopted in the laboratory and industry, respectively[33]. Nickel is commonly used in multi-layer devices as inner electrodes[170].

The poling process means that the materials are placed in an electric field, which can force or align the orientation of the domains over a period of time under the particular poling temperature (which is below T_C). The strength of the poling process relies on various factors, including the poling temperature, the poling field and the poling time[171–174]. For KNN-based materials, the preferred poling conditions are still debated. Normally, it is considered that poling at high temperatures (close to PPT) is more favourable for KNN-based ceramics due to the decreased coercive field and enhanced domain switching[175]. However, KNN-based ceramics are well known for their tricky densification process and the evaporation of K/Na; a high poling temperature also causes the movement of vacancies, leading to sudden increases in conductivity[175]. It is reported that 120-140°C is the best poling temperature range for KNN-based ceramics[172]. As for the poling electric field, higher piezoelectric property values can be obtained in higher electric fields[172]. However, a saturated piezoelectric property can also be reached under a higher applied electric field (~3 – 4.5 kV/mm)[172], which may be related to the domain vibration, domain-wall movement, domain switching, electric field-induced phase transition, etc[176]. The preferred poling time is the shortest period that allows nearly all domains to finish switching. Compared with PZT, KNN-based ceramics tend to reach a saturated degree in a shorter time[175], which may be due to the lower c/a ratio KNN has (c/a=1.005 for KNN[177] and c/a=1.025 for PZT[178]). The lower c/a ratio indicates the smaller distortion, the potential barrier is then smaller as well as the switching of non-180^o domain is much easier than in PZT[175]. The three factors discussed above are all important for the success of the poling process. Thus, the appropriate poling of KNN-based materials needs to be carefully controlled.

2.5 Summary

This chapter has comprehensively reviewed the background of piezoelectric-photovoltaic materials, from the fundamentals and mechanism of work principles and the corresponding fabrication

processes. KNN-based ceramics are usually sintered at the high sintering temperature, leading to the evaporation of Na_2O and K_2O during the sintering process, and then the low density, abnormal grain growth and degrading functional properties were obtained. Hence, it is important to develop a simple and commercial fabrication way. Moreover, the multifunctional material is a new idea and there are many aspects that need to be explored and researched. Despite the enormous studies on KNN materials, still more problem is needed to be addressed. For example, how to lower the bandgap whilst at the same time enhancing the piezoelectric properties? How to improve the piezoelectric properties whilst at the same time maintaining the temperature stability? The specific review of energy harvesting technology and the structure of hybrid energy harvesters using multifunctional materials will be given in next chapter.

Chapter 3. Energy harvesters

3.1 General introduction for energy harvesting technology

Non-renewable resources or finite resources, such as fossil fuels (coal, petroleum, natural gas), metal ores and ground water, are natural resources that cannot be readily replaced by natural. With the rapidly developing economy and growing global population, non-renewable resources cannot satisfy the requirements of worldwide energy. Figure 3.1 shows global energy consumption from 1800 to 2018[179]. According to this figure, as modern science and technology improve, the need for resources increases. Natural gas, crude oil and coal have become the most important resources used both as raw materials and for electricity generation used for residential and industrial purposes since the mid-19th century.

Today, with the development of modern technology, electricity has become one of the main sources of energy for many systems (illumination, computing, heating, etc.) used worldwide. Computers, phones and other equipment could not be used without it. Conventionally, electricity is generated by steam driven electro-mechanical generators via the combustion of fossil fuels[180]. These contain carbon, sulphur and other chemical elements, thus this combustion produces harmful by-products (carbon dioxide, sulphur dioxide and nitrogen oxide, etc.,)[181]. The emission of these harmful gases causes air pollution, global warming and other serious environmental problems[182]. It is unrealistic and also impossible to stop developing the economy or reduce human living conditions in order to decrease harmful gas emissions, hence, the use of renewable, clean energy sources, such as solar energy, kinetic energy and bio-energy need to be widely exploited to address concerns about shortages of non-renewable resources and the environmental problems they cause.

One particular rapidly emerging application in our daily life is wireless sensor networks[183] (WSNs, see figure 3.2[184]). WSNs comprise a set of sensors, which is spatially dispersed and dedicated, for the use of monitoring and recording the physical conditions of the environment as well as organising the collected data at the control centre and have been widely used in many areas. These include military battlefield surveillance[185–187], industrial process monitoring and control, machine health monitoring[188–193], public safety including hill-creep monitoring[194], searching and salvaging[195], fire monitoring[196,197], structural monitoring of bridges and buildings[198,199] and aerospace damage detection[200,201]. Most WSNs are powered either by batteries or via the mains electricity system. These two modes of power supply limit the practicability and usability of WSNs. The application range of

wire-powered WSNs tend to be restricted to indoor locations or places with a mains (hard wired) electricity supply. WSNs powder by batteries are also affected by severe energy limitations due to the short life span of the batteries which is likely to be only a few months or years[202]. In order to address this problem, the regular manual maintenance work, including recharging or replacement of the battery, is unavoidable. In most cases, WSNs are installed in remote, dangerous places and may consist of hundreds or even thousands of sensor nodes. For example, some WSNs are used to control chemical processes in hazardous environments, therefore the maintenance of these will increase the risk to workers' personal safety and manual maintenance costs. If energy harvesting technology can be successfully developed and widely deployed, people's lives could become simpler, safer, more efficient and environmentally friendly.

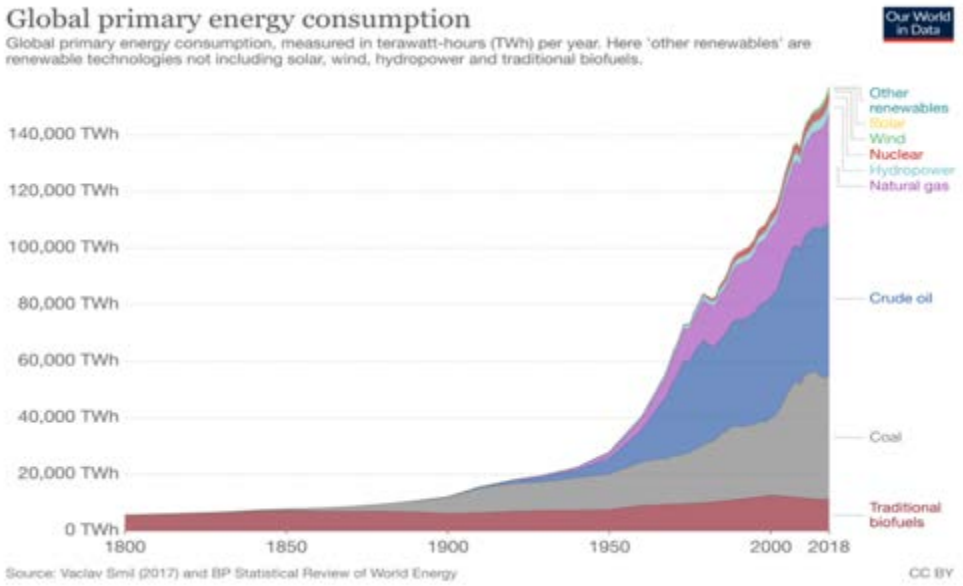

Figure 3.1 Global primary energy consumption, measured in terawatt-hours (TWh) per year[179]

Energy harvesting (EH) technology has received increased interests due to its potential impact on electric power systems via the harvesting of renewable resources such as wind, tide, vibration, heat and solar energy[203]. In fact, energy harvesting is not a new concept, it has been in operation for millennia. Since at least the first century BC[204], water wheels have been used to harvest energy from the currents of streams to power mills. Also, machines powered by the wind have been known from the first century AD[205].

Today the same natural resources are being harvested but by using modern technology. In modern society, energy harvesting, also named as energy scavenging, is the process by which energy is

captured from a variety of ambient energy sources such as heat, light, fluid, wave, sound and kinetic/motion energy and converted into usable low-energy electric power (from micro watt to milli watt) to charge wireless sensor networks[202,206,207]. The EHer (see figure 3.3[208]) is the technology required to collect, accumulate and convert the energy. The widespread use of energy harvesting technology can minimise the maintenance, the cost of operation and enable wireless and portable electronic devices to be completely self-sustaining and truly “smart”.

Figure 3.2 Architecture of wireless sensor networks[184]

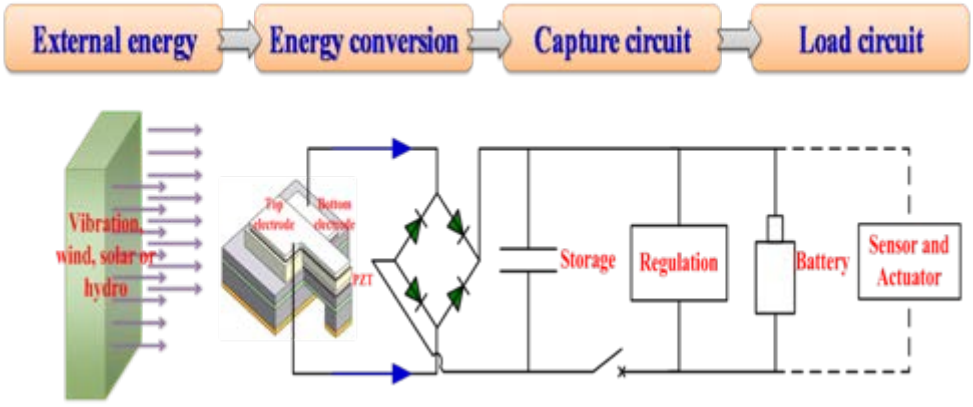

Figure 3.3 Schematic diagram of (Pb, Zr)TiO_3 cantilever-typed energy harvester system[208]

3.2 The source for energy harvesting and the structure of related energy harvester

In the environment, there are many different sources of energy available for generating electricity, such as light, heat, wind, vibration/motion, temperature variations, electromagnetic and radiation sources[209]. Table 3-1 summarises the estimated power of the various different ambient energy sources from a recent study. As shown in the table, solar energy is considered as a significant energy source, the power density generated from solar energy is thousands of times greater than those generated from other energy sources. However, power density is extremely dependent on location. The power density produced from indoor sources is about 1000 times less than that produced by outdoor resources. As regards thermal energy, the power density is low due to the temperature gradient across the components being typically low and being difficult to maintain due to temperature diffusion. Apart from solar and thermal energy, vibration energy is a very important energy source. The power density generated from vibration is moderate, but it is highly dependent on its particular application, also, there are abundant sources of vibration, such as ocean waves, wind, human motion, machine vibration, water flow, road, bridge vibration, etc. The abundant sources make vibration available anytime and anywhere. EHers can be classified in accordance with their energy source, for example, vibration, radio frequency, solar and thermal energy harvesters. According to the working principle, they can also be classified as photovoltaic energy, Seebeck-type energy, electromagnetic energy, electrostatic energy and piezoelectric energy harvesters. The output of the photovoltaic energy and Seebeck-type energy harvesters is direct current (DC output), and the output of the others is alternating current (AC output). Figure 3.4[210] explains the hierarchy of the main energy harvesting technologies.

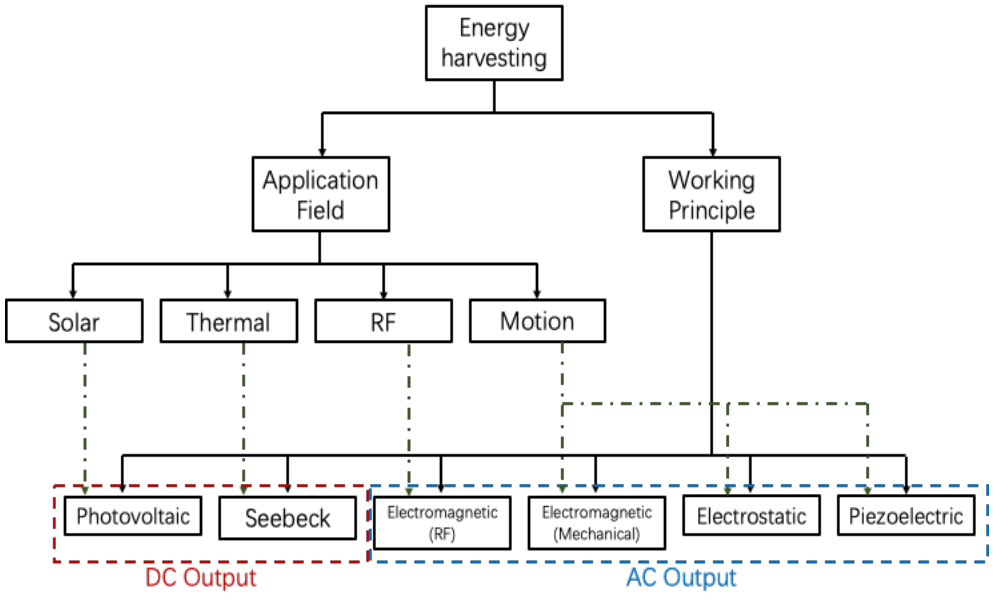

Figure 3.4 A classification of energy harvesters[210]

Table 3.1 the comparisons of the power density from various ambient energy sources

Energy Source	Performance	Reference
Acoustic Noise	0.003 μW/cm^3	211
Temperature variation (human)	60 μW/m^2	212
Temperature variation (industry)	10 mW/cm^2	202
Solar (outdoors)	100 mW/cm^3	213
Solar (indoors)	10-20 μW/cm^3	214
Vibration (human)	4 μW/cm^3	215
Vibration (machine)	800 W/cm^3	215
Vibration (piezoelectric)	200 μW/m^3	216
Airflow	360 μW/cm^2	217
Radio frequency (RF-GSM)	1 mW	218,219
Radio Frequency (RF-WiFi)	16-54 μW	220,221
Radio Frequency (RF-AM)	0.5-2.39 μW	222,223
Wind	177 μW/m^2	202

3.2.1 Solar energy and photovoltaic energy harvesting

Solar energy comprises energy in the form of heat and radiation from the sun[224,225]. Every year, the overall solar energy absorbed by the Earth, by its atmosphere, oceans and land is ~3.85 × 10^6 exajoules[226] which is nearly twice as great as that obtained from the combination of the Earth's non-renewable resources[227]. Typically, a common PVEHer possesses a parallel-capacitor structure[228], which consists of top electrode, photovoltaic materials and bottom electrode[229]. This design simplifies the fabrication of solar cells and reduces the cost. The schematic diagram of a ferroelectric oxide-based solar cell is shown in figure 3.5[230]. Because conventional solar cells are out of the scope of this thesis, only a simple discussion is presented here.

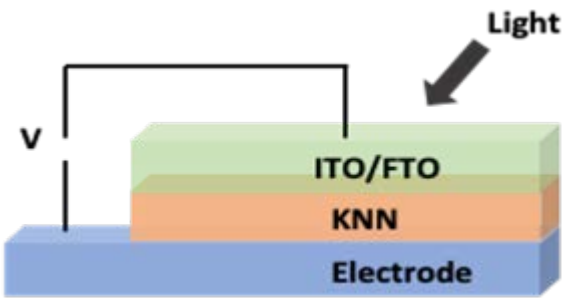

Figure 3.5 The schematic diagram of ferroelectric oxide-based solar cell, reproduced from ref[230]

3.2.2 Kinetic energy and the piezoelectric energy harvester

3.2.2.1 Kinetic energy

In a broad sense, kinetic energy harvesters (KEHers) can convert mechanical motion energy, in the form of vibration, random displacements, fluid motion, stress and strain, into electrical energy[203]. Vibration energy harvesters, a subset of KEHers, are dedicated to the conversion of vibration energy into electricity[203]. The usable vibration energy that can be effectively harvested usually exists in building/construction vibration, human daily life, as such walking or machine operation[13]. Based on the energy transformation mechanism, the vibration energy harvesters can be divided into three types: electromagnetic energy (EMEHers)[231], electrostatic energy (ESEHers)[232] and piezoelectric energy harvesters (PEEHer)[233]. The power level of these three types of energy harvester is microscale power levels (<W).

PEEHers are based on the piezoelectric effect[13]. The vibration of piezoelectric materials, such as $Pb(Zr,Ti)O_3$[234], $(K,Na)NbO_3$[235], $BaTiO_3$[153], Poly(vinylidene fluoride)[236], causes the separation of negative and positive charges across the devices. PEEHers provide higher voltage and power density levels than EMEHers[207]. However, the performance of PEEHers is highly impacted by the properties of the piezoelectric materials, in other words, to make a high-output PEEHer, piezoelectric materials with outstanding piezoelectric properties are needed.

3.2.2.2 Coupling mode and cantilever structure of the piezoelectric energy harvester

It is crucial to understand the coupling mode of the operation which has been reported to improve harvested power by selecting a proper structure[237]. Figure 3.6[238] illustrates two common coupling modes of the operation (“31”mode and “33”mode). Similar to the review in chapter 2 concerning the direction of the piezoelectric crystal, the coupling mode is related to the poling method. The direction of the applied force/stress is in the same direction of charges accumulating along axis “3”,it is called “33-mode”(figure 3.6 a) , and if the force/stress is applied to the “1”-axis, which is perpendicular to the direction of charge generation(axis “3”), it is called the “31-mode” (figure 3.6 b)[239]. Another coupling mode is “15”mode, in this mode, the applied force is along the shear direction (“5”-axis) and the voltage is generated along the“1”-direction.

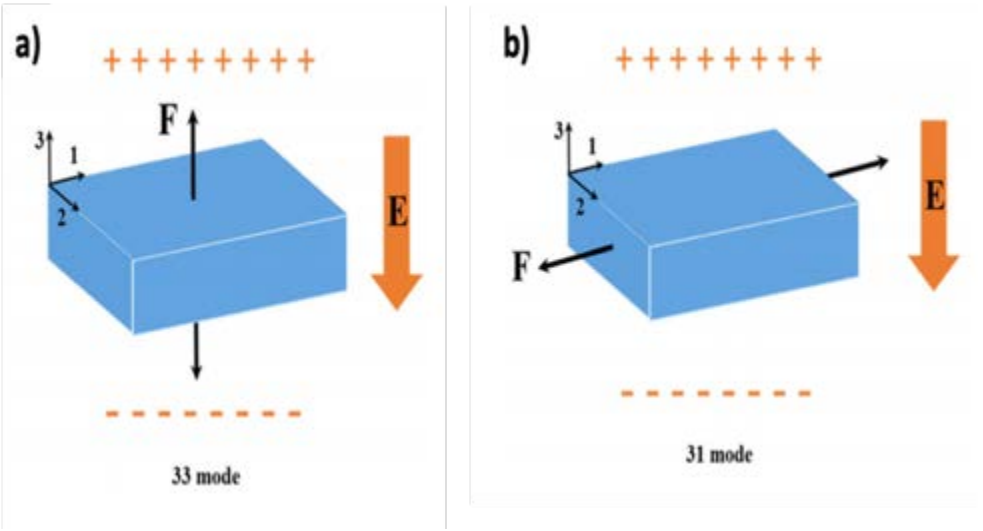

Figure 3.6 a) "33" and b) "31" operation mode for the piezoelectric energy harvester[238]

Amongst these three coupling modes, the "15" mode possesses a higher piezoelectric charge constant[240], however, due to the complex fabrication of the electrodes caused by the different direction of poling and charge collection, the "15" coupling mode is not widely used[241]. Compared to the PEEHer in the"33" operation mode, the PEEHer with the "31" operation mode has a relatively simple electrode configuration which consists of top and bottom electrodes (TBEs), while the electrodes of "33" operation mode PEEHer are usually interdigital electrodes (IDEs), *e.g.* as designed by Hagood *et al*[242]. and Wilkie *et al*[243]. IDEs requires fine patterning of the electrodes, while the TBEs need only simple coating of larger areas. In addition, the "33" mode PEEHer needs a higher poling voltage because the distance between the electrodes in TBE is generally narrower than finger spacing of the IDE, which may cause device failure due to electric breakdown[241]. Apart from the advantage of simple electrode design, PEEHer with the"31" coupling mode produces a better performance when a low level force is applied[244].

The cantilever structure is one of the most widely used structures for PEEHer, due to its simplicity and the ease of producing relatively high average strains for a given force input[245–247]. PEEHer with a simple cantilever beam structure consists of a piezoelectric element, an elastic support layer and a tip mass, as shown in figure 3.7[213]. The piezoelectric element, poled in the thickness-direction, is attached to an elastic support to form a unimorph-cantilever which is fixed one side and free the other side. A proof mass is fixed on the free end to provide inertial force. When the fixed side of the cantilever vibrates at a certain frequency, the cantilever beam moves up and down due to the inertial force provided by the proof mass, causing the piezoelectric element to be in tension status when the cantilever bends downwards or in compression status when the beam bends upwards. The deformation of the

piezoelectric element generates an electric charge based on the piezoelectric effect. Thus, the PEEHer can continuously generate AC output voltage as long as the cantilever keeps vibrating.

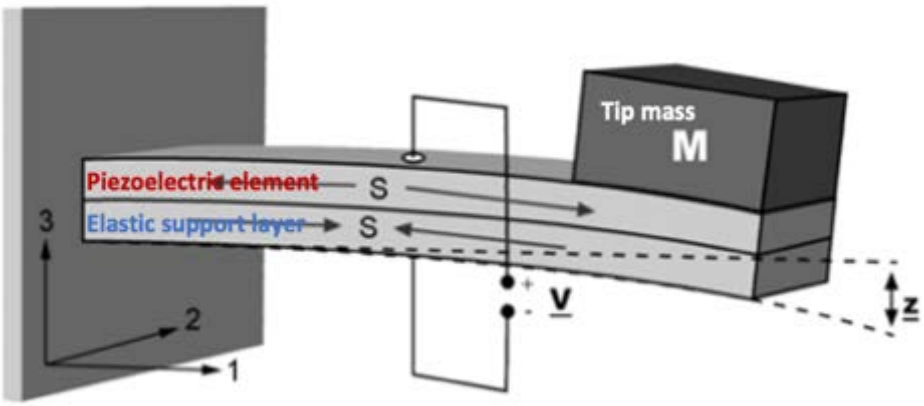

Figure 3.7 Schematic diagram of a basic piezoelectric cantilever configuration, S is strain, V is voltage, M is proof mass and the z is vertical displacement[213]

As previously mentioned, the PEEHer has two commonly used coupling modes, the"31" mode and the "33" mode. Figure 3.8[239] illustrates a schematic graph of the unimorph cantilever energy harvester in "31" mode (a) and "33" mode (b). The "33"-mode PEHer tends to generate a higher voltage output due to a higher piezoelectric coefficient and a longer distance between the electrodes, while the "31"-mode PEHer has the advantage of producing a larger current output and has a simple electrode design[248].

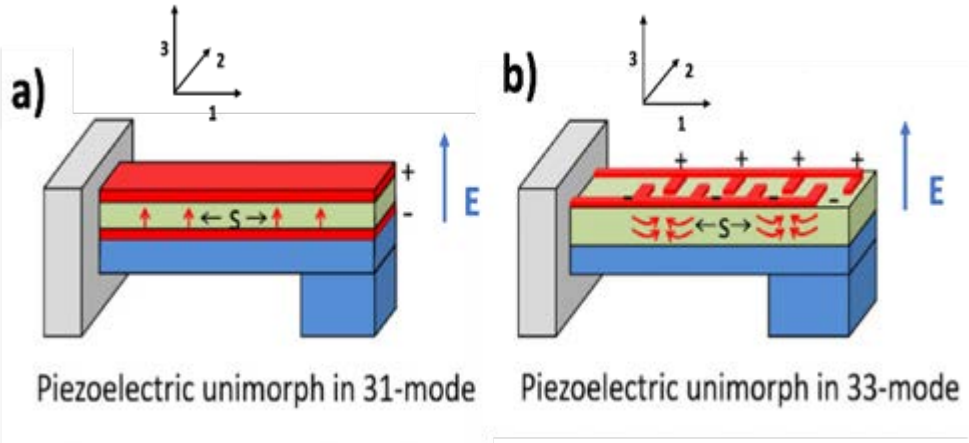

Figure 3.8 a) "31-mode" and b) "33-mode" unimorph cantilever configuration[239]

3.2.3 Hybrid energy harvesting (HEHer)

As reviewed above, there are various different energy harvesters, which depend on different working principles. Compared to the conventional method of generating electricity from fossil fuels, the novel EHers system is suffers from the disadvantage that it is designed for capturing and converting only one specific type of energy source. This can lead to an unstable output which can be adversely affected by the weather (solar, wind) as well as other factors[249]. In other words, solar-energy panels are specifically made for harvesting light and wind turbines are only for wind energy or airflow. If the sun is hidden by clouds, the temperature variation is very weak or a machine is turned off, the output of the individual-source energy harvester will decrease dramatically. In order to satisfy the power requirements of the wireless network system or other electronic devices, a hybrid energy harvester (HEHer, figure 3.9[249]), incorporating two or more conversion mechanisms in one system/materials, has been proposed. In addition, in the environment, many different kinds of energies coexist. For example, the sun can provide light and heat and machines can also provide vibration and heat at the same time. The combination of these energy sources enables the hybrid energy harvester to generate more continuously.

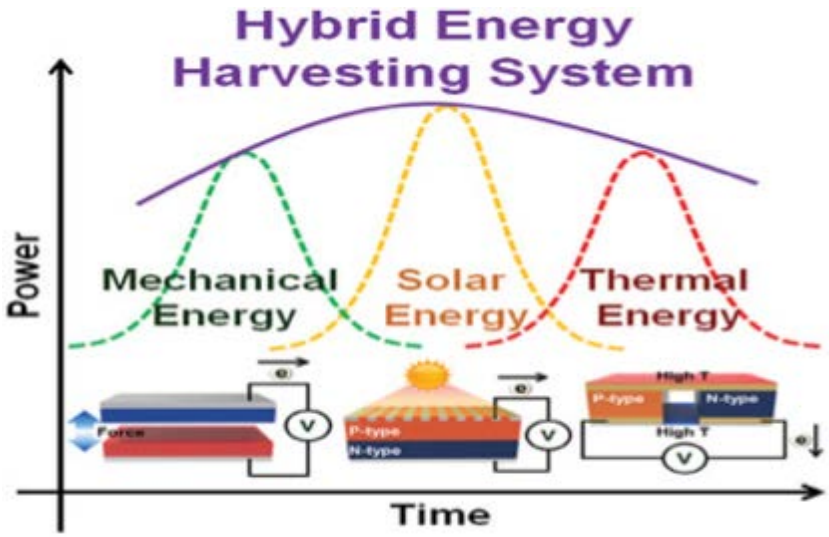

Figure 3.9 A schematic description of a sustainable hybrid energy harvesting system via natural and artificial energies[249]

There are two types of HEHer. The first type of HEHer integrates different conversion materials or configurations so that different energy sources are usable in a single energy harvester via a structure optimisation which not only compensates for the other's disadvantages but also helps to increase overall efficiency[13]. For instance, Li *et al.*[250] incorporated the piezoelectric-electromagnetic conversion mechanism (kinetic energy) into a single system which could be operated at higher frequencies (60 -

120 Hz). Yoon *et al.*[251] reported a mechanical and solar HEHer based on piezoelectric and photovoltaic principles. The 2D ZnO nanosheets were selected as the piezoelectric energy harvester and the poly(3-hexylthipphene) (P3HT) and [6,6]-ohenyl-C_{61}-butyric acid methyl ester ($PC_{60}BM$) were used as the photovoltaic generator. Figure 3.10[251] demonstrates the schematic diagram of this HEHer, where it was reported that the output of this HEHer increases by about 75% compared to a single-source EHer.

The second type of HEHer uses multifunctional materials to achieve multisource energy harvesting[13]. Compared to the configuration optimisation of type HEHer, the HEHer fabricated with multifunctional materials enables the use of multiple energy sources and avoids complex structures. The requirements of multifunctional materials are:

1) Different energy conversion mechanisms can co-exist;

2) The conversion mechanism can be triggered simultaneously;

3) The different conversion mechanisms should not counteract or cancel each other.

Y. Bai *et al.*[18] have demonstrated a new hybrid energy harvester which uses the coupling of the photovoltaic, piezoelectric and pyroelectric effects made using a single multifunctional material. Table 3-2 summarises the representative examples of the hybrid energy harvester in terms of working principles, output voltage, output power and output power density.

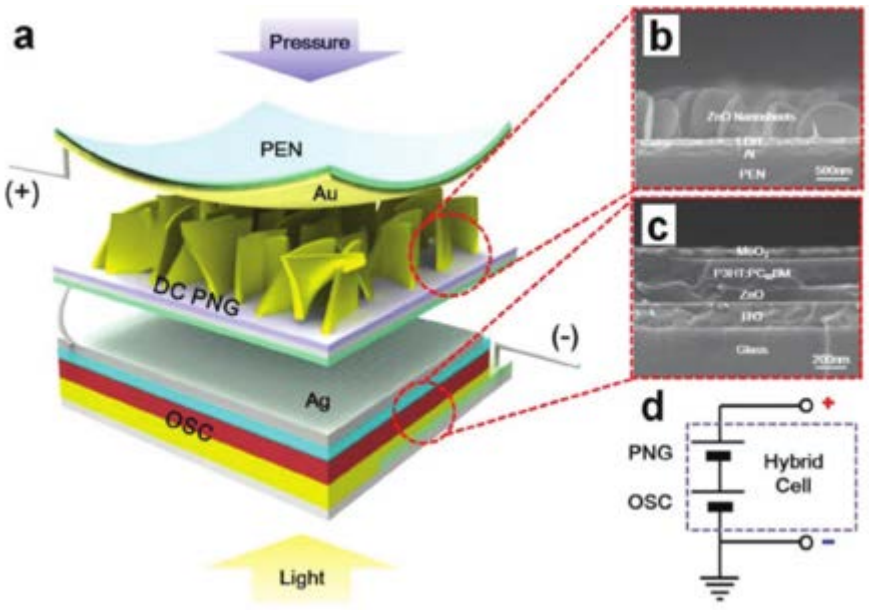

Figure 3.10 Piezoelectric-photovoltaic HEHers (PNG: piezoelectric nanogenerator; OSC: organic solar cell; PEN: polyethylene naphtalate; DC: direct current)[251]

Table 3.2 Comparison of hybrid energy harvesters ('-' means unavailable in the literature)

Conversion principle	Output voltage	Output power	Output power density	Ref
Electromagnetic + Piezoelectric	-	176 μW	790 μW cm^{-3}	[253]
Electromagnetic + Piezoelectric	0.71 V	10.7 mW	-	[254]
Electromagnetic + Piezoelectric	4 V	0.32 mW for PEEHer 1.23 mW for EMEHer	-	[255]
Electromagnetic + Piezoelectric	3.6 V	40.62 μW	-	[256]
Electromagnetic + Piezoelectric	-	2.16 mW	-	[257]
Electromagnetic + Piezoelectric	2 V	229.31 μW	-	[258]
Electromagnetic + Triboelectric	2.8 V	10.07 mW	344 W m^{-3}	[259]
Triboelectric + Photovoltaic	7 V	0.27 μW	-	[260]
Triboelectric + Piezoelectric	20 V	-	-	[261]
Piezoelectric + Electrostatic	-	-	1.79 μW cm^{-2} for PEEHer 1.59 nW cm^{-2} for ESEHer	[262]
Piezoelectric + Photovoltaic	0.8 V	-	-	[263]
Piezoelectric + Photovoltaic	-	-	34.5 μW cm^{-2}	[264]
Photovoltaic + Thermoelectric	-	621 μW	-	[265]
Triboelectric + Photovoltaic + Chemical	60 V	-	-	[266]
Piezoelectric + Electromagnetic + Photovoltaic	-	499.4 mW	-	[267]
Photovoltaic + Pyroelectric + Thermoelectric + Photothermal	2.75	-	17.3 mW cm^{-2}	[268]

3.3 Coupling of PEEHer and PVEHer

As introduced above, one form of the PVEHer possesses a similar structure to a PEEHer, with a piezoelectric element – 'sandwich structure'. Thus, it is possible to integrate them to fabricate a hybrid energy harvester as long as the requirements of high mechanical energy input and high lighting intensity can be satisfied simultaneously. A cantilever-type structure may be a good choice. On the one hand, a cantilever-beam can provide high vibration energy and the fabrication is relatively easy. On the other hand, the top-surface can be used as a lighting area. Therefore, a cantilever-structure was selected as the structure of the HEHers. In order to maximise the output of the HEHer, optimisation for the structure is needed. For the PEEHer part, the beam theory needs to be taken into consideration to enhance the piezoelectric output via the structure design. After optimising the host structure, the selection and arrangement of the electrodes need to be considered to enhance the performance of the PVEHer part.

3.3.1 Structure optimisation – cantilever beam

3.3.1.1 Resonant frequency

In order to design a suitable cantilever structure to enhance the output of the PEEHer, the resonant frequencies need to be considered, as the maximum output can only be obtained under optimum working conditions[6,214,248,269,270]. In general, the resonant frequency of the PEEHer can be easily tailored by either adjusting the dimensions of cantilever and proof mass or the physical/elastic properties of the used materials[271,272].

3.3.1.2 Band width

The full width at half maximum (FWHM) of the output-input frequency spectrum divided by the resonant frequency is defined as the bandwidth of a PEEHer, which is exhibited in figure 3.11[273]. The maximum energy is generated when the PEEHer is excited at its resonant frequency. If the excitation frequency shifts, the performance of the PEEHer is reduced dramatically[274]. In other words, high efficiency can be only obtained within a certain bandwidth range. However, for most PEEHers, the bandwidth is very narrow, for example, the bandwidth of a cantilever with proof mass is <5%[275,276], which means the efficiency of the PEEHer is limited[277]. To overcome this drawback, broadband techniques were developed. Many methods of broadening the bandwidth have been proposed, including resonance tuning, multi-modal or array generators and frequency up-conversion methods.

After altering the length of the cantilever beam[278] or tuning the tip mass, the resonant frequency of PEEHer can be easily tuned[279,280].

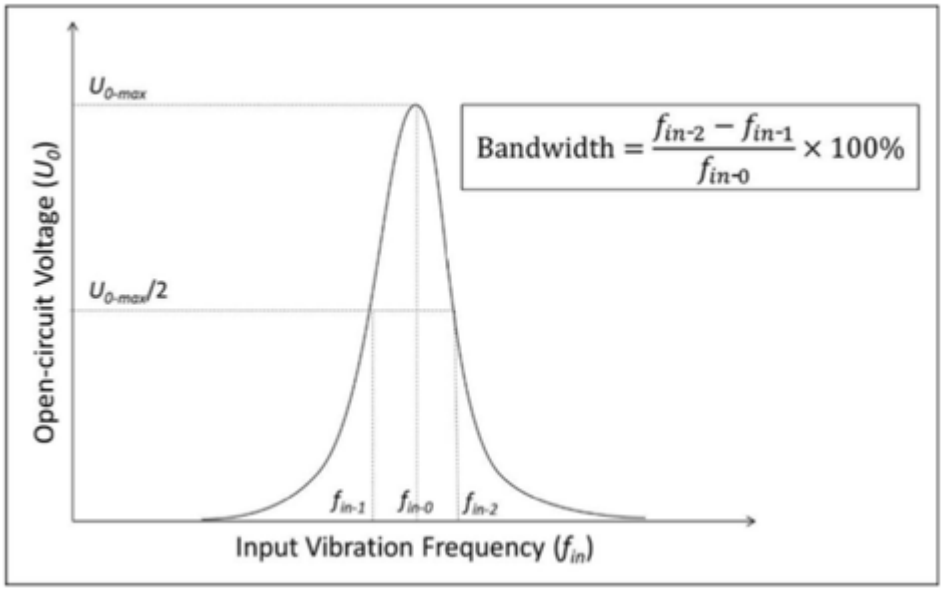

Figure 3.11 The definition of the bandwidth of vibrational energy harvesters[273]

3.3.2 Structure optimization - selection of the electrodes

In the case of the PEEHer, the type of electrodes may not affect the results. However, it would cause huge differences for the PVEHer. Thus, the selection of the electrodes is very important for the hybrid energy harvester.

In the "electrode/FE-PV materials/electrode" structure (figure 3.5), the work function of the electrodes could affect the performance of the solar cell (as reviewed in section 2.3.3). Following the FE-PV principle, the separation of the photo-induced carriers is driven by E_d and E_{bi}, and the E_{bi} is the internal net potential (Equation 2-7) which is related to the work function of the top/bottom electrodes[99] (equation 2-7, 2-9 and 2-10).

A schematic diagram of the energy-band of the "metal/PLZT/ITO" structure solar cell is given in figure 2.18[99]. The photoelectric-effect of metal enable to enhance the photovoltaic properties of FE-PV materials. The Schottky barrier height between FE-PV materials and electrodes is expressed in Equation 2-7, 2-9 and 2-10[99]. It is obvious that the metal electrode with lower work function can construct smaller barrier height. Thus, the electrons in the electrode can be emitted into the FE-PV

layer and participate in the separation process when the photon energy is larger than the barrier height (Φ_B)[99]. Zhang *et al*.[99] compared the influence of Pt, Mg and Ag electrodes on the performance of the common "PLZT-Sandwich" structure FE-PVer. Amongst these three different electrodes, Mg has the lowest work function, thus, the "ITO/PLZT/Mg" sample has a 150 times larger photovoltaic current and a twice higher photovoltage than those of the "ITO/PLZY/Pt" samples with the highest work function, respectively.

3.3.3 Structure optimization – arrangement of the electrodes

The driving force of the charge carriers-pair separation in FE-PV materials is the internal electric field originating from ferroelectric polarisation. Therefore, the photo-voltage is proportional to the inter-electrode distance in the polarisation direction and it is not limited by the energy bandgap[76,88]. The arrangement of the electrodes is another factor which affects the performance of the HEHers. In general, there are two typical electrode configurations for the HEHers which are shown in figure 3.12[72]. The HEHers with vertical-electrode architecture could provide a relatively large photo current but a small voltage, whereas the HEHers with lateral-electrode architectures could offer a relatively high voltage but a low photocurrent[228]. For the vertical-structure HEHers, a transparent electrode is needed to collect the light and the thickness of FE-PV material also displays a significant impact on the performance of the device. There is no electrode selectivity for lateral structure devices and the performance can be tuned by adjusting the spacing between the electrodes. Thus, the choices for the lateral structure are more abundant. In addition, the lateral structure can be viewed as several "devices" connected in series (figure 3.13), the output of which is the sum of the photo-voltage of each "device". Furthermore, a very low electric field is required for the poling process due to the small electrode spacing[281,282].

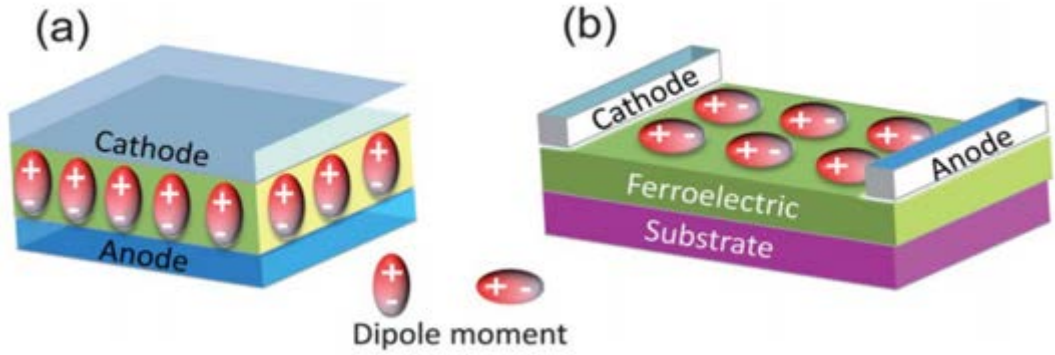

Figure 3.12 The arrangement of the electrode for FE-PV energy harvester: (a) vertical architectures, (b) lateral architecture[72]

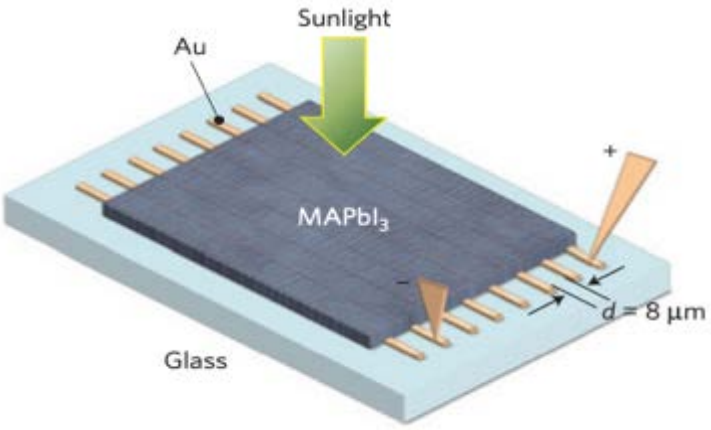

Figure 3.13 Schematic of the lateral-type HEHer devices with more electrode, $MAPbI_3$ represents the hybrid organic-inorganic perovskites (MA: $CH_3NH_3^+$)[281]

3.4 Requirements of the multifunctional materials for photovoltaic-ferroelectrics (PV-FEs)

The performance of the devices can be affected by the structure and configuration of the device and electric circuitry. However, the main factors that determines the performance of the HEHers are the properties of the materials. Because the EHer is made for power supplying, the open-circuit voltage, output power and energy conversion efficiency are the most important criteria.

3.4.1 Piezoelectric properties

The important properties of piezoelectric materials for the energy harvester include piezoelectric charge constant d, piezoelectric voltage constant g, electromechanical coupling factor k, mechanical quality factor Q_m, and dielectric constant ε_r.

As stated before, the maximum output of the PEEHer is obtained when it vibrates at its resonant frequency. However, because of the volume constraint of the prepared PEEHer, it is hard to match the resonant frequency of the piezoelectric material with the input frequency of the main body, therefore, the energy harvester is usually operated at off-resonance conditions. In this condition, the magnitude of transduction is determined by g. The open-circuit output voltage V under an applied force F can be given by Equation 3-1 and 3-2[283,284].

$$V = E \times t = -\frac{g \times F \times t}{A} \quad \text{3-1}$$

$$g = \frac{d}{\varepsilon_0 \varepsilon_r} \quad \text{3-2}$$

Where the E represents the electric field, t is the thickness of the piezoelectric element, A represents the area of the electrode, d is the piezoelectric charge constant, ε_0 and ε_r are the vacuum dielectric constant (8.54×10^{12} F m^{-1}) and relative dielectric constant, respectively. From Equation 3-7, it can be revealed that a piezoelectric material with a higher g enable to produce a higher open-circuit voltage, this can be obtained when the materials possess higher d and lower ε_r.

Also, at the low-frequency condition, the piezoelectric element can be viewed as a parallel plate capacitor, and the electric energy U or the energy per unit volume u of it can be expressed by Equations 3-3 and 3-4[283].

$$U = \frac{1}{2}CV^2 \quad 3\text{-}3$$

$$u = \frac{1}{2}(d \times g) \cdot (\frac{F}{A})^2 \quad 3\text{-}4$$

A piezoelectric material with higher g and d prefers either a larger current in the short circuit or a larger voltage in the open circuit, therefore it is sought after for the design of the higher power output from EHers[285].

For the cantilever-type PEEHer, the efficiency of energy conversion η can be expressed by Equation 3-5[286].

$$\eta = \frac{1}{2}\frac{k^2}{1-k^2} / (\frac{1}{Q_m} + \frac{1}{2}\frac{k^2}{1-k^2}) \quad 3\text{-}5$$

Where k and Q_m represent the electromechanical coupling factor and mechanical quality factor, respectively. Thus, to achieve a higher conversion efficiency, the piezoelectric materials should have large k^2 and Q_m. A dimensionless figure of merit (DFOM) proposed by Priya[283] is also used to evaluate piezoelectric material for EHers (Equation 3-6).

$$DFOM = (\frac{d \times g}{tan\delta})_{off-resonance} \times (\frac{k^2 \cdot Q_m}{S^E})_{on-resonance} \quad 3\text{-}6$$

Where $tan\delta$ is the dielectric loss and s^E is the elastic modulus of piezoelectric materials. From equation 3-6, it can be interpreted that increased DFOM can be obtained with the increasing of $d \times g$ and $k^2 \cdot Q_m$, as well as the decreasing of the $tan\delta$ and S^E[287].

3.4.2 Photovoltaic properties

From the HEHers point of view, solar cells need to meet the demand of adequate absorption of solar radiation, efficient separation of the photo-induced carriers and a lower charge recombination rate[288]. Therefore, the requirements of ferroelectrics are[289]:

1. Narrow bandgap (E_g);
2. High spontaneous polarisation;
3. Low poling electrical field, etc[289].

A wide bandgap (>3 eV) beyond the visible-light range leads to poor sunlight absorption capabilities (only 8%-20%)[144,288]. For example, $BiFeO_3$ has a relatively low bandgap of 2.67 eV, however, BFO cannot absorbed the photons with wavelengths larger than 464 nm (>80% of the solar spectrum)[144] which leads to a low conversion efficiency. The separation of the photo-excited charge carriers is driven by the built-in potential originating from spontaneous polarisation, larger polarisation can promote the separation of the carriers. Therefore, in order to design a HEHer with excellent performance, both piezoelectric and piezo-photovoltaic properties need to be considered. The desirable piezoelectric properties are helpful to improve the photovoltaic properties. Nevertheless, it is still very complicated to evaluate which parameter is the most important in designing a HEHer, as each can affect the performance of the device. Therefore, it is significantly essential to carry out a practical study on each material case.

3.5 Summary

This chapter gives a broad and general introduction about EH including the energy situation the world now faces, renewable energy sources, working principles as well as structures for different types of EHer and the optimisation of HEHers as well as requirements for multifunctional materials. Much research has been done for the single-type EHer. However, the efficiency of the normal EHer is still too low and unstable to replace the conventional way of generating electricity from fossil fuels. Hence, the HEHer is proposed to improve the drawbacks of the single-type EHer. As regards the EHer system, the performance of system is significantly influenced by its structure and the functional properties of the materials. However, the properties of the materials are the dominant factor influencing the final performance of the device. The ability to fabricate multifunctional materials with improved properties together with optimisation of the device structure can ensure that the potential of the materials can be fully realised.

Chapter 4. Aims and objectives

4.1 Motivation and Aims

The consumption of non-renewable energy and the associated environmental pollution have driven the development and research of sustainable energy. As reviewed in chapter 3, both solar energy and kinetic energy are abundant resources and hold the promise of replacing fossil fuels in many application areas. However, the efficiency of single-source energy harvesters is highly dependent on the working environment and time. To date, ferroelectric material has been regarded as a potential multifunctional candidate to improve the drawbacks of single-source energy harvesters due to their versatile piezoelectric and photovoltaic properties.

In chapter 2, it was shown that the driving force underpinning photovoltaic properties in ferroelectric materials is polarisation, with higher polarisation inducing better photovoltaic properties. However, in practice, the wide bandgaps of ferroelectric oxides limit their applications. Chemical doping is a suitable way to reduce the bandgap by introducing oxygen vacancies. However, large concentrations of oxygen vacancies affect the polarisation. Thus, oxygen-vacancy is the key factor to affect the ferroelectric and photovoltaic properties of ferroelectric oxides. As reviewed in Chapter 2, a strategy of narrowing the bandgap without decreasing the polarisation has been explored by substituting Nb^{5+} with lower valence transition metals.

Considering the ionic radius, electronegativity and structure, in this study, $Ba(Nb_{0.5}Ni_{0.5})O_{3-\delta}$ (BNNO) materials were selected to introduce into KNN ceramics. Ba is adopted to retain the stability of the perovskite structure and the charge neutrality. The Ni is used to increase the covalency of the oxygen bonding and reduce the bandgap. Apart from the intrinsic properties, the fabrication method also affects the performance of the prepared energy harvester. Low sintering density, off-stoichiometry and large grain size highly degrades the piezoelectric properties (As reviewed in chapter 2). Therefore, a suitable sintering method needs to be carefully controlled to produce KNN-based ceramics.

The aim of this project is to provide fundamental knowledge and experimental evidence of the sintering mechanisms of KNN-based ceramics, investigate effect of chemical addition upon the functional properties of KNN-based materials as well as demonstrate the materials in experimental energy harvesters. Thus, this study can provide a general view and the mechanism of KNN-based photo-ferroelectric multifunctional materials as well as hybrid energy harvesting.

4.2 Objectives:

The key objectives can be summarised as follows:

- To fabricate $(K_{0.5}Na_{0.5})Nb_3$ bulk ceramics via conventional single-step sintering and two-step sintering methods to study the sintering ability of the KNN system and to optimise the processing method.
- To study the sintering mechanism of $(K_{0.5}Na_{0.5})Nb_3$ by characterising and comparing the microstructure and piezoelectric behaviour of $(K_{0.5}Na_{0.5})Nb_3$ bulk cermaics using two different sintering methods.
- To fabricate 0.98 $(K_{0.5}Na_{0.5})Nb_3$-0.02 $Ba(Ni_{0.5}Nb_{0.5})O_{3-\delta}$ bulk ceramics via conventional single-step sintering and two-step sintering methods to study the sintering ability of the doped KNN system and to optimise the processing method.
- To fabricate a set of KNN-based bulk materials with different amounts of $Ba(Ni_{0.5}Nb_{0.5})O_{3-\delta}$ doping and investigate the sintering ability and phase transition phenomenon of doped KNN materials with respect to $Ba(Ni_{0.5}Nb_{0.5})O_{3-\delta}$ addition.
- To characterise and investigate the impact of $Ba(Ni_{0.5}Nb_{0.5})O_{3-\delta}$ addition upon the structure, dielectric, piezoelectric, ferroelectric and optical properties of the $(K_{0.5}Na_{0.5})Nb_3$ system.
- To demonstrate and compare the performance the piezoelectric energy harvester prepared by $(K_{0.5}Na_{0.5})Nb_3$ and the hybrid energy harvester prepared by doped $(K_{0.5}Na_{0.5})Nb_3$.

Chapter 5. Experiments and characterisation

5.1 Introduction

The experimental methodology used for the research reported in this project is divided into two parts. The first part is concerned with the synthesis, fabrication and characterisation of multifunctional materials, including the fabrication of ceramics and the characterisation of their structural and functional properties. The second part describes the preparation and testing of hybrid energy harvesters. Two piezoelectric systems were investigated in this thesis: $(K_{0.5}Na_{0.5})NbO_3$ (5KNN) and (1-y) $(K_{0.5}Na_{0.5})NbO_3$ – y $Ba(Ni_{0.5}Nb_{0.5})O_{3-\delta}$ (y=0-0.10).

5.2 Fabrication of bulk ceramics

Conventional solid-state and pressure-less sintering methods were used to fabricate the bulk ceramics of 5KNN and KNN-based materials. The information of raw materials used are summarised in table 5.1.

Table 5.1 Reagents for fabricating piezo-ceramics

Materials	Purity	Company
K_2CO_3	≥99.0%	Sigma-Aldrich, UK
Na_2CO_3	≥99.50%	Sigma, UK
Nb_2O_5	≥99.90%	Aldrich, UK
$BaCO_3$	≥99.95%	Alfa Aesar, UK
NiO	≥99.995%	Aldrich, UK

5.2.1 Powder synthesis

As reviewed in chapter 2, the compositions of $(K_{0.5}Na_{0.5})NbO_3$ and (1-y) $(K_{0.5}Na_{0.5})NbO_3$ – y $Ba(Ni_{0.5}Nb_{0.5})O_{3-\delta}$ were selected as the piezoelectric elements, the chemical formulas and abbreviations presented in this work are listed table 5.2.

The first step involved vibro-milling the as-received powders of Na_2CO_3, K_2CO_3, $BaCO_3$, NiO and Nb_2O_5 with Zirconia ball (YSZ Grinding media, 10 mm in diameter × 10 mm in length, round cylinder, π PI-KEM Ltd.) and ethanol (99.9%, Flake, UK) for 24 hours in plastic bottles (15 ml, Scientific Laboratory Supplies, UK) ($M_{powder}: M_{ZrO_2 ball}: M_{ethanol} = 1: 5: 1.5$ wt%). After drying in an oven (Lenton WF60,

UK) at 65°C for 12 h to remove the ethanol, the powders were then weighed out by high precision balance (±0.0001 g, SECURA224 – 1S, Sartorius Lab, Germany) in stoichiometric quantities according to the molar ratio of the designed composition. Typical batch sizes were 50 g, and the actual amount of each powder for each system is summarised in Appendix I. Mixing of the powders was completed in ethanol using a tubular mill (Turbula T2F powder mixer shaker, Glen mills, Inc.) for 24 h with a zirconia ball as the milling media in a 150 ml plastic bottle (M_{powder}: $M_{ZrO_2 ball}$: $M_{ethanol} = 1: 4: 1.5$ wt%). After removing the ethanol in an oven at 65°C for 12 h, the powders were loaded into a closed alumina crucible (Diameter: 62.2 mm and height: 19.2 mm, >99.8%, Almath Ltd., UK) and calcined at 900°C for 2 h with a 5°C/min ramp rate (up and down) in a muffle furnace (Lenton Muffle Furnace, UK). Finally, the as-prepared powders were milled again by using vibro-milling to break the powder agglomeration in the same ratio of powder, balls and ethanol for 24 h and dried using the same process described above.

Table 5.2 List of the selected compositions

Abbreviation	Doping level	Theoretical chemical formula
5KNN	0	$(K_{0.5}Na_{0.5})NbO_3$
5KNN-2BNNO	0.02	$0.98(K_{0.5}Na_{0.5})NbO_3 - 0.02Ba(Ni_{0.5}Nb_{0.5})O_{3-\delta}$
5KNN-4BNNO	0.04	$0.96(K_{0.5}Na_{0.5})NbO_3 - 0.04Ba(Ni_{0.5}Nb_{0.5})O_{3-\delta}$
5KNN-6BNNO	0.06	$0.94(K_{0.5}Na_{0.5})NbO_3 - 0.06Ba(Ni_{0.5}Nb_{0.5})O_{3-\delta}$
5KNN-8BNNO	0.08	$0.92(K_{0.5}Na_{0.5})NbO_3 - 0.08Ba(Ni_{0.5}Nb_{0.5})O_{3-\delta}$
5KNN-10BNNO	0.10	$0.90(K_{0.5}Na_{0.5})NbO_3 - 0.10Ba(Ni_{0.5}Nb_{0.5})O_{3-\delta}$

5.2.2 Shaping and sintering

All green bodies of bulk samples, including 5KNN samples and doped KNN samples, were shaped by uniaxial single-ended dry pressing in a stainless-steel die with 13 mm diameter (13 mm Evacuable pellet Die GS03000, Specac Ltd.). Before being pressed into pellets, a water-based polyvinyl alcohol binder (5 wt% concentration of PVA binder, Flaka, UK in water) were mixed with the calcined powders (1 wt% for 5KNN composition and 2 wt% for doped KNN compositions) in an agate mortar (agate mortar, Sigma, UK) from wet condition to dry condition manually. Each grinding batch was 10 g of powder. After mixing with PVA binder, the powders were sieved through a mesh (400 μm, Endecotts, UK). The following bulk sample pressing step was carried out on a dry press kit (Spectroscopy sample

packs, Specac ltd., UK) using a pressure of 200 MPa (~27 kN for the 13 mm diameter die) for 1 min. The mass and resulting thickness of each powder compact were approximately 0.4 g and 1 mm.

Densification of 5KNN composition was investigated using both single step sintering (SSS) and two-step sintering (TSS) in a closed alumina crucible (L × W × H: 54 × 22.5 × 12 mm, >99.8 %, Almath Ltd., UK) in same muffle furnace as for calcination. The heating profile for these two methods is given in figure 5.1 a) (6 samples for each sintering condition were made).

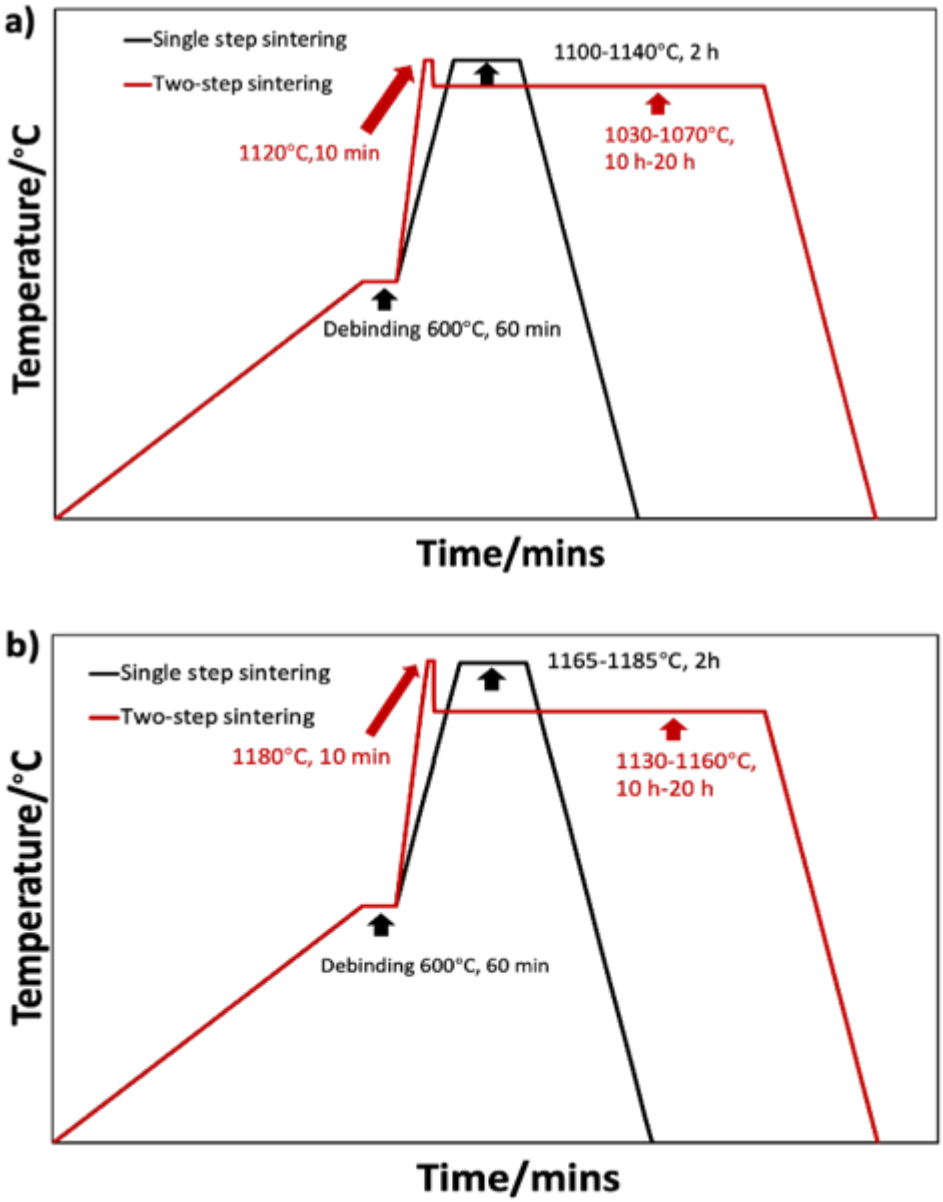

Figure 5.1 Sintering schematic diagram of sintering routes for SSS (black line) and TSS (red line), a) 5KNN ceramics, b) 5KNN-2BNNO ceramics

PVA binder removal was completed for all samples at a heating rate of 1°C/min to a final temperature of 600°C and held for 1 h. Samples sintered using SSS were heated at 5°C/min to a peak temperature in the range of between 1080 – 1140°C and held for a 2 h dwell. The samples were then allowed to cool naturally in the furnace. For samples sintered using TSS, the first step involved heating to an initial temperature, T_1, in the range 1040 – 1140°C using a heating rate of 10°C/min and a very short dwell of 10 mins. The samples were then cooled rapidly at 30°C/min to a lower temperature, T_2, in the range of 1030-1070°C and dwelled for a further 10-20 h. Similarly, the doped KNN samples (5KNN-2BNNO) were also sintered by SSS and TSS, the heating profile for these two methods is given in figure 5.1 b. The sintering programmes of all the compositions are summarised in table 5.3. In order to minimise the volatilisation of Na and K during sintering (figure 5.2 a), all undoped samples were buried in a powder bed with a composition equivalent to that of the pellets. However, the Ni in BNNO doped 5KNN will react with alumina crucible, causing the inhomogeneous elements distribution. Hence, all the doped KNN samples were covered by platinum foil (0.02 mm thickness, Goodfellow Ltd, UK) and sintered without a powder bed to avoid a reaction between the nickel in the powder and the alumina crucible (figure 5.2 b).

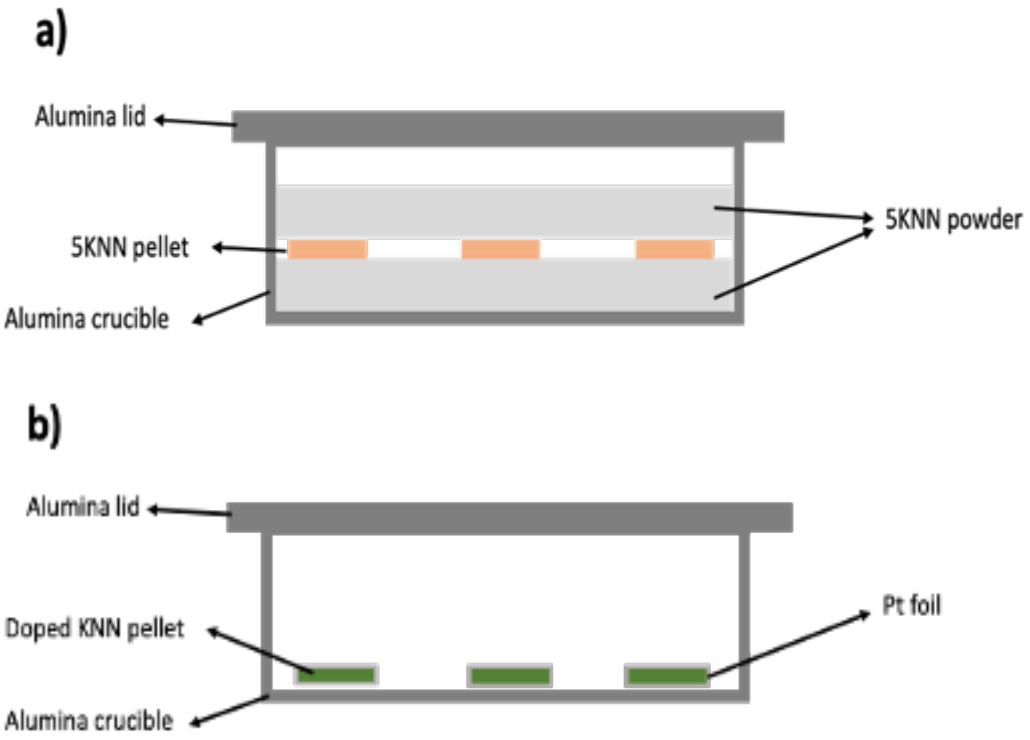

Figure 5.2 Schematic illustration of the arrangement of a) 5KNN ceramics and b) BNNO doped KNN ceramics in the alumina crucible

Table 5.3 Sintering conditions for selected compositions

Materials		Heating rate/°C min^{-1}	T_1/°C	t_1/h	T_2/°C	t_2/h
5KNN	SSS	5	1100	2	/	/
		5	1120	2	/	/
		5	1140	2	/	/
	TSS	10	1120	0.16 (10 min)	1030	10
		10	1120	0.16 (10 min)	1050	10
		10	1120	0.16 (10 min)	1070	10
		10	1120	0.16 (10 min)	1070	15
		10	1120	0.16 (10 min)	1070	20
5KNN-2BNNO	SSS	5	1165	2	/	/
		5	1170	2	/	/
		5	1175	2	/	/
		5	1180	2	/	/
		5	1185	2	/	/
	TSS	10	1180	0.16 (10 min)	1130	10
		10	1180	0.16 (10 min)	1140	10
		10	1180	0.16 (10 min)	1150	10
		10	1180	0.16 (10 min)	1160	10
		10	1180	0.16 (10 min)	1140	20
		10	1180	0.16 (10 min)	1150	20
		10	1180	0.16 (10 min)	1160	20
5KNN-4BNNO		5	1185	2	/	/
5KNN-6BNNO		5	1185	2	/	/
5KNN-8BNNO		5	1190	2	/	/
5KNN-10BNNO		5	1195	2	/	/

5.3 Electrode depositing and poling

The planar faces of all sintered samples were first ground into a smooth surface finish using 20 μm silicon carbide paper. A magnetic sputter coater (K575X, Emitech) was employed to coat the polished surfaces with a 40 nm chromium layer followed by two 200 nm gold layers.

Prior to performing any electrical measurements, the contact poling process were employed to all bulk samples in silicone oil. As mentioned in Chapter 2, the poling electric fields of 3.5 and 4.5 kV/mm were used to pole 5KNN samples and doped KNN samples, respectively. The electric fields were powered by a power supply (Alpha III, Brandenburg Ltd., UK), and all the pure KNN samples were poled at 120°C for 30 min whilst the doped KNN samples were poled at room temperature for 10 min. Since the doped KNN contains a large concentration of oxygen vacancies, leading to high leakage currents and large coercive fields, a high temperature activates the movement of the oxygen vacancies which makes the poling process more difficult. Thus, the electric field was increased and poling was done at room temperature and for a shorter time for the doped KNN samples. After poling, the sample was removed from the field and the oil immediately, a tissue dipping the acetone was used to wipe the sample and help the cooling of sample. After cooling, the sample was washed with acetone (99.5%, Sigma) in an ultrasonic bath (Ultrasonic bath, Grant Ltd.).

5.4 Material characterisation

5.4.1 Density measurement

The Archimedes method is usually adopted to measure the density of the bulk ceramics, involving immersion of the samples in water. However, due to the solubility of KNN in water, the Archimedes method was not suitable for the KNN system. Consequently, in this work the density values were determined from measurements of the mass and volume of the samples (equation 5-1). The mass (m) of the ceramics was measured using an accurate electronic balance (± 0.0001 g, SECURA224 – 1S, Sartorius Lab, Germany) and the volume was calculated from the external dimensions of the cylindrical samples, *i.e.* diameter (d) and thickness (t). The thickness was measured by a Micrometer (Electronic Digital Micrometer IP54, 0 – 30 mm / 0.001 mm / ± 0.002 mm, TESA, Switzerland) and the diameter was measured by a Vernier Caliper (Electronica Digital Calliper, 0 – 150 mm / 0.01 mm / ± 0.002 mm, RS, UK). Each sample was randomly measured at 3 positions for diameter values and 5 points for thickness values. Then the average value was obtained to calculate the density, ρ, using equation 5-1:

$$\rho = \frac{mass}{volume} = \frac{m}{\pi(\frac{d}{2})^2 t} \qquad 5\text{-}1$$

The diameter shrinkage was calculated using equation 5-2:

$$\frac{(13mm - diameter\ after\ sintering)}{13mm} \times 100\% \qquad 5\text{-}2$$

5.4.2 Particle size, thermodynamics property and shrinkage characterisation

A particle size analyser (Gracell, SympaTec, Bury, UK) were employed to measure the particle size of the raw materials as well as the powders after milling. In this work, ethanol was used as solvent medium. At first, ~0.3 g powder, ~3 g ethanol as well as one drop of $Na_4P_2O_7$ (0.1 M, dispersant, Simpatico Gmbh Ltd.) were put in a 5 ml glass tube and then loaded into an ultrasonic bath to prepare a suspension. After a reference measurement in particle size analyser, the suspension was then added into the integral ultrasonic bath of the analyser (approximately 26-32% concentration) for about 15 s to break the soft agglomerates in the suspension by adopting the inbuilt sonication. During the measurement, the laser beam passed through the dispersed particles in suspension and the light was scattered onto a lens. After calculating the measured angular variation in intensity of scattered light using software supplied with the instrument, the particle size distributions were obtained.

The reaction process of the raw powder mixture was analysed by a thermogravimetric analyser (TGA) and differential scanning calorimeter (DSC). A NETZSCH simultaneous thermal analyser (STA 449C Cell) was employed to measure the variation in heat flow and weight of materials versus temperature at a constant heating rate. To observe the reactional behaviour of the 5KNN and doped 5KNN mixture, precursor samples of the powder mixture (approximately 0.02 g) were placed in alumina crucibles (80 µl alumina crucible, NETZSCH, Germany) in the machine and heated from room temperature to 1000°C with a heating rate of 10°C/min.

Measurements of the phase transition temperatures for 5KNN sintered pellets (d~5 mm, m~0.02 g) were taken using a DSC (404C, NETZSCH, Germany), and heated from 40°C to 500°C using a 10°C/min heating rate in an argon atmosphere.

The shrinkage of the 5KNN and 5KNN-2BNNO green bodies (covered by Pt foil) versus temperature was measured by dilatometry (NETZSCH 402E-1600°C furnace) in a nitrogen atmosphere. Samples (dimensions are 5 mm in diameter and 10 mm in length) were first heated to 600°C at 1°C/min heating rate and dwelled for 1 h to remove the PVA binder, then heated to maximum temperatures of 1130°C and 1250°C with a 10°C/min heating rate for the 5KNN and 5KNN-2BNNO samples, respectively. Finally, the samples were directly cooled down to room temperature at 10°C/min cooling rate. The appropriate sintering temperatures for 5KNN and 5KNN-2BNNO ceramics were selected at temperatures higher than the onset of shrinkage.

5.4.3 Microscopy characterisation

Scanning electron microscopy (SEM) was applied to characterise the microstructure, *i.e.* morphology, grain (particle) size and porosity, of as-calcined powder and sintered ceramic pellets. The morphologies and fracture of the calcined powder, 5KNN pellets and doped KNN pellets were analysed by SEM instruments (Scanning electron microscopy 7000f, JEOL, Japan) at 15-20 kV depending on the resolution. In order to observe the morphology of single particles, the calcined powders were dispersed in acetone for 5 min under an ultrasound environment to break the agglomeration, and then 1-2 drops of the suspension were dropped onto single-sided copper tapes, attached to an alumina stub and allowed to dry. The sintered samples were firstly polished and then thermally etched at 150°C below the sintering temperature (T_1 for TSS) for 30 min. After sticking the as-etched sample to an aluminium stub using conductive carbon adhesive tape, the sample was coated with a carbon layer (15 nm) by a sputter coater (K575X, EMITECH). The average grain sizes of the sintered ceramics were then obtained using the linear intercept method[290,291] on images observed using back-scatter electrons (BSE) in order to improve the contrast. The element proportions and distribution were analysed by EDS (Energy-dispersive X-ray spectroscopy, Oxford INKA), conducted at 10 mm working distance with 15 kV operating voltage.

5.4.4 X-ray diffraction characterisation

X-ray diffraction is usually adopted to assess the phase purity and crystal structure of materials. For crystalline material, all atoms are arranged as a periodic array. Three integers (h, k, l), known as Miller indices, are used to determine the family of atomic planes. As shown in figure 5.3, where the X-ray beam interacts with atomic plane in incident angle, θ, a portion of scattered X-rays produced diffraction according to the Bragg's law (Equation 5-3).

$$2d_{hkl}\sin\theta = n\lambda \qquad 5\text{-}3$$

Where d_{hkl} is lattice spacing, λ is wavelength of Cu Kα radiation, θ and n represent the diffraction angle and number of diffractions, respectively.

The phase purity and crystal structure of the powders and pellets were assessed by X-ray diffraction instrument (Bruker D8 advanced X-ray diffractometer, Cu Kα=1.5405Å). The X-ray diffraction data were then collected by measuring the variations in intensity of X-rays against the movement of X-ray source (40 kV, 40 mA) and detector between 10° to 60° 2θ range with a step size of 0.0142°. The refinement of the diffraction pattern was using the pseudo-Rietveld method and the quantitative

phase analysis was conducted using Rietveld method[292–294]. The initial diffraction patterns were refined via TOPAS-Academic software and jEdit software by comparing to reference data in the crystal structure database (the Inorganic Crystal System Database, ICSD) to approximately estimate the phase composition.

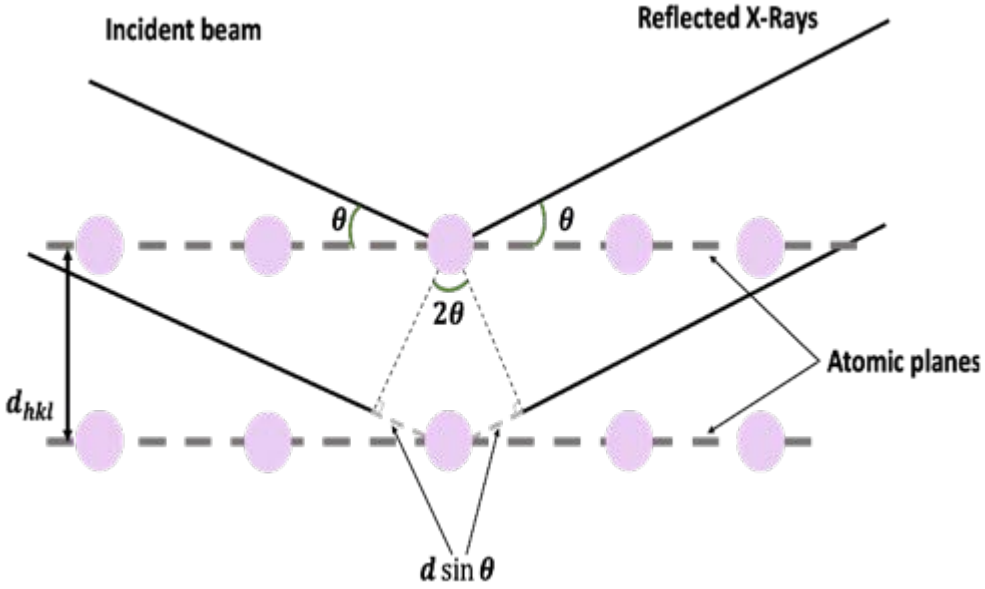

Figure 5.3 Diffraction of X-rays in a crystalline material

5.4.5 Raman spectroscopy

Raman spectroscopy is an extremely accurate analysis tool for determining the phase of a material based on the direct measuring of molecular vibrations in the samples. As shown in figure 5.4, when a single frequency of laser irradiates a sample, the electron cloud is oscillated and excited to a virtual vibrational state. If the scattered energy is similar to the incident beam, this elastic scattering is known as Rayleigh scattering. However, Raman spectroscopy is used to observe the in-elastically scattered radiation to identify the phase structure. It is well-known that there are two kinds of inelastic scattering, Stokes and anti-Stokes. For the former, the energy will transfer from incident photons to molecular to induce the nuclear motion, therefore the scattered energy is smaller than the incident beam. For the anti-Stokes scattering, the energy is transferred from the molecular to scattered photons, thus the scattered energy is larger than the incident beam. Raman scattering usually records Stokes scattering.

In this study, powdered form samples were adopted for the Raman spectroscopy measurement to avoid the influence of inner stress, where sintered ceramics were first crushed by hammer and then

hand ground into power in an agate mortar and pestle. The Raman spectra were obtained from a Raman spectrometer (Renishaw InVia Reflex) with a 488 nm excitation laser (~2 mW power). The information of peak position, peak intensity and peak width for the Raman spectra were collected by Renishaw Wire 4.4 software. For the variable temperature analysis (from 30°C to 500°C), the powders were poured into a cold/hot stage (THMS600, Linkam) and heated at 1°C/min in 1 bar Argon flowing at 100 ml/min. The Raman spectrum was collected every 30 seconds and the power was held below 1mW, which did not significantly raise the sample temperature. Then these data were analysed using the Renishaw Wire 4.4 and MATLAB R2019a software to investigate the dependence of the vibrational modes (shifts of peak position, changes of intensity and broadening of width, etc.) on temperature.

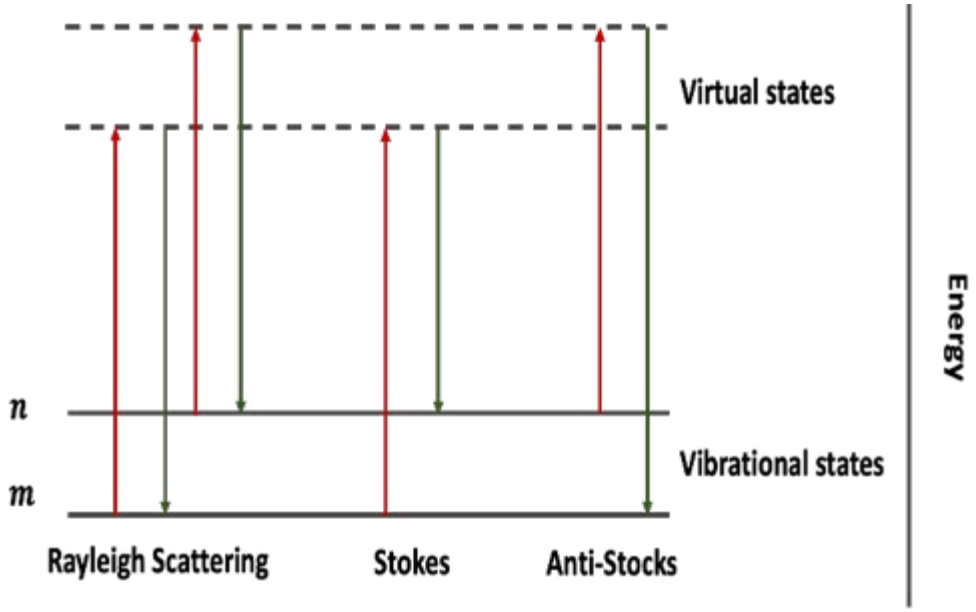

Figure 5.4 Schematic diagram of Rayleigh and Raman scattering processes

5.4.6 UV-vis-NIR spectrophotometer

An Ultraviolet-visible-Near Infrared spectrophotometer (UV-vis-NIR spectrophotometer, Cary 5000 Scan, Varian, Palo Alto, USA) with an integrating sphere attachment (UV0902M216, Palo Alto, USA) was used to measure the diffuse reflectance of the samples. When the light impacts on a flat polished surface of a solid, it would be partly reflected, partly absorbed and partly refracted. Through reflectance spectra, the electronic transition of the different orbitals of the solid can be given. The spectra obtained were used to identify the bandgap via the Kubelka-Munk function[295] (equation 5-4 and 5-5):

$$(F(R)) = \frac{(1 - R_\infty)^2}{2R_\infty} \quad 5\text{-}4$$

$$(F(R) \cdot hv)^{1/\gamma} = A(hv - E_g) \quad 5\text{-}5$$

Where R is the reflectance of the sample, A is a scaling constant, γ factor is equal to ½ or 2 for the direct and indirect transition bandgaps, respectively. The direct and indirect transitions are well defined by figure 5.5. h and v represent the Planck constant and photon's frequency, respectively, hv represents photon energy; and E_g is the bandgap energy. In this thesis, $\gamma = 2$ is used to calculate the direct bandgap. By plotting $(F(R) \cdot hv)^2$ as the function of the energy (hv), the direct bandgap of the pellets can be collected via linear section.

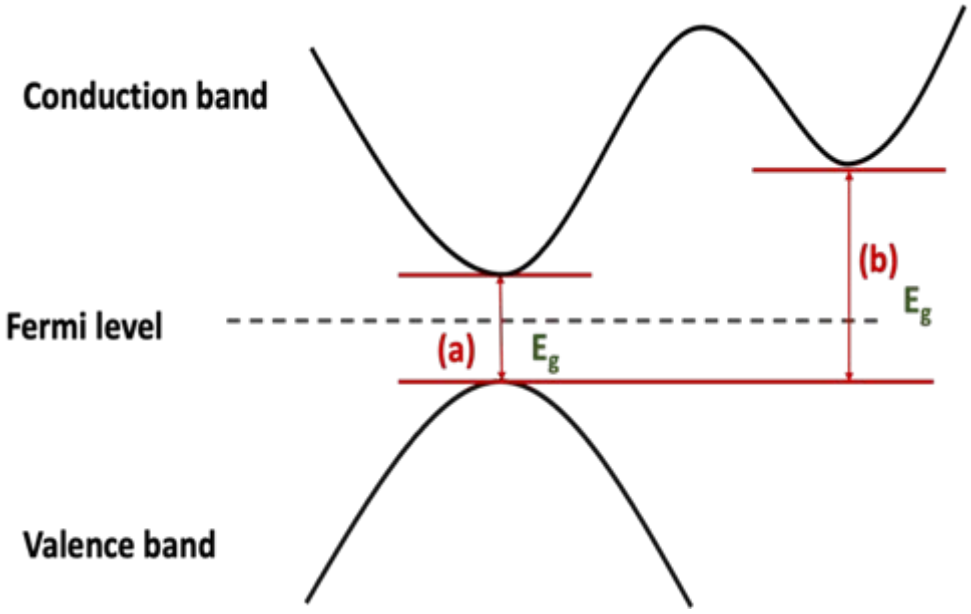

Figure 5.5 Simplified band transition representation: (a) direct bandgap; (c) indirect bandgap

5.4.7 Dielectric, piezoelectric and ferroelectric property characterisation

Dielectric property characterisation

The dielectric properties of sintered discs at room temperature, including capacitance (C) and dielectric loss factor ($tan\delta$), were measured at 1 kHz using an impedance analyser (±0.08%, 4294A, Agilent, USA) with a bespoke jig. The equations of permittivity (ε), vacuum permittivity (ε_0) and relative permittivity (ε_r) are shown in equations 5-6 and 5-7, where t and r refer to the thickness and radius ($r = d/2$) of the pellets, respectively.

$$\varepsilon = C \cdot \frac{t}{\pi r^2} \quad 5\text{-}6$$

$$\varepsilon_r = \frac{\varepsilon}{\varepsilon_0} \quad 5\text{-}7$$

The temperature dependent dielectric properties were analysed by an electrochemistry impedance spectrometer (Solartron 1260) by using 1°C/min heating rate on consecutive temperature steps, stepped by 20°C, between 30°C to 500°C. The *Zview* software was used to analyse the measured data. The impedance measurement was applied to measure the real (Z') /imaginary (Z'') part of impedance of ceramics from 0.1 Hz to 1 MHz. The real part permittivity (ε') was calculated by adopting equation 5-8 and 5-9 and its relationship to temperature was observed.

$$C = -\frac{1}{\omega} \times \frac{Z''}{(Z^2 + Z'^2)} \quad 5\text{-}8$$

$$\varepsilon' = \frac{Cd}{\varepsilon_0 A} \quad 5\text{-}9$$

Where ω is frequency in angular.

Piezoelectric property characterisation

The piezoelectric charge coefficient (d_{33}) was directly measured by a quasi-static piezoelectric coefficient testing meter (YE2730A, SINOCERA, China) 24 h after poling. 7 random points of each sample were tested, and the average value was calculated from 5 of the values, thus rejecting the largest and smallest values, resulting in the final d_{33} values.

The frequency method[296] was used to measure the piezoelectric properties (k_{eff}, k_p, Q_m). The resonant frequency ($f_m \approx f_r \approx f_s$) and anti-resonant frequency ($f_n \approx f_a \approx f_p$) of materials were characterised by impedance spectra collected from the impedance analyser (4294A, Agilent, USA) with a bespoke jig at room temperature. The electrical impedance spectra are shown in figure 5.6.[46,297] Based on these parameters, electromechanical coupling coefficients (k_{eff}, k_p), and the mechanical quality factor (Q_m) were calculated from equation 5-10, 5-11 and 5-12.

$$k_{eff}^2 = \frac{f_p^2 - f_s^2}{f_p^2} \quad 5\text{-}10$$

$$k_p^2 \cong 2.51\frac{f_a - f_r}{f_r} - \left(\frac{f_a - f_r}{f_r}\right)^2 \quad 5\text{-}11$$

$$Q_m = \frac{1}{2\pi f_m |Z| C^T k_{eff}^2} \quad 5\text{-}12$$

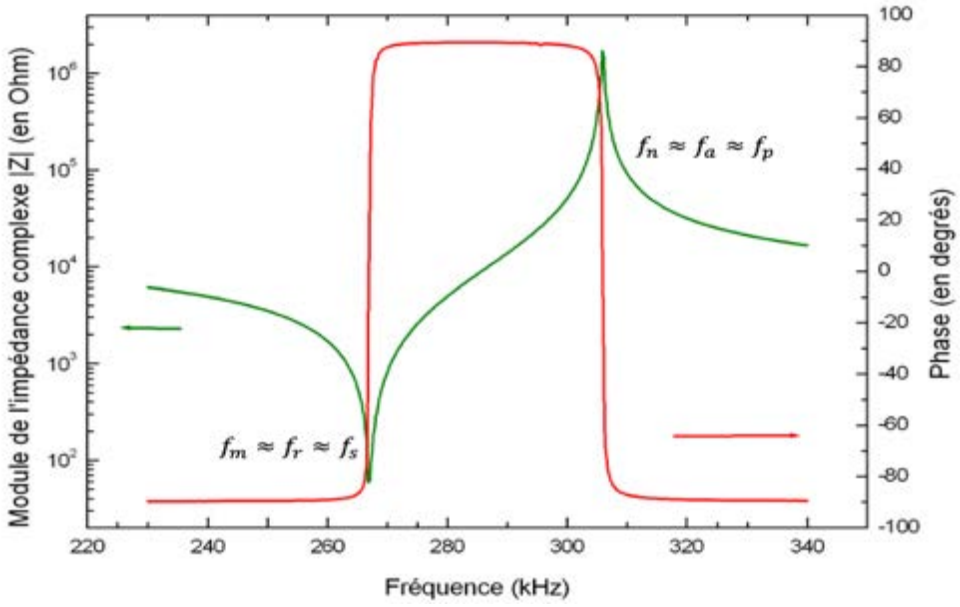

Figure 5.6 Electric impedance magnitude and phase diagram as a function of frequency for a poled KNN ceramics[46,297]

Ferroelectric property characterisation

The polarisation-hysteresis loop (P-E loop) was measured on unpoled ceramics using a Piezoelectric Evaluation System (Precision Premier II Ferroelectric Tester, RADIANT technologies Inc., US) in which a triangular wave voltage with a maximum amplitude of E=3 kV mm^{-1} and frequency of 10 Hz was utilised. The collected data were analysed by Vision 5 Data Acquisition software, where E_C and P_r of ceramics can be obtained directly.

5.5 Fabrication of energy harvesters

5.5.1 Photo-ferroelectric cell

The photo-ferroelectric cell was prepared to measure the photo-response and the bandgap reduction nature of doped KNN composition (5KNN-2BNNO). First of all, 5KNN-2BNNO sintered pellets were crushed and vibro-milled with ethanol and Zirconia balls (M_{powder}: $M_{ZrO_2 ball}$: $M_{ethanol} = 1:4:1.5$ wt%) for 24 h to obtain ceramic powder with a homogenous particle size, which is similar to the powder synthesis part (section 5.2.1). After that, the 5KNN-2BNNO slurry was put in the oven at 65°C overnight to remove the ethanol. Secondly, 1.2 g of dried powder was mixed with 60 µl ethylene glycol, 60 µl Triton-X (as an adherent) and 400 µl ethanol (dispersant) to prepare the 5KNN-2BNNO

paste[298]. This solution was mixed in a microplate mixer (Multi-Microplate Genie SI-4000, Scientific Industries, Inc.) for 5 minutes and homogenised in an ultrasonic bath for 20 minutes.

Thirdly, the fabrication of the photo ferroelectric cell was conducted. Fluorine doped thin oxide coated glass (FTO, $2 \times 2 \times 2$ cm, surface resistivity 7 ohm/sq, Sigma-Aldrich Ltd.) were used as the electrodes. Carbon was used as the counter-electrode (figure 5.7). The 5KNN-2BNNO paste was deposited on the FTO glass by casting manually. After deposition, the photoelectrode was put on a hot plate at 125°C for 10 minutes to dry the solution and then the temperature was increased to 350°C for 45 mins to remove the organic compounds from 5KNN-2BNNO paste.

Finally, the counter electrode (carbon coated FTO glass) and photoelectrode (5KNN-2BNNO coated FTO glass) were set together (figure 5.8). After 24 hours, an electrolyte (I^-/I^{3-}, Arbor Scientific Ltd.) was dropped into the gap between the counter electrode and photoelectrode to help the transport of the photo induced carriers.

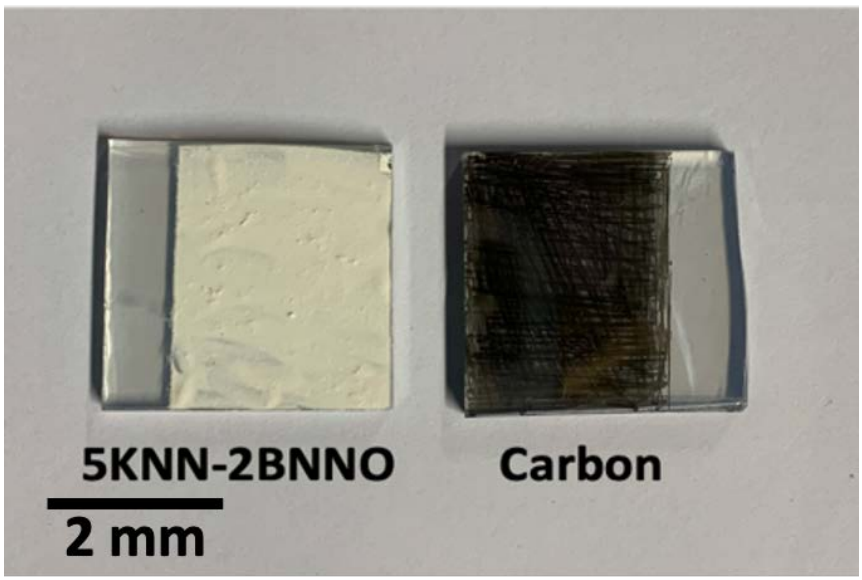

Figure 5.7 Components of the 5KNN-2BNNO photo ferroelectric cell, 5KNN-2BNNO as the photoelectrode and carbon as the counter electrode

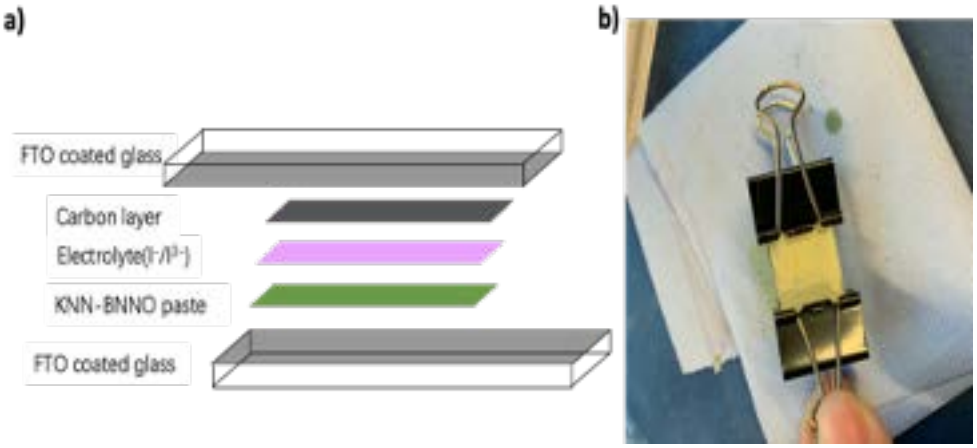

Figure 5.8 a) Schematic diagram for the components of photo ferroelectric cell (reproduced from[298]), b) Final prototype of cell

A schematic graph of the photo ferroelectric cell is shown in figure 5.9, and the blue numbers represent the working steps. First, the light is absorbed by the 5KNN-2BNNO layer with electrons consequently being promoted from their ground states to excited states and transformed from the valence band to the conduction band. In the second step, these electrons are transported between the 5KNN-2BNNO paste and diffuse towards the 1-FTO electrode. Then in the third step, the electrons flow toward the counter electrode (2-FTO) through the external circuit where they can be collected for powering a load. Lastly, the electrons at counter electrode flow into the electrolyte (I ion redox mediator) to reduce I_3^- to I^-, equation 5-13[299].

$$I_3^- + e^- \leftrightarrow 3I^- \qquad 5\text{-}13$$

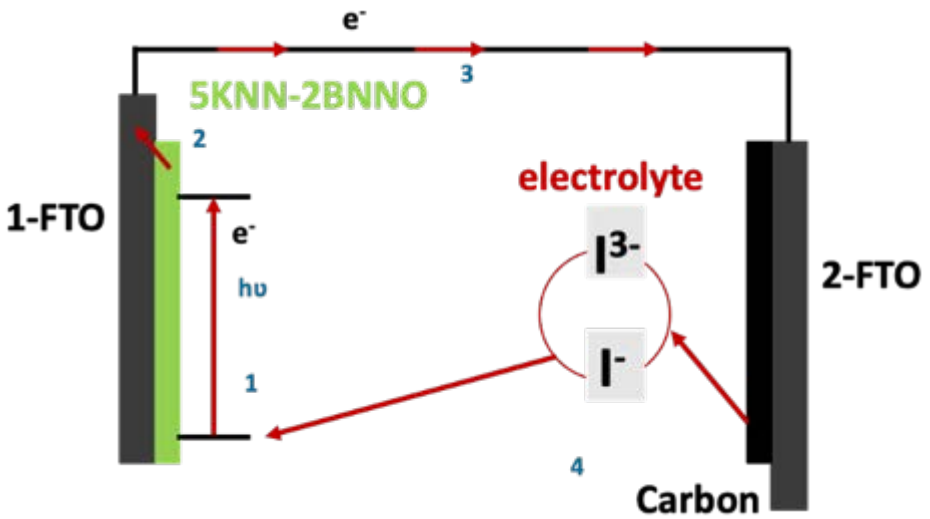

Figure 5.9 A schematic diagram of 5KNN-2NNO photo ferroelectric cell, with the blue numbers representing the working steps

5.5.2 Cantilever energy harvester

Cantilever-type energy harvesters were used to test the energy harvesting performance. Sintered pellets, including 5KNN and 5KNN-2BNNO ceramics, with a diameter of 10 mm and a thickness of 0.9 mm, were polished into squares (8 mm $\times$ 8 mm $\times$ 0.12 mm). The piezoelectric energy harvesters made by 5KNN piezoelectric elements (TSS and SSS) were used to study the impact of microstructure and density upon the performance of piezoelectric energy harvester. Hence, only gold electrodes were needed (section 5). For the energy harvester made by 5KNN-2BNNO, both photovoltaic and piezoelectric performance are of interest. Consequently, 5KNN-2BNNO elements were coated on one side with a Cr/Au electrode as described in section 5, and the other side was coated with an Indium Tin oxide electrode (ITO, 200nm, >80 % transmission between the range of 400 nm to 700 nm, ~30-60 Ohms/sq) to ensure that light could still be absorbed by the sample. As a comparison, a 5KNN piezoelectric element densified by TSS and using the same electrodes as the 5KNN-2BNNO ceramics was used to investigate the effect illumination on pure 5KNN composition. After electroding with suitable electrodes and poling, this piezo element was fixed onto a stainless-steel substrate (110 mm $\times$ 20 mm $\times$ 0.5 mm) using silver epoxy paste. Two sections of copper tape were cut and attached to the sample by silver epoxy paste (Conductive Adhesive Epoxy, RS Components Ltd), one on each side. Two copper wires were then connected to the copper tapes by soldering. A schematic representation of the final energy harvester is presented in figure 5.10.

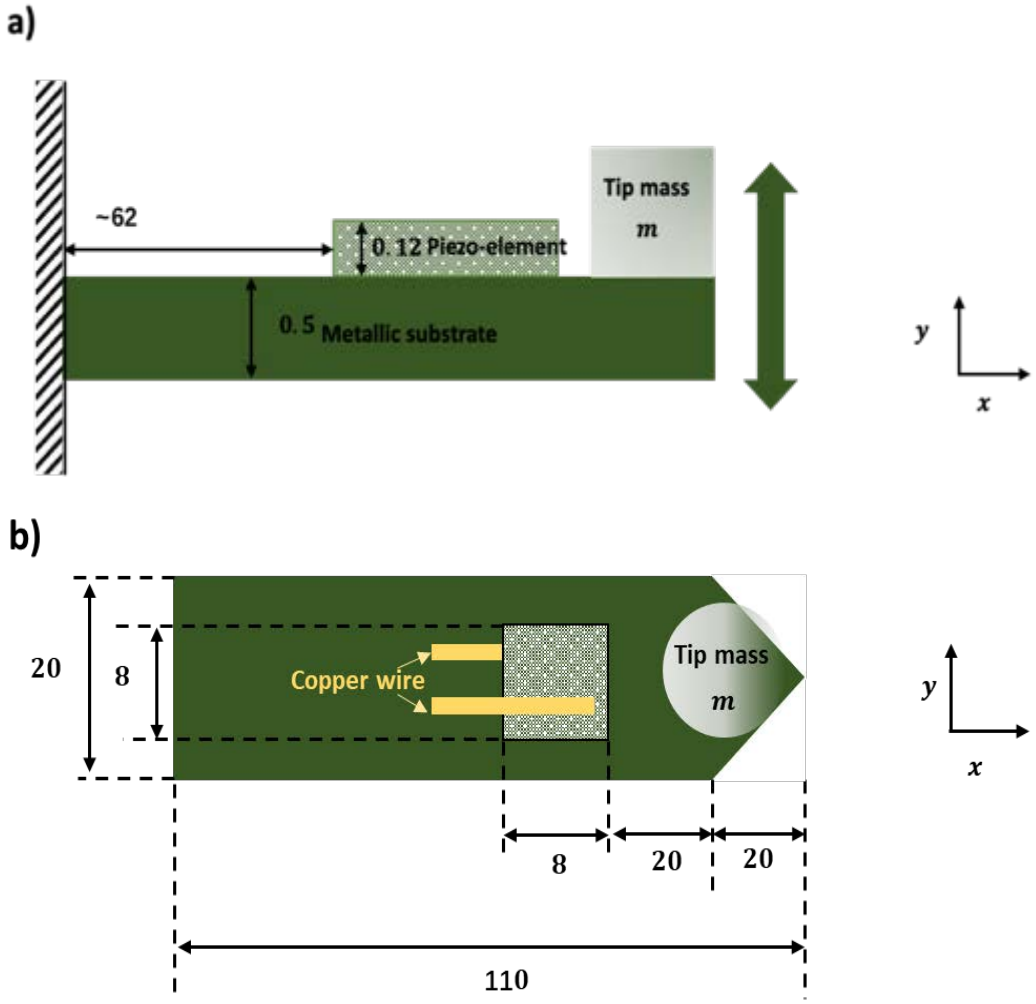

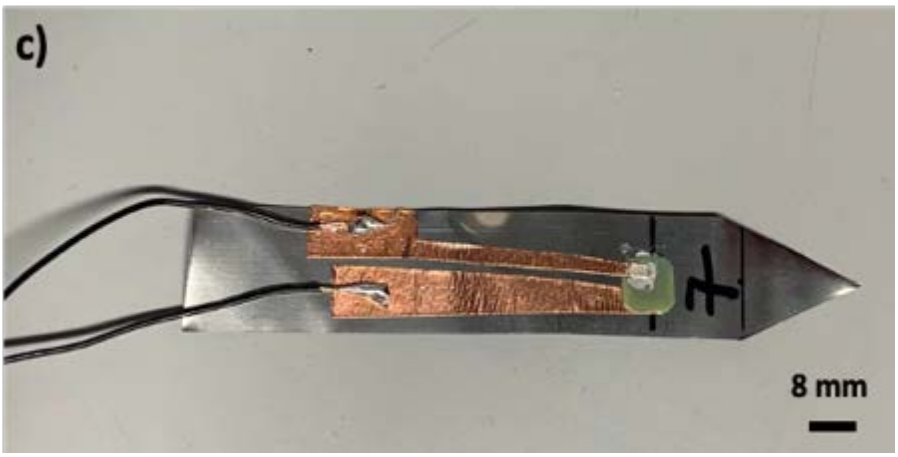

Figure 5.10 Schematic graph of the bulk energy harvester, a) side view, b) top view and c) final prototype of cantilever energy harvester

5.6 Photo-vibration testing of the energy harvester

5.6.1 Photo-response testing for photo-ferroelectric cell

Figure 5.11 demonstrates the photo-response measurement for a photo-ferroelectric cell. Figure 5.11 a) shows the measurement equivalent circuit and b) shows true measurement in the lab. In figure 5.11 b) the green multi-meter (range: 20 µA ± 0.05% ± 2 digits DC, Digital multi-meter 318 DMM, Rapid Electronics Ltd.) was used as ampere meter and the yellow multi-meter (range: 2000 mV ± 0.05% ± 3 digits DC, Handheld digital multi-meter, Premier Farnell Ltd.) was used as voltmeter. The photo-response of the 5KNN-2BNNO photo-ferroelectric cell was tested under the illumination of a linear tungsten halogen lamp (wavelength from 200 nm to 1200 nm, 230-240 V, 500 W max, China). The range of the variable resistor is from (100 ohm to 1 Mohm, RS component Ltd.) and the active area of the cell is approximately 5 cm^2.

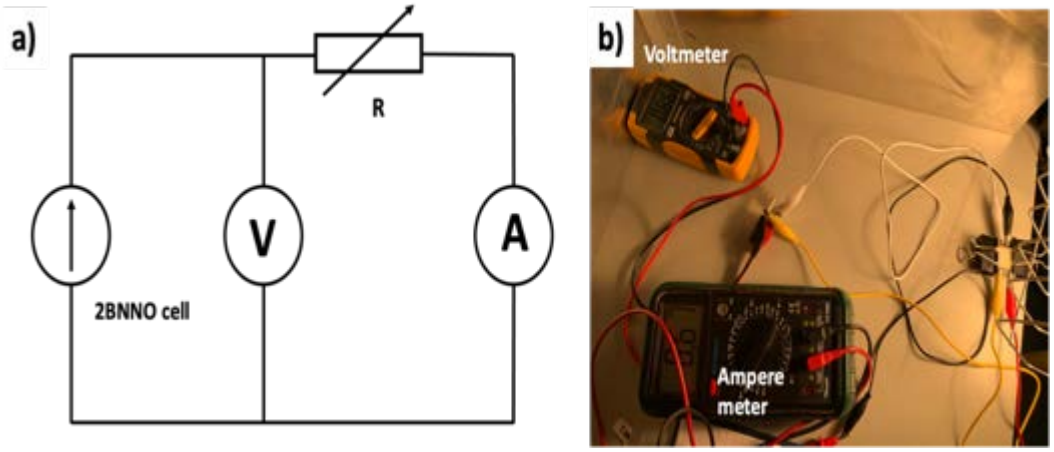

Figure 5.11 a) Equivalent circuit and b) Photo-response measurement

The short current (I_{sc}) was measured without connecting any resistor by reading the values shown by the green multi-metre, and open circuit voltage (V_{oc}) was measured without connecting with an amper meter by reading the values shown by the yellow multi-meter. The current density (J_{sc}) instant power (P) and fill factor (FF) can be calculated by the equations 5-14, 5-15 and 5-16:

$$J_{sc} = \frac{I_{sc}}{A} \quad \text{5-14}$$

$$P = VI \quad \text{5-15}$$

$$FF = \frac{P_{max}}{V_{oc} \cdot I_{sc}} \quad \text{5-16}$$

Where V and I are the instant voltage and current by connected with resistor with different resistance, A is the active area of the cell (5 cm^2).

5.6.2 Piezoelectric response and hybrid energy harvesting performance testing

The as-fabricated cantilever energy harvesters were mechanically clamped by a metal cap that fixed onto an electromagnetic shaker (Gearing & Waston electronics, UK) head which is illustrated in figure 5.12. One end of the cantilever was fixed on the shaker and the other end was attached to a proof mass (~3.0 g) by Blu Tac, a re-usable adhesive (Bostik Hotline). A sinusoidal signal was input by the power amplifier and was tuned by the functional generator to the shaker in order to make the cantilever beam vibrate. Also, for the hybrid energy harvesting performance testing, a tungsten-halogen lamp (500 W, wavelength from 200 nm to 1200 nm) were used to provide light to activate the photocurrent of the energy harvester, figure 5.12. The energy harvesters were directly connected with varies resistors (R) for measuring the output voltage and power. During the vibration, the bending stress of the energy harvester generated a voltage output across the resistor (R) which was collected by a 4-channel oscilloscope (Pico 4204, Pico Technologies, UK) and recorded by Picoscope software on the computer. The input impedance of the Pico oscilloscope was 1 MΩ and the maximum sampling rate was 80 MS s^{-1}.

The output power (*P*) and power density (P_d) can be mathematically expressed by equations 5-17 and 5-18:

$$P = \frac{V_r^2}{R} \quad \text{5-17}$$

$$P_d = \frac{P_{RMS}}{cantilever\ volume} \quad \text{5-18}$$

Where V_r, P_{RMS} are the voltage across the resistor and root mean square of P in 30 cycles, respectively.

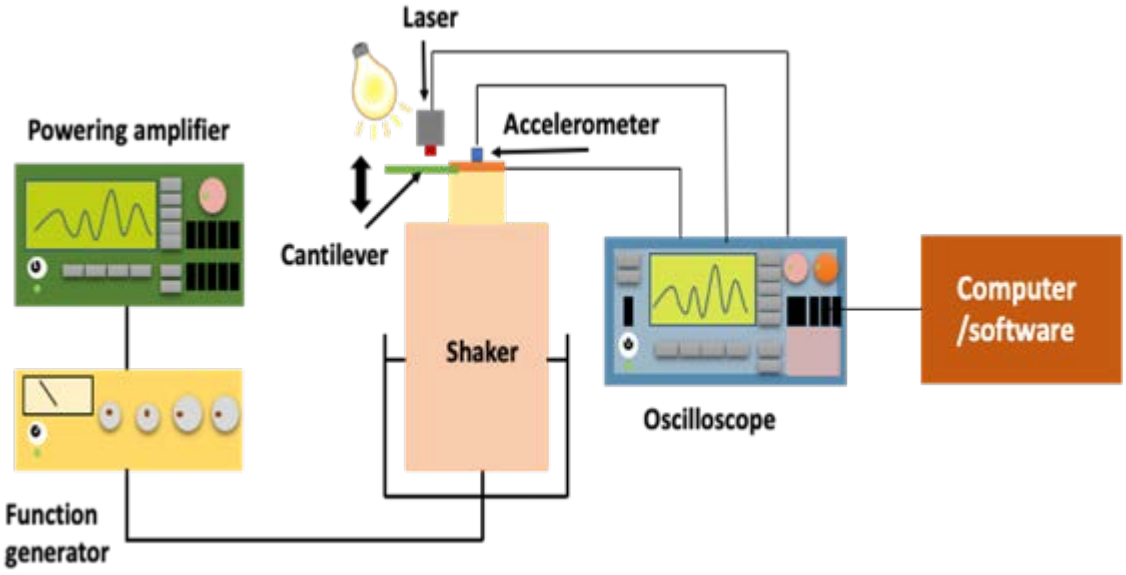

Figure 5.12 Schematic diagram of the vibration-illumination testing system

Chapter 6. The investigation of $(K_{0.5}Na_{0.5})NbO_3$ composition

6.1 Introduction

This chapter focused on the process-ability of $(K_{0.5}Na_{0.5})NbO_3$ ceramics (5KNN). Poor sinter-ability leads to high porosity and poor piezoelectric properties, and then limits the application of 5KNN ceramics. High evaporation rates of potassium as well as sodium at temperatures at and below the sintering temperature and the narrow sintering window are the main reasons causing the low sinter-ability of KNN ceramics. In this chapter, the processing conditions of single-step sintering (SSS) and two-step sintering (TSS) have been investigated and optimised to fabricate piezoelectric ceramic of 5KNN with as a high density and as fine a grain size as possible. In accordance with fundamental sintering theory and the principal mechanisms of SSS and TSS, the densification and resultant evolution of the 5KNN microstructure has been systematically analysed at each stage of the sintering process. Based on the functional properties of the 5KNN piezoelectric ceramics produced, a discussion is presented on the comparative benefits of TSS over conventional SSS and the potential of TSS as a means of delivering fine grain size, dense, lead-free $(K_{0.5}Na_{0.5})NbO_3$ ceramics.

6.2 KNN powder synthesis

The particle size of the raw materials is summarised in table 6.1. Although there are no significant requirements on the particle sizes of the starting oxides and carbonate powders, it affects the reaction process during calcination. It is reported[300,301] that homogenous and smaller staring particle size (< 10 μm) helps to improve the mixing degree during the preparation of powder precursor and calcination. Therefore, before mixing the 5KNN precursor, the raw materials were vibro-milling for 24 h to decrease the particle size. After that, stoichiometric mixtures of the constituent precursor oxide and carbonate powders were prepared by glen mill, as described in section 5.2.1. The particle sizes of the powder mixtures obtained are also summarised in table 6.1. All the particle size were directly measured by particle size analysis. Each value was an average of three independent measurements.

To study the reaction process of the 5KNN precursor powder, a DSC-TGA was used to analyse the reaction progress (as illustrated in figure 6.1). The summary reaction is described by equation 6-1:

$$0.5K_2CO_3 + 0.5Na_2CO_3 + Nb_2O_5 \rightarrow 2(K_{0.5}Na_{0.5})NbO_3 + CO_2 \uparrow \qquad 6\text{-}1$$

Table 6.1 Summary of raw materials and 5KNN precursor particle size

Powder	Before milling: D_{50}/ μm	After milling: D_{50}/ μm
K_2CO_3	21.7±0.48	3.0±0.08
Na_2CO_3	16.3±0.87	3.1±0.05
Nb_2O_5	12.64±0.42	2.3±0.40
5KNN precursor	/	2.8±0.26

From theoretical calculation, the total mass loss of 5KNN composition is expected to be 12.29% due to the releasing of carbon dioxide. Because the ratio of sodium and potassium is 1:1, the attribution of CO_2 of K_2CO_3 and Na_2CO_3 are both 6.145%. It can be seen from figure 6.1 that the TGA pattern exhibits a ~12 % reduction in overall mass when temperature increased to ~730°C. The large weight loss of 10% from 300°C to 730°C may correspond with the decomposition of the carbonates. It is interesting to see there is a slight mass increasing after TGA curve gets level-off, which may be due to proton incorporation from water dissociation[302], as the sample is heated in air. When the temperature was ~900°C, a sharp endothermic peak was observed but no further significant weight loss was detected, which confirms the completion of the formation and crystallisation of the 5KNN system. In order to confirm this, the 5KNN precursor powders were calcined at a range of temperatures from 200°C to 1000°C for 2 h in muffle furnace to study the reaction process. The structural information was investigated by XRD and is shown in figure 6.2. The major Bragg peaks detected correspond to the 5KNN perovskite orthorhombic structure. It can be observed that the reaction started when temperature higher than 400°C, the perovskite structure was formed from 500°C and a pure perovskite structure was acquired when T>600°C. A high calcination temperature would yield a larger grain size and harder particles, leading to low sintering efficiency in the sintering procedure. Therefore, 900°C was considered as the optimum calcination temperature.

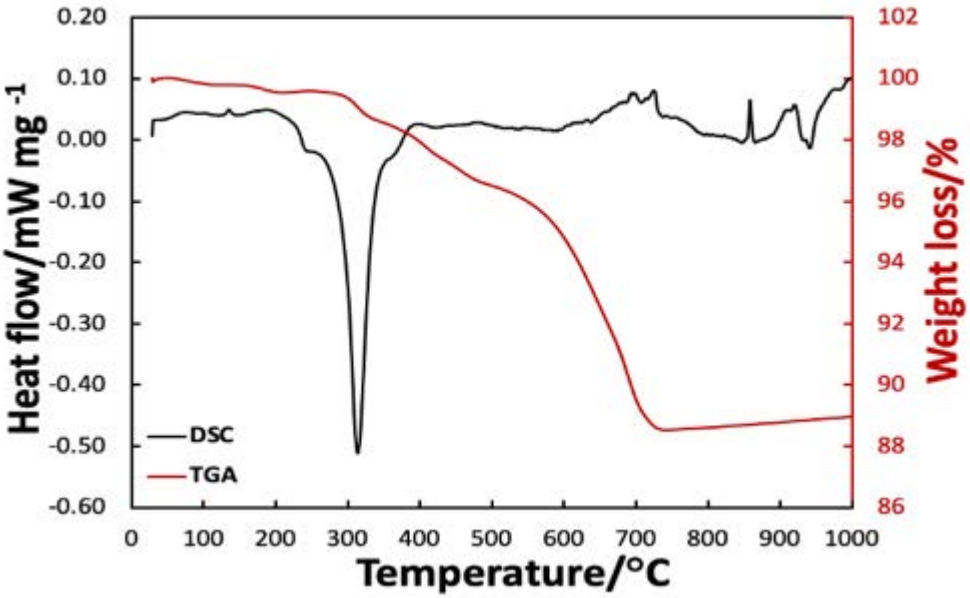

Figure 6.1 The DSC-TGA curves of the 5KNN precursor powder mixture

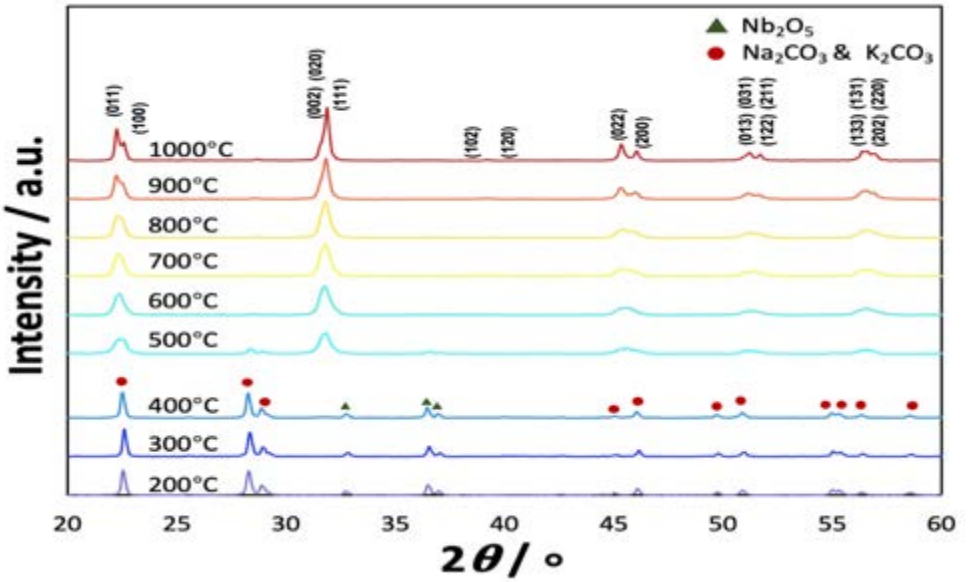

Figure 6.2 XRD patterns of 5KNN powders at different calcined temperature. Peaks have been indexed assuming a perovskite structure

The microstructure of the 5KNN powder calcined at 900°C is shown in figure 6.3 and reveals a highly-facet surface morphology. The overall shape of the particles is highly irregular with multiple cubic domains growing outwards in a concertina-like structure. This morphology indicates the nucleation and growth of the KNN grains were orientated. The mean crystallite size range of the particles was ~300 – 500 nm, whilst the overall particle size was closed to 1 – 2 µm.

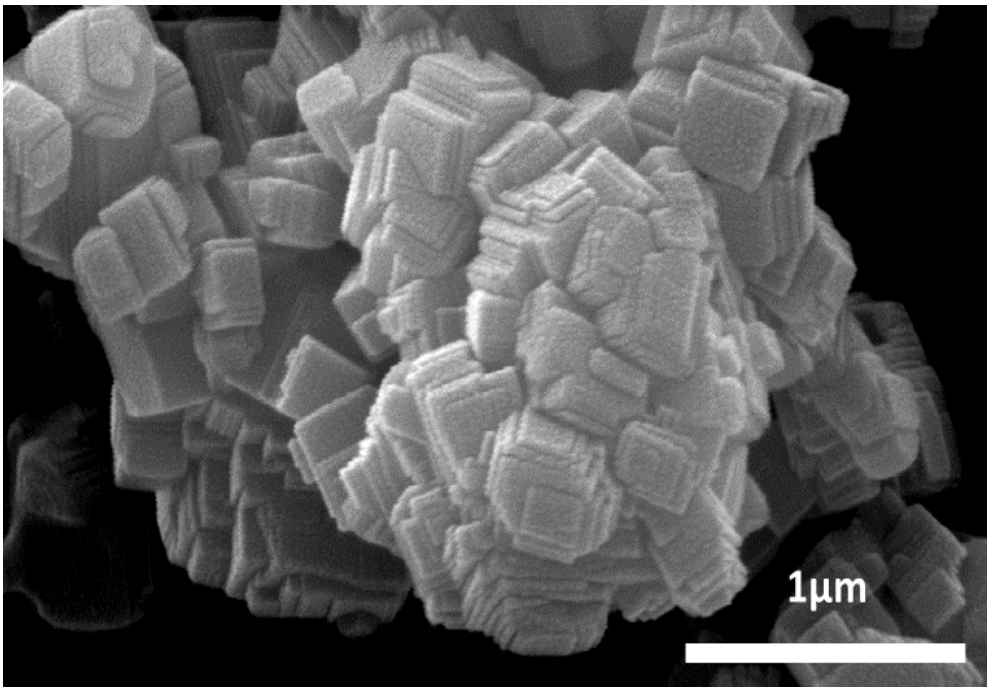

Figure 6.3 A representative morphology of 5KNN powder calcined at 900°C for 2 h

6.3 Sintering optimisation

The dynamic shrinkage curve of a 5KNN powder compact heated to 1130°C by using 5°C/min heating rate is presented in figure 6.4 and the shrinkage rates is also provided. The powder compact began shrinking at ~900°C, where a steep slope in the shrinkage curve could be observed. A rapid increase in shrinkage into a largely linear shrinkage rate occurred at 1000 – 1070°C; beyond 1080°C, the shrinkage rate decreased as the curve begins to level off, with the 5KNN powder compact reaching its highest level of shrinkage at ~1120°C. It can be seen from the $KNbO_3$-$NaNbO_3$ phase diagram[168,303], which was discussed in chapter 2 and presented in figure 2.16, this densification limitation corresponds with the generation of a K-rich liquid phase at ~1110°C. Although the presence of such a liquid phase provides a faster medium for diffusion, it also reduces the energy for grain boundary migration. This promotes rapid grain growth, reducing the amount of free energy available and the driving force for the further densification such that no further shrinkage occurs beyond 1120°C[150]. Gas phase release associated with the volatilisation of Na and K at above 1000°C is also likely to be a contributing factor[150]. From these results, the sintering window of pure 5KNN was considered to be 1080 – 1120°C. A schematic diagram of the sintering profiles was provided in chapter 5 (figure 5.1) and the mechanisms will be discussed in the next section.

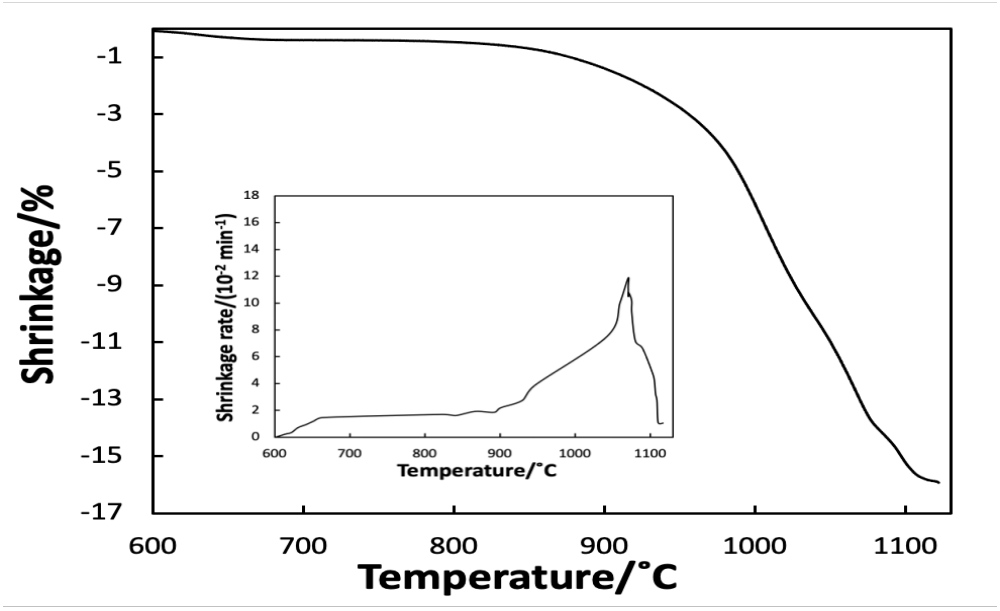

Figure 6.4 Shrinkage as a function of temperature for the calcined 5KNN powder compact sintered at temperatures up to 1130°C at 5°C/min. Inset: shrinkage rates above 600°C.

6.3.1 Single-step sintering

Based on the results shown in figure 6.4, 5KNN ceramics were produced by single-step sintering (SSS), each batch (6 samples) sintered at different peak temperatures of 1080°C, 1100°C, 1120°C and 1140°C for 2 h. The relative density and corresponding grain sizes of these materials are shown in figure 6.5. As can be observed, higher relative densities were achieved when the ceramics were sintered at higher temperatures, as expected. The peak density achieved was 91% at sintering temperatures of both 1120°C and 1140°C.

Micrographs of the microstructures of the 5KNN ceramics sintered using SSS are presented in figure 6.6 a)-c). As shown in figure 6.6 a), after sintering at 1100°C, a largely homogenous microstructure was achieved with a relatively fine average grain size of ~10 µm. Figure 6.6 b) – d) shows that, along with marginal improvements in density, increases in temperature promote appreciable amounts of grain growth, the mean grain size increasing to ~16 µm at 1120°C and ~21 µm at 1140°C. This result is in agreement with the concept that rapid grain growth, due to the generation of the K-rich liquid phase at ~1110°C[150,168,303], is the principal cause of the limited densification observed at temperatures beyond 1120°C. While the grains in the 1120°C and 1140°C specimens remain primarily equiaxial in form, the wide size distribution of the grains would indicate that the grain growth experienced is abnormal. As reviewed at chapter 2 (section 2.4.2.3), there are many reasons causing abnormal grain growth. As it can be seen in figure 6.3, KNN powder particles possessed faceted features in which oriented grain boundaries move faster than disoriented ones. As a result, some particles will be well-

oriented and have a grain boundary of high mobility. Also, the evaporation of Na will lead to K and Nb segregation, generating sites that are K-rich and Nb-rich at the grain boundary. A K-rich liquid-solid phase mixture forms preferentially, which, as described above, reduces the energy for grain boundary migration, causing the grains to expand rapid. Meanwhile, Nb-rich grain boundaries remain in a state of solid-phase sintering and, thus, continue to grow at a normal rate.

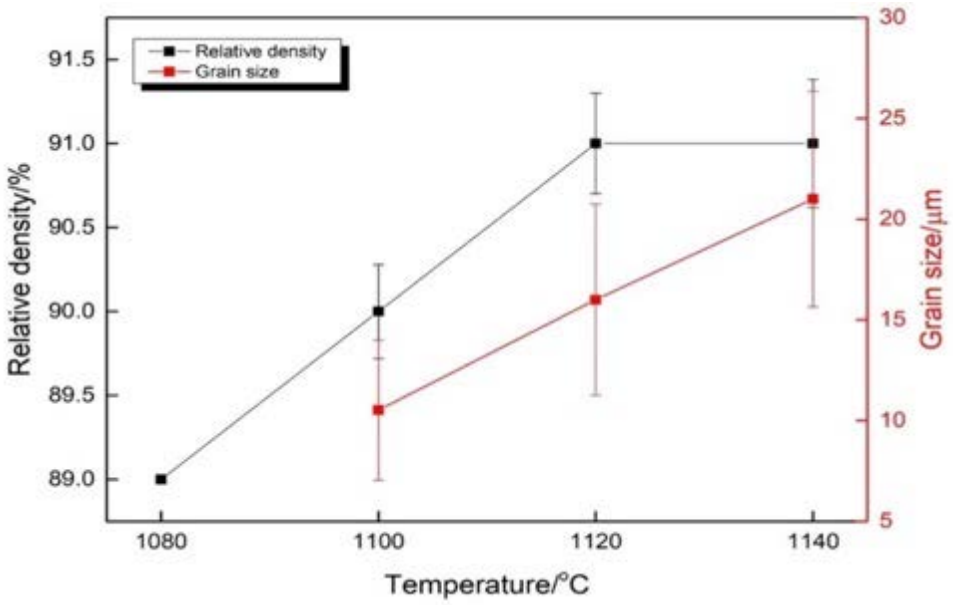

Figure 6.5 Relative density and grain size as a function of sintering temperature for 2 h

The low density of all the 5KNN ceramics sintered using SSS corresponds with considerable amounts of both inter- and intra-granular porosity retained within the microstructures. It can be seen from figure 6.7 that there are three different kinds of pores that exist in KNN ceramics: 1) small, thin inter-granular pores with a straight line edge, mostly located at triple-junctions – residual pores due to incomplete densification; 2) intra-granular closed pores of an irregular morphology – caused by rapid grain growth trapping such pores inside grains; and 3) intra-granular pores of a cubic morphology – associated with gas phase release that results from the volatilisation of Na and K at ~1000°C[150]. Pores with a similar structure can be found during the sintering of NaCl, where the {100} surface have the lowest activation energies for vapourisation[304]. In addition, a fourth type of "porosity" can be observed as a result of sample preparation; large inter-granular pores with a smooth, irregular shape generated by grain pull-out are forming during grinding and polishing.

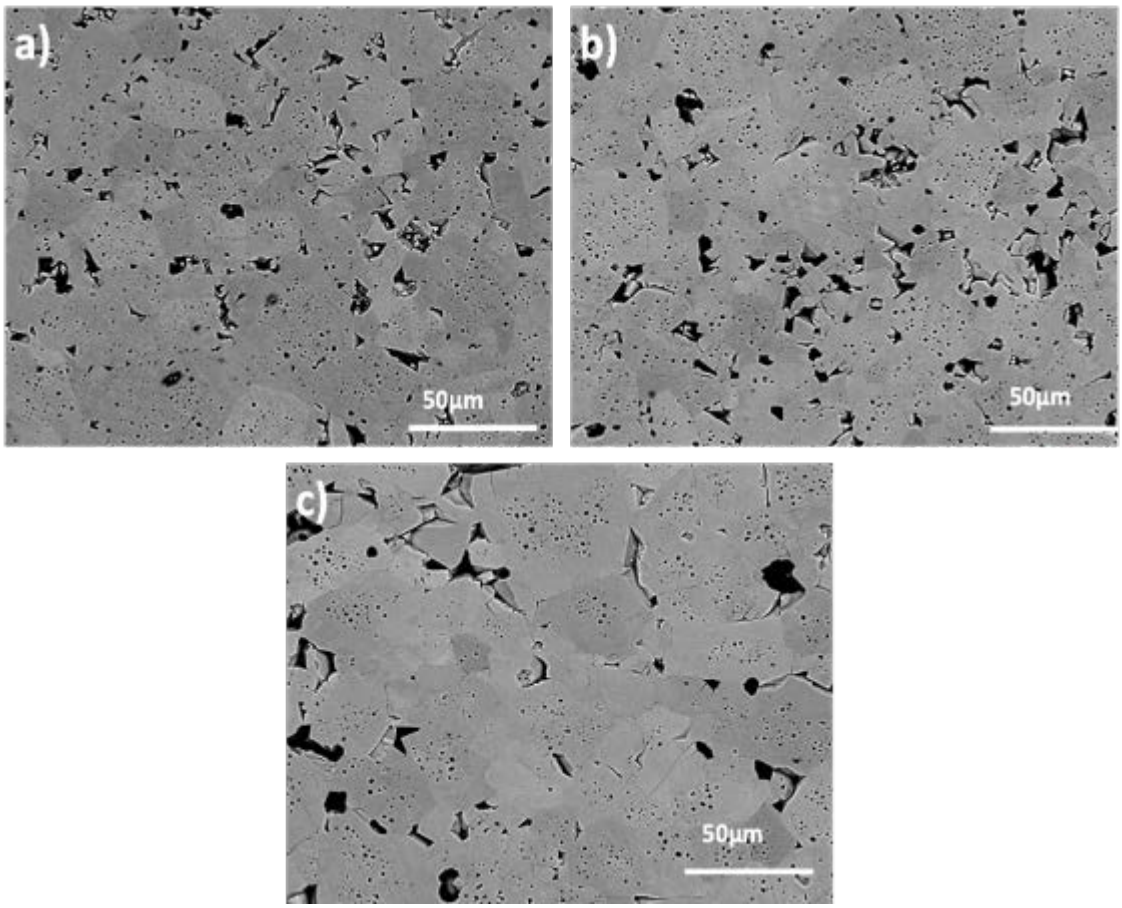

Figure 6.6 Microstructures of 5KNN ceramic densified using SSS for 2 h: a) 1100°C, b) 1120°C and c) 1140°C.

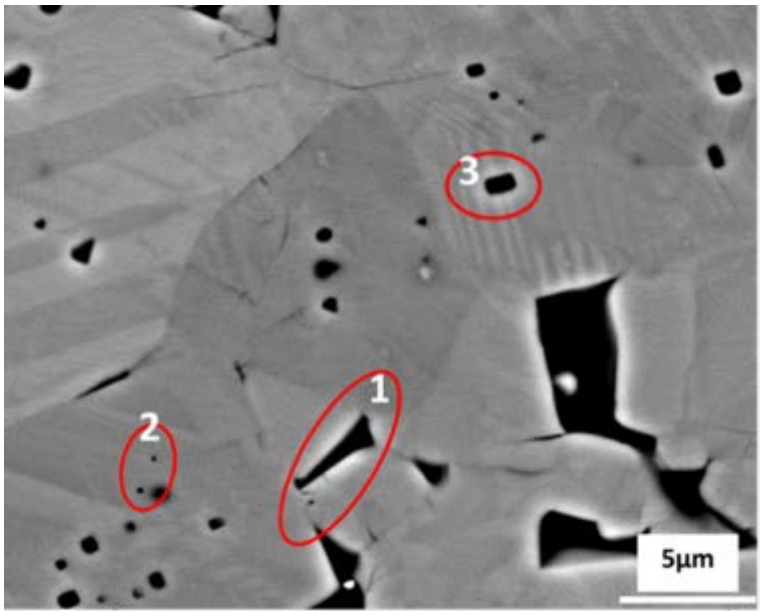

Figure 6.7 Pore morphology of 5KNN sintered at 1100°C for 2 h

The loss of the alkali elements results in a moderate mass loss in the sintered samples, as shown in table 6.2. Without a significant decrease in volume, this negatively influences the final density of the

KNN ceramics. Based on the dilatometry data shown in figure 6.4, the maximum shrinkage of 5KNN via SSS was achieved at 1120°C. This would suggest that samples sintered at >1120°C will not achieve higher densities, a result that is confirmed by the fact that the 1140°C specimen had a density equivalent to that of the 1120°C samples.

Table 6.2 Mass loss of 5KNN ceramics sintered using SSS (sintering time 2 h)

Samples	Mass loss/%	Δ/%
1100°C / 2 h	1.8	0.04
1120°C / 2 h	2.0	0.02
1140°C / 2 h	2.5	0.11

6.3.2 Two-step sintering

In order to achieve high density ceramics with a fine microstructure, two-step sintering (TSS) was used to sinter 5KNN ceramics. For TSS, a sufficiently high intermediate density (>75%) must be obtained during the first sintering step. This is required to ensure that any residual pores that are subjected to second step sintering are of a subcritical size and unstable against shrinkage due to the capillary action. The critical relative density that must be achieved during first step sintering is material dependent and requires careful optimisation of the T_1 temperature[169]. Figure 6.8 shows the relative density of 5KNN pellets partially sintered at different T_1 temperatures and demonstrates that T >1060°C provides the minimum level of densification required (>75%) within the short dwell period of 10 mins. The relative density then exhibits a plateau at 1100°C and 1120°C before decreasing at 1140°C, the latter being consistent with the results in section 6.3.1 and reductions in sample mass due to the loss of Na and K. Figure 6.8 also shows that higher T_1 temperatures leads to significant increases in grain size, from ~0.7 µm at T_1 = 1080°C to 9.5 µm at T_1 = 1140°C.

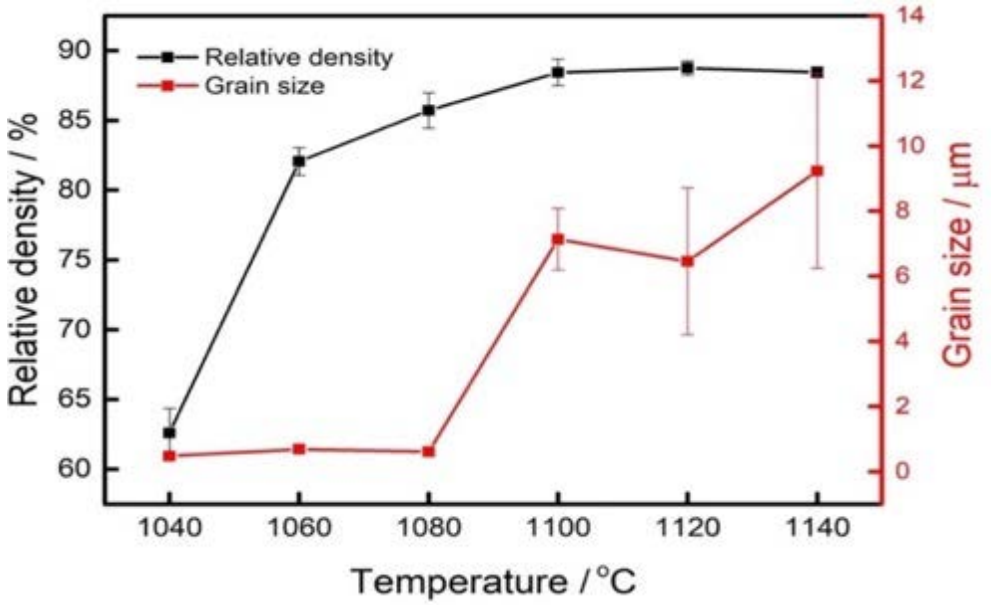

Figure 6.8 Relative density (black line) and grain size (red line) of 5KNN specimens sintered for 10 mins and the as a function of first step temperature

Figure 6.9 a-f) shows the fracture morphologies of 5KNN samples sintered at different T_1 temperatures. At 1040°C, limited densification has occurred, the morphology of the 5KNN powder is still clearly visible. There are some signs of the fusing of particles, but significant inter-granular porosity remains. This suggests that only the particles with the lowest activation energy have been activated at this T_1 temperature; most probably the smaller particles with the highest surface free energy. At T_1 temperatures >1040°C, it is apparent that significant densification has occurred, and that triple-points have formed. Below 1100°C, the microstructure remains homogenous and exhibits no intra-granular porosity. However, above 1100°C, grain growth clearly has an increased contribution on the evolution of the microstructure and intra-granular porosity begins to develop. At 1120°C and 1140°C, samples are found to contain fewer pores and are smoother in terms of their grain morphology. This is associated with the formation of K-rich liquid-phase at ~1110°C, which has coated the particle surfaces and partially-filled intra-granular pores, see figure 6.9 f).

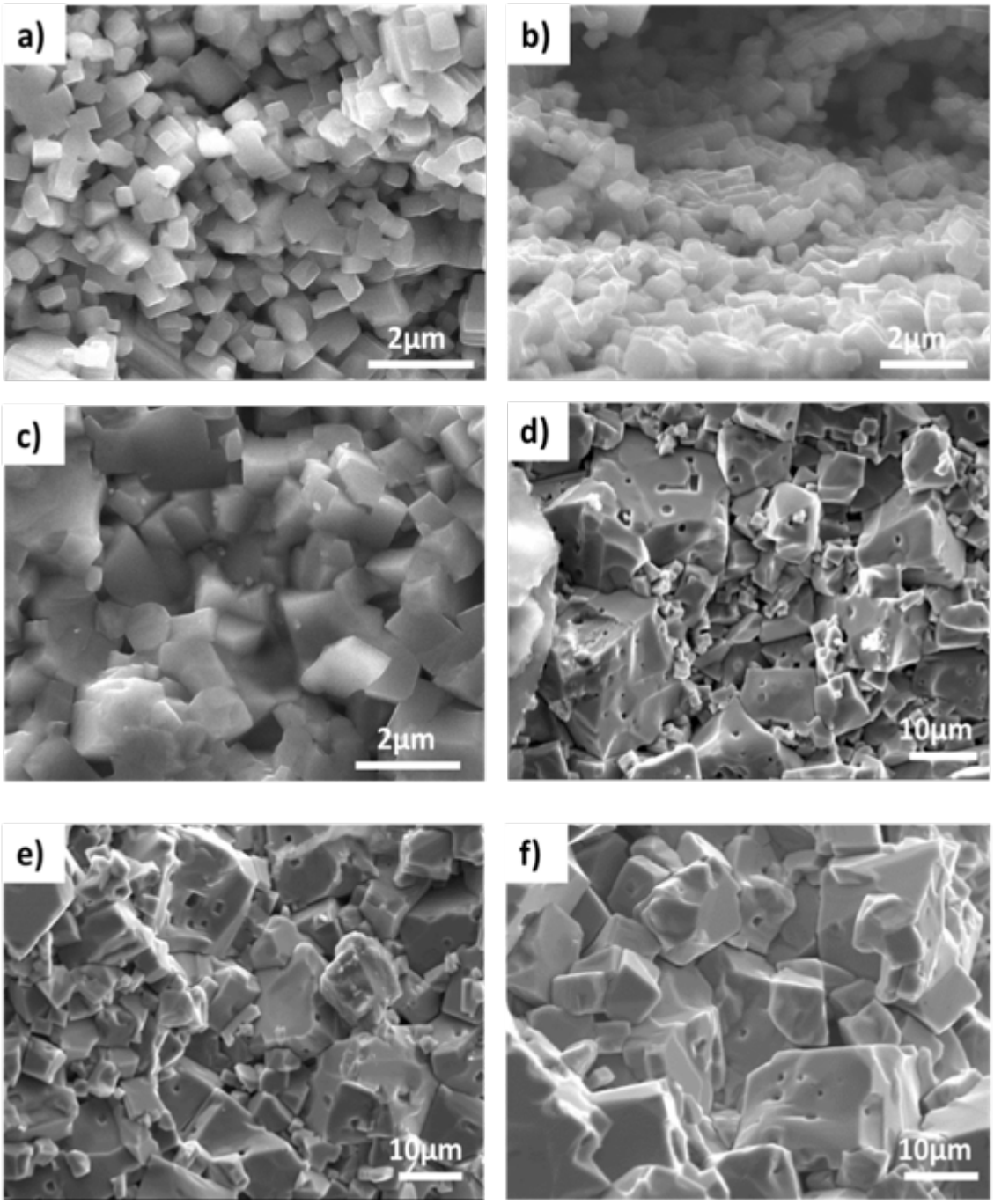

Figure 6.9 Fracture morphologies of 5KNN ceramics sintered at different first step temperatures T_1 for 10 mins. T_1 = a) 1040°C, b) 1060°C, c) 1080°C, d) 1100°C, e) 1120°C and f) 1140°C

It clearly demonstrates that, the 5KNN powder particles are still in the initial sintering stage, where the particles are just starting to connect with necks when T_1 is lower than 1080°C. Here, the capillary force is too low to shrink the pores. However, within the 10 min dwell period, the 5KNN ceramics sintered at temperatures higher than 1080°C have transitioned from the initial and intermediate sintering stages, dominated by bulk diffusion and sample shrinkage, into the final sintering stage

dominated by grain growth[305]. From the report of Chen[169], ZrO_2 ceramics can obtain a high density during the second step provided the first step density is higher than 75%. However, this critical value is different for different materials. As discussed in section 6.3.1, the amount of K-rich phase displays a significant impact upon the densification process of KNN ceramics; excess liquid-phase would cause abnormal grain growth (in the SSS method) preventing the densification of KNN. However, a suitable liquid phase formation could assist the sintering process by providing adequate wetting of the grain boundary, allowing dense microstructures to be achieved in the second step[154]. Therefore, the requirements of high density, small grain size and suitable liquid phase amount need to be satisfied in the first step. As mentioned above, the formation of K-rich liquid phase starts when the temperature is >1110°C [168,303]. The samples sintered at T_1=1120°C for 10 min obtained the highest density and lowest grain size when sintering temperature higher than 1110°C. Also, the amount of liquid phase can be well controlled by short dwell time (10 min) in first step. Thus, 1120°C was chosen as the T_1 sintering temperature for 5KNN.

Given that the aim of T_2 and t_2 is to achieve a maximum density without significant grain growth and to minimise the evaporation of Na and K, the optimum temperature T_2 and dwelling time t_2 needed to facilitate the maximum amount of densification. Recalling the dynamic sintering curve in figure 6.4, the highest densification rates were achieved at temperatures between 1030-1070°C. As such, this is the temperature range that was exploited for use as T_2. Figure 6.10 a) shows the relative densities and grain size of samples sintered at a T_1 of 1120°C for 10 mins and then T_2 temperatures of 1030/1050/1070°C for 10 h. From the results, a T_2 of 1070°C was able to achieve the highest density and the finest grain size. In order to explore whether the density could be further improved by increasing the dwell time at the T_2 stage, additional samples were sintered at 1070°C for extended dwell periods of 15 h and 20 h. The results are shown in figure 6.10 b) and reveal that longer dwell times lead to a decrease in sample density, associated with increased amounts of alkali evaporation, a view supported by the mass loss data in shown in table 6.3, and the associated gaseous phase release. Based on the findings, a T_2 of 1070°C for 10 h yielded pure 5KNN ceramics with the highest relative density via TSS, which was measured to be ~95% of theoretical.

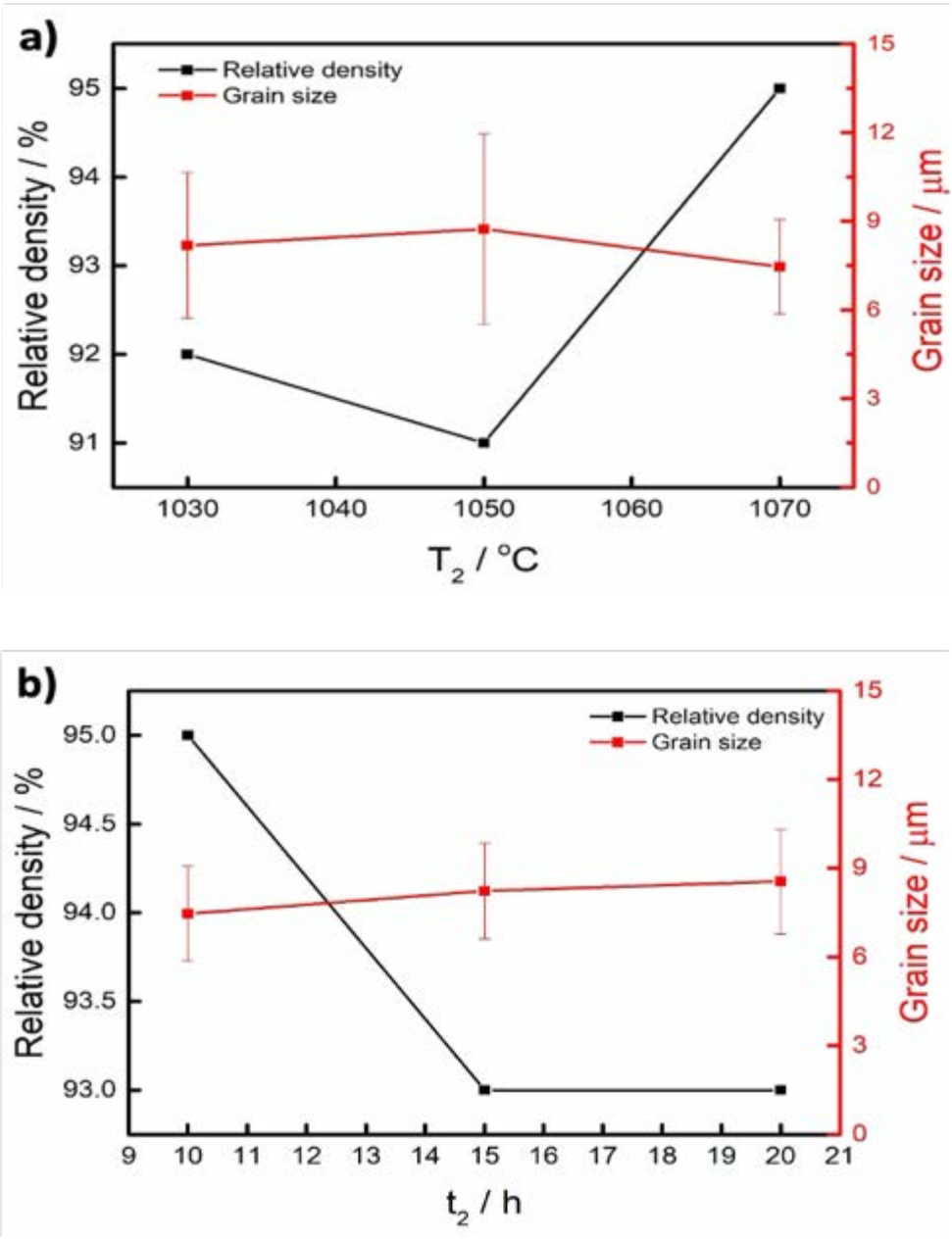

Figure 6.10 Relative density and the grain size of 5KNN specimens sintered at T_1 = 1120°C for 10 min: a) held for 10 h at different T_2 temperatures, and b) held for different dwell periods at a T_2 temperature of 1070°C

Table 6.3 Mass loss of 5KNN ceramics sintered using TSS (different dwelling time)

Samples	Mass loss/%	Δ/%
1120°C/10 min/1070°C/10 h	1.51	0.061
1120°C/10 min/1070°C/15 h	1.77	0.052
1120°C/10 min/1070°C/20 h	1.89	0.071

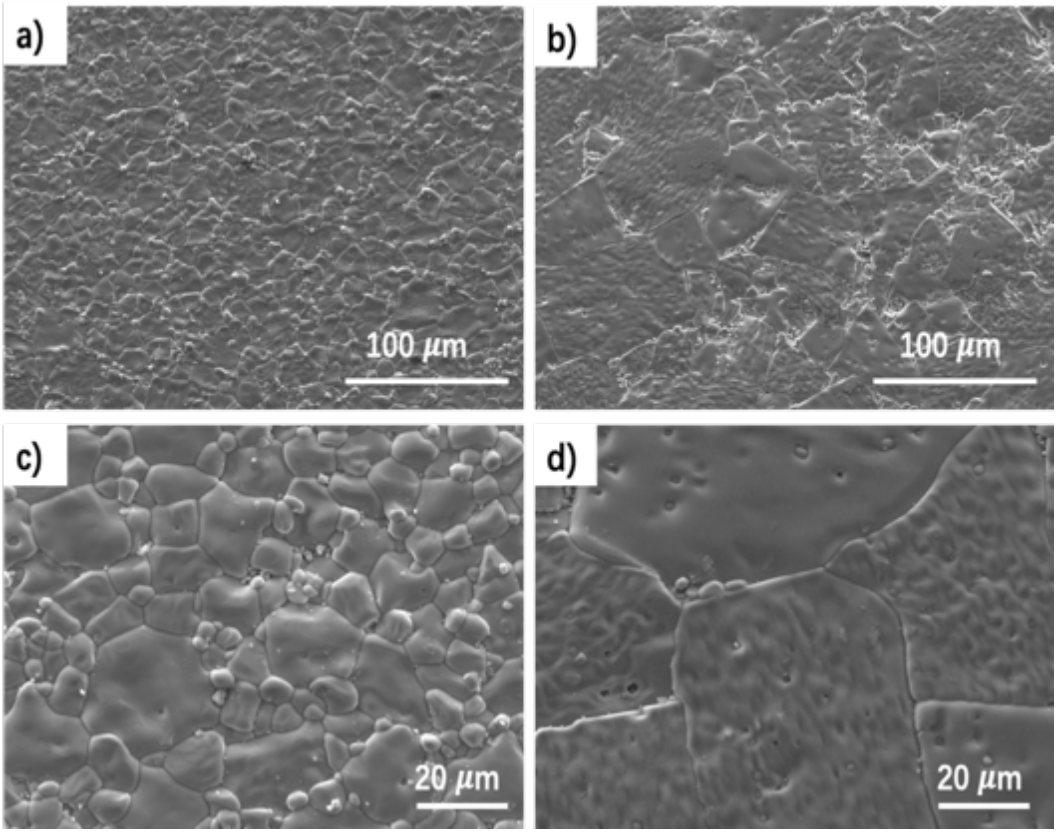

Figure 6.11 Microstructure of sintered surface of 5KNN: a), c) densified by TSS (1120°C /10 min/1070°C /10 h) and b), d) densified by SSS (1120°C /2 h)

Figure 6.11 shows the surface morphology of 5KNN pellets sintered by TSS: 1120°C/10 min/1070°C/10 h (a, c) and SSS: 1120°C/2 h (b, d). Both sintering procedures produce samples with dense microstructures but with different morphologies. SSS-5KNN ceramics tend to form large and faceted grains (> 50 μm) with some gas pores. By comparison, the pellets sintered by TSS a, c) exhibit relatively homogenous and smaller grains (~20 μm) with smooth edges surrounded by smaller grains (1-2 μm). This demonstrates that the TSS method results in higher nucleation rates and helps suppress grain growth. In order to avoid the influence of directly imaging the sintered surfaces, the microstructures of polished surfaces have also been investigated, and are shown in figure 6.12.

Figure 6.12 presents representative microstructures of 5KNN pellets sintered using the optimised TSS and SSS procedures, polished surfaces in a) and b), and fracture morphologies in c) and d). The relative densities and grain size of 5KNN ceramics densified by using different sintering route are summarised in figure 6.13. Compared with the sintered surfaces shown in figure 6.11, the micrographs of the polished and fracture surfaces of both TSS and SSS-5KNN ceramics (figure 6.12) exhibit smaller grain size and higher porosity. It is also clear from figure 6.12 that the samples fabricated via TSS exhibit both higher densities and finer and more homogenous microstructures. Through a systematic study,

the morphologies of 5KNN ceramics fabricated by both SSS and TSS confirm that the porosity due to incomplete densification (small inter-granular pores at triple-junctions) is an unavoidable event, and even remains a prevalent feature in high density samples sintered by TSS, see figure 6.12 c). These pores are caused by the intrinsically low sinter-ability of KNN. The improved density of 5KNN sintered by TSS is thus achieved by supressing grain boundary migration such that fewer pores are trapped insides grains. Moreover, by comparing data in table 6.3, the inhibition of mass loss via Na and K evaporation also plays a significant role in the ability of the TSS method to produce higher density specimens. As mentioned before, the mean grain size of SSS samples increased from 10.5 µm to 21.3 µm when the sintering temperature was increased from 1100°C to 1140°C. For the TSS samples, in figure 6.13, the grain size is approximately 50% less than SSS. The finest grain size and highest density 5KNN sample in this work was obtained at optimum TSS conditions of T_1 = 1120°C for 10 min, T_2 = 1070°C for 10 h.

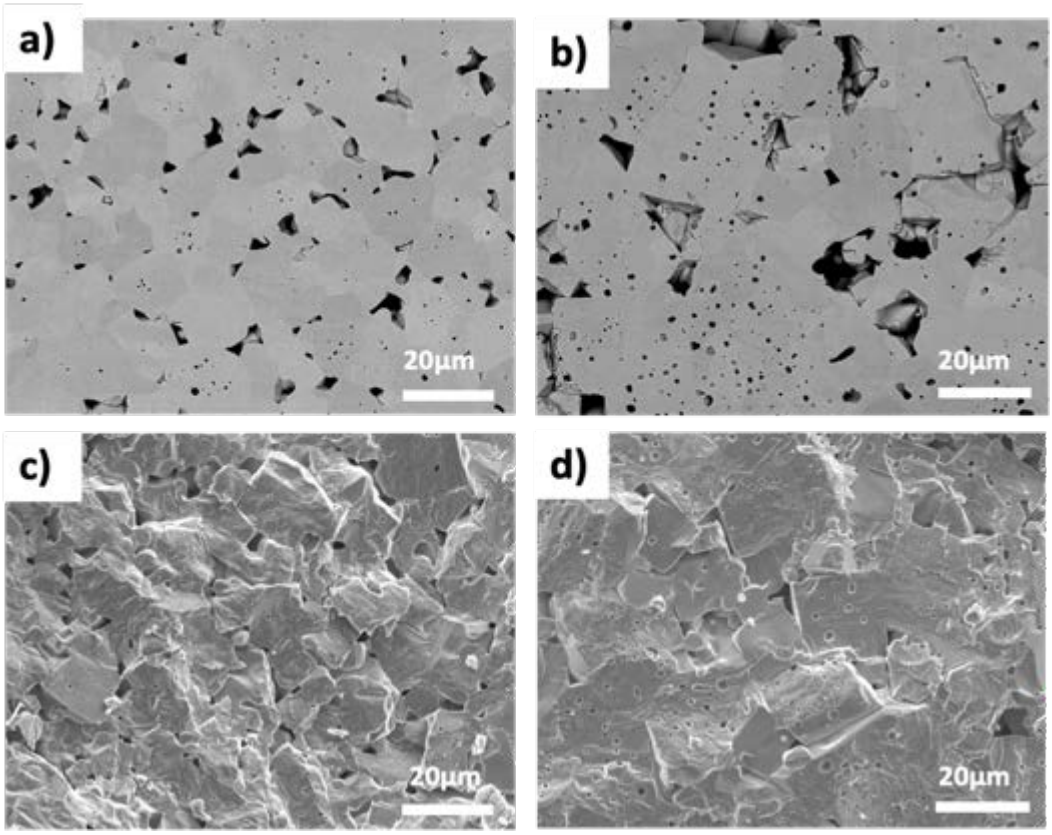

Figure 6.12 Microstructure of 5KNN ceramics polished surfaces: a) densified by TSS (1120°C/10 min/1070°C/10 h and b) densified by SSS (1120°C/2 h); fracture morphologies of 5KNNN ceramics: c) densified by TSS (1120°C/10 min/1070°C/10 h) and d) densified by SSS (1120°C/2 h)

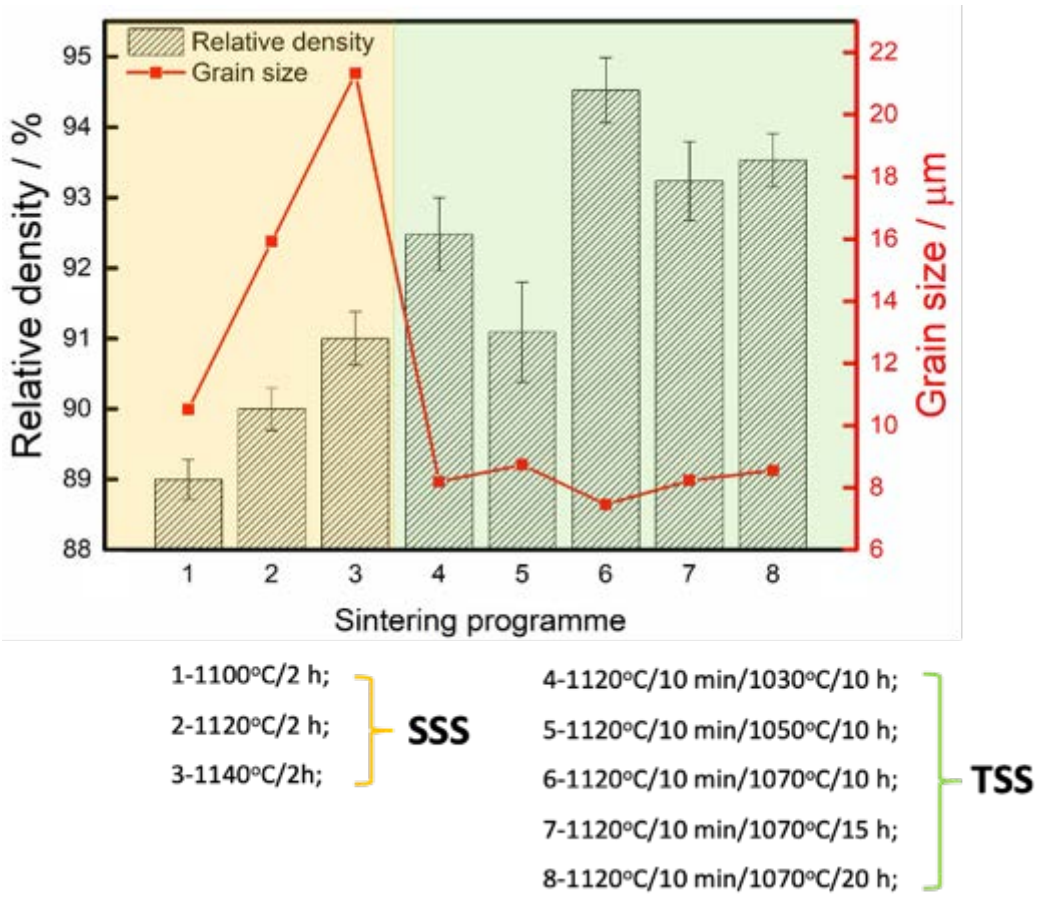

Figure 6.13 Relative densities and grain sizes of representative 5KNN ceramics densified by SSS and TSS

6.4 Structural characterisation

The XRD patterns of both the KNN powder calcined at 900°C and ceramics sintered by SSS and TSS are presented in figure 6.14. The major Bragg peaks detected corresponded to a pure KNN perovskite orthorhombic structure, with the evidence of a clear splitting of the (022)/(200) peak observed at ~45.5°. Therefore, the calcined powder and sintered samples may be considered reasonably pure with no impurity phases within the detection limit of XRD (~2%). As expected, the peaks of the sintered 5KNN specimens were narrower and with a better-defined orthorhombic split compared to those of the powder calcined at 900°C; this is most likely to be associated with the larger crystal size in the ceramics and a higher degree of crystallization after sintering.

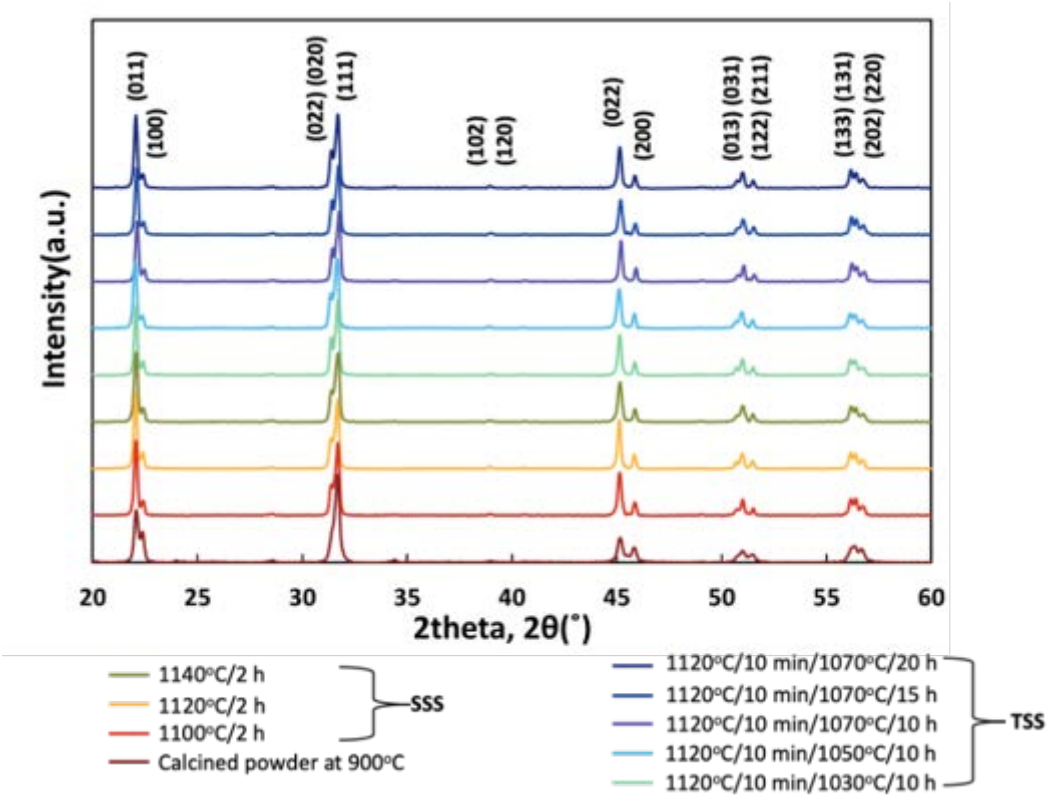

Figure 6.14 XRD patterns across a 2θ range of 20-60° for the calcined 5KNN powder and ceramics sintered at various temperature and times using SSS and TSS

The DSC pattern of 5KNN sintered at 1120°C/10 min/1070°C/10 h is presented in figure 6.15 and shows phase transition information. The first gradient changes at around 60 – 70°C (marked with a green arrow) may be caused by the stabilisation progress of the DSC from a cold state to the heating circumstance[33]. The second and third peaks occur at ~200°C and ~411°C, respectively, and are considered as the thermal response of the 5KNN phase transition behavious. According to the phase diagram of KNN exhibited in chapter 2 (figure 2.16), these two phases transitions are interpreted as the orthorhombic – tetragonal phase transition (200°C) and tetragonal – cubic phase transition (410°C, Curie Temperature), respectively[110]. Compared with the literature, the difference between phase transition temperature is not very great (only 1°C different in Curie temperature), revealing the improvement of density and microstructure will not affect the intrinsic properties of the 5KNN ceramics.

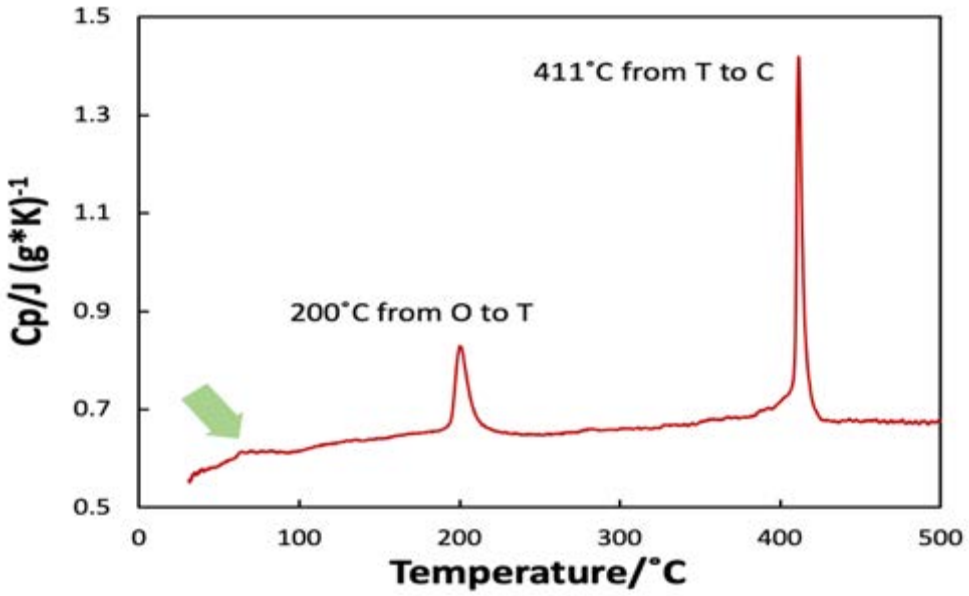

Figure 6.15 DSC trace of 5KNN sintered at 1120°C/10 min/1070°C/10 h

6.5 Electrical characterisation

6.5.1 Dielectric property characterisation

The room temperature relative permittivity (ε_r) and dielectric loss ($tan\delta$) factor of 5KNN discs fabricated using SSS and TSS, and poled at 120°C are presented in table 6.4. The functional property measurements were taken at the 24th hour after electrical poling. Compared with the literature values in table 6.4 and chapter 2, 5KNN ceramics prepared by TSS exhibits higher dielectric constants (ε_r) values but similar dielectric loss ($tan\delta$).

For 5KNN ceramics sintered by the SSS route (Sample No. 1-3), with the raise of sintering temperature, the increased relative permittivity while decreased dielectric loss can be observed. Presumably this was mainly due to the improved density. For 5KNN ceramics sintered by TSS for 10 hours (Sample No. 4-6), a similar trend can be observed, but higher relative permittivity values were obtained. This improvement is due to the lower porosity and finer microstructure. Further prolonging dwell time in the second step led to both ε_r and $tan\delta$ decreasing. The latter may relate to the higher level of alkali evaporation.

According to the previous study with $BaTiO_3$ ceramics, both density and grain size present a significant effect upon relative permittivity[306] so it is reasonable to assume that the increase in relative

permittivity of 5KNN may also because of the increase in density and decrease in grain size, these effects are discussed below.

Table 6.4 Room temperature dielectric properties of 5KNN ceramics fabricated using SSS and TSS sintering routes (A comparison with typical literature values reported is included)

No.	Sintering conditions (T_1 t_1 / T_2 t_2)	Tanδ /%	ε_r
1	1100°C / 2 h	8.9±1.4	297±1.7
2	1120°C / 2 h	6.1±2.0	294±7.9
3	1140°C / 2 h	4.8±5.5	305±5.8
4	1120°C 10 m / 1030°C 10 h	9.3±1.0	327±20.0
5	1120°C 10 m / 1050°C 10 h	7.4±1.0	310±13.2
6	1120°C 10 m / 1070°C 10 h	4.8±0.3	337±7.0
7	1120°C 10 m / 1070°C 15 h	3.9±0.1	329±8.7
8	1120°C 10 m / 1070°C 20 h	4.4±0.1	279±9.4
	Literature 5KNN[102]	4	290

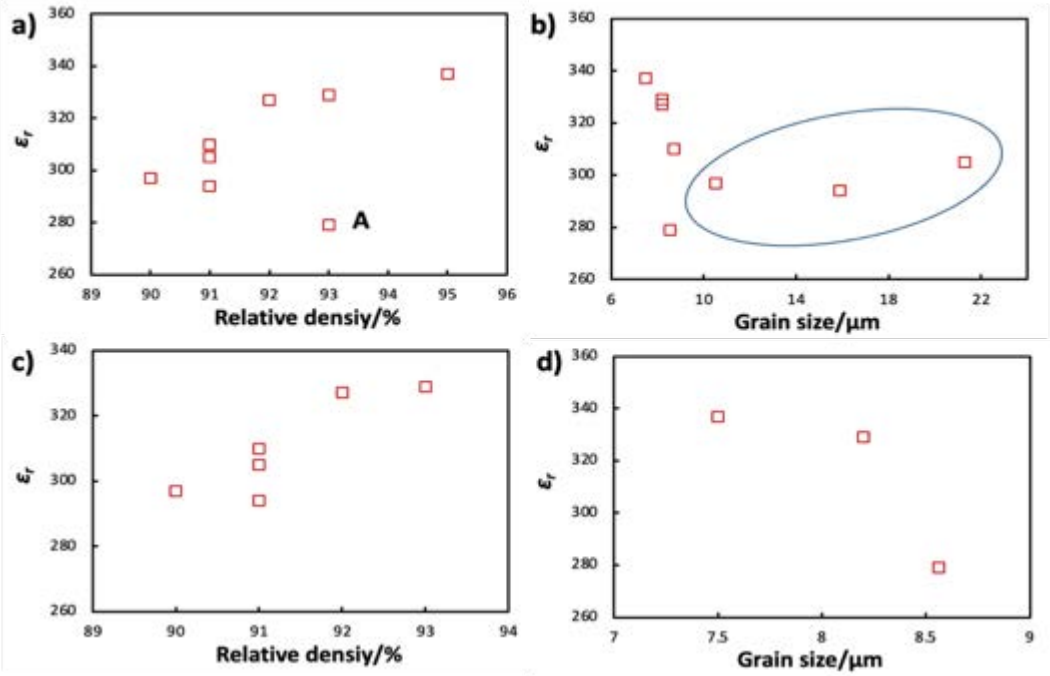

Figure 6.16 Relative permittivity as function of a) relative density and b) grain size, respectively; relative permittivity as function of c) relative density (relative density < 93%) and d) grain size (relative density > 93%), respectively

Figure 6.16 exhibits the relationship between relative permittivity and relative density/grain size. From figure 6.16a, generally, the relative permittivity increased with an increase in relative density.

However, the data point marked A (sample No. 8) with 93% density possessed a lower relative permittivity, this may be due to the off-stoichiometry caused by higher evaporation of alkali following a longer dwell time. For figure 6.16b, the impact of grain size upon the dielectric permittivity is more complex. The permittivity value decreased with the increase in grain size when the latter was less than ~10 μm and increased again with larger grain sizes. It can be concluded that the relative density plays a dominant role upon the relative permittivity when the relative density is lower than 93% since the permittivity increased with improved density, figure 6.16c. And when the relative density exceeded 93%, the grain size may play the dominant role for the relative permittivity, figure 6.16d.

6.5.2 Piezoelectric property characterisation

The piezoelectric charge coefficient (d_{33}), coupling factor (k_p) and mechanical quality factor (Q_m) of 5KNN ceramics fabricated using SSS and TSS are presented in table 6.5, including relative density and grain size. Compared with the literature values in table 6.5 and chapter 2, 5KNN ceramics prepared by TSS exhibits higher piezoelectric charge coefficient (d_{33}) value but similar coupling coefficient (k_p) and smaller mechanical quality factor (Q_m). Such improvements for two-step sintered 5KNN ceramics are attributed to the denser microstructures, the improved stoichiometry and the finer grain sizes achieved in the TSS samples. Denser microstructures yield superior piezoelectric properties by retaining lower amounts of porosity, the presence of which impedes the negative/positive charge transfer path[307]. Whilst porosity will always lead to a reduction in piezoelectric constants, studies have demonstrated a preference for fewer, larger pores over a greater number of smaller pores[307]. As such, the ability for TSS to inhibit the amount of mass lost due to the evaporation of Na and K compared to SSS will have contributed to the improved properties of the KNN ceramics fabricated by TSS by limiting the generation of porosity, as shown by figure 6.7 and figure 6.12. In addition, the retention of Na and K will reduce shifts in the composition of 5KNN from stoichiometry, which is associated with improved piezoelectric properties[307]. It is well known that the piezoelectric properties can be significantly enhanced along the MPBs (morphotropic phase boundaries) and any deviation from stoichiometry will degrade the properties due to the deviation from the MPB[308]. In terms of the grain size, this affects performance by reducing the contribution of the domain wall to the piezoelectric properties[309]. The domain wall contribution is determined by the domain wall density and mobility. The former is the number of domain walls per unit volume and is typically estimated by measuring the average domain width exhibited by piezoelectric ceramics after poling. 5KNN is an orthorhombic structure at room temperature and, thus, has a very complicated domain pattern with 60°-, 90°-, 120°-, and 180°-domain walls all co-existing[310]. As a result, it is difficult to accurately measure the exact domain size of

KNN because it exhibits such significant variance from grain-to-grain[311]. Nevertheless, it is generally acknowledged that smaller domain widths exist within smaller grains[312,313]. This translates into a higher domain wall density, increasing the domain wall contribution by increasing the total domain wall activity[309,312]. Further contributions are made by the relaxation of grain boundary pinning effects at smaller grain sizes, which enable the smaller domain walls to re-orient more easily and respond more actively to an external signal due to higher domain wall mobility[151,309]. Furthermore, an inhomogeneous microstructure, particularly a bimodal grain size distribution, such as that seen in the SSS samples in the present work, will diminish the piezoelectric properties as well. The relationship of piezoelectric properties and relative density/grain size are shown in figure 6.17; they showed similar trend to that of the permittivity.

Table 6.5 Piezoelectric and dielectric properties of 5KNN ceramics fabricated using SSS and TSS sintering routes (A comparison with typical literature values reported is included)

No.	Sintering conditions (T_1 t_1 / T_2 t_2)	Rel. density /%	Grain size /μm	d_{33} /pC N^{-1}	k_p /%	Q_m
1	1100°C / 2 h	90±0.3	10.5±3.5	97±2.9	34±2.0	17±6.3
2	1120°C / 2 h	91±0.3	15.9±4.8	101±1.0	33±1.0	32±4.2
3	1140°C / 2 h	91±0.4	21.3±6.1	94±2.9	25±0.4	22±12.9
4	1120°C 10 m / 1030°C 10 h	92±0.5	8.2±2.5	112±1.1	35±1.0	34±2.0
5	1120°C 10 m / 1050°C 10 h	91±0.7	8.7±3.2	104±1.6	31±2.0	42±5.0
6	1120°C 10 m / 1070°C 10 h	95±0.5	7.5±1.6	122±0.1	36±3.0	76±5.2
7	1120°C 10 m / 1070°C 15 h	93±0.6	8.2±1.6	118±0.8	34±3.0	45±2.6
8	1120°C 10 m / 1070°C 20 h	93±0.4	8.6±1.8	108±5.0	33±0.3	39±0.7
	Literature 5KNN[102]	94	-	80	36	130

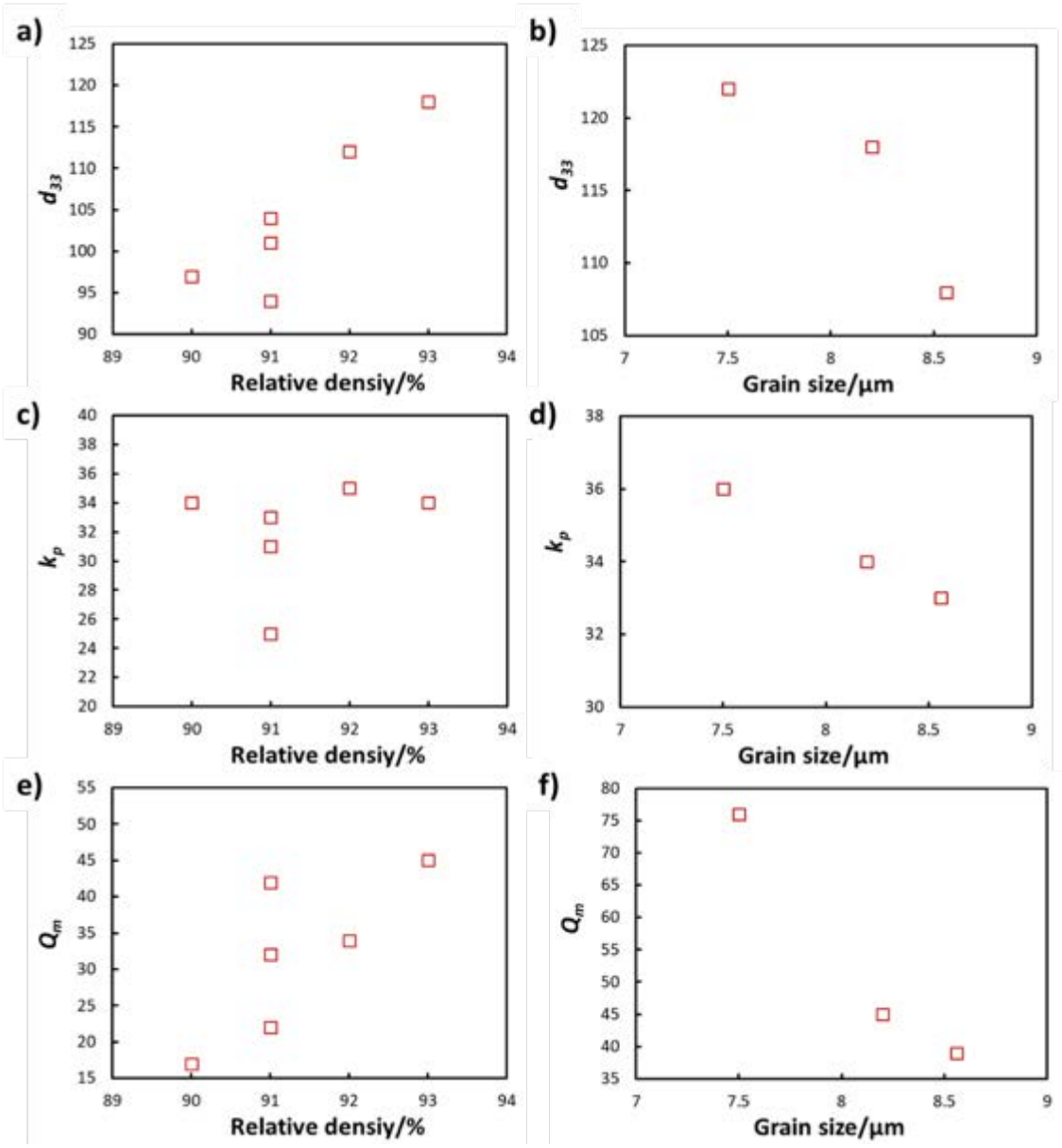

Figure 6.17 a) d_{33}, c) k_p and e) Q_m as function of relative density (relative density < 93%) and b) d_{33}, d) k_p and f) Q_m as function of grain size (relative density > 93%), respectively

6.5.3 Ferroelectric property characterisation

The room temperature polarisation-electric field hysteresis loops of 5KNN sintered at 1120°C/2 h and 1120°C/10 min/1070°C/10 h are illustrated in figure 6.18. 5KNN fabricated by TSS exhibited higher spontaneous and remanent polarisations, which were about ±16.1 μC/cm^2 and ±12.9 μC/cm^2 on average, respectively. Also, a larger coercive electric field of approximately ± 9.2 kV/cm was obtained. The larger coercive electric field of 5KNN ceramics densified by TSS may be due to the smaller grain size. As mentioned in section 6.5.4, the smaller domain usually exits in smaller grain size, therefore, 5KNN ceramics densified by TSS exhibits higher domain wall density. Although it is easier to re-orient

the smaller domain (grain size), the increasing of the number of the domain wall also increase the difficulty of poling. It is easy to understand that the single crystal (single domain) is easier to be oriented compared with poly-crystals (multi-domain). Also, as reviewed in chapter 2, the A-site defect in 5KNN ceramics may help to enhance the mobility of domain. The TSS-route sintered 5KNN exhibits higher density and lower evaporation of Na and K, revealing lower A-site defect formed. Hence, 5KNN ceramics densified by TSS shows higher coercive electric field. The results in figure 6.18 exhibit good consistency with the piezoelectric properties discussed in section 6.5.2.

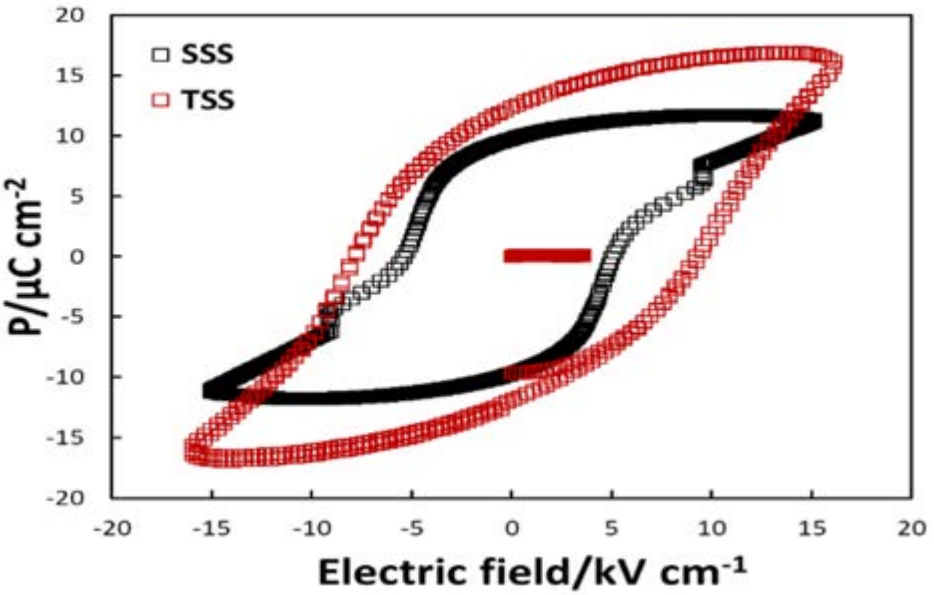

Figure 6.18 Polarisation-electric field hysteresis loops of 5KNN sintered at 1120°C/2 h and 1120°C/10 min/1070°C/10 h

6.5.4 Energy harvester related property characterisation

As well as the dielectric, piezoelectric and ferroelectric properties listed in table 6.4 and 6.5 and shown in figure 6.18, there are two important parameters to evaluate piezoelectric materials for energy harvesting applications[287]. The first is the energy conversion efficiency, η, which can be calculated using the piezoelectric electromechanical coupling factor, *k*, and Q_m based on the following equation (3-5)[286]. In addition, piezoelectric energy harvesting devices usually work at anti-resonance, which means piezoelectric materials need to generate a high energy density, u, which is calculated by equation (3-3 and 3-4)[314]. From equation 3-4, at equivalent *F* and *A*, *u* is proportional to the product of *d* and g (transduction coefficient), thus the values of $d \times g$ are commonly used to represent the energy density.

Figure 6.19 compares the efficiency of energy conversion, η, and transduction coefficient, $d_{33} \times g_{33}$, of the 5KNN ceramics produced via SSS and TSS under different sintering conditions are shown in. The data show that, in general, the 5KNN ceramics sintered using TSS exhibited superior piezoelectric properties, due to the higher densities and finer microstructures achieved; this has translated into improved energy harvesting characteristics. The highest values of η and $d_{33} \times g_{33}$ for SSS and TSS are 58% and 3925 $\times$ 10^{-15} m^2 N^{-1} (for 1120°C/2 h) and 80% and 4985 $\times$ 10^{-15} m^2 N^{-1} (for 1120°C/10 mins/1070°C/10 h), respectively. In order to evaluate the power generation characteristics directly, these two sets of sintering conditions were selected to fabricate ceramics for use in prototype piezoelectric energy harvesters. The comparison and discussion regarding to the energy harvester will be provided in the Chapter 8.

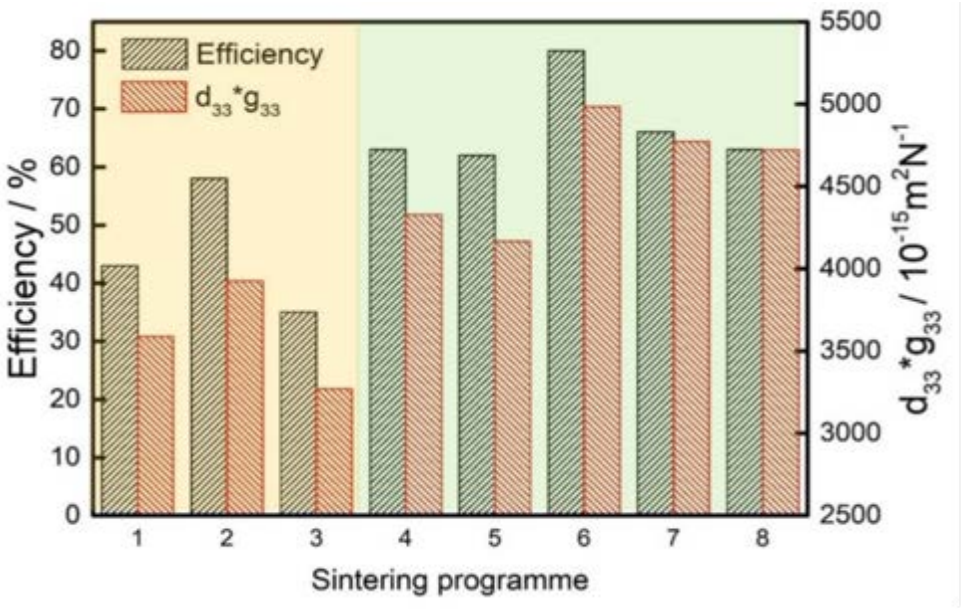

Figure 6.19 Influence of different sintering conditions on the efficiency of energy conversion and $d_{33} \times g_{33}$ values of 5KNN ceramics (processing condition numbers are given in Table 6-4 and 6-5)

6.5.5 Temperature stability of 5KNN fabricated by TSS

Figure 6.20 shows the temperature-dependent permittivity plot of 5KNN sintered at 1120°C/10 min/1070°C/10 h from 30°C to 500°C. With the raise of temperature, the permittivity increased. Two anomalous peaks can be observed at ~475.13K (200°C) and ~688.13K (413°C), relating to two phase transitions; orthorhombic to tetragonal phase and tetragonal to pseudo-cubic phase. When the heating temperatures >~413°C, the ferroelectric phase of 5KNN had changed to the para-electric cubic phase where long–range–ordered ferroelectric domains disappeared, leading to the loss of the

piezoelectricity. These phase transition temperatures are in agreement with that measured from the DSC results presented in figure 6.15.

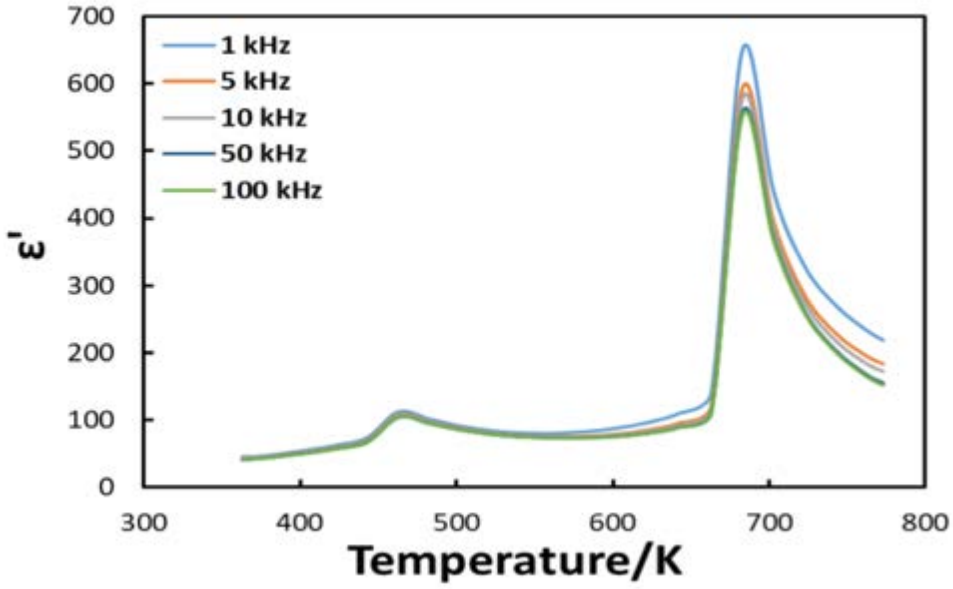

Figure 6.20 Temperature-dependent permittivity of 5KNN sintered at 1120°C/10 min/1070°C/10 h from 30°C to 500°C

6.6 Summary

In this chapter, 5KNN ceramics were fabricated using both SSS and TSS routes. The effects of the different sintering methods on the sintering mechanism, densification, microstructure, functional properties (dielectric, piezoelectric and ferroelectric properties), energy harvester related parameters and the relationship between properties and density/grain size were systematically investigated. The findings of this chapter can be summarised as the following:

1. Compared to the SSS approach, the short soak time at high temperature (T_1) in the TSS process route can generate suitable amount K-rich liquid phase to help densification and reduce the evaporation of sodium and potassium. Moreover, the use of a lower T_2 sintering temperature decreased the grain boundary migration rate and helped gas pore removal. Hence, 5KNN ceramics with enhanced density and finer grain size were obtained. However, the low sinter-ability of pure 5KNN results in pores located at triple-points that remain difficult to eliminate, even using the TSS method.

2. Improved functional properties were obtained by the 5KNN ceramics densified by TSS route. Denser microstructures yield superior piezoelectric properties by retaining lower amounts of porosity. Moreover, finer grain sizes enable the smaller domain walls to re-orient more easily

and respond more actively to an external signal due to higher domain wall mobility. Furthermore, less evaporation in TSS can also help to reduce off-stoichiometry.

3. The density and grain size play important roles for the functional properties. When the relative density was lower than 93%, the functional (dielectric and piezoelectric) properties improved with an increase in density. However, when relative density exceeded 93%, the grain size played the dominant role.

Chapter 7. An investigation of BNNO doped KNN materials

7.1 Introduction

A comprehensive investigation of 5KNN bulk ceramics was reported in Chapter 6, including the sintering mechanism, phase transition and the correlation between the microstructure and functional properties. In chapter 7, the synthesis, fabrication and characterisation of BNNO-doped 5KNN ceramics is reported. As discussed in chapter 2, ferroelectrics can boost high photo-induced voltages because of the bulk photovoltaic effect. However, because of the wide bandgap of most ferroelectric materials, the capability of light absorption is very poor; typically <20% of the solar spectrum can be absorbed. Ilya et al[14]. proposed that a potential way to narrow the bandgap without degrading the ferroelectric properties was through transition metal doping. Considering the charge compensation, electronegativities and ionic radius, in this work, $Ba(Ni_{0.5}Nb_{0.5})O_{3-\delta}$, BNNO, was selected as a dopant to investigate the impact upon the dielectric, piezoelectric, ferroelectric and optical properties of 5KNN.

This work was structured as follows. Initially, the sintering conditions of the BNNO-doped 5KNN ceramics, (1-y) $K_{0.5}Na_{0.5}NbO_3$ – y $Ba(Ni_{0.5}Nb_{0.5})O_{3-\delta}$, y refers to the BNNO doping amount, y = 0 – 0.1, were investigated using the $0.98(K_{0.5}Na_{0.5})NbO_3$-$0.02Ba(Ni_{0.5}Nb_{0.5})O_{3-\delta}$, 5KNN-2BNNO, composition as an example. Following this, ceramics with increased dopant amounts (y = 0.04-0.10) were fabricated and their sintering conditions optimised, allowing the influence of BNNO addition upon the functional properties of KNN-based ceramics to be investigated. Then, the phase structure and functional properties of the doped 5KNN ceramics were researched. Finally, the photovoltaic behaviour of the 5KNN-2BNNO composition was measured. The main findings of this study are detailed and discussed in this chapter.

7.2 Powder synthesis

The particle sizes of the raw materials, NiO and $BaCO_3$, are summarised in table 7.1. Each value was an average of three independent measurements. As for the synthesis of the 5KNN, the raw materials were vibro-milled first to decrease the particle size and then the powders were mixed using a Glen mill for 24 h to prepare the precursor. Note: The manufacturer information of Na_2CO_3, K_2CO_3, Nb_2O_5, NiO and $BaCO_3$ was provided in chapter 5, particle size information of Na_2CO_3, K_2CO_3 and Nb_2O_5 was provided in Chapter 6 and the composition and the weights of each material and batch size are listed in Appendix I.

Table 7.1 Summary of the raw material particle sizes

Powder	Before milling: D_{50} / μm	After milling: D_{50} / μm
$BaCO_3$	6.4±0.43	1.7±0.09
NiO	18.8±0.35	2.8±0.01

The particle sizes of the BNNO doped 5KNN powder mixtures after glen milling are summarised in table 7.2, suggesting that the particle sizes of the mixed and milled doped 5KNN mixtures were suitable for subsequent calcination.

Table 7.2 Summary of particle sizes of the BNNO doped 5KNN mixture

Precursor composition	D_{50}/ μm
$0.98(K_{0.5}Na_{0.5})NbO_3$-$0.02Ba(Ni_{0.5}Nb_{0.5})O_{3-\delta}$	3.3±0.08
$0.96(K_{0.5}Na_{0.5})NbO_3$-$0.04Ba(Ni_{0.5}Nb_{0.5})O_{3-\delta}$	3.1±0.05
$0.94(K_{0.5}Na_{0.5})NbO_3$-$0.06Ba(Ni_{0.5}Nb_{0.5})O_{3-\delta}$	4.4±0.10
$0.92(K_{0.5}Na_{0.5})NbO_3$-$0.08Ba(Ni_{0.5}Nb_{0.5})O_{3-\delta}$	4.6±0.22
$0.90(K_{0.5}Na_{0.5})NbO_3$-$0.10Ba(Ni_{0.5}Nb_{0.5})O_{3-\delta}$	4.2±0.42

The reaction progress of the 5KNN-2BNNO powder can be assessed from the thermal data shown in figure 7.1. From the theoretical calculation, the total mass loss of the 5KNN-2BNNO composition was expected to be 10.08% from the release of CO_2, which can be attributed to Na_2CO_3 (4.94%), K_2CO_3 (4.94%) and $BaCO_3$ (0.20%). From the TGA curve, figure 7.1, the total mass loss was ~11%, which was in agreement with the theoretical calculation. The mass reduction started from ~150°C and was completed when the temperature exceeded 750°C; this indicated that the Na_2CO_3, K_2CO_3 and $BaCO_3$ had fully decomposed by this temperature. Four endothermic peaks can be observed in the DSC data at 750°C (a double peak), 900°C and 950°C, together with an exothermic peak at 340°C. The latter peak, and associated mass loss, is considered to arise from the start of the decomposition of the carbonates. As for the 5KNN, figure 6.1 and figure 6.2, the sharp endothermic peak at ~900°C had no corresponding mass losses, indicating that reactions had finished by this temperature. The crystallography of the 5KNN-2BNNO powders calcined at 900°C for 2 h was investigated by XRD and is shown in figure 7.2, revealing the formation of a perovskite structure. Thus, the BNNO-doped 5KNN precursors were all calcined at 900°C.

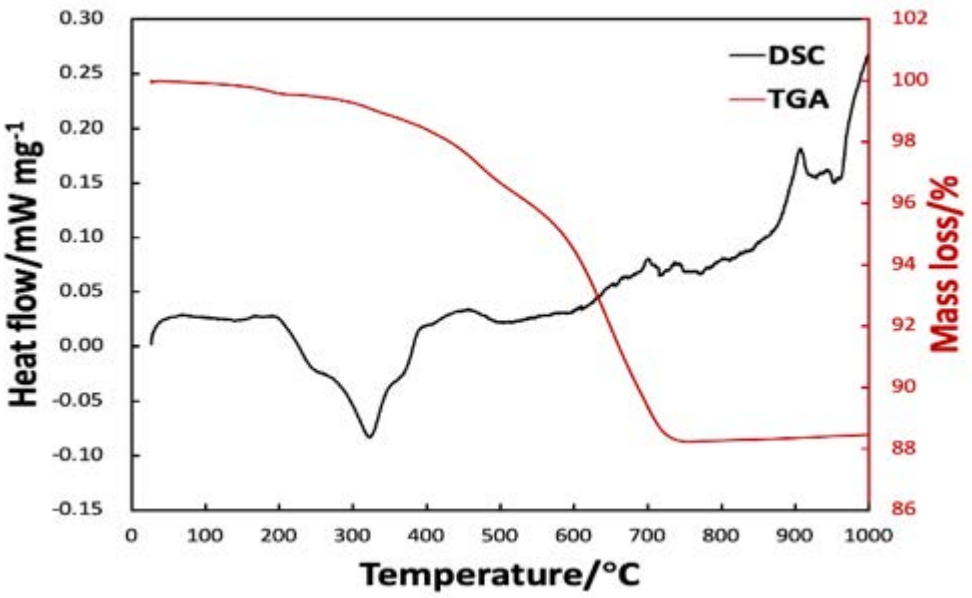

Figure 7.1 TGA-DSC curves of the 5KNN-2BNNO precursor powder measured from 50°C– 1000°C with a heating rate of 5°C/min in air

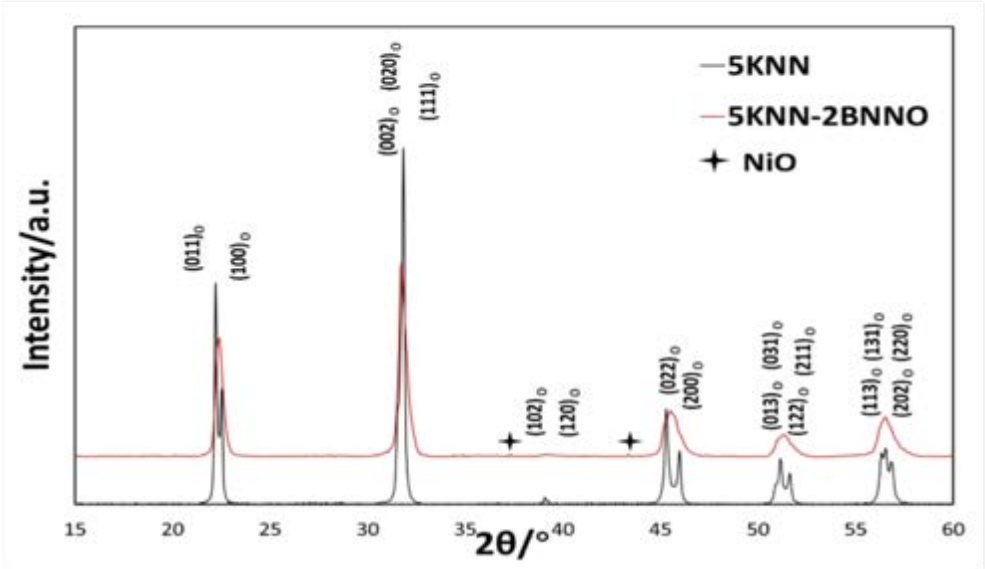

Figure 7.2 XRD patterns of 5KNN and 5KNN-2BNNO powders calcined at 900°C for 2 h. Peaks have been indexed assuming an orthorhombic perovskite structure

The morphology of the 5KNN-2BNNO powder after calcination and vibro-milling for 24 h is shown in figure 7.3, a faceted structure can be seen that is similar to that of the undoped 5KNN powder, figure 6.3, though the 5KNN-2BNNO powder exhibited a smaller grain size, ~100 – 200 nm and a more inhomogeneous grain size distribution (*e.g.* see the grains highlighted by black circles). This, in turn, may be due to an inhomogeneous elemental distribution. Considering the aim of the calcination was to pre-form the desired phase, figure 7.2, the calcination temperature at 900°C was considered sufficient for BNNO-doped 5KNN powders.

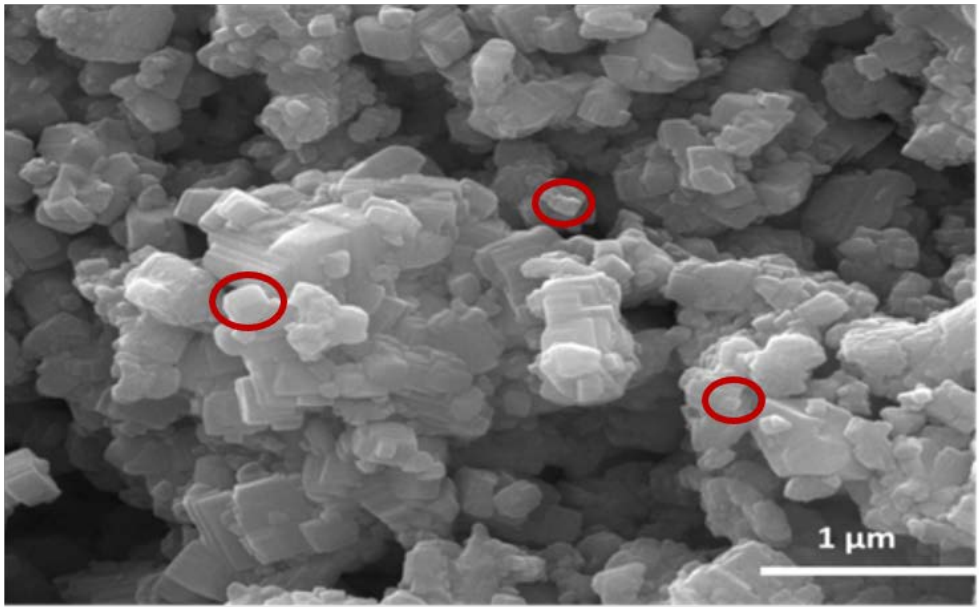

Figure 7.3 Microstructure of 5KNN-2BNNO powders after calcination (at 900°C for 2 hrs) and vibro-milling for 24 h

7.3 Sintering behaviour of 5KNN-2BNNO ceramics

In order to assess any modifications required to the sintering conditions for the doped KNN compared to the undoped, the shrinkage behaviour of a 5KNN-2BNNO powder compact was measured at increasing temperature using a dilatometer as described in Section 5.4.2. Figure 7.4 demonstrates the dynamic shrinkage curve of the 5KNN-2BNNO powder compact in the temperature range from 600°C to 1250°C. Because the powder compact was covered with platinum foil, the observed initial expansion may be due to the latter's expansion. It can be seen from figure 7.4 that the compact started shrinking at ~1090°C, and a rapid increase in shrinkage, into a largely linear shrinkage rate, was observed between 1100°C – 1200°C. The maximum shrinkage was observed at ~1200°C. The apparent decrease in shrinkage beyond 1200°C is due to the melting of the sample. Compared with 5KNN, the temperature at which the maximum shrinkage was observed for the 5KNN-2BNNO increased ~90°C, indicating that the doped KNN required a higher temperature to densify. Therefore, temperatures in the range 1165°C – 1200°C were selected as appropriate sintering temperatures to explore for the BNNO-doped 5KNN ceramics.

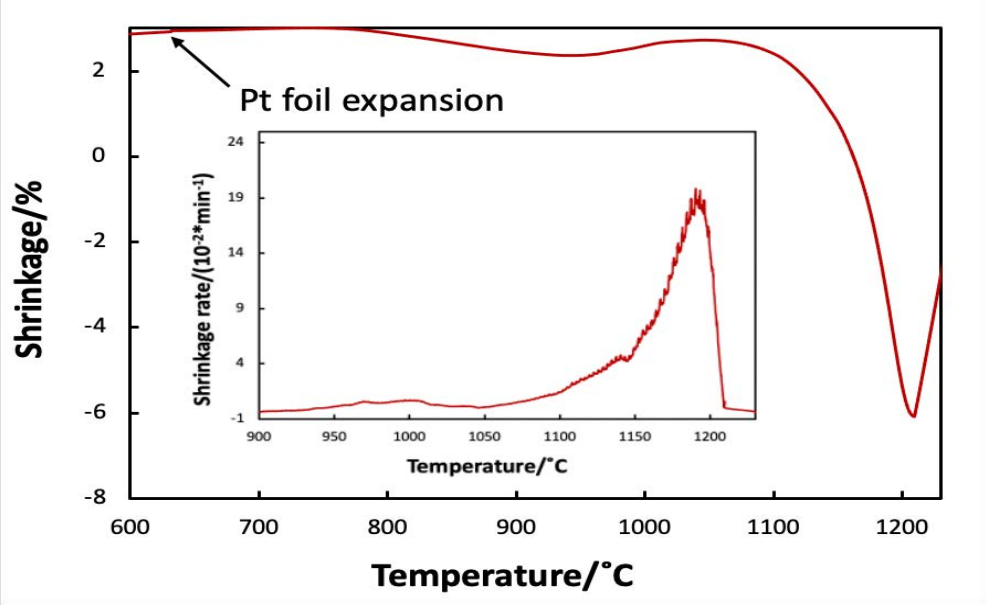

Figure 7.4 Dynamic shrinkage curve of a 5KNN-2NNO powder compact from 600°C to 1250°C in air with a heating rate of 5°C/min. Inset: shrinkage rates above 900°C.

7.3.1 Single-step sintering

The consequent density change and grain size for the 5KNN-2BNNO ceramics with the increasing of sintering temperature for 2 hours is demonstrated in figure 7.5. Each point was an average of six values from a batch of six samples. The theoretical density of 5KNN-2BNNO is 4.553 g/cm, which was calculated from XRD results measured at room temperature. As indicated above, figure 7.4, compared with 5KNN, 5KNN-2BNNO ceramics need to be sintered at a higher temperature to densify and hence higher temperatures were used than for the KNN ceramics. From 1165°C to 1185°C, densification increased, but it decreased again after reaching a maximum of 98.3±1.2 % of theoretical after sintering at a temperature of 1175°C. The latter is probably due to over-sintering. Also, with the raising in sintering temperature, the average grain size of the 5KNN-2BNNO increased, from ~300 nm – 600 nm.

Pictures of the sintered 5KNN-2BNNO pellets are shown in figure 7.6. The colour of the material is dependent on the light it absorbs, whilst the bandgap determines the wavelength absorbed. 5KNN ceramics possess >3 eV bandgap, which means they cannot absorb visible light and hence appear white. After doping with BNNO, the ceramics were either green or yellow, indicating a reduction in the bandgap. The microstructure (grain size, shape, porosity, etc.) also affects the appearance of the samples. After sintering, grain boundaries are formed and porosity is decreased and hence the light absorption and scattering by the sample are changed[315,316]. It can be observed from figure 7.6 that the 5KNN-2BNNO ceramics disc sintered at 1165°C showed a very “light green” colour, which may be due

to its low density. When the sintering temperature raised to 1170°C and 1175°C, the level of densification increased, figure 7.5, and hence the samples appeared darker. It will be noted from figure 7.6 that the 5KNN-2BNNO ceramics discs sintered at 1175°C showed homogenous colour, whilst samples sintered at 1180°C and 1185°C exhibited an inhomogeneous mixture of dark and light green. An SEM micrograph for a 5KNN-2BNNO ceramic sintered at 1170°C is shown in figure 7.7. It can be seen that the lighter green colouration in the bottom of the sample was linked to the presence of increased porosity in the sample, suggesting that the latter caused light scattering[317,318]. When the sintering temperature was further raised to 1180°C and 1185°C, the sample surface became very inhomogeneous with many white spots appearing on the surface; these may have been due to Ni ex-solution[319]. The phenomena described above were further studied by utilising both SEM and XRD, as shown in figures 7.8 – 7.13 and discussed further below.

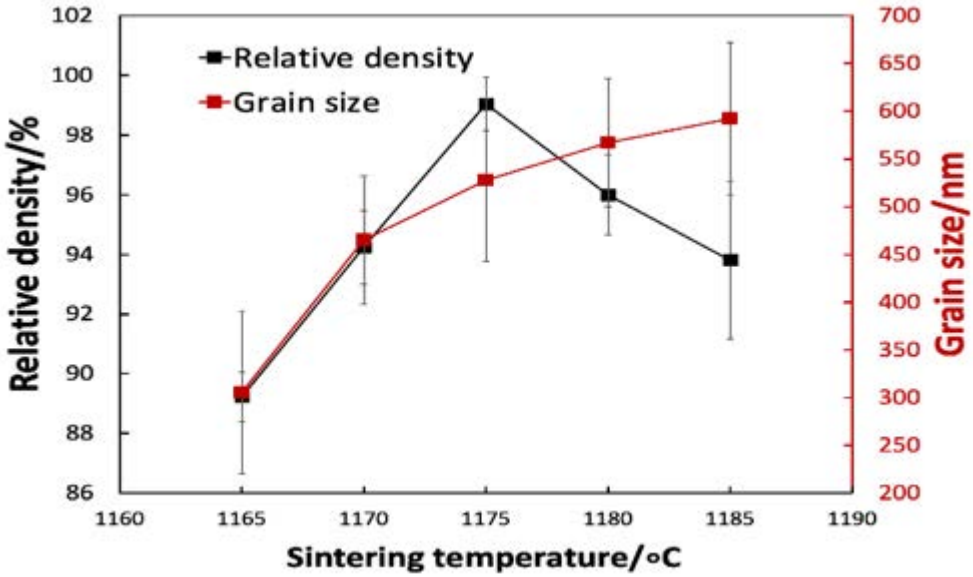

Figure 7.5 Relative density and grain size of 5KNN-2BNNO as a function of sintering temperature for 2 h with a heating rate of 5°C/min

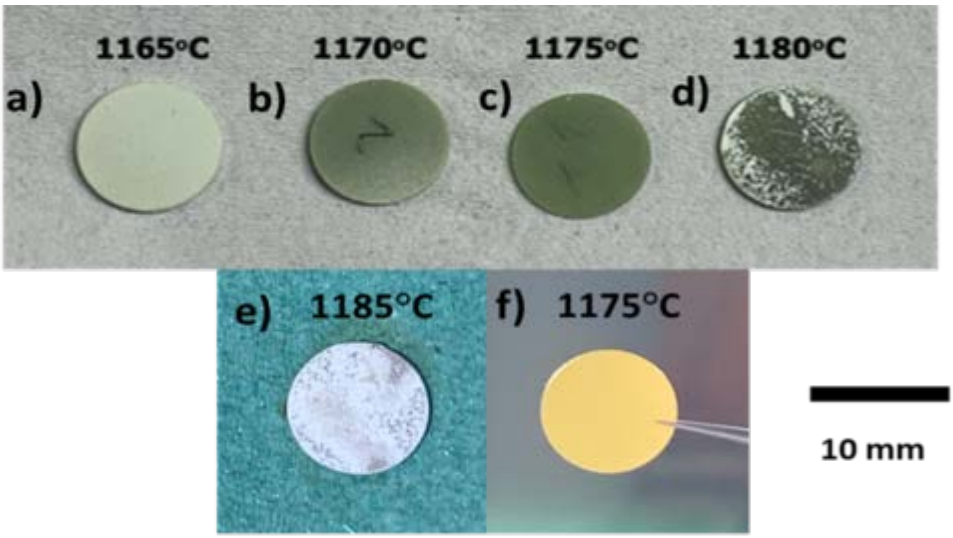

Figure 7.6 Pictures of 5KNN-2NNO ceramics sintered for 2 h at: a) 1165°C; b) 1170°C; c) 1175°C; d) 1180°C; e) 1185°C and f) transparency in a 5KNN-2BNNO ceramic sintered at 1175°C for 2 h

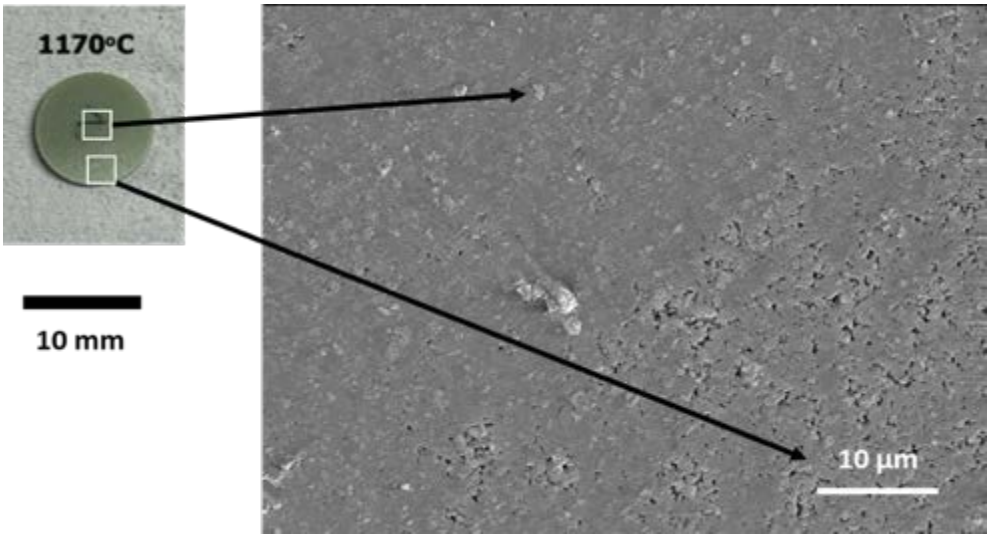

Figure 7.7 SEM micrograph for a 5KNN-2BNNO pellet sintered at 1170°C for 2 h, together with an indication of their relationship to the appearance of the bulk sample surface

The top surface of the 5KNN-2BNNO ceramics were polished and thermally etched at 150°C below the sintering temperature for 30 min, and SEM micrographs of the surfaces are presented in figure 7.8. It can be observed that all the ceramics possesses a homogenous microstructure with approximately square grains (grain are cuboids in 3D). Compared with the 5KNN ceramic microstructures, figure 6.6 and figure 6.12, all the sintered 5KNN-2BNNO ceramics exhibited denser, finer and more homogenous microstructures. For example, the TSS-densified 5KNN ceramics had a mean grain size of ~7 µm (5KNN TSS), whilst the 5KNN-2BNNO ceramics displayed a submicron microstructure. The grain size reduction is attributed to grain growth inhibition by the presence of the dopant[320–322]. The SEM image and EDS elemental line scanning map across the grain (5KNN-2BNNO composition) is shown in figure 7.9,

exhibiting compositional segregation between the grain-interior region (core) and the grain-outer region (shell). The grain-outer region presents higher Ba and Ni concentration, relative to the Nb-rich inner core. The K and Na elements were approximately consistent across the entire grain. With BNNO doping, it can be seen from figure 7.9 that the Ba^{2+} and Ni^{2+} tended to concentrate near the grain boundaries, this probably reduces their mobility during densification and hence suppresses grain growth. In addition, it would be expected that the Ba^{2+} doping generates K^{+} and Na^{+} vacancies at the A-sites, which can also lead to domain pinning and a reduction in grain growth rate, thus resulting in reduced grain size compared to 5KNN[320–322]. Similar tendencies in grain growth inhabitation have been reported in, for example, the (1-x) $(K_{0.5}Na_{0.5})NbO_3$-x $(Ba_{0.9}Sr_{0.1})(Zr_{0.1}Ti_{0.9})O_3$[320], Ba-doped $Pb(Zr_{0.532}Ti_{0.468})O_3$[321] and $(Pb_{0.63}Ba_{0.37})$ $(Zr_{0.7}Ti_{0.3})O_3$ systems[323,324]. When 5KNN-2BNNO ceramics were sintered at 1165°C for 2 h, figure 7.8a, the resulting microstructures were relatively inhomogeneous and contained large 1 – 2 μm pores. The latter explains the low density and also light green colour shown in figures 7.5 and 7.6, respectively. When the ceramcis were sintered at 1170°C-1180°C, more densified microstructures were obtained, figure 7.8b-d, however when the sintering temperature was further raised to 1185°C, much larger grains were observed, together with the re-introduction of porosity; the microstructure in figure 7.8e clearly reveals over-sintering, explaining the decrease in density observed in figure 7.5.

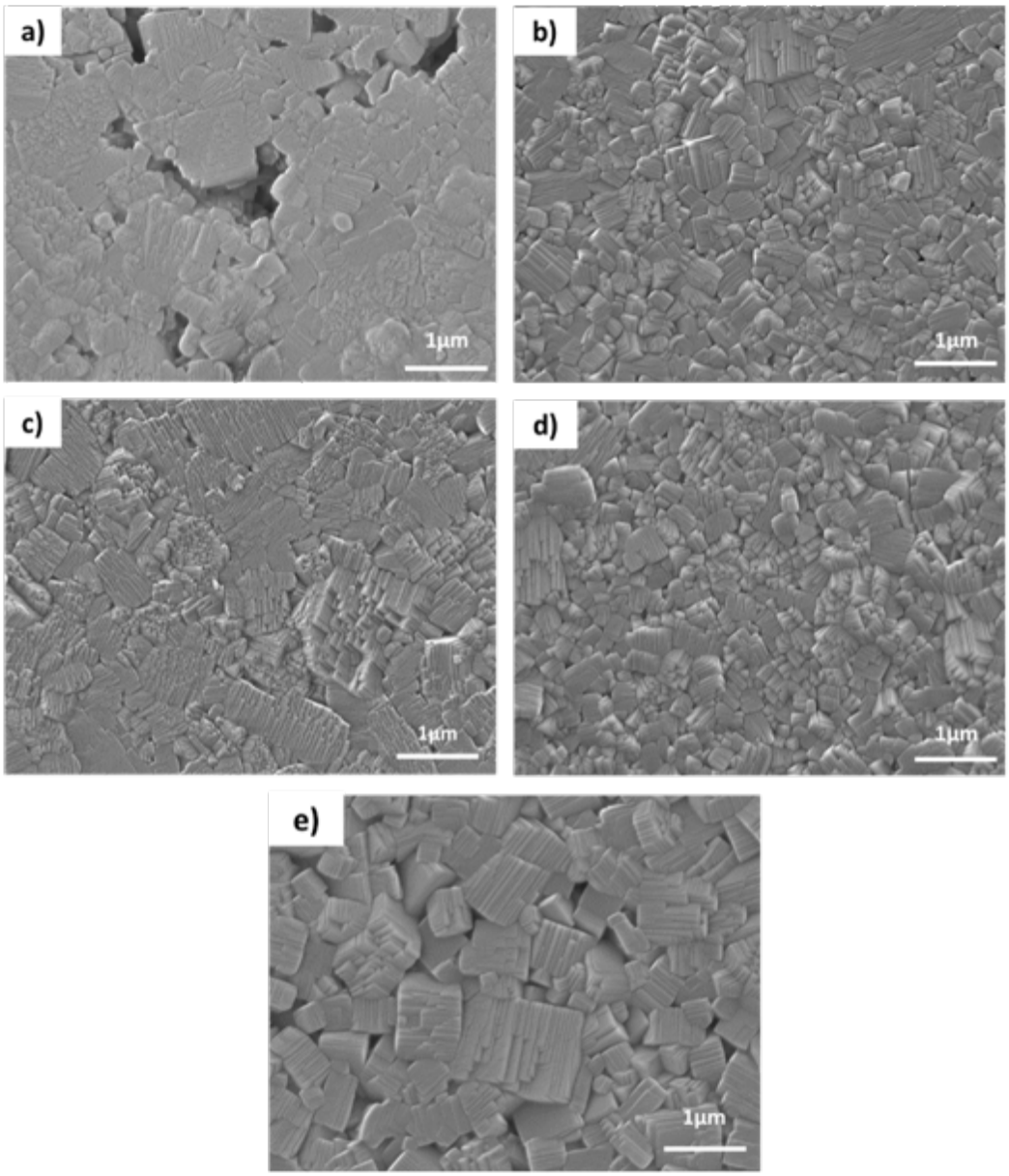

Figure 7.8 The SEM images of polished and thermally etched 5KNN-2BNNO ceramic surfaces after sintering for 2 h at: a) 1165°C, b) 1170°C, c) 1175°C, d) 1180°C and e) 1185°C

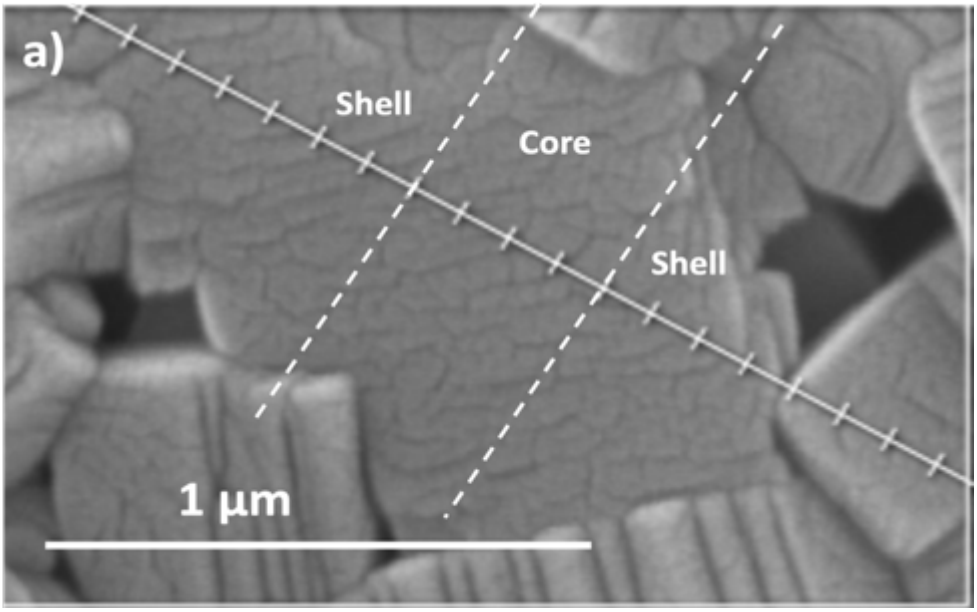

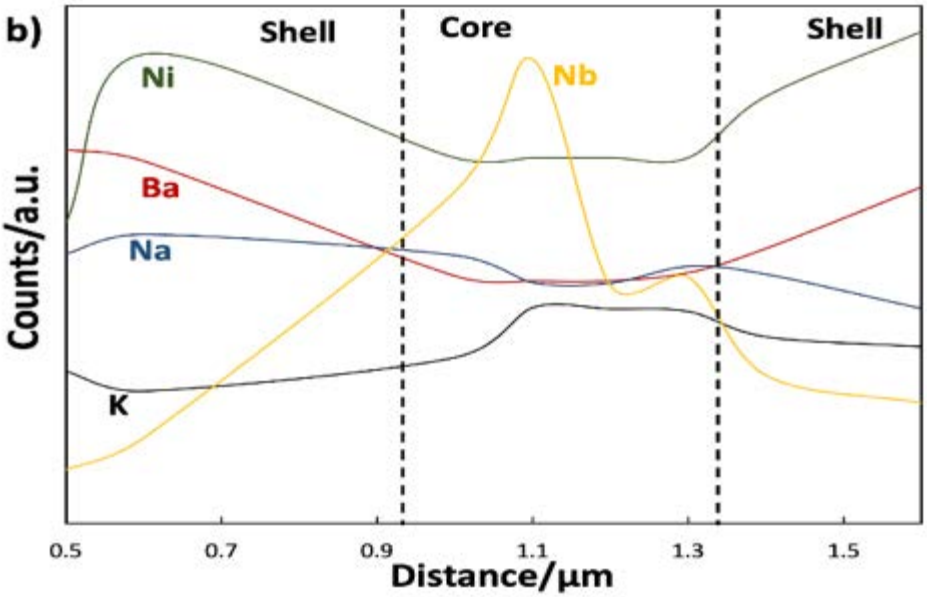

Figure 7.9 SEM-EDS line scan mapping of 5KNN-2BNNO ceramics sintered at 1175°C for 2 h: a) The position of the line scan in SEM image, b) EDS elemental line scanning map across the entire grain

As mentioned previously, one explanation for the white spots in the 5KNN-2BNNO ceramics sintered at 1180°C and 1185°C may be due to Ni ex-solution[325–327]. Normally, this occurs after sintering in a reducing atmosphere[328,329], suggesting that the forming of oxygen vacancy in the perovskite oxides could be the driving force for the ex-solution process[326,330]. For the BNNO-doped KNN ceramics, the doping of Ni introduces oxygen vacancies, which can contribute towards Ni overcoming the energy barrier to diffuse to the surface, leading to an inhomogeneous element distribution[330]. Doping with Ni^{2+} and Ba^{2+} ions will also cause the generation of oxygen vacancies due to charge compensation and

thus can be expected to have a similar effect as sintering in a reducing atmosphere. The acceptor dopants (Ni^{2+} ions) are dissolved into the 5KNN lattice matrix 5KNN first and then anchored to the surface. The whole process can be summarised as four physical sub-processes: diffusion, reduction, nucleation and growth[326]. With increasing sintering temperature, Ni^{2+} ions first diffuse from the bulk to the surface and are then reduced to Ni metal, before assembling into nanoparticles that grow in size over the heat-treatment time[326]. Since the 5KNN-2BNNO ceramics were sintered in air, the Ni was further oxidised into NiO. The whole Ni ex-solution process is illustrated in figure 7.10. The generation of oxygen vacancies destabilises the perovskite lattice stoichiometry, leading to the segregation and ex-solution of B-site cations to maintain structural stability. Thus, the sintering temperature of doped KNN ceramics needs to be carefully controlled. Figure 7.11 illustrates the as-sintered microstructure of 5KNN-2BNNO sintered at 1180°C for 2 h, whilst figure 7.12 shows the as-sintered microstructure and EDS mapping of 5KNN-2BNNO sintered at 1185°C for 2 h. The Ni particle nucleation and growth along the KNN grain boundaries and oxidation into NiO during the sintering process can be directly observed.

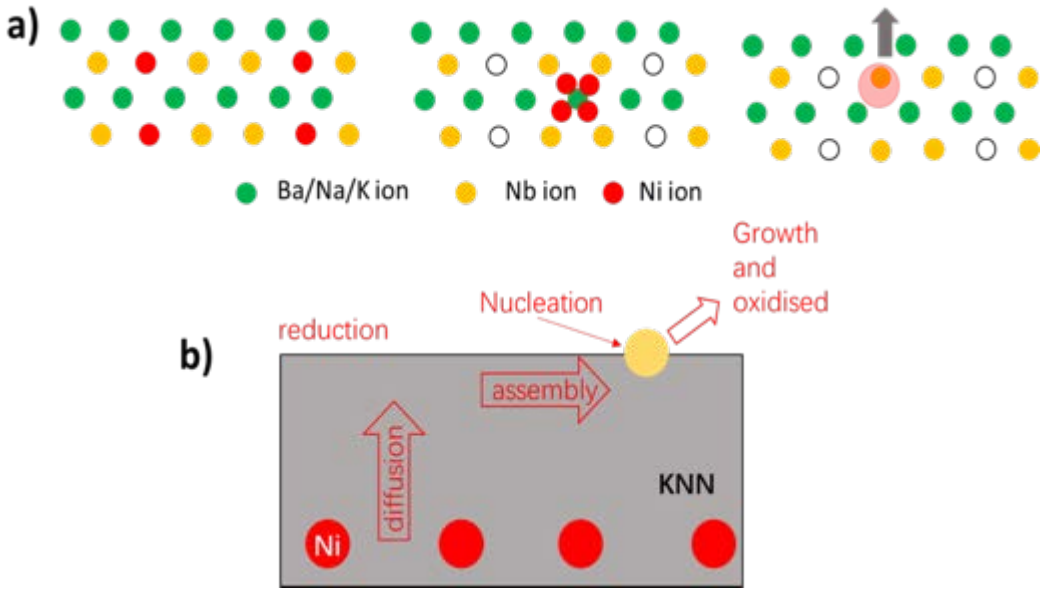

Figure 7.10 a) Schematic diagram of Ni ex-solution from the KNN matrix and b) illustration of the ex-solution process

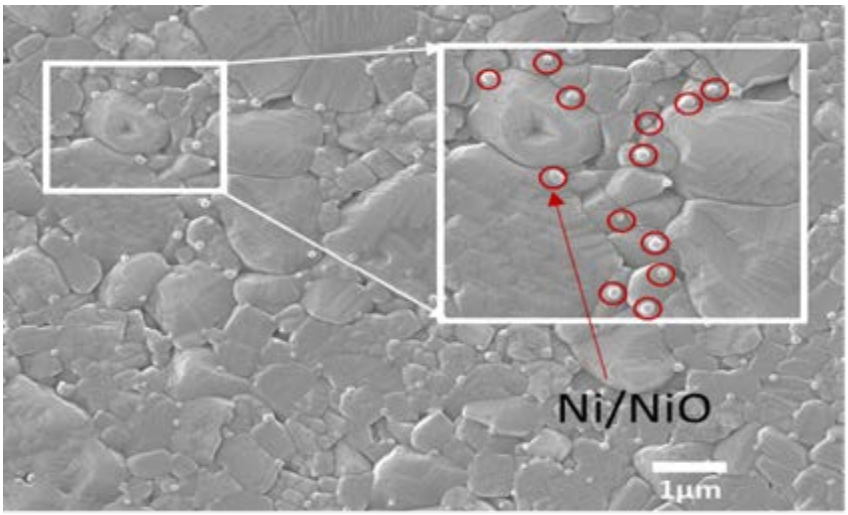

Figure 7.11 SEM image of the as-sintered surface microstructure of a 5KNN-2BNNO pellet sintered at 1180°C for 2 hrs in air

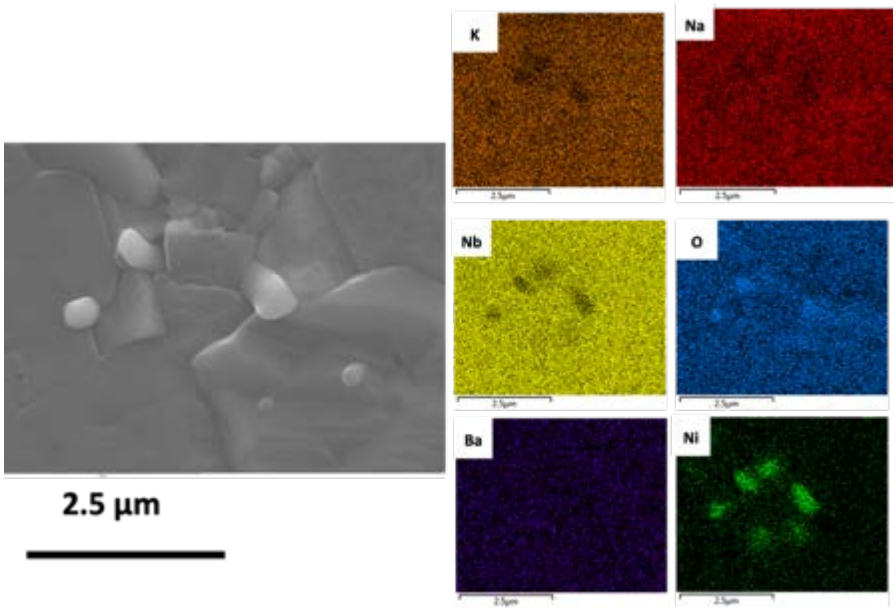

Figure 7.12 SEM image and EDS elemental maps of the as-sintered surface microstructure of a 5KNN-2BNNO pellet sintered at 1185°C for 2 h in air

The room temperature XRD patterns of the sintered 5KNN-2BNNO pellets sintered at temperature from 1165-1185°C, together with the corresponding pattern of a 5KNN ceramic fabricated using TSS (discussed in chapter 6), are shown in figure 7.13. All the patterns show reflections consisting of a perovskite orthorhombic phase but it can be seen that all the diffraction peaks become broader in the doped materials with less apparent splitting of peaks at ~45° compared to 5KNN. This could be due to the effect of grain size[331] and lattice strain[332]. According to Scherrer's formula[332], smaller grains cause a broadening effect for XRD diffraction peaks. From the discussion above and figure 7.8, 5KNN-2BNNO ceramics exhibit much finer grain size than 5KNN ceramics, which might explain the peak broadening

observed. Another reason might be the lattice strains that arise because the ionic radius of Ni^{2+} and Ba^{2+} differ from the ionic radius of K^{+}, Na^{+} and Nb^{5+}, table 7.3. In addition, with increasing sintering temperature, the level of crystallinity increased leading to a slightly sharper (022) peak. However, when the temperature was >1180°C, a peak split for the (022)/(002) diffraction become more apparent, supporting the argument for the ex-solution of Ni discussed above. The ex-solution of Ni helps to maintain the structure stability of KNN-based system through pushing the relatively larger B-site doping ions (Ni) out the lattice, leading to the stability of original phase structure of 5KNN (orthorhombic structure). Based on all of this evidence, the best single-sintering temperature for the 5KNN-2BNNO ceramics was identified as 1175°C for 2 hours.

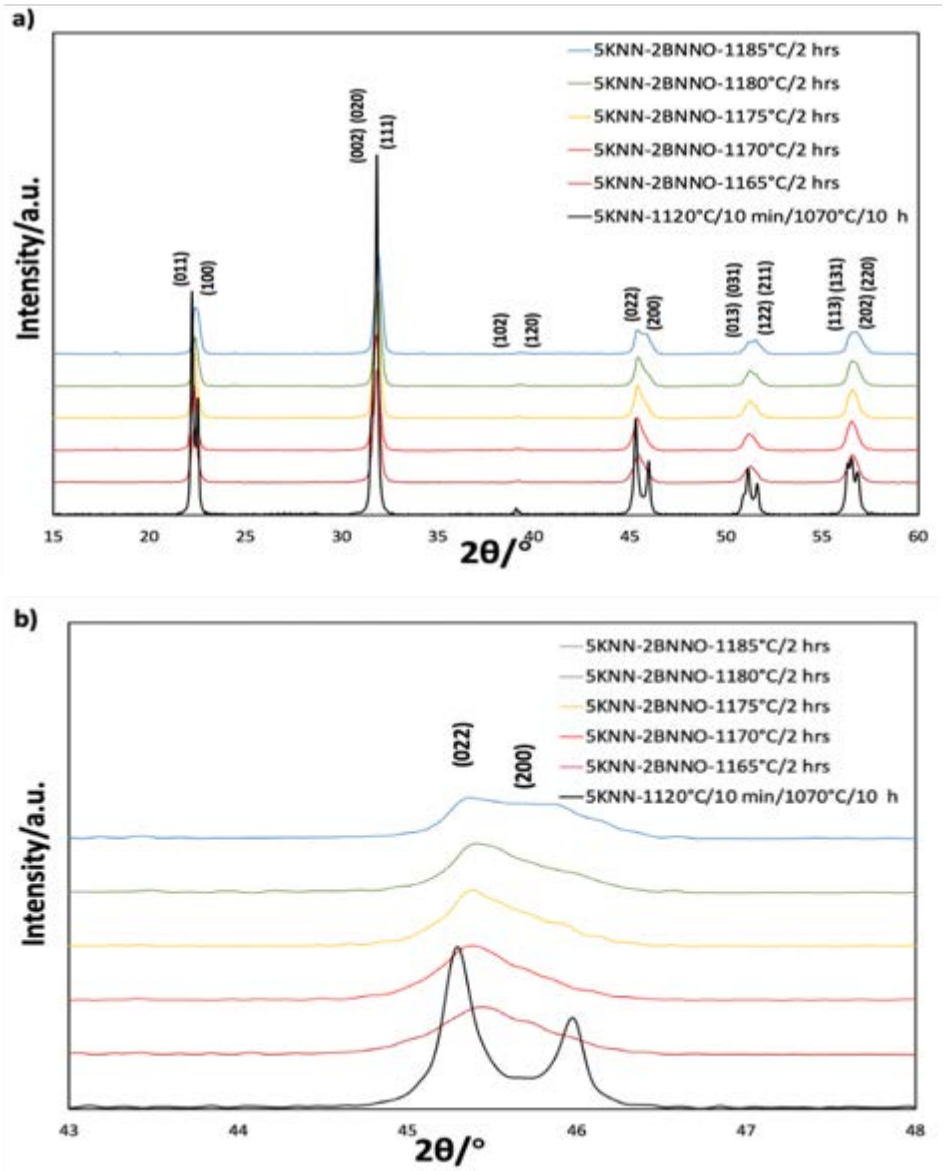

Figure 7.13 XRD patterns of sintered 5KNN-2BNNO ceramics sintered at different temperatures for 2 h and a two-step sintered 5KNN ceramic sintered at 1120°C/ 10 mins/1070°C/10 hrs: a) 2θ = 15 - 60°; b) 2θ = 43 - 58°

Table 7.3 Ionic radii of relevant elements[333]

Element	Coordination number	Charge	Ionic radius/Å
Na	12	1+	1.12
K	12	1+	1.46
Nb	6	5+	0.64
Ba	12	2+	1.38
Ni	6	2+/3+	0.69/0.56
O	6	2-	1.4

7.3.2 Two-step sintering

5KNN-2BNNO ceramics were also fabricated by two-step sintering. Figure 7.14 illustrates the relative density of these ceramics after partial sintering at a range of different first step temperatures from 1170 to 1195°C. It can be seen that there is a maximum in the curve and the highest density was obtained at 1180°C (relative density: 94.4±0.02%); the lower shrinkage and density values obtained at higher T_1 temperatures may be due to the evaporation of the alkali metals (chapter 6) and Ni ex-solution. Hence, 1180°C was selected as the first step sintering temperature for further investigation.

From the dynamic sintering curve in figure 7.4, the highest densification rates were achieved at temperatures between 1100 – 1200°C. Hence the range 1130 – 1160°C was selected to investigate the optimum value for T_2, the second step sintering temperature; and the results are shown in figure 7.15. Although there was no significant increase in final density when T_2 = 1130°C, higher temperatures did lead to a slightly higher level of densification with final densities in the range of 96 – 97%. Higher T_2 temperatures were not investigated since the increase in density was both modest and levelled off by 1160°C. The final dwell time was extended to 20 h and the results are also exhibited in figure 7.15. It can be seen that the longer dwell time led to a decrease in sample density for all different T_2 temperatures, which might be due to the evaporation of alkali. Hence, 10 h was selected as the best second soaking time identified.

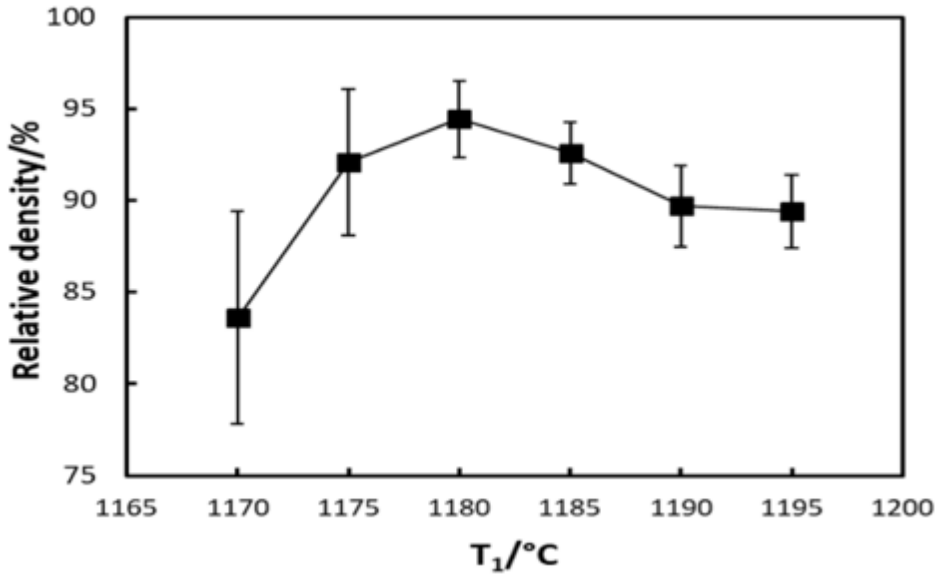

Figure 7.14 Relative density of 5KNN-2BNNO ceramics sintered for 10 mins with a heating rate of 10°C/min as a function of first-step temperature

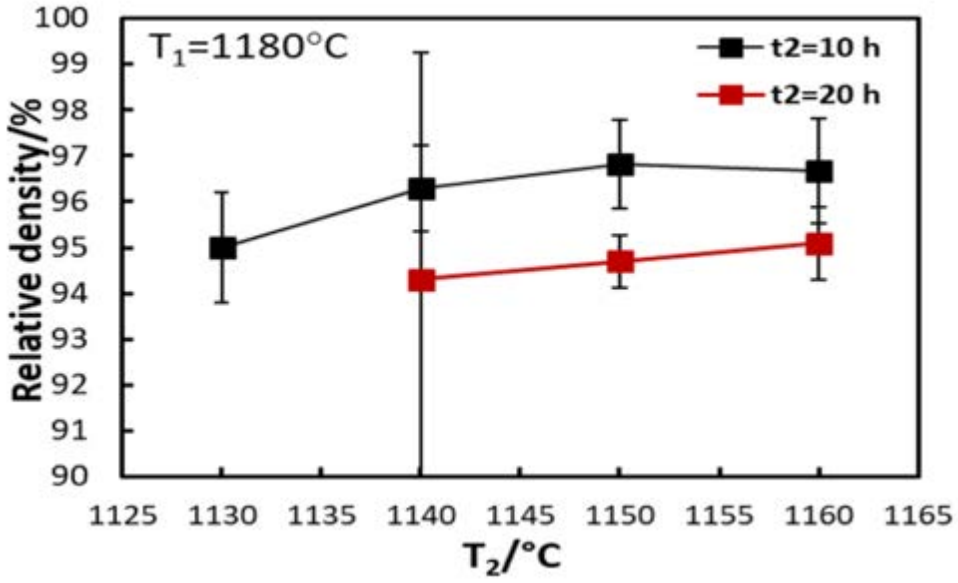

Figure 7.15 Relative density of 5KNN-2BNNO ceramics sintered at T_1 = 1180°C for 10 min and then held for 10 h at different T_2 temperatures. The cooling rate from T_1 to T_2 was 30°C/min

The surface morphology of 5KNN-2BNNO ceramics densified by TSS were investigated by thermally etching polished samples at 150°C below the first step sintering temperature for 30 min. SEM image is shown in figure 7.16. In general, the microstructures were similar in structure to those obtained by SSS. For 5KNN-2BNNO densified by TSS, comparison with figure 7.8 reveals a slightly larger grain size and abnormal grain growth had occurred (circled in red).

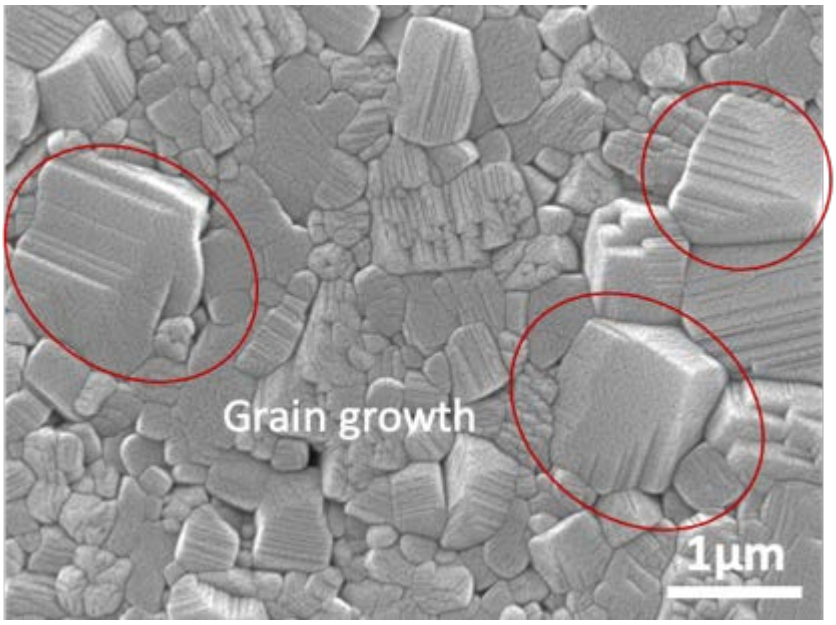

Figure 7.16 The SEM images of polished and thermally etched 5KNN-2BNNO ceramic surfaces densified by TSS (1180°C/ for 10 mins / 1150°C/ for 10 h)

7.3.3 Property comparison of 5KNN-2BNNO ceramics fabricated by SSS and TSS

The dielectric and piezoelectric properties of 5KNN-2BNNO ceramics fabricated using the best SSS and TSS conditions are presented in table 7.4. It is clear from the latter, together with figures 7.8 and 7.15, that 5KNN-2BNNO ceramics densified by SSS exhibited slightly higher relative densities, by approximately 1.5%, and finer, more homogenous microstructures. Although these different microstructures had relatively little effect on the properties, where there were significant differences, *e.g.* the tan δ and Q_m values, the SSS ceramics exhibited slightly better values.

In general, it can be concluded that doping 5KNN with Ba and Ni aids to enhance the density and suppress grain growth. Having said that, the sintering temperature of the 5KNN-2BNNO composition is limited by the Ni ex-solution process and cannot exceed 1180°C during SSS. Although TSS contributes to extending the sintering window, the long soaking time at high temperature involved seems to cause significant sodium and potassium evaporation. Thus, based on the evidence obtained, a single-step sintering (SSS) schedule involving 2 h at temperatures >1175°C was selected as the basis of the sintering method for the doped KNN ceramics.

Table 7.4 Density, grain size and dielectric and piezoelectric properties of 5KNN-2BNNO ceramics fabricated using the best SSS and TSS sintering route conditions

	SSS 1175°C / 2 h	TSS 1180°C for 10 mins / 1150°C for 10 h
Relative density	98.3±1%	96.8±1%
Mean grain size / nm	429±67	486±94
ε_r	742±46	752±81
tan δ / %	3.8±0.1	8.5±3.2
d_{33} / pC N^{-1}	132±3	129±5
k_p / %	42±1	43±1
k_{eff} / %	36±1	36±1
Q_m	90±3	63±13
Efficiency / %	84±6	83±3
Energy density / $10^{-15} m^2 N^{-1}$	1389±164	1269±268

7.4 The effect of composition on sintering behaviour

BNNO doped 5KNN powders were prepared and calcined at 900°C for 2 h as described in section 7.2. The resulting room temperature XRD patterns are presented in figure 7.17 together with data for undoped 5KNN calcined powders. All the patterns were indexed based on the perovskite cubic phase; the occurrence of any phase transitions will be discussed in section 7.5. Figure 7.17 a) shows the data from 15 – 60°, whilst b) shows zoomed views of the key peaks at 2θ values of ~22°, 32° and 46°, corresponding to the (001), (011) and (002) peaks, which can be seen to shift initially towards a lower angle with an increase in BNNO concentration, 5KNN-2BNNO, 5KNN-4BNNO and 5KNN-6BNNO, and then towards a higher angle again with further increase in BNNO dopant, 5KNN-8BNNO and 5KNN-10BNNO.

As discussed previously in section 7.3.1, the lattice strain and grain size changes caused by the presence of the dopant may have led to the broadening and shifting of the peaks. The strain induced in the KNN lattice will have been due to the substitution of the small cations Nb^{5+} and Na^{+} by the larger cations Ni^{2+} and Ba^{2+}, see table 7.3, and this is an effect that has been studied using Williamson-Hall (W-H) analysis[334]. The lattice strain can be easily calculated from the peak width (β) and diffraction angle (θ)[334]. Plots of βcosθ as a function of 4sinθ were linearly fitted and the lattice strain was calculated from the slope; the resulting values are exhibited in figure 7.18. As the dopant

concentration raised from y=0 to y=0.1, a small increase in strain from 0.0017 to 0.0063 was observed, as expected.

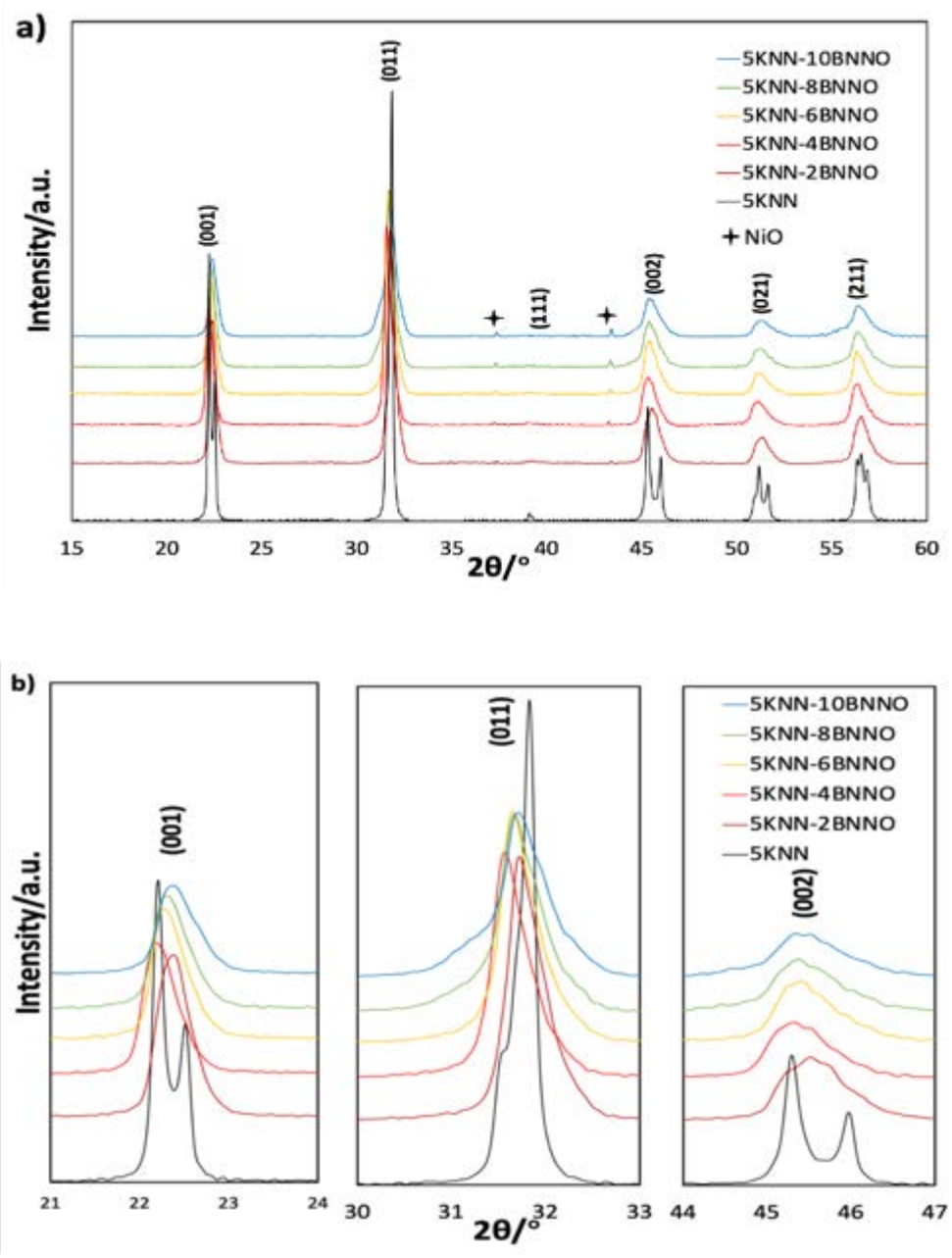

Figure 7.17 The room temperature XRD patterns of 5KNN powder and BNNO doped 5KNN powder calcined at 900°C for 2 h: a) 2θ = 15 – 60°; b) 2θ = 21 – 24°, 30 – 33° and 44 – 47°

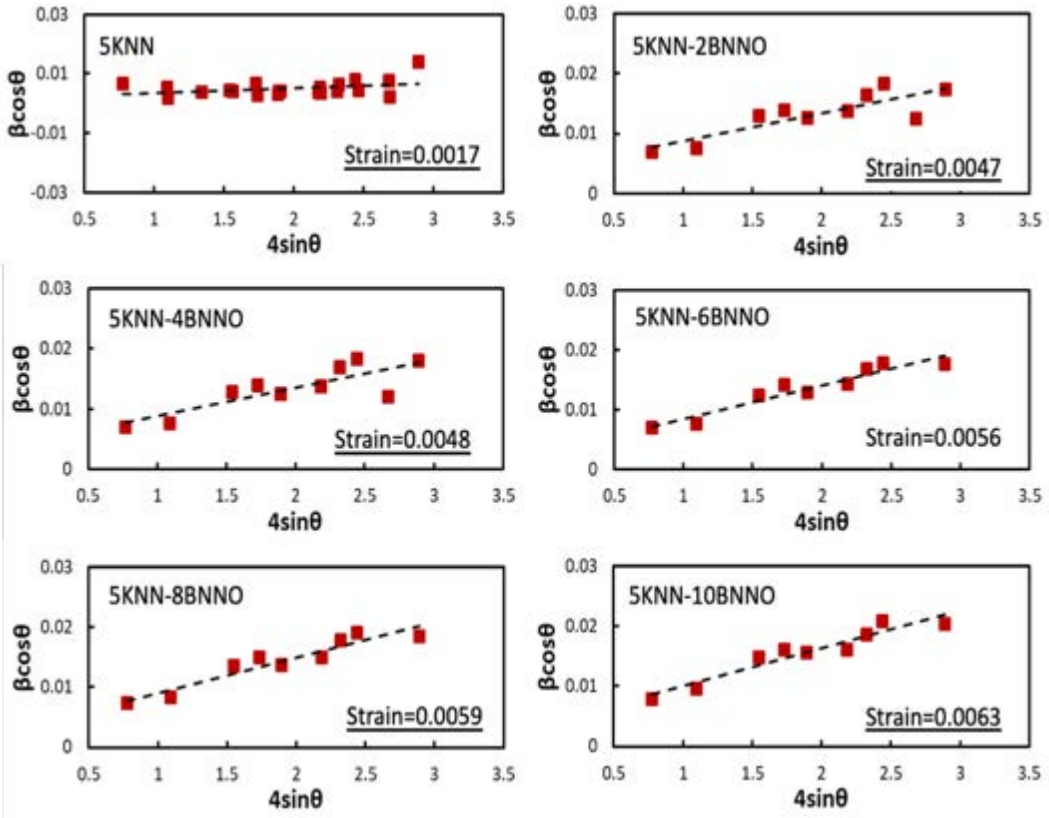

Figure 7.18 Williamson-Hall plots of 5KNN and BNNO doped 5KNN compositions. The resulting calculated strain values are also provided for each composition

The relative densities of the BNNO doped 5KNN ceramics, 5KNN-4BNNO – 5KNN-10BNNO compositions, sintered for 2 h are shown in figure 7.19. Two things can be observed; first, all the plots exhibit a maximum in the density with sintering temperature and second, a higher sintering temperature was required for the higher dopant concentrations. The best sintering temperature for each composition and the relative density achieved, as a result of calculating the theoretical density for each composition from the XRD results measured at room temperature and presented in section 7.5, are summarised in table 7.5. Notably, all the compositions exhibited densities >96% of theoretical, lessening the impact of density upon the subsequent dielectric, piezoelectric, ferroelectric and photovoltaic properties achieved. The microstructures of the thermally etched BNNO doped 5KNN sintered ceramics are shown in figure 7.20. As expected given the density values achieved, all exhibit minor levels of porosity (circled in red); they also exhibit a similar faceted morphology, but with less sharp edges, compared to the 5KNN-2BNNO ceramics, figure 7.8. In addition, the relationship between BNNO doping amount and grain size is also exhibited in figure 7.21, it can be observed that with a raise in BNNO dopant level a decrease in the mean grain size may be observed. The presence of NiO could also be observed (circled in yellow, as shown in figure 7.11-7.12). These microstructural features are

probably explained by the high sintering temperatures causing the evaporation of sodium and potassium, discussed in chapter 6, and the ex-solution of Ni, discussed in section 7.3.1.

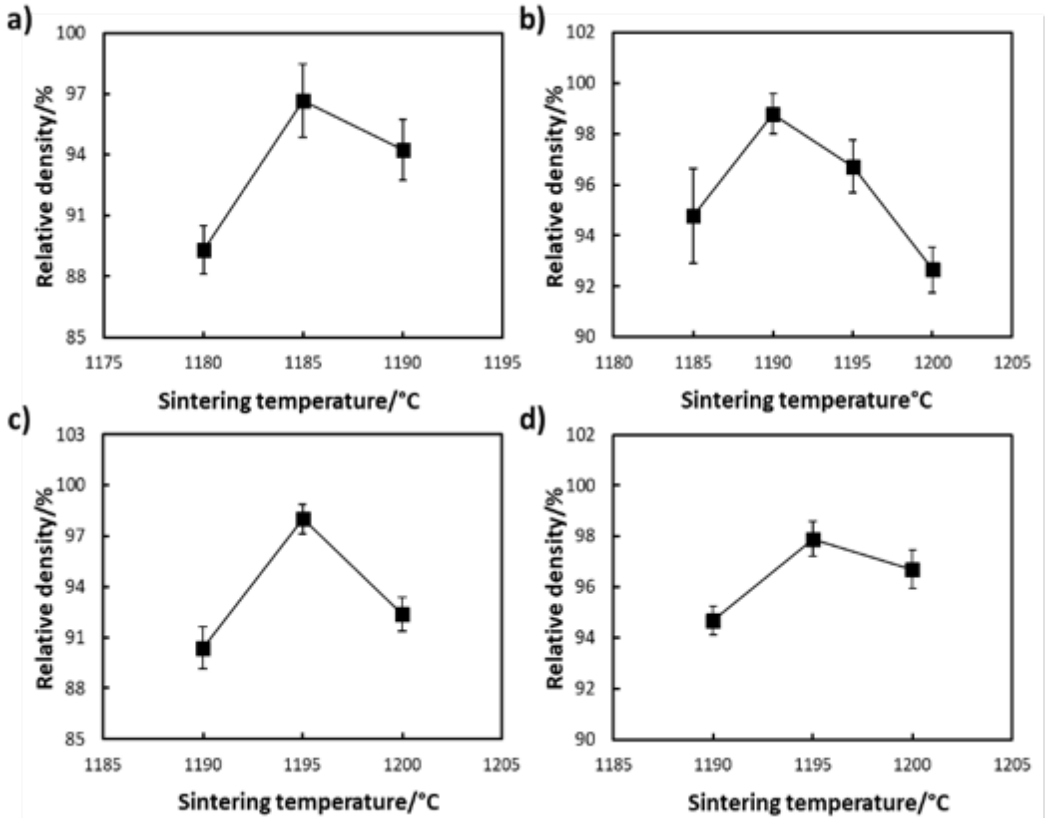

Figure 7.19 Relative density as a function of sintering temperature for 2 h with a heating rate of 5°C/min: a) 5KNN-4BNNO, b) 5KNN-6BNNO, c) 5KNN-8BNNO and d) 5KNN-10BNNO

Table 7.5 Sintering temperatures at which the maximum relative density was observed for BNNO doped 5KNN samples ceramics after sintering for 2 h

Composition	Sint temp / °C	Theoretical density / g cm^{-3}	Density / g cm^{-3}	Relative density / %
5KNN-2BNNO	1175	4.553	4.47±0.04	98.2±0.89
5KNN-4BNNO	1185	4.595	4.44±0.31	96.7±0.75
5KNN-6BNNO	1190	4.626	4.57±0.04	98.5±0.78
5KNN-8BNNO	1195	4.663	4.56±0.05	97.8±0.99
5KNN-10BNNO	1195	4.690	4.59±0.27	97.9±0.68

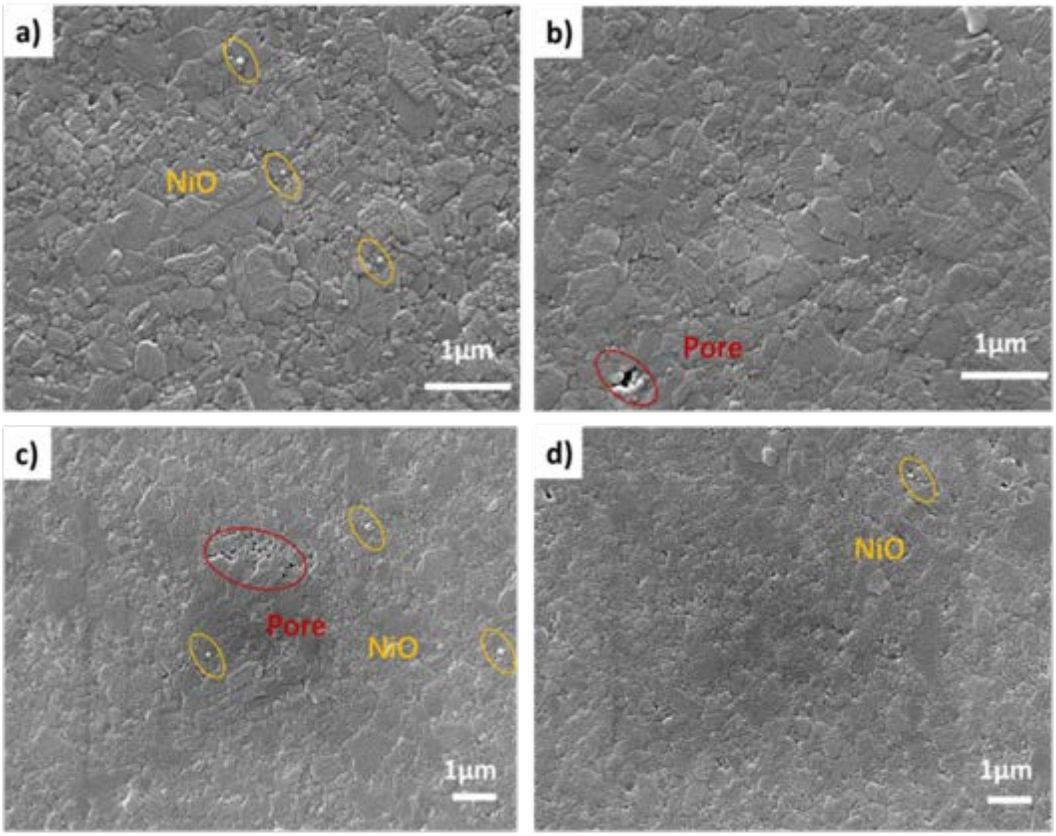

Figure 7.20 Surface microstructure of BNNO doped 5KNN ceramics pellets sintered at their individual optimised temperatures for 2 h, see table 7.5, and thermally etching for 30 mins at 150°C below the sintering temperature, a) 5KNN-4BNNO sintered at 1185°C, b) 5KNN-6BNNO sintered at 1190°C, c) 5KNN-8BNNO sintered at 1195°C and d) 5KNN-10BNNO sintered at 1195°C

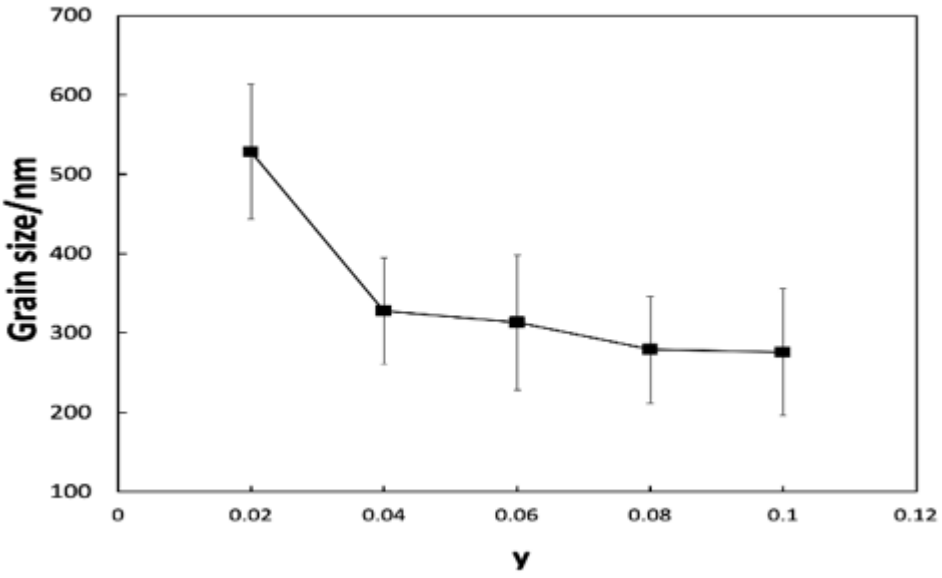

Figure 7.21 Grain size of doped 5KNN ceramics as a function of BNNO doping amount, y=0.02 represents the 5KNN-2BNNO composition, y=0.04 represents the 5KNN-4BNNO composition, y=0.06 represents the 5KNN-6BNNO composition, y=0.08 represents the 5KNN-8BNNO composition and y=0.1 represents the 5KNN-10BNNO composition

7.5 Structural characterisation

It is commonly known that the piezoelectric properties of ferroelectric ceramics are significantly influenced by their structure[33]. In order to exclude the impact of internal macro-structure stresses upon the results, the sintered pellets used for XRD and Raman measurements were shattered using a hammer and then manually ground into powder in an agate mortar and pestle. In this section, different BNNO doped 5KNN composition are represented by the dopant amount, *e.g.* y=0 represents the 5KNN composition, y=0.02 represents the 5KNN-2BNNO composition and y=0.1 represents the 5KNN-10BNNO compositions (see chapter 5, table 5.2). Each composition was sintered at its optimum sintering temperature as shown in table 7.5. The room temperature XRD patterns of the BNNO doped 5KNN (y = 0 – 0.1) samples are shown in figure 7.22; they all exhibit a perovskite structure, revealing the formation of homogenous, stable solid-solution of (1-y) 5KNN – y BNNO. Compared with the XRD patterns of the calcined powders, figure 7.17, the powders arising from the crushing of sintered pellets show sharper diffraction peaks and smaller impurity peaks, *e.g.* for NiO, indicating an improvement in crystallinity and homogeneity. Peak broadening can also be observed after doping with BNNO, which may be due to the reduction in mean grain size and the increased lattice strain developed (as discussed in section 7.3.1).

It was reviewed in chapter 2 that the KNN-based ceramics experience the paraelectric-ferroelectric transition followed by three ferroelectric-ferroelectric transition with successive phase transition of Cubic phase (C phase) – Tetragonal phase (T phase) – Orthorhombic phase (O phase) – Rhombohedral phase (R phase) during cooling down[17,335]. It can be seen from figure 7.22 that, at room temperature, pure 5KNN exhibits orthorhombic phase (O phase). As the BNNO dopant amount increases, the (011)/(100) peaks around 22.5° start to broaden and form $(001)/(100)_T$ and $(022)/(200)_O$, meanwhile, peaks at 45° are broadened and coalesce to form a single $(002)/(200)_T$ peak, revealing that the doped KNN samples experience a orthorhombic – tetragonal phase transition. The substitution of Ni^{2+} and Ba^{2+} into the lattice also generates oxygen vacancies and an internal stress field, which could break the balance between the Nb-O orbital hybridisation and change the local deformation of the perovskite structure, possibly contributing to the observed structural phase transitions[322].

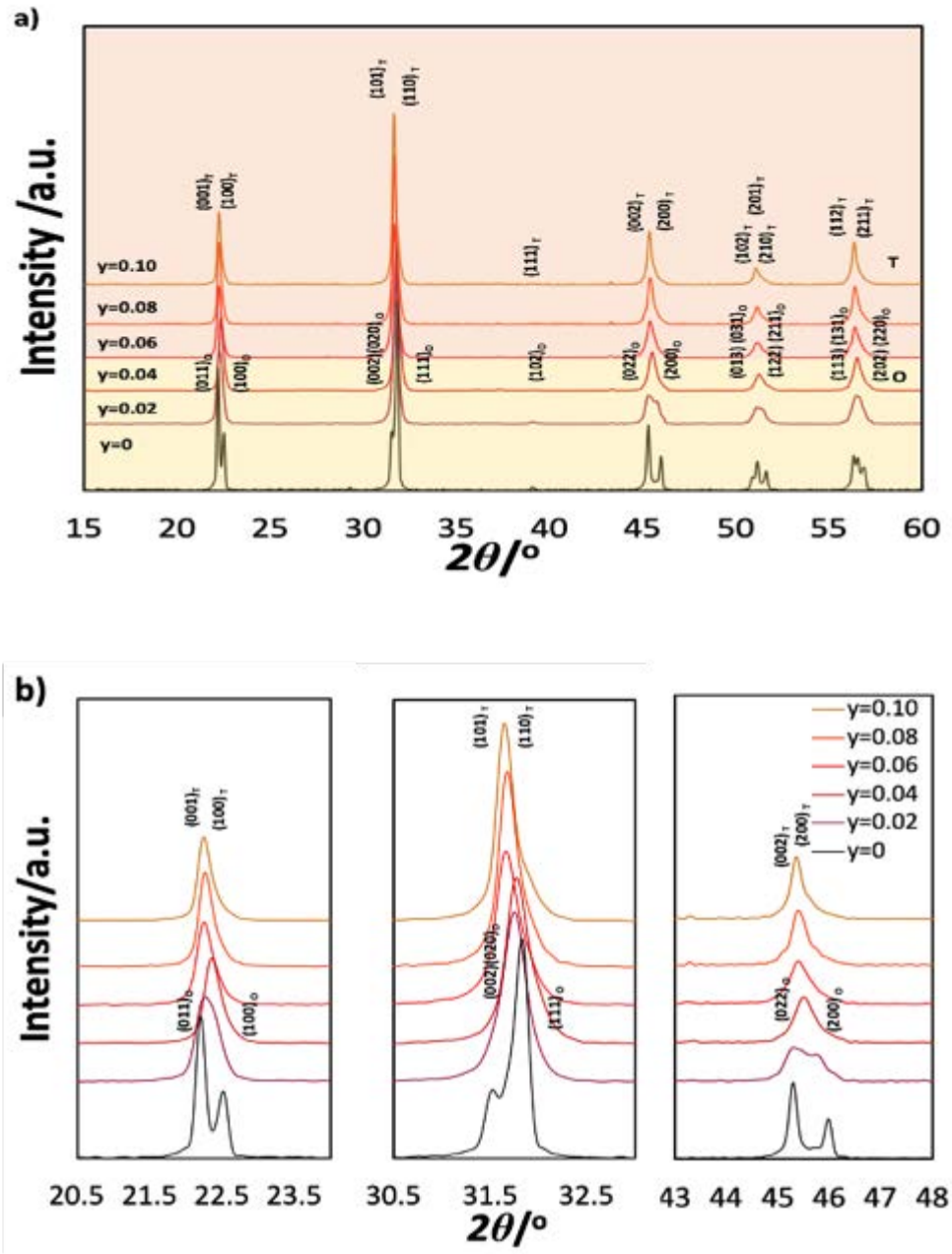

Figure 7.22 Room temperature XRD patterns for BNNO doped 5KNN ceramics (y=0-0.10) samples sintered at their optimum sintering temperature for 2 h (O and T refer to orthorhombic and tetragonal phase, respectively): a) 2θ = 15° – 60°; b) 2θ = 20.5° – 24°, 2θ = 30.5° – 33° and 2θ = 43° – 48°

It can also be seen from figure 7.22 b) that, with increasing BNNO dopant amount, the XRD peaks consistently shifts towards the lower diffraction angles (2θ), indicating the expansion of the unit cell volume. The unit cell volume (V) as the function of BNNO doping is displayed in figure 7.23 and shows a trend of increasing V with greater additions of Ba^{2+} and Ni^{2+}, which have a larger ionic radius than those of Na^{+} and Nb^{5+}. The relationship between the unit cell volume of doped 5KNN compositions and the BNNO doping amount exhibits an approximately linear relationship, revealing a good substitution of Ba^{2+} and Ni^{2+} in the 5KNN unit cell based on the empirical Vegard's law[336]. However,

the dramatic change around y=0.04 could be associated with the phase transition. Rietveld refinement fitted by Pseudo-Voigt function via TOPSA-Academic software and the phase percentages were determined by the intensity of the (022)/(200)$_O$ and (002)/(200)$_T$ peaks. It can be seen from the figure 7.22 b) that the peak around 45° exhibits an overlapping peak without clear peak slitting, indicating the mixed phases in the sample, therefore, a mixed phase fitting model were used to refine the patterns. For y=0.00 composition, the XRD pattern was analysed based on an orthorhombic perovskite phase with the space group Bmm2. The structural analysis for the sample y=0.02 – 0.06 composition was carried out via a mixing structural model of Bmm2 (O phase) + P4mm (T phase). And the structural analysis for the sample y=0.08 – 0.10 composition were based on the structural model of P4mm (T phase) + $Pm\bar{3}m$ (C phase). The quantitative phase analysis of each composition at room temperature are summarised in table 7.6. It indicates that, with increased BNNO doping, the fraction of T phase increases and the T phase becomes the primary phase at room temperature.

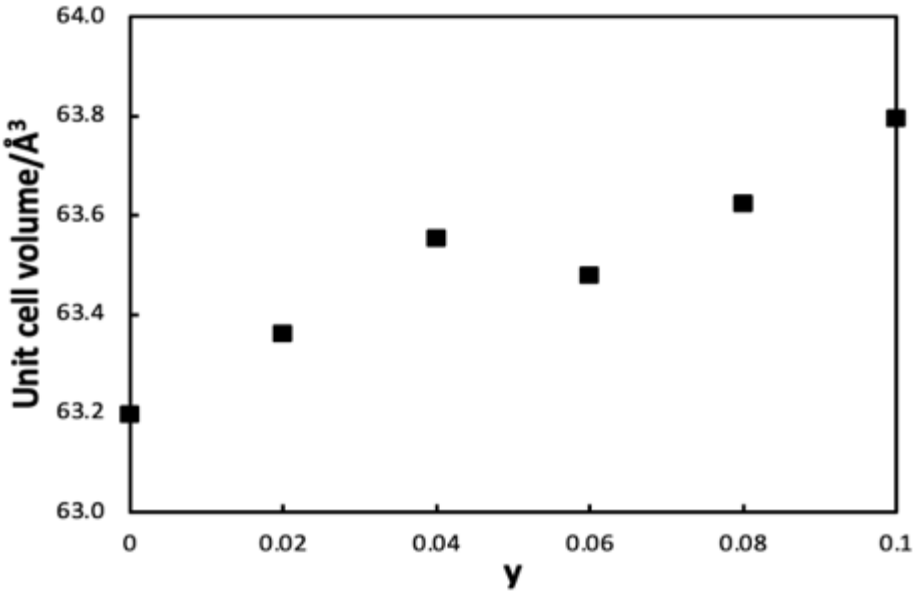

Figure 7.23 Unit cell volume as a function of increasing quantity of BNNO-dopant (y=0 – 0.10)

Table 7.6 Quantitative analysis results from Rietveld refinement of BNNO doped 5KNN ceramics (y=0-0.10) calculated from XRD patterns (O: orthorhombic, T: tetragonal and PC: pseudo-cubic)

Composition	Goodness of fit	Results
y=0	1.55	O: 100 wt%
y=0.02	1.26	O: 82.2 (19) wt% T: 17.8 (19) wt%
y=0.04	1.28	O: 59.0 (3) wt% T: 41.0 (3) wt%
y=0.06	1.31	O: 12.0 (7) wt% T: 88.0 (7) wt%
y=0.08	1.35	T: 95.1 (3) wt% PC: 4.9 (3) wt%
y=0.10	1.45	T: 96.5 (3) wt% PC: 3.5 (3) wt%

Raman spectroscopy is an extremely sensitive tool for identifying local structural distortions in perovskites caused by the tilting of oxygen-octahedra and cationic displacements[337]. It is very susceptible to changes in binding energies resulting from molecular vibrations, which reflect information about non-uniform distortions in short-range ordering[338]. Thus, the phase transitions in the doped KNN samples were further investigated by using Raman spectroscopy to obtain stronger evidence of the phase transitions. The vibration of 5KNN-based materials is divided into translational modes of the isolated cations, such as K^+ and Na^+, and vibration modes of coordination polyhedra[339]. The small peaks in the region below 200 cm^{-1} are mainly regarded as the translational modes of $Na^+/K^+/Ba^{2+}$ isolated cations as well as the rotation of NbO^6 octahedral[339,340]. It has been reported that NbO_6 octahedral group demonstrates 6 normal vibrations ν_i[177]:

$$\Gamma_{vib} = \nu_1 + \nu_2 + \nu_3 + \nu_4 + \nu_5 + \nu_6 \qquad 7\text{-}7\text{-}1$$

Where ν_1 mode is symmetric A_{1g} type stretching vibration mode of Nb-O bond, ν_2 and ν_3 represent doubly degenerated E_g type stretching vibration mode of O-Nb-O bonds and triply degenerated T_{1u} type stretching vibration mode of Nb-O bonds, respectively[341]. ν_1, ν_2 and ν_3 vibration modes involve mainly oxygen displacements of Nb-O bonds of the NbO_6 octahedra[342]. Finally, ν_4, ν_5, ν_6 associate to triply degenerated F_{1u} type bending vibration mode, F_{2g} type vibration mode and F_{2u} type bending vibration mode of the NbO_6 group, respectively[341]. In this work, the most significant modes are associated with the ν_1, ν_2 and ν_5 peaks, which show the vibration of an NbO_6 octahedron, figure 7.24. Figure 7.25 shows the Raman spectra of (1-y) 5KNN – y BNNO ceramic powder (y=0.00 – 0.10) measured at room temperature.

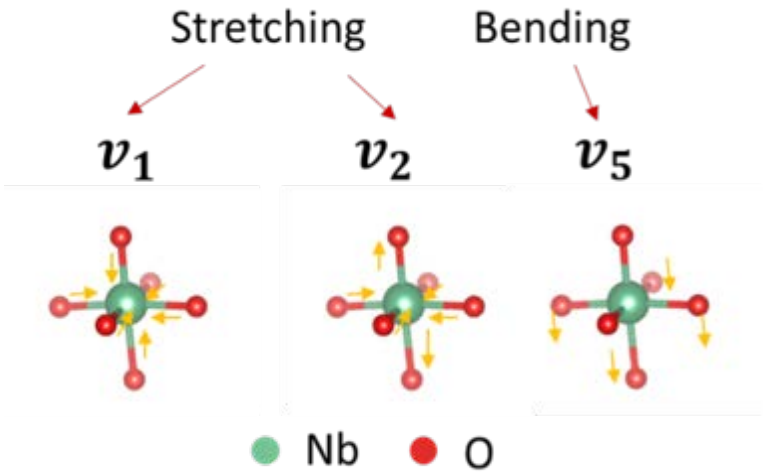

Figure 7.24 Illustration of the ν_1, ν_2 and ν_5 vibration modes of an NbO_6 octahedron

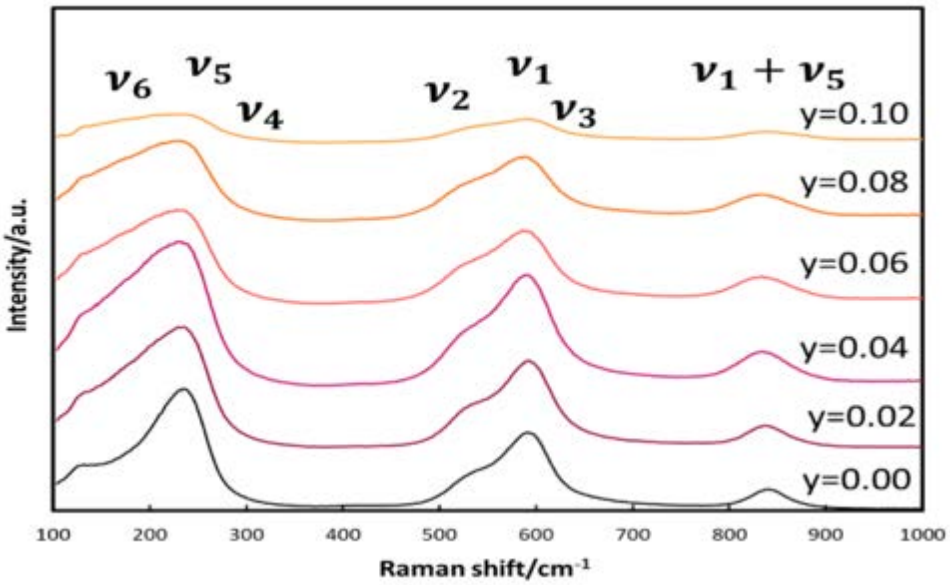

Figure 7.25 Room temperature Raman spectra for 5KNN and doped BNNO ceramic powder samples: Raman shift = 100 cm^{-1}-1000 cm^{-1}

The Raman peaks at around 135 cm^{-1} are related to the K/Na/Ba-O vibration within nanometre-sized clusters, revealing the rich in Ba^{2+}, K^{+} and Na^{+} cations[322,341]. With increasing of BNNO, all Raman peaks gradually broaden, indicating that the addition of BNNO increases the ionic disorder and lattice distortion[343]. It can be also observed from figure 7.25 that increasing the BNNO addition leads to the ν_1 and ν_2 peaks at around 600 cm^{-1} broadening and shifting to lower wavenumbers, accompanied by gradual fading of the ν_2 peak due to the substitution of Ni^{2+} into the NbO_6 octahedral, which leads to a reduction of distortion and an increase of crystal symmetry[344,345]. Since the 5KNN-based ceramics discussed here are polycrystalline materials, the characterised Raman spectra, especially the peak intensities, may differ at different locations due to the variation of grain orientations and the presence of grain interactions[339]. Hence, the shifts of the peaks and the full width at half maximum (FWHM) were analysed. The introduction of hetero-valent cations into the A-site or B-site of the KNN leads to variations in the distortion of the O-Nb-O angles and the NbO_6 force constant, causing a shift of the Raman peaks. The Raman spectra were fitted with the multiple Lorentz function to deconvolute the spectra to study the dependence of the Raman shifts and FWHM[341] on BNNO doping amount.

The composition dependence of the ν_1, ν_2, ν_5 and $\nu_1 + \nu_5$ peak positions are shown in figure 7.26. The shifting of Raman peaks is due to a decrease in the compressive strain and binding strength[338,346–350]. The vibration of the NbO_6 octahedron is very sensitive to the phase transitions. The Raman peak positions shift is regarded as one criterion to estimate the structure transformation[351]. In other words, the Raman shift is always qualitatively different (discontinuous changes) when passing a phase

boundary[351]. From figure 7.26, there is a qualitatively different change at around y = 0.04 which confirms the results of room temperature XRD. Also, as the concentration of BNNO raised from 0.02 to 0.1, the ν_1 peak becomes broader, indicating the enhancement of relaxor-type degree of dispersion, indicative of an increase of the optical transparency[344].

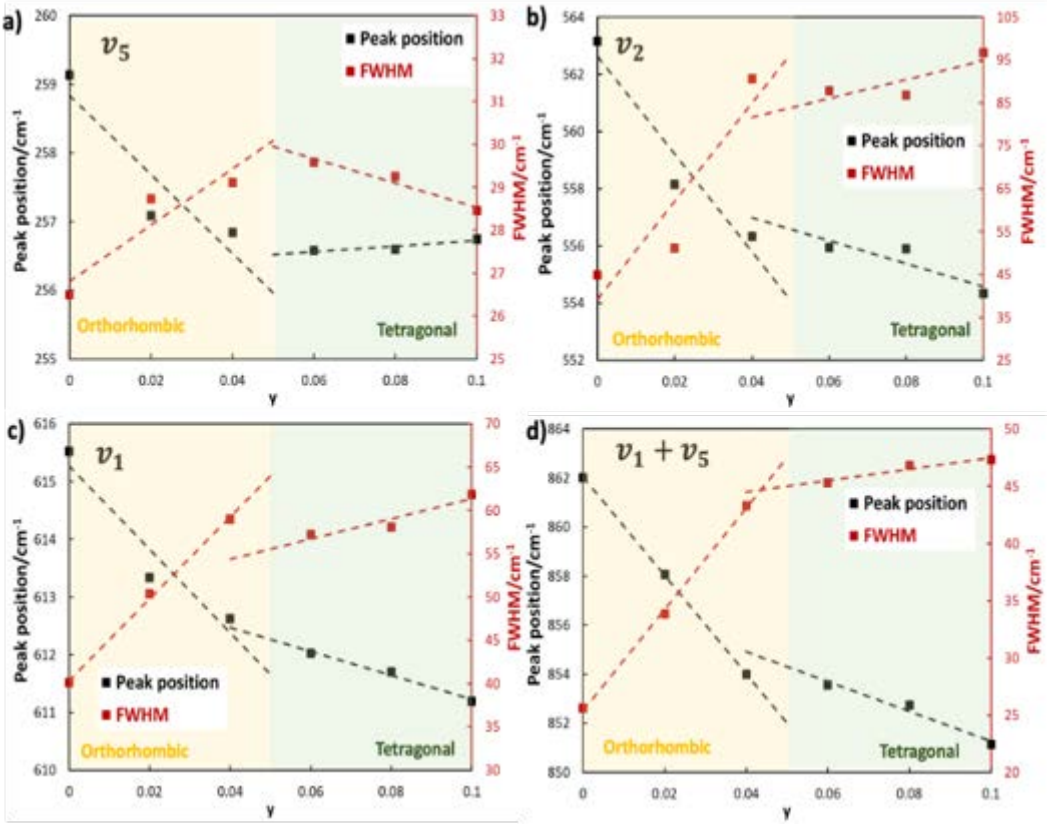

Figure 7.26 Shifts and FWHM of Raman peaks around a) 270 cm^{-1} (ν_5), b) 560 cm^{-1} (ν_2), c) 610 cm^{-1} (ν_1) and d) 850 cm^{-1} ($\nu_1 + \nu_2$) in the Raman spectra of powdered sintered ceramics measured at room temperature as the function of increasing BNNO doping amount (y=0-0.10, y=0 refer to 5KNN)

In order to investigate the impact of changing temperature upon the phase transition, the temperature dependence of the Raman spectra for each composition was measured between 30°C and 500°C. Figure 7.27 illustrates the Raman spectra of the 5KNN-2BNNO composition at 50°C, 250°C and 450°C, respectively. The three temperatures are corresponding to the orthorhombic, tetragonal and cubic phases, respectively, which can be recognised by the disappearance of the ν_2 peak and the broadening of the ν_1 peak[110]. These temperature were carefully selected far from the phase transitions to avoid phase co-existence or adaptive diffraction phenomenon of nano-domains on phase boundaries[335,352,353]. The variation of peak position and FWHM of ν_1, ν_2, ν_5 and ν_{1+5} are presented in figure 7.28 a) – d). In general, the FWHM increases with increasing temperature. The gradient changes of frequency shifts and FWHM could fundamentally be related to the thermally-

induced phase transition, which is accompanied with symmetry rearrangement and the reassignment of the symmetry operation after the phase transition. Therefore, in figure 7.28, the gradient change has been identified as the *O-T* and *T-C* phase transitions at approximately 176°C and 372°C, respectively. The phase transition temperature of y=0.02 composition identified by the ν_1, ν_2 and ν_5 peaks are presented in the figure 7.28 and summarised in table 7.7, the averaged phase transition temperature values are identified as the phase transition temperatures of y=0.02 composition, *i.e.* T_{O-T} is 177±2.9°C and T_{T-C} is 374±2.9°C. As the phase transition induced by temperature is first-order[354], the onset temperature in figure 7.28 a) – d) can be considered to be the phase transition temperature. The changes of peak position and FWHM in BNNO doped 5KNN (y=0.04 – 0.10) are provided in Appendix III, whilst the temperature of phase transition of the doped and undoped KNN ceramics are listed in table 7.8. From these Raman data, a phase diagram of the (1-y) 5KNN-y BNNO (y=0-0.10) system has been constructed and is shown in figure 7.29. It agrees well with the room temperature XRD results, the composition with y = 0 – 0.04 showing an orthorhombic structure, and the composition with y = 0.06 – 0.10 possessing a tetragonal structure. Similarly, with pure 5KNN ceramics, the results confirm that the BNNO doped 5KNN ceramics experience paraelectric-ferroelectric transitions with the phase transition sequence of cubic phase (C) – tetragonal phase (T) – orthorhombic phase (O). With the increase in BNNO doping amount (y), the phase transition temperatures T_{O-T} and T_{T-C} both decrease, indicating the narrower working temperature range of doped 5KNN ceramics.

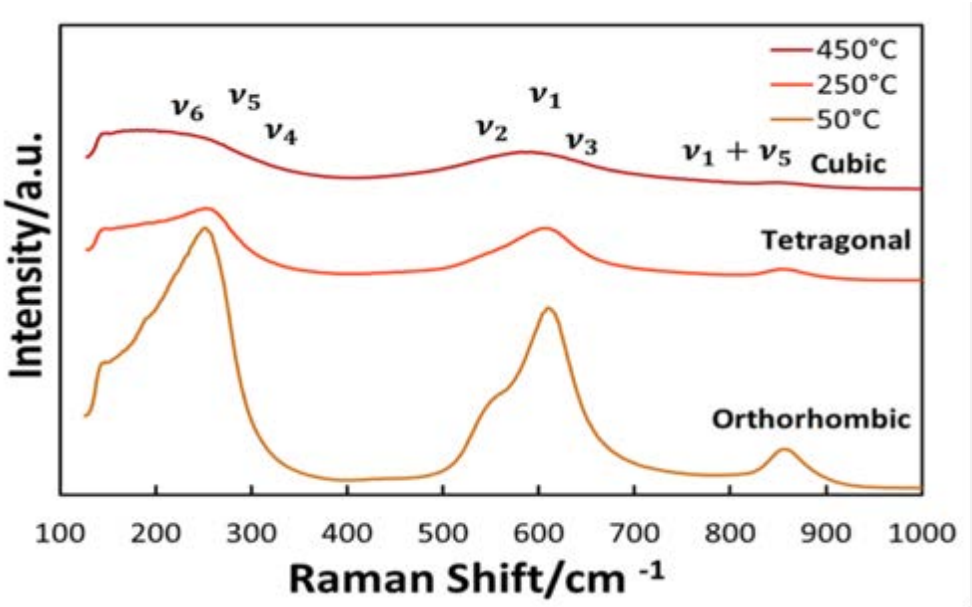

Figure 7.27 Raman Spectra of 5KNN-2BNNO samples as the function of Raman shift at different temperatures

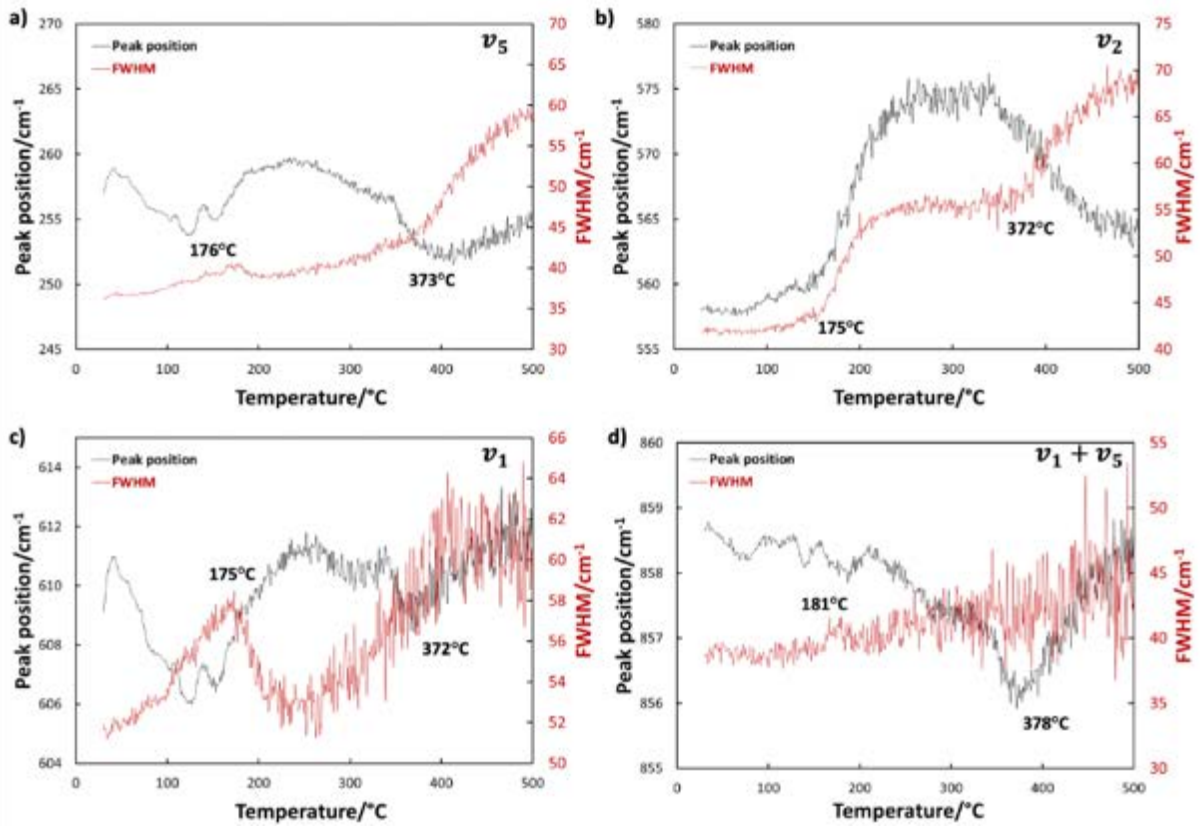

Figure 7.28 The changes of shifts and FWHM of Raman peaks around a) 270 cm^{-1} (ν_5), b) 560 cm^{-1} (ν_2), c) 610 cm^{-1} (ν_1) and d) 850 cm^{-1} ($\nu_1 + \nu_2$) in the Raman spectra of 5KNN-2BNNO powdered sintered ceramics as the function of increasing temperature

Table 7.7 The phase transition temperatures of 5KNN-2BNNO identified by different Raman peaks

Peak name	$T_{O\text{-}T}$ /°C	$T_{T\text{-}C}$ /°C
ν_1	175	372
ν_2	175	372
ν_5	176	373
$\nu_1 + \nu_5$	181	378
Average	177±3	374±3

Table 7.8 Phase transition temperatures for KNN-based ceramics from Raman spectra analysis

Composition	$T_{O\text{-}T}$/°C	$T_{T\text{-}C}$/°C
y=0	197±2	417±1
y=0.02	177±3	374±3
y=0.04	156±3	364±5
y=0.06	/	346±6
y=0.08	/	274±2
y=0.10	/	168±3

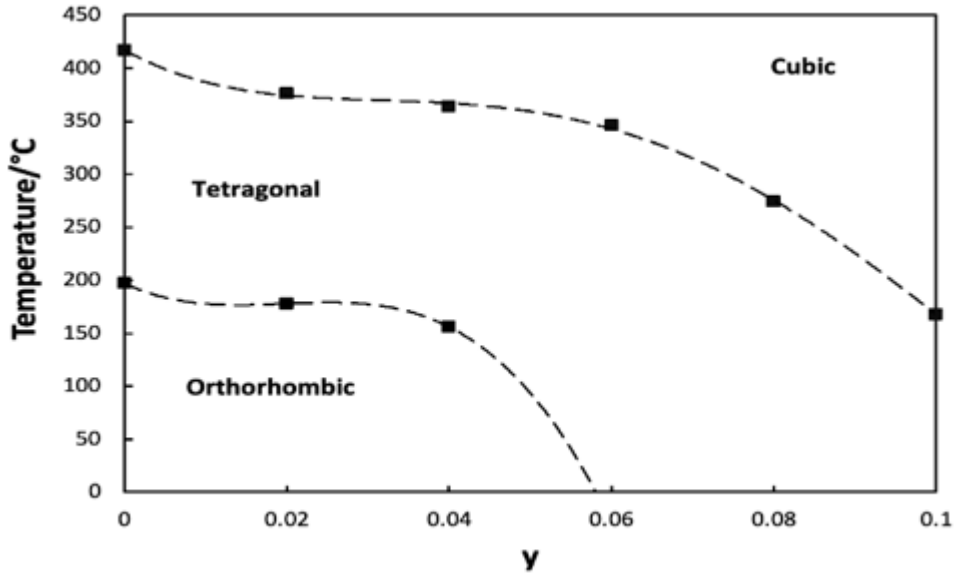

Figure 7.29 Phase diagram of BNNO doped KNN compositions (y = 0 – 0.10) derived from Raman spectroscopy measurements

7.6 Electrical characterisation

7.6.1 Dielectric property characterisation (ε_r and $tan\delta$)

The ε_r and $tan\ \delta$ of doped KNN sintered at their individually optimised sintering temperatures for 2 h are presented in figure 7.30. All the ceramic pellets were measured 24 hours after poling and each value is an average of a batch of six samples. Overall, the relative permittivity and dielectric loss factor increased with increasing BNNO doping. Firstly, compared with the undoped 5KNN ceramics ($\varepsilon_r \approx$ 329±36), all the doped ceramics exhibited a higher relative permittivity and, secondly, the relative permittivity of the doped ceramics increased with increasing BNNO dopant concentration. The highest relative permittivity was obtained in 5KNN-10BNNO ($\varepsilon_r \approx$ 1059±91), which was roughly 3 and 1.5 times larger in comparison with the 5KNN and 5KNN-2BNNO ($\varepsilon_r \approx$ 728±18.8), respectively. Generally, the relative permittivity can be related to the composition, density, grain size and the presence of defects in the material[355]. The BNNO dopant was helpful in enhancing densification and suppressing grain growth, as indicated in figures 7.8 and 7.21 and discussed in section 7.3. Also, as reviewed in section 2.2.3.1, the relative permittivity can be affected by a change of phase. In section 7.5, it was discussed that BNNO doping in 5KNN induces an orthorhombic – tetragonal phase transition, causing a first-order dielectric relaxation phenomena[356]. Thirdly, a higher amount of BNNO doping also leads to a larger measured dielectric loss. It can be seen from figure 7.30 that 5KNN-10BNNO ($tan\ \delta \approx$ 16.2±2%) possessed a value nearly four-times larger than that of the 5KNN ($tan\ \delta \approx$ 4.8±0.1%). BNNO doping in the KNN system introduces oxygen vacancies in order to preserve charge neutrality, with a higher

dopant concentration causing increased formation of oxygen vacancies. The latter will significantly affect the ionic conductivity, both in the grain and at the grain boundaries[357], *i.e.* the presence of oxygen vacancies may cause a raise in the electrical conductivity and dielectric loss. From a theoretical perspective, there were 0.17 and 0.83 mol% oxygen vacancies in the 5KNN-2BNNO and 5KNN-10BNNO compositions, respectively[18]. Thus, it would be expected that a higher dielectric loss and conductivity would be obtained[358]. The DC conductivities of the 5KNN and doped ceramics were calculated using equation 7-2[359] and figure 7.31 confirms that the conductivity increased as expected.

$$\sigma_{DC} = \frac{\varepsilon_r}{(1 + tan\delta)^{1/2}} \times \varepsilon_0 \omega tan\delta \qquad 7\text{-}7\text{-}2$$

Where ω is the angular frequency and ε_0 is the vacuum permittivity (8.854×10^{-12} F/m).

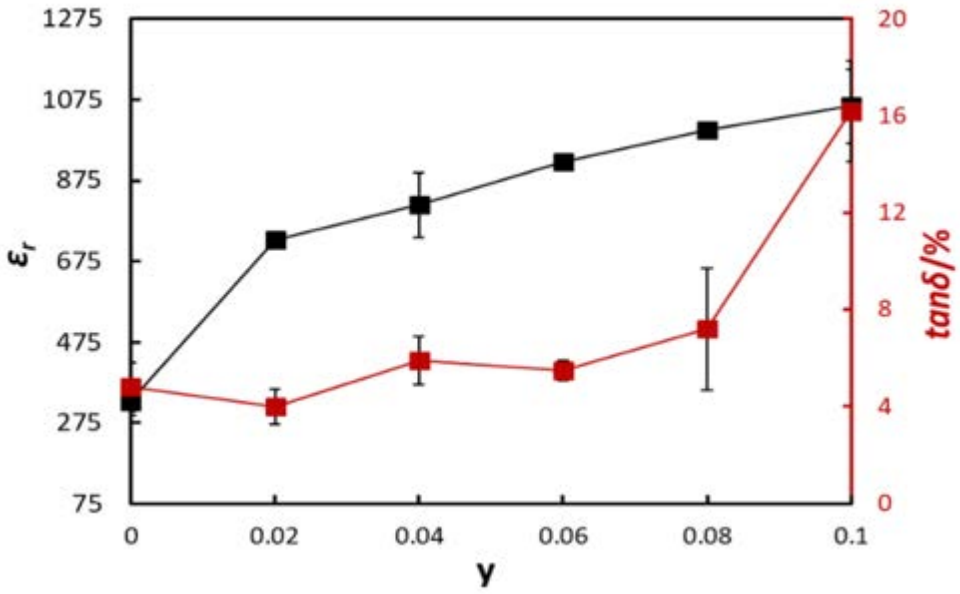

Figure 7.30 Measured relative permittivity and dielectric loss of BNNO doped 5KNN ceramic discs (y=0 – 0.10) at room temperature

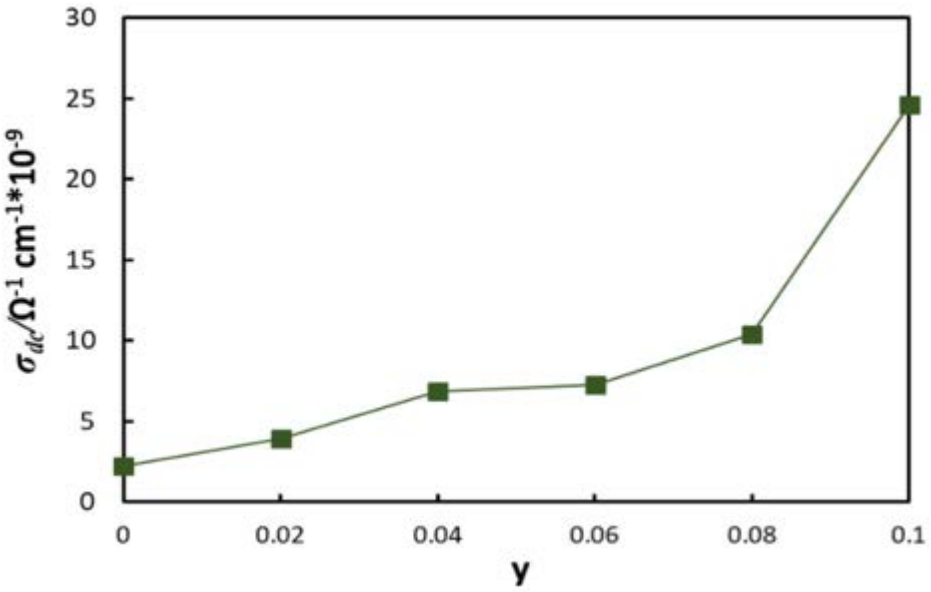

Figure 7.31 Calculated DC conductivity of BNNO doped 5KNN ceramic discs (y=0 – 0.10) at room temperature

7.6.2 Piezoelectric property characterisation ($d_{33}, k_{eff}, k_p, Q_m$)

The piezoelectric properties of the doped 5KNN samples sintered at their individually optimised temperatures are listed in table 7.9; each value represents an average of measurements from 6 samples. It can be seen that the 5KNN-4BNNO – 5KNN-8BNNO samples exhibited a poor piezoelectric response whilst the 5KNN-10BNNO samples had no piezoelectric response, these results being consistent with the phase transitions and high concentration of oxygen vacancies in these samples as discussed above. Samples with just 2 mol% BNNO doping, however, exhibited increased piezoelectric properties and relative permittivity compared to the undoped 5KNN, which may be a result of the improvements in density and microstructure dominating any deleterious effect of the increase in oxygen vacancy concentration. The oxygen vacancies formed by the introduction of the Ni^{2+} dopant ion may generate $(Ni_{Nb}''' - V_{\ddot{O}})$' defect dipoles with oxygen vacancies preferentially generated at the apex position, rather than at equatorial positions of the oxygen octahedra. This makes the whole system more stable when defect dipoles are aligned with the long axis of the unit cell[15,360]. Defect dipoles are pulled towards the depolarisation field direction, degrading the polarisation, figure 7.32[361], whilst the generation of oxygen-vacancy increases the conductivity of the doped KNN ceramics, figure 7.31, causing large leakage currents. Figure 7.33 shows that a large leakage current, beyond the range of the meter on the high voltage power supply, was induced by an applied voltage of only a 0.5 kV voltage for the 5KNN-10BNNO samples. Therefore, in order to obtain an ideal balance between bandgap and ferroelectricity, a carefully controlled doping amount is clearly needed in these materials.

Table 7.9 Piezoelectric property of 5KNN and BNNO doped KNN ceramics (- means un-measurable)

Composition	d_{33}/pC N^{-1}	k_{eff}	k_p	Q_m
5KNN	122±2.2	0.34±0.01	0.36±0.05	76±3
5KNN-2BNNO	132±1.7	0.36±0.01	0.42±0.01	90±14
5KNN-4BNNO	45±6.6	0.13±0.08	0.15±0.01	47±10
5KNN-6BNNO	11±0.6	-	-	-
5KNN-8BNNO	3±0.6	-	-	-
5KNN-10BNNO	-	-	-	-

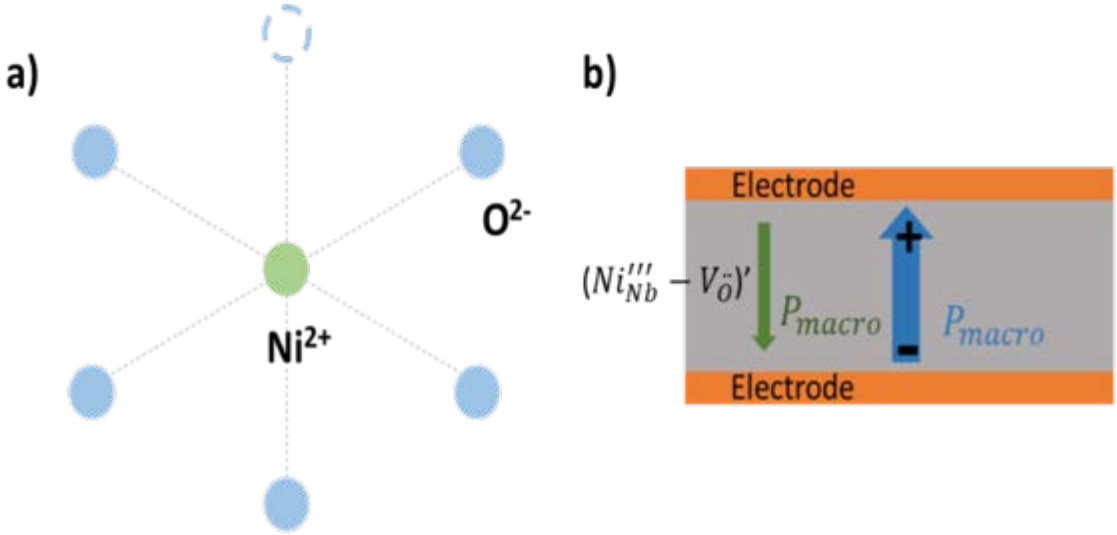

Figure 7.32 Schematic diagram of a) $(Ni'''_{Nb} - V_{\ddot{O}})'$ defect dipole and b) defect dipole direction in a macro capacitor

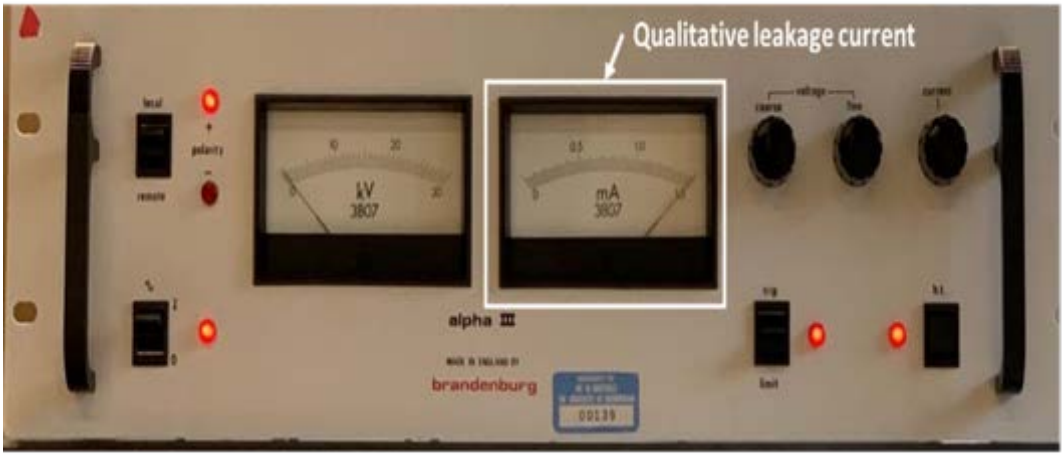

Figure 7.33 The leakage current during poling of 5KNN-10BNNO was off the scale on the high voltage power supply at only a 0.5 kV applied across an approximately ~1 mm thick samples

7.6.3 Ferroelectric property characterisation (P_s, P_r, E_c)

The room temperature measurement of polarisation with various electric field (P-E loops) for the BNNO-doped 5KNN ceramics (y = 0.0 – 0.1) was carried out under a series of electric fields at 10 Hz, figure 7.34. The 5KNN samples show a P-E loop typical of a ferroelectric response and that for the 5KNN-2BNNO sample is very similar, however both the remanent polarisation and coercive field decrease significantly when further increasing BNNO doping amount. Moreover, the shape of the P-E loops become increasingly slimmer with increasing addition of BNNO, indicating an enhancement in the conductivity, figure 7.31, and a decrease in the ferroelectric properties.

The saturated polarisation, remanent polarisation and coercive field measured at 20 kV/cm as a function of BNNO doping are summarised in figure 7.35. The E_c and P_r are the average value of E_+, E_- and P_{r+}, P_{r-}, where E_+ and E_- represent the electric field when the polarisation reaches 0 and P_{r+} and P_{r-} as the remanent polarisation when the electric field reaches 0 in the P-E loop patterns. It can be observed from figure 7.35 that the maximum remanent polarisation was obtained in 5KNN-2BNNO ceramics (13.62 μC/cm^2), the value being slightly higher than that of the undoped 5KNN ceramics (12.42 μC/cm^2). However, on further increasing the level of BNNO dopant, the polarisation decreased right down to 0.007 μC/cm^2 in 5KNN-10BNNO ceramics. This agrees well with the previous dielectric and piezoelectric properties results.

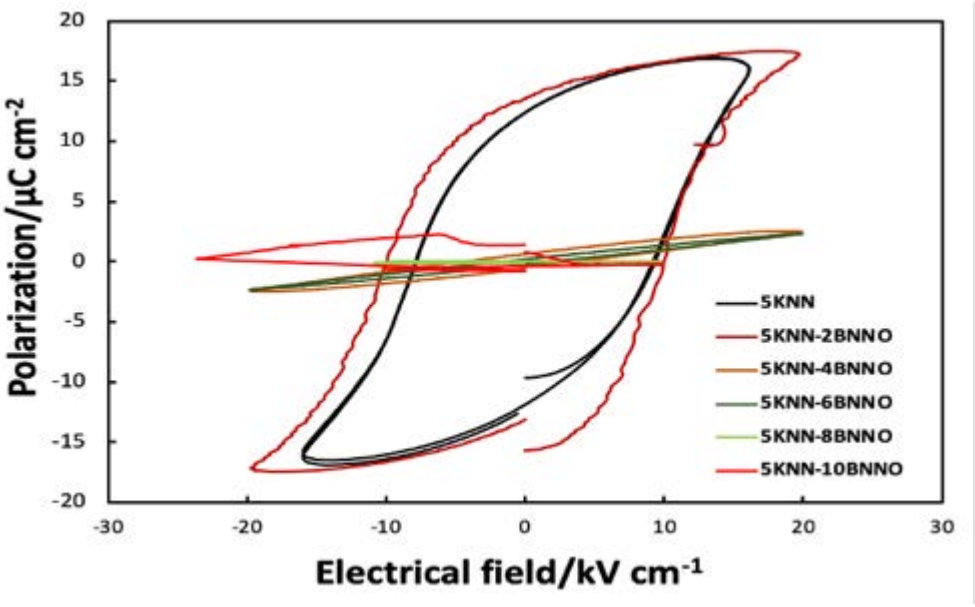

Figure 7.34 Polarisation hysteresis measurements for 5KNN and BNNO doped 5KNN ceramics at room temperature and 10 Hz

As discussed above, based on the ionic size (table 7.3) and Pauling's rules, the Ni^{2+} ion is more likely to replace the Nb^{5+} ion in the octahedral sites, with the increasing of the oxygen-vacancy concentration in the anion array maintaining charge balancing. As has been discussed, the latter enhances the conductivity. Also, the defect dipoles are pulled toward the depolarisation field direction, decreasing the polarisation, figure 7.32[361]. Furthermore, Ba^{2+} ions replace the Na^{+} ions in the A-sites of the 5KNN due to its large ionic size, which creates local electric and elastic fields caused by the difference in valence and ionic radius. The random fields produced by the local electric and elastic fields break the long-range alignment, leading to the generation of polar nano-regions, which increase in number with an increase in the level of BNNO dopant and that degrade the polarisation[362]. Last, but not least, according to the discussion in section 7.5, as the level of BNNO dopant is raised, the ceramic experiences an orthorhombic – tetragonal phase transition. The 5KNN, 5KNN-2BNNO and 5KNN-4BNNO compositions had an orthorhombic structure, whilst the 5KNN-6BNNO, 5KNN-8BNNO and 5KNN-10BNNO compositions were tetragonal. The orthorhombic phase contains 60°-, 90°-, 120°- and 180°- domains, whereas in the tetragonal phase there are mainly 90°- and 180°- domains[310] and it has been reported that oxygen vacancies tend to clamp 90° domains[363]. The unswitched or less switched 90°-domains with a clamped domain wall led to a low remanent polarisation (ferroelectric properties will be discussed in section 7.6.3) for BNNO doped 5KNN ceramics (except 5KNN-2BNNO composition). Therefore, with an increasing in the level of BNNO doping beyond y=0.02, the ferroelectric properties of KNN-based ceramics decrease.

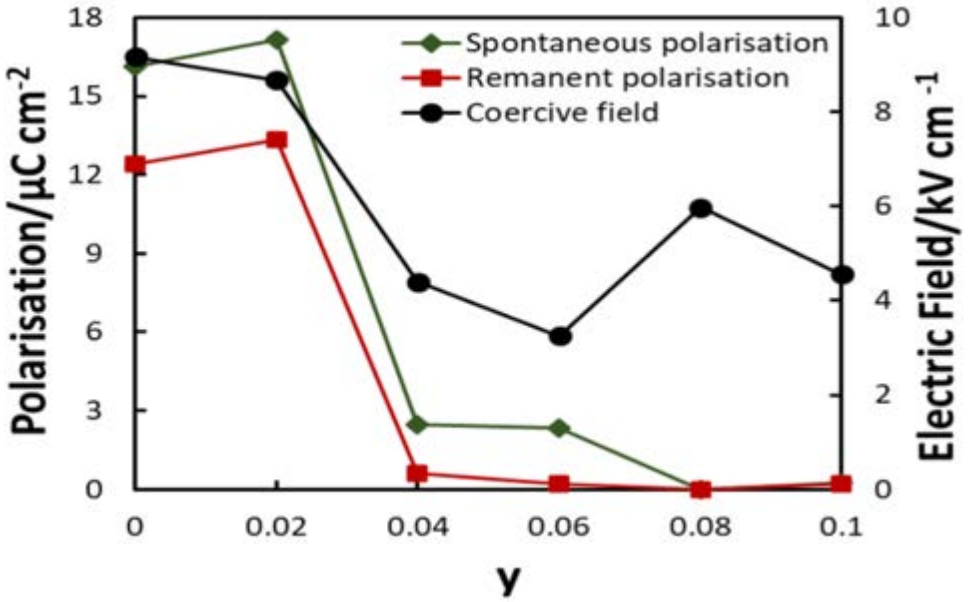

Figure 7.35 Polarisation and coercive field as a function of BNNO doping at room temperature: y=0.02 represents the 5KNN-2BNNO composition, y=0.04 represents the 5KNN-4BNNO composition, y=0.06 represents the 5KNN-6BNNO composition, y=0.08 represents the 5KNN-8BNNO composition and y=0.1 represents the 5KNN-10BNNO composition

7.6.4 Energy harvester related property characterisation

The transduction coefficient $d_{33} \times g_{33}$ and efficiency η can be utilised to evaluate piezoelectric materials for piezoelectric energy harvesting devices. These parameters have been discussed in section 6.5.4, thus no repeat discussion regarding these two parameters will provided here. Table 7.10 demonstrates the transduction coefficient and efficiency values of the doped KNN ceramics. As for the piezoelectric properties, it can be seen that the 5KNN-2BNNO composition exhibited the best average properties, with the properties deteriorating dramatically at higher doping levels.

Table 7.10 Energy harvester related properties of 5KNN and doped KNN ceramics (- means un-measurable)

Composition	$d_{33} \times g_{33}$/10^{-15} m^2N^{-1}	η/%
5KNN	4985±129.3	80±5.0
5KNN-2BNNO	1389±163.5	84±5.5
5KNN-4BNNO	159±15.4	27±19.8
5KNN-6BNNO	6±1.3	-
5KNN-8BNNO	1±0.1	-
5KNN-10BNNO	-	-

7.7 Optical property characterisation

7.7.1 Bandgap characterisation

A bandgap schematic diagram of the bandgap of 5KNN and its doped ceramics is presented in figure 7.36. The excitation process of charge carriers across the bandgap in a ferroelectric semiconductor can be easily understanding as a charge excite from the oxygen *2p* states at the VBM to the Nb *d* states at CBM. As discussed above, the BNNO doping introduce a combination of Ni^{2+} and oxygen vacancies that can lift the electronic states of the host 5KNN ceramics (lifted VBM) resulting in the reduction of bandgaps.

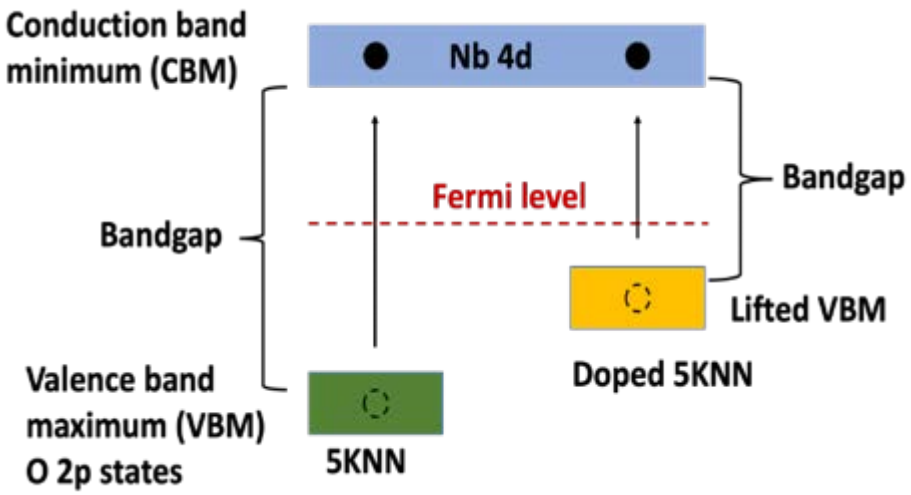

Figure 7.36 A diagrammatic representation of the bandgap for 5KNN and doped 5KNN ceramics

The study of optical properties of the doped KNN ceramics was based on the results obtained from UV-vis-NIR diffused reflectance spectroscopy, as described in section 5.4.6. It can be observed in figure 7.37 that the diffuse reflectance spectra from 300 to 850 nm obtained from 5KNN and doped 5KNN ceramics; it can be observed that the reflectance edge of the 5KNN occurs at a lower wavelength compared to the doped KNN. The band gaps for the 5KNN and doped 5KNN materials were calculated using an $F(R)\cdot h\upsilon^2$ plot (as shown in Chapter 5)[364]. The band gap energies are easily calculated from the intercept of the tangent line in a plot of $F(R)\cdot h\upsilon^2$ with the change of photon energy, as shown in figure 7.38. The resultant bandgap values are shown in table 7.11, with that for 5KNN being 3.33 eV and doping leads to narrower bandgaps; 1.60 eV for 5KNN-2BNNO and 1.47 eV for 5KNN-10BNNO. This reveals that most visible and ultraviolet parts of the solar spectrum could be absorbed by all the doped KNN compositions. The anomalies in the 5KNN-8BNNO and 5KNN-10BNNO curves, figure 7.38, may correspond to the ~1 μm intra/inter-granular pores in doped 5KNN ceramics; they may result in the reflection, refraction or scattering of the light and then display absorption peaks. In another words, these pores could trap charges that would normally be moved under lighting, whilst the additional absorption peaks at ~1-1.3 eV induced by the pores cannot create electron-hole pairs in the materials[365].

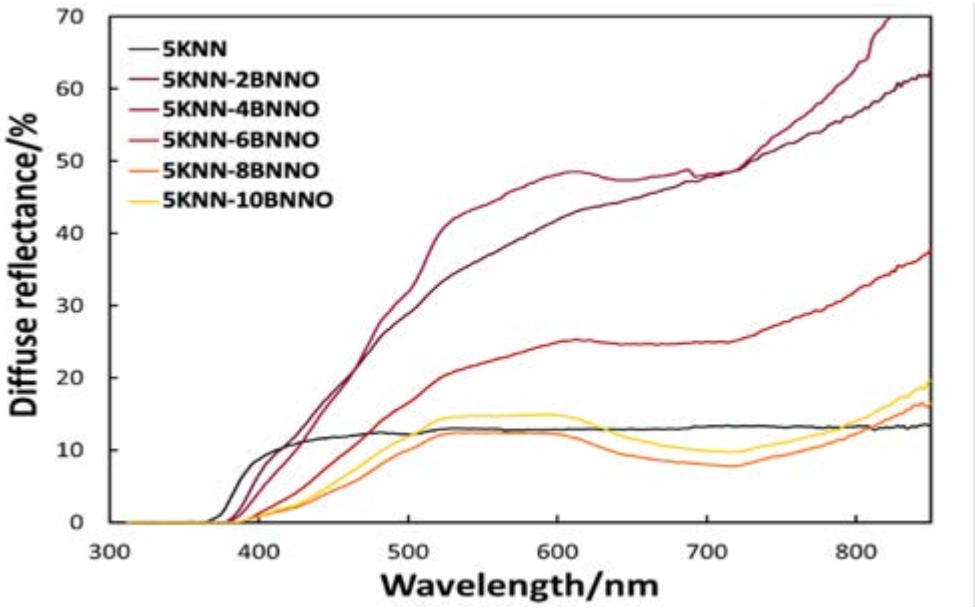

Figure 7.37 Diffuse reflectance spectra as a function of increasing wavelength for the 5KNN and doped 5KNN ceramics

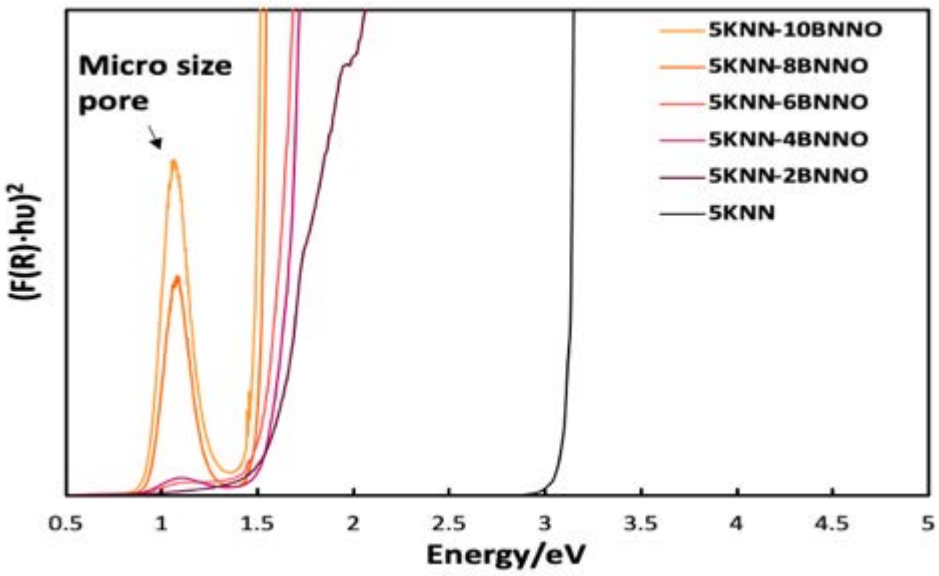

Figure 7.38 Bandgap determination for the 5KNN and doped 5KNN ceramics

Table 7.11 Bandgap values of the 5KNN and doped 5KNN materials

Composition	Bandgap / eV
5KNN	3.33
5KNN-2BNNO	1.60
5KNN-4BNNO	1.54
5KNN-6BNNO	1.53
5KNN-8BNNO	1.51
5KNN-10BNNO	1.47

7.7.2 Photo-response measurements

In order to confirm the narrowing of the bandgap for the BNNO-doped KNN ceramics, a solar cell was prepared using the 5KNN-2BNNO composition and photo-response measurements were conducted using two multi-meters and a range of load resistors from 1 kohm to 1 Mohm. The fabrication and the mechanism of the photo ferroelectric cell have described in section 5.5.1. Carbon was selected as the counter electrode and I^-/I^{3-} was employed as an electrolyte to help the transport of the photo-induced charges[298]. The 5KNN-2BNNO was in powder form.

The electric current and power with the change of voltage generated by the 5KNN-2BNNO photo ferroelectric cell under direct illumination is shown in figure 7.39. The open circuit voltage, V_{oc}, short circuit current, I_{sc}, and current density, J_{sc}, were obtained to be approximately 0.25 V, 7.5 µA and 1.52 µA cm^{-2}, respectively. Experiments involving changing the value of the parallel resistance, from 0 ohm to 1 Mohm, showed that the 5KNN-2BNNO exhibited a maximum operational power of 0.94 µW at 1 kohm. The fill factor (FF) was calculated from equation 5-13 to be 49.12%; this value is compared with data from the literature in table 7.12 below.

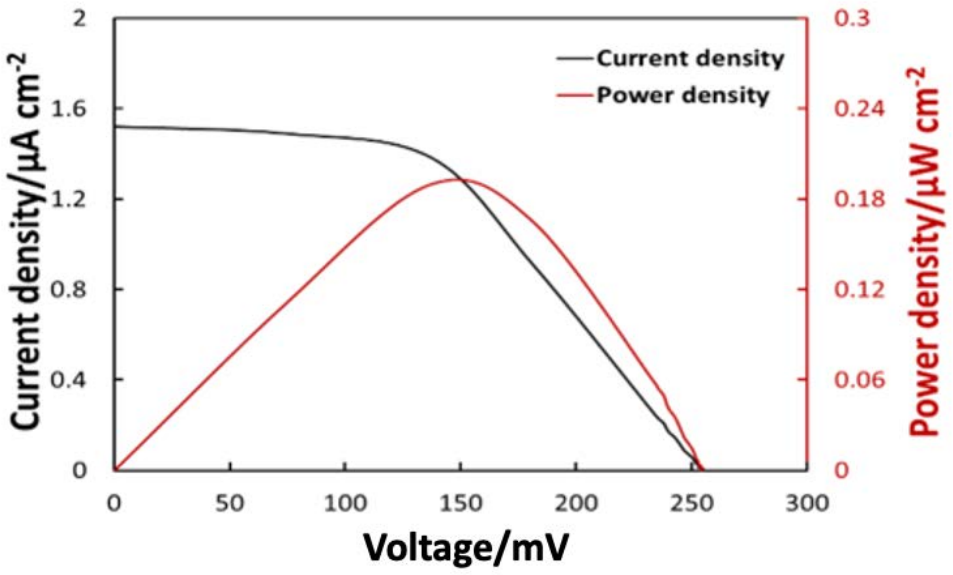

Figure 7.39 The current density (black) and power density (red) as the function of voltage of the 5KNN-2BNNO photo ferroelectric cell under direct illumination

Table 7.12 Photo-response reported in ferroelectric materials

Material	Form	V_{oc}/V	I_{sc}/μA	J_{sc}/μA cm^{-2}	P_{max}/μW	FF	Ref
5KNN-2BNNO	Powder	0.25	7.5	1.52	0.94	49.12%	This study
KN-BNN	Polycrystalline Thin film	0.0007	/	0.1	0.00007	/	[14]
KNMN	Polycrystalline thin film	5	/	0.0032	0.016	/	[366]
KNBF	Powder	0.16	/	0.24	0.0384	/	[298]
PZT	Epitaxial thin film	-0.9	0.72	/	/	41.9%	[367]
BFO	Epitaxial thin film	0.79	/	11700	/	36%	[144]
BTO	Epitaxial thin film	8	0.0002	/	0.0016	/	[71]
PLZT	thin film	0.84	/	0.025	0.021	/	[368]

Notes: KN-BNN: (1-x)($KNbO_3$)-yBa ($Ni_{0.5}Nb_{0.5}$)$O_{3-\delta}$; KNMN: ($K_{0.5}Na_{0.5}$)($Mn_{0.005}Nb_{0.995}$)O_3; KNBF: (1-y)($KNbO_3$)-y $BiFeO_3$; PZT: $Pb(Zr_xTi_{1-x})O_3$; BFO: $BiFeO_3$; BTO: $BaTiO_3$; PLZT: (Pb_xLa_{1-x}) (Zr_yTi_{1-y})O_3

As the cells are used as electrical power source, the higher open-circuit voltage, higher current density and larger power density would be good for the powder supply. It can be seen from table 7.12 that, compared with KN-BNN material, the 5KNN-2BNNO photo ferroelectric solar cell produces a higher photovoltaic output (higher open-circuit voltage, current density and power density), however, the open-circuit voltage and current density are still lower than some of the other materials listed (*e.g.* BFO film), which may be due to the fabrication method. As indicated above, the cell was produced in this work via a 5KNN-2BNNO paste, *i.e.* individual powder particles that will have been randomly aligned, whilst most of the ferroelectric solar cells (such as BFO epitaxial thin film) listed in the table were made from poled thin film or thin bulk samples where the orientation polarization may have helped to align the photo-induced carriers and then improve the final output. Therefore, the bulk hybrid energy harvester fabricated by poled 5KNN-2BNNO ceramics is needed (which will be discussed in chapter 8).

7.8 Temperature dependence of the dielectric properties of BNNO-doped KNN ceramics

Figure 7.40 shows a temperature-dependent permittivity plots from 303.15 to 773.15K at a range of frequencies from 1 to 100 kHz for the 5KNN-2BNNO ceramic sintered at 1175°C for 2 h. Two dielectric anomalies are clearly visible, at ~463 K and ~643 K, corresponding to the orthorhombic-tetragonal and tetragonal-cubic phase transitions, respectively. This is consistent with the results from the XRD and Raman studies discussed in section 7.5. The temperature-dependent permittivity plots at 1 kHz

from 303.15 to 773.15K for BNNO doped 5KNN ceramics are presented in figure 7.41. It can be observed that the materials exhibit highly depressed and diffused permittivity peak when increasing BNNO doping amount (y>0.02). Note that the highly suppressed and broaden anomalies at around 650-700K can be observed for the 5KNN-4BNNO – 5KNN-10BNNO ceramics in figure 7.41. The depression and diffusion of the permittivity curves may result from grain size effect[369,370], the relaxation characteristics of the dielectric properties caused by oxygen vacancies[359] and chemical inhomogeneity effect (core-shell structure)[371,372].

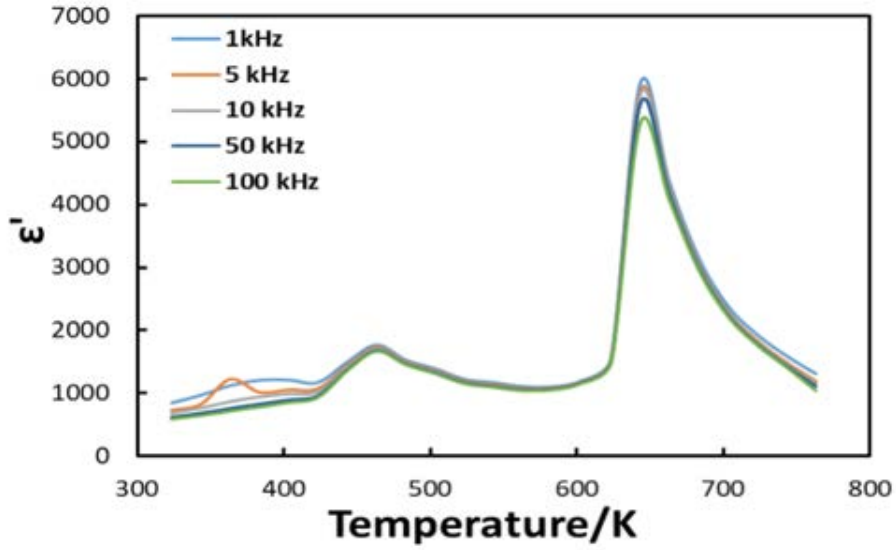

Figure 7.40 The dependence of relative permittivity on temperature of 5KNN-2BNNO ceramics sintered at 1175°C for 2 h and measured at 1-100 kHz

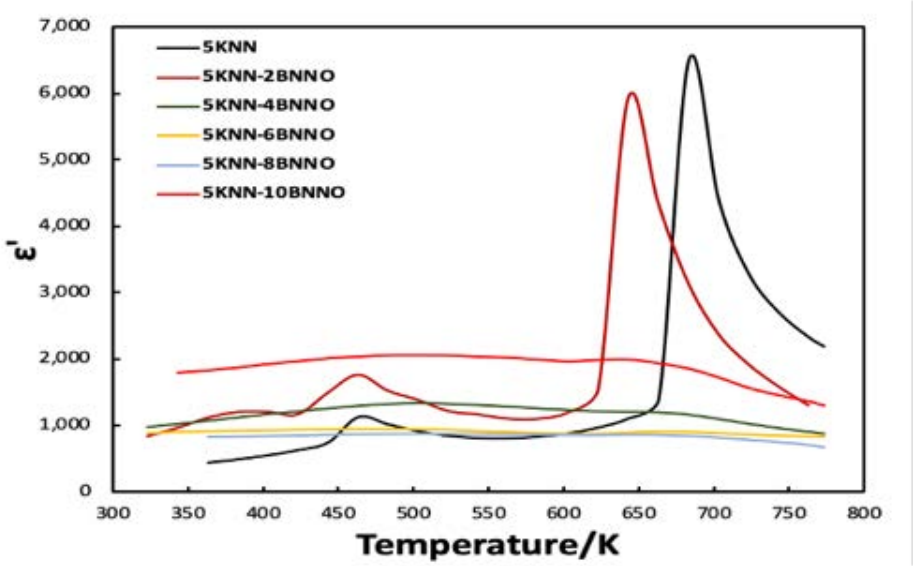

Figure 7.41 The dependence of relative permittivity measured at 1 kHz on temperature for 5KNN and for 5KNN-2BNNO, 5KNN-4BNNO, 5KNN-6BNNO, 5KNN-8BNNO and 5KNN-10BNNO ceramics, respectively, sintered at their individually optimised sintering temperatures for 2 h

As exhibited in figure 7.21, the grain size of BNNO doped 5KNN ceramics reduces with the increase in BNNO doping amount. The decreased grain size may cause the suppressed permittivity peaks. It has been proposed that with a decreasing in grain size in a polycrystalline ceramic, a raised average value of the internal stresses can be observed[369], thereby inhibiting the polarisation of 5KNN ceramics and ultimately lead to a suppression in the dielectric permittivity.

Figure 7.42 presents the complex impedance plots of Z' versus Z'' across the temperature range 410 – 500°C, and the equivalent RC circuit were also provided in the inset of figure. For polycrystalline materials, Cole-Cole curve usually has two semicircles due to the effect in grain (bulk) and grain boundary, respectively. Hence, the combination of two parallel RC circuits was used to fit the Cole-Cole plot. In figure 7.42, the dot lines represent the experimental data and the solid lines show the fitting line. As relaxation time for grain boundary is much quicker than that of bulk (grain), the semicircle at high frequency range can be ascribed to the grain while grain boundary is associated with low frequency region[373–375]. The tail of the curve may attribute to the electrode effect due to the electron transfer at the electrode-ceramics interface. It can be observed that the radius of the semicircles in figure 7.42 represents the resistance (the sum of the resistance in grain and grain boundaries) of the ceramics, indicating negative temperature coefficient (relaxation) of resistivity behaviour. Moreover, the radius also decreased with increasing BNNO dopant concentration, revealing an increasing in conductivity with an increase in temperature and BNNO dopant. This is in agreement with the discussion in section 7.6.1. Figure 7.43 provides the variation in the normalised imaginary part of the impedance (Z''/Z''_{max}) with angular frequency, for 5KNN-4BNNO to 5KNN-10BNNO ceramics. From figure 7.43, it is clear that all curves shift to higher frequencies with increases in temperature, revealing the thermal activated relaxation behaviour. This behaviour indicates that the raising temperature accelerates the hopping or migration of charge carriers (electrons, holes and ions).

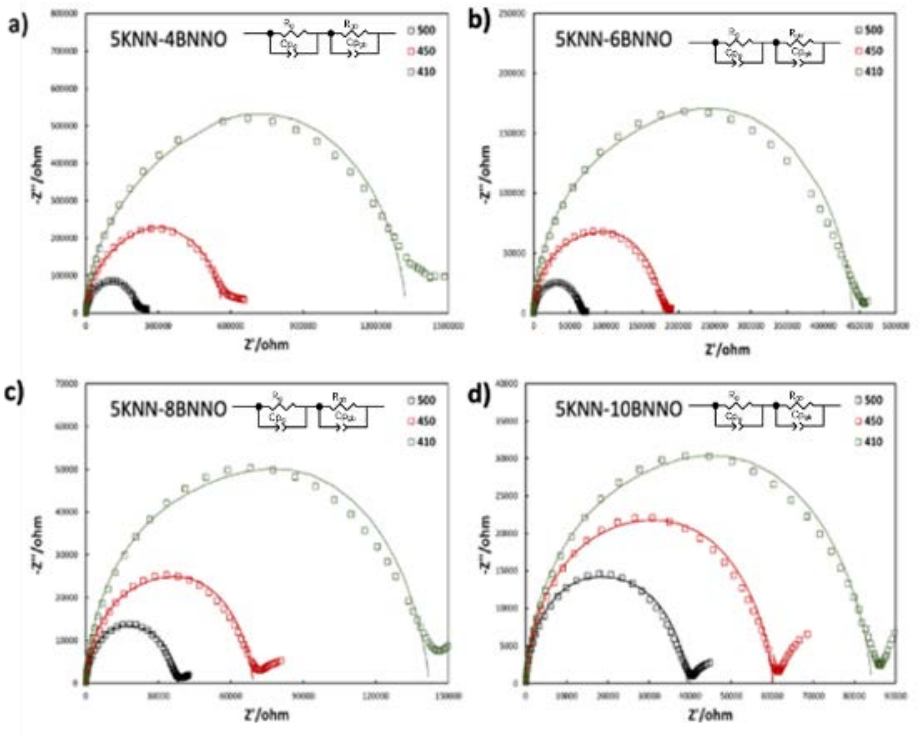

Figure 7.42 Complex impedance plots of Z' versus Z'' at different temperatures for a) 5KNN-4BNNO, b) 5KNN-6BNNO, c) 5KNN-8BNNO and d) 5KNN-10BNNO ceramics, respectively., sintered at the individually optimised sintering temperatures for 2 h. Insert circuit is the fitting equivalent RC circuit.

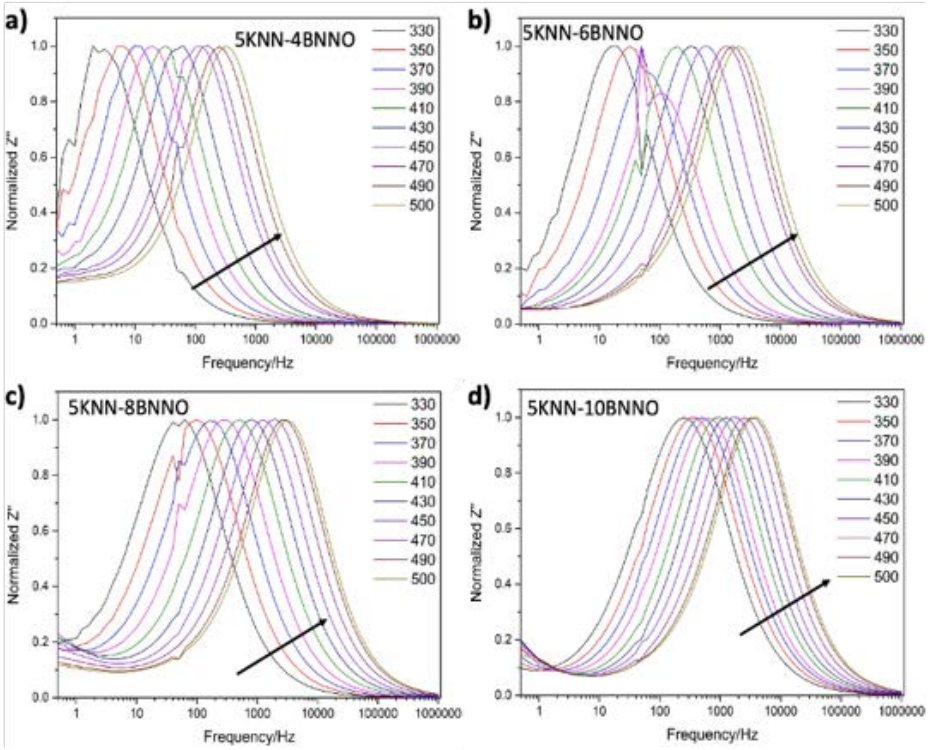

Figure 7.43 The normalized imaginary parts Z''/Z''$_{max}$ of impedance as a function of frequency for a) 5KNN-4BNNO, b) 5KNN-6BNNO, c) 5KNN-8BNNO and d) 5KNN-10BNNO ceramics, respectively., sintered at the individually optimised sintering temperatures for 2 h

Activation energy of relaxation can be calculated by the Arrhenius law[359]:

$$\omega_p = \omega_0 \cdot \exp\left(\frac{-E_a}{k_\beta T}\right) \quad 7\text{-}3$$

where ω_0, E_a, k_β and T are the constant on relaxation behaviour, activation energy of relaxation, Boltzman constant (8.617×10^{-5} eV/K) and absolute temperature, respectively.

The experimental data were fitted by equation 7-3 and the results are shown in figure 7.44 with the relaxation active energies being obtained to be 1.29 eV, 1.21 eV, 0.91 eV and 0.78 eV for 5KNN-4BNNO, 5KNN-6BNNO, 5KNN-8BNNO and 5KNN-10BNNO ceramics, respectively. It can be clear seen that the activation energy decreases with the raising of BNNO concentration. It is been reported[359] that stoichiometric ABO_3 perovskite has E_a = 2 eV, whilst the value of E_a is 1 eV for $ABO_{2.95}$ and 0.5 eV for $ABO_{2.90}$, hence, it is reasonable that the relaxation behaviours of the doped ceramics is associated with thermal process of oxygen vacancies.

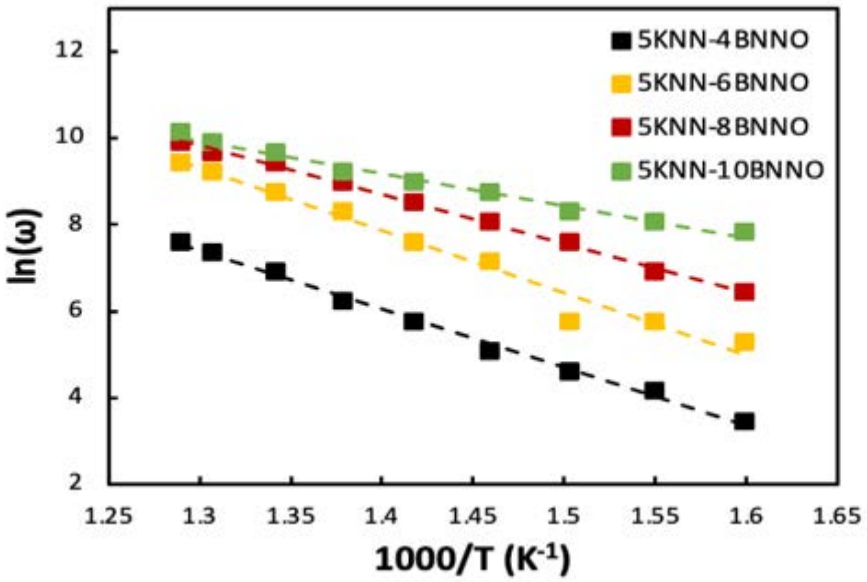

Figure 7.44 ln(ω) as a function of 1000/T for 5KNN-4BNNO, 5KNN-6BNNO, 5KNN-8BNNO and 5KNN 10BNNO ceramics, respectively. The dotted lines are a fit to the Arrhenius law.

Similarly, activation energy of conductivity can be also calculated by the Arrhenius law[359]:

$$\sigma_{ac} = \sigma_0 \cdot \exp\left(\frac{-E_{con}}{k_\beta T}\right) \quad 7\text{-}4$$

where σ_0 and E_{con} are the constant on σ_{ac} and activation energy of conductivity, respectively.

The experimental data were also fitted by equation 7-4 and the results are shown in figure 7.45 with the conductivity active energies being obtained to be 0.46 eV, 0.70 eV, 0.87 eV and 0.91 eV for 5KNN-4BNNO, 5KNN-6BNNO, 5KNN-8BNNO and 5KNN-10BNNO ceramics, respectively. Compared with relaxation energy, when BNNO doping amount is lower than 6 mmol, the E_a is larger than E_{con}. With increasing of BNNO doping, the E_{con} is gradually increasing and when BNNO doping is higher than 8 mmol, the Econ is larger than E_a., indicating the relaxation is dominated by the short-range hopping of oxygen vacancies. It is known that the activation energy of single-ionised oxygen vacancies was about 0.3-0.5 eV and ~1 eV for double-ionised oxygen vacancies[359]. Hence, for low BNNO doping, the conductivity process is governed by single-ionised oxygen vacancies and for high BNNO doping, the conductivity process is governed by double-ionised oxygen vacancies.

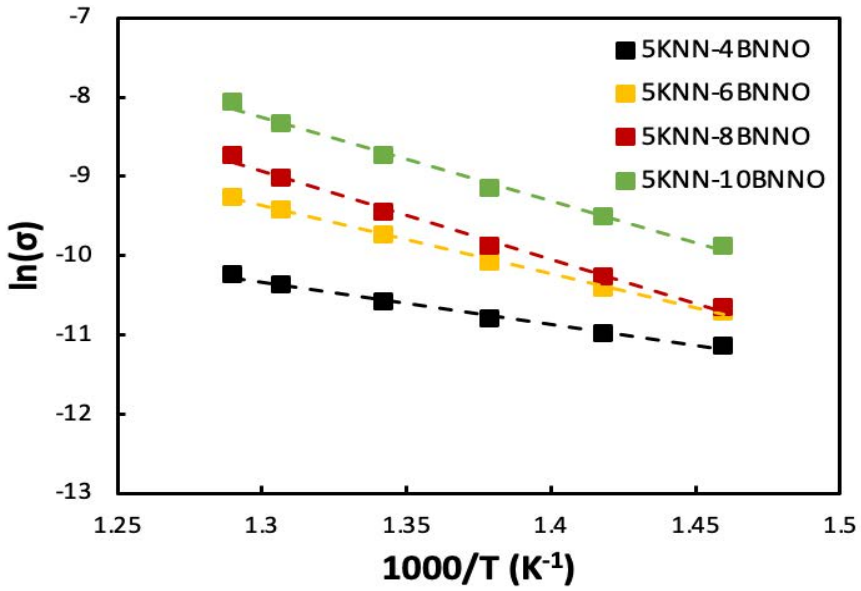

Figure 7.45 ln(σ) as a function of 1000/T for 5KNN-4BNNO, 5KNN-6BNNO, 5KNN-8BNNO and 5KNN-10BNNO ceramics, respectively. The dotted lines are a fit to the Arrhenius law.

The chemical inhomogeneity is also a reason to cause the suppression and broadening of the permittivity peaks[371,372]. As mentioned in section 7.3.1, the dopants tend to segregate along the grain boundaries, resulting in the inhibition of the grain growth. The SEM image and EDS elemental line map across the entire grain shown in figure 7.9 also proved this. A composition gradation can produce the multiple Curie points and additional Curie peaks from different compositional regions can be observed[372]. The suppressed permittivity peak at around 650 – 700K occurs at similar temperature to the Curie temperature of the 5KNN composition. Hence, the SEM-EDS line mapping, in figure 7.9, and the peak position in the permittivity-temperature curve, in figure 7.41, confirm the core of the grain

consisted of pure 5KNN. The ferroelectric long-range interactions of the 5KNN composition were disrupted by non-ferroelectric grain boundaries, which could also explain the peak broadening observed for the high BNNO doped 5KNN ceramics with y>0.02.

7.9 Summary

In the work reported in this chapter, the sintering conditions of doped KNN ceramics were initially optimised and then the structural, dielectric, piezoelectric, ferroelectric and optical properties were measured and discussed. The findings of this chapter can be summarised as follows:

1. The addition of BNNO to 5KNN ceramics meant that a higher sintering temperature was required but also that density was improved and grain growth was suppressed. The maximum sintering temperature that could be used, however, was restricted by the occurrence of Ni ex-solution at >1180°C.
2. The sintering conditions required for 5KNN-2BNNO ceramics was optimised using both single-stage sintering, SSS, and two-stage sintering, TSS, though it was found that the former was sufficient for the doped KNN ceramics. The optimised SSS sintering temperatures were: 1175°C, 1185°C, 1190°C, 1195°C and 1195°C for the 5KNN-2BNNO, 5KNN-4BNNO, 5KNN-6BNNO, 5KNN-8BNNO and 5KNN-10BNNO compositions, respectively
3. With increasing BNNO dopant concentrations and measured at room temperature, the doped KNN ceramics underwent a phase transition from orthorhombic phase (5KNN-2BNNO and 5KNN-4BNNO compositions) to tetragonal phase (5KNN-6BNNO, 5KNN-8BNNO and 5KNN-10BNNO compositions), a result that was corroborated by both XRD and Raman spectroscopy. This enabled a structural phase diagram to be constructed from RT to 500°C across the full doping range investigated (5KNN and BNNO doped 5KNN).
4. The piezoelectric and ferroelectric properties of sintered ceramics of the 5KNN-2BNNO composition were improved compared to undoped 5KNN. However, both sets of properties degraded for the higher dopant concentrations from 5KNN-4BNNO, 5KNN-6BNNO and 5KNN-8BNNO ceramics and eventually reducing to zero for 5KNN-10BNNO ceramics. It was proposed that this resulted from the opposing effects of defect dipole polarisation and oxygen vacancy pinning. Consequently, in order to achieve a trade-off between ferroelectricity and the reduction in the band gap, a precisely controlled doping concentration needed to be maintained and the composition of 5KNN-2BNNO was determined to be the best value.

5. The doping of 5KNN by BNNO was an effective strategy to narrow the bandgap of the sintered 5KNN ceramics, facilitating the transfer of charge from the oxygen *2p* states at VBM to the transition-metal *d* states at CBM.
6. The 5KNN-2BNNO composition was selected to be used to prepare a photo ferroelectric cell. A short-circuit current of 7.5 μA and open-circuit voltage of 0.25 V were measured, confirming the narrow band gap nature of the doped KNN ceramics.
7. The occurrence of suppressed and broadened permittivity peaks as a function of temperature for the doped 5KNN ceramics (y=0.02) was proposed to be due to the grain size effect, relaxation behaviour owing to the formation of oxygen vacancy and the chemical inhomogeneity.

Chapter 8. Energy harvester fabricated by KNN-based ceramics

8.1 Introduction

Chapter 3 has reviewed and summarised the principles and structures of HEHers. In the last two chapters, the results from the systematic investigation of 5KNN and BNNO doped 5KNN ceramics were reported, including the optimisation of the sintering conditions, phase transitions and functional properties. The next logical step was to investigate how these ceramics would perform in an energy harvester. Consequently, this chapter discusses the performance of two compositions, 5KNN and 5KNN-2BNNO, in laboratory-made energy harvesters. The fabrication and testing methods of the cantilever-based energy harvester were provided in chapter 5; this chapter initially compares the energy harvester related parameters of the 5KNN and 5KNN-2BNNO ceramic discs and then compares and discusses the energy output of the energy harvesters themselves.

8.2 Property comparison of 5KNN and 5KNN-2BNNO ceramic discs

As the doped KNN is intended to replace 5KNN as a potential candidate for hybrid energy harvesting applications, it is crucial to compare here the functional properties of both compostions with respect to energy harvesting, including dielectric, piezoelectric, ferroelectric and optical properties. 5KNN-2BNNO ceramics sintered at 1175°C for 2 h were selected as the best doped composition (see chapter 7) and were compared with 5KNN ceramics two-step sintered at 1120°C for 10 min & 1070°C for 10 h (see chapter 6). Figure 8.1 shows the property comparison of the two types of ceramic with respect to ε_r, $tan\delta$, d_{33}, k_p, k_{eff} and Q_m, figure 8.2 shows the comparison of energy harvester-related parameters with respect to u and η, whilst figure 8.3 shows the comparison of P_r, band gap and Curie temperature, which have been extracted from tables 6.4, 6.5, 7.8, 7.9, 7.10 and 7.11 and figures 6.19, 6.20, 7.31, 7.32, 7.35, 7.36, 7.39 and 7.42.

In general, it can be seen that the 5KNN-2BNNO exhibited improved dielectric and piezoelectric properties. Theoretically, a higher dielectric permittivity (ε_r) and mechanical quality fator (Q_m) can yield a higher resonant output power for a piezoelectric energy harvester[273] and it can be seen from figure 8.1 that the 5KNN-2BNNO shows consistently better properties, though the differences are small for the coupling factors (~2% difference in effective coupling factor, k_{eff}, and ~8% difference in planer coupling factor, k_p) and dielectric loss (<1% difference in $tan\ \delta$). Figure 8.2 compares the energy density and energy conversion efficiency of the two ceramics, with the doped KNN showing a higher

energy conversion efficiency but much lower energy density. The higher energy density value for the 5KNN yields an obvious advantage for vibration energy harvesting applications in anti-resonance and it may be due to the ceramic's lower dielectric permittivity ($g_{33} = d_{33}/\varepsilon_{33}$), despite the doped ceramic exhibiting a higher piezoelectric response (figure 7.9). A comparison of the remanent polarisation, optical properties and Curie temperature are displayed in figure 8.3 a), b) and c), respectively. The 5KNN-2BNNO shows a larger remanent polarisation and narrower band gap than the parent 5KNN, indicating that the doped ceramics does have potential to be used as a hybrid energy harvester. Note, however, that the doped 5KNN possesses a lower Curie temperature, figure 8.3 c), indicating a narrower operating working temperature range.

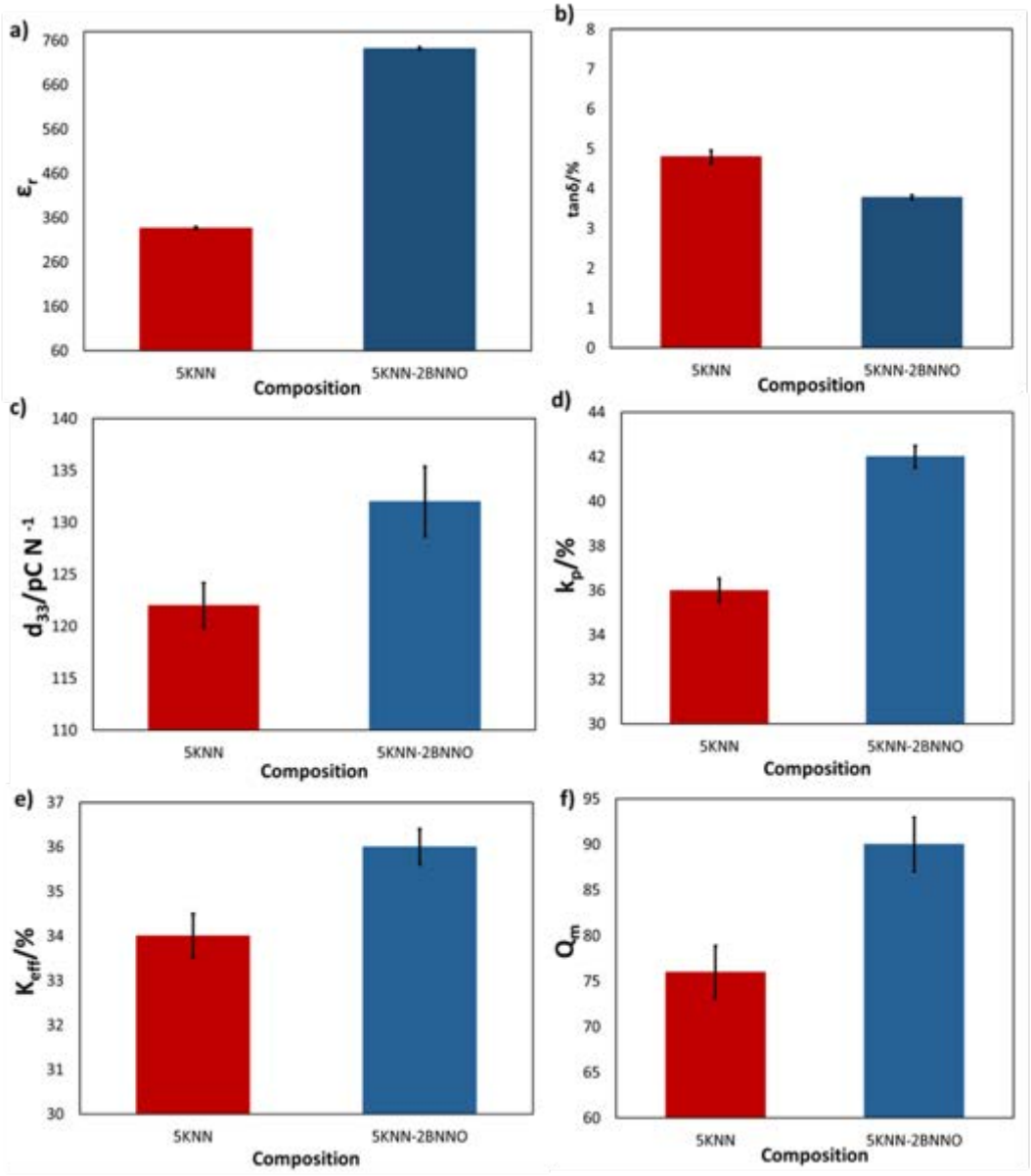

Figure 8.1 Property comparison of 5KNN sintered at 1120°C for 10 min & 1070°C for 10 h and 5KNN-2BNNO sintered at 1175°C for 2 h, a) ε_r, b) t*an* δ, c) d_{33}, d) k_p, e) k_{eff} and f) Q_m

Since all of the parameters discussed above could have a significant influence on practical energy harvestering performance, it was difficult to predict the performance of the resulting energy harvester. Moreover, there are two different energy harvesting convertion mechnisms in a 5KNN-2BNNO hybrid energy harvester, *i.e.* vibration and illumination.

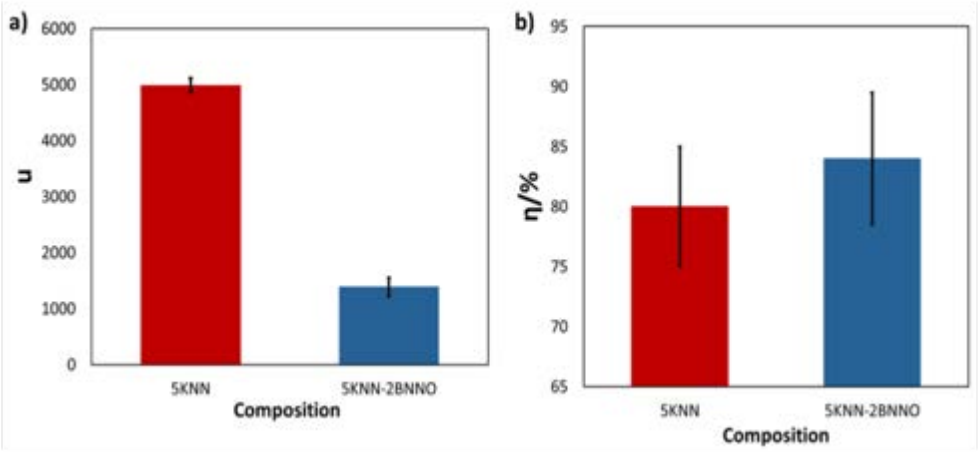

Figure 8.2 Property comparison 5KNN ceramics sintered at 1120°C for 10 min & 1070°C for 10 h and 5KNN-2BNNO ceramics sintered at 1175°C for 2 h of a) transduction coefficient and b) energy conversion efficiency of

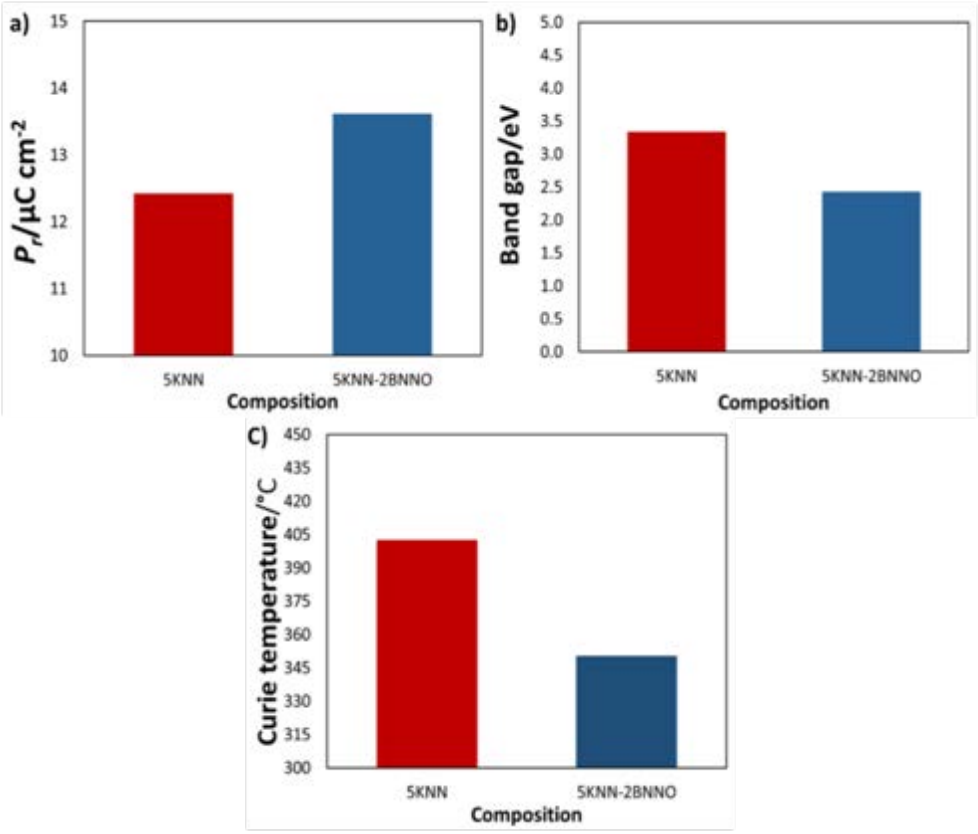

Figure 8.3 Property comparison of 5KNN ceramics sintered at 1120°C for 10 min & 1070°C for 10 h and 5KNN-2BNNO ceramics sintered at 1175°C for 2 h a) remanent polarisation, b) band gap and c) Curie temperature

8.3 Energy harvesting performance of KNN-based energy harvesters

8.3.1 5KNN vibrational energy harvester

Two 5KNN piezoelectric elements sintered by SSS (at 1120°C for 2 h) and by TSS (at 1120°C for 10 min & 1070°C for 10 h) were used to fabricate vibrational energy harvesters to compare the effect of sintering methods on device performance. Figure 8.4 shows their variation in the open-circuit voltage with time, with the higher value of the open-circuit peak voltage, 1.68 V, being obtained for the TSS-densified piezoelectric element. This suggests that the improved microstructure and density observed will lead to superior energy generation performance.

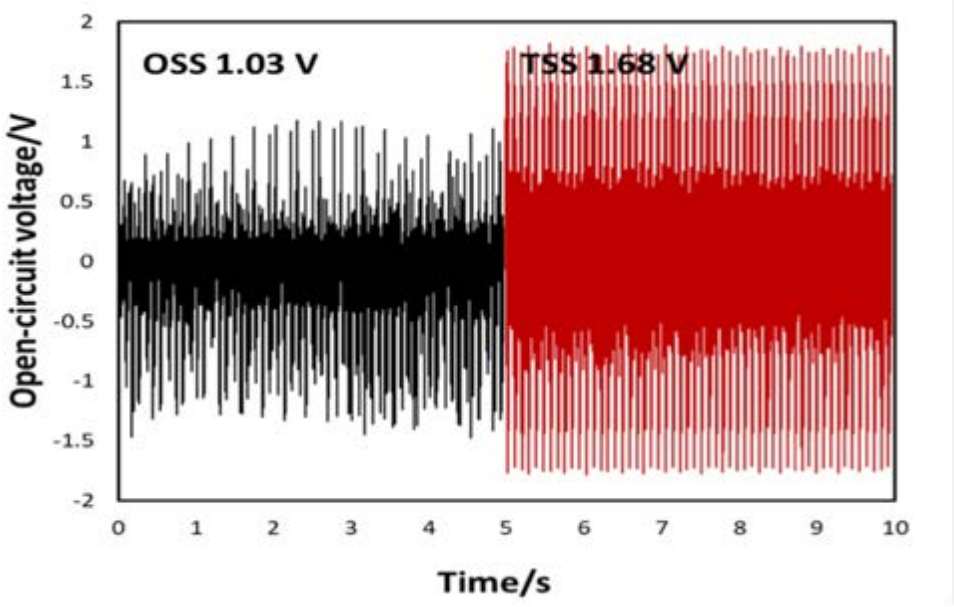

Figure 8.4 Measured open-circuit voltage of bulk 5KNN energy harvester fabricated via SSS and TSS

To measure the output power, the energy harvesters were connected in parallel with variable resistors and the output power can be calculated from equation 5-16; figures 8.5 and 8.6 show the peak-output voltage and output power as a function of load resistance. As the latter increased, the output voltages of both energy harvesters show a slowly increasing trend, with the TSS-based energy harvester displaying a higher value. With both energy harvesters, the relationship between power density and load resistance shows a trend of increasing first and then decreasing. The maximum power density was obtained at 540 kΩ for both; the maximum values being 107.3 and 56.5 μW cm^{-3} for the TSS- and SSS-based harvesters, respectively. Thus, the results reveal that the energy harvester made from the lead-free 5KNN ceramic using TSS for densification demonstrates promising performance.

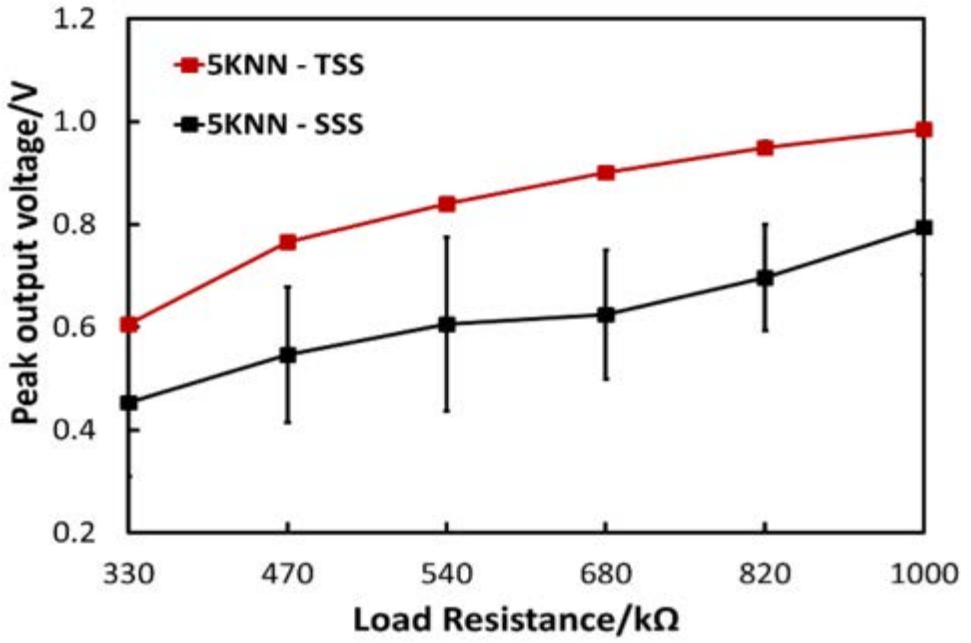

Figure 8.5 Comparison of measured open-circuit voltage of 5KNN energy harvesters fabricated by SSS and TSS as a function of load resistance

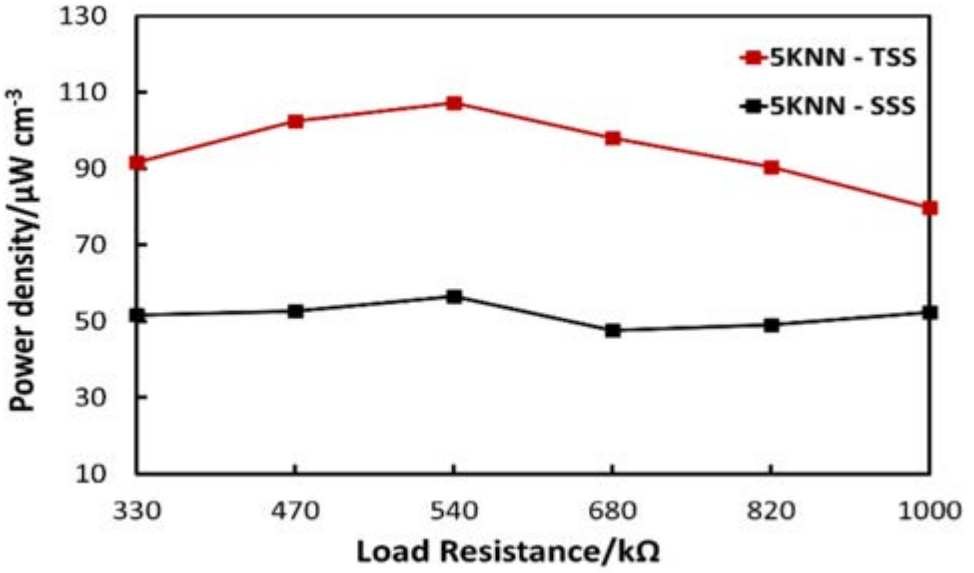

Figure 8.6 Comparison of the power density of 5KNN energy harvesters fabricated by SSS and TSS as a function of load resistance

8.3.2 5KNN-2BNNO photo-vibrational energy harvester

The theoretical model of a photo-vibration HEHers is illustrated in figure 8.7. After electrical poling, the ferroelectric dipoles in 5KNN-2BNNO ceramics are aligned parallel or close to the direction of the external electric field. These spontaneous electric dipoles (P_r, marked as green ellipses in figure 8.7)

automatically induce an internal electric field ($E_{int.}$, marked by the dotted arrow) that is in the opposite direction to the applied electric field. When the 5KNN-2BNNO hybrid energy harvester was illuminated, the photo-induced electron-hole pairs will have drifted due to the $E_{int.}$, leading to the observed rise in the recorded open-circuit voltage. Due to the wide bandgap for 5KNN ceramics, this phenomenon will not have been observed in the energy harvesters made from this ceramic.

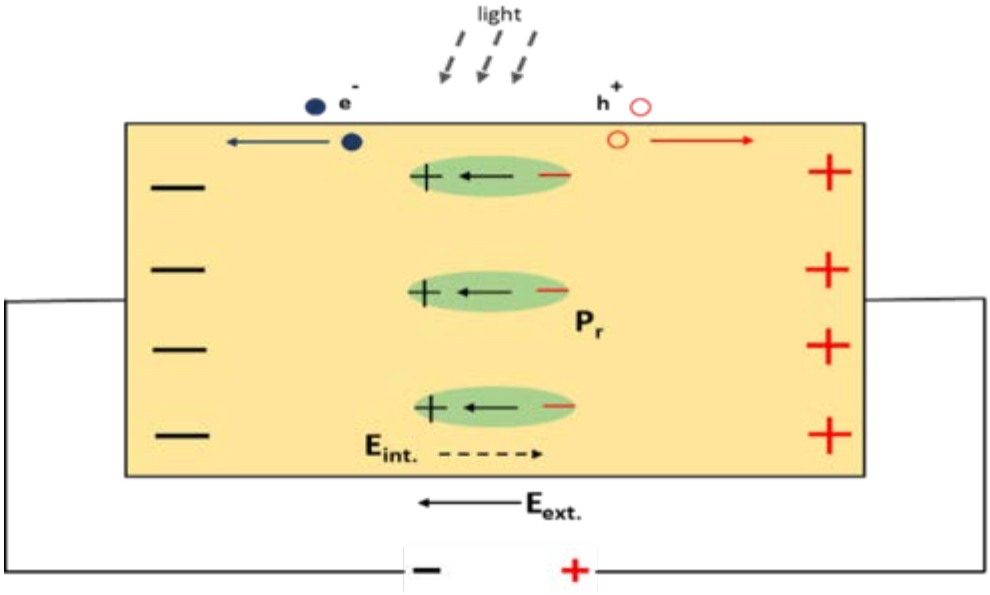

Figure 8.7 Schematic diagram of a hybrid energy harvester, reproduced from ref [16]

5KNN-2BNNO ceramics sintered at 1175°C for 2 h were selected to prepare the HEHer. In order to observe the coupling between piezoelectric and photovoltaic effects, the hybrid energy harvester was firstly assessed using vibration only (V) and then a combination of vibration and illumination (V&I) and the root mean square (RMS) open-circuit peak voltages generated are shown in figure 8.8. It can be observed from figure 8.8 that it increased from ~1.26 V to ~1.77 V when the illumination was turned on. 5KNN-based energy harvester fabricated using TSS was also tested under the combination of vibration and illumination and the results are presented in figure 8.9. The open-circuit voltage values for the 5KNN energy harvesters with and without illumination were similar, with only a 0.02 V difference, revealing that illumination doesn't affect the output of the energy harvester. As already noted above, the 5KNN-2BNNO energy harvester demonstrated a comparable open-circuit voltage, 1.77 V, when exposed to both vibration and illumination, whilst it was much lower, 1.26 V, when exposed only to vibration.

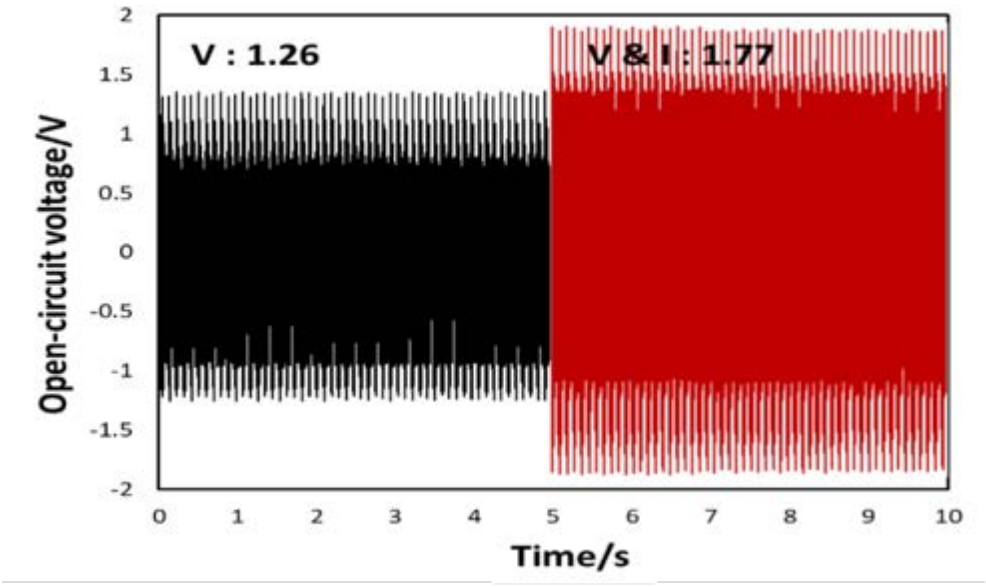

Figure 8.8 The photo- and piezo open-circuit voltage of the 5KNN-2BNNO energy harvester generated using vibration and illumination; V: vibration only, V&I: vibration & illumination

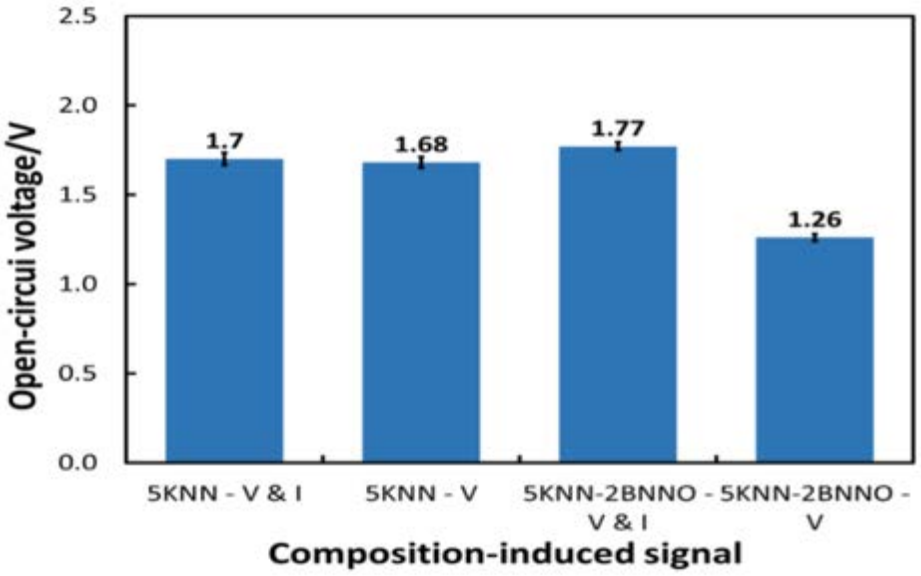

Figure 8.9 Dependence of RMS open-circuit voltage of 5KNN and 5KNN-2BNNO energy harvesters induced by 10 Hz vibration and illumination; V: vibration only, V&I: vibration & illumination

As discussed in Chapter 7, the addition of BNNO introduced oxygen vacancies into the 5KNN system lead to a large leakage current. However, since the piezoelectric energy harvester is a capacitive voltage source, the leakage current will affect the voltage across the capacitor's geometry[360] and this could be the reason for the reduced open-circuit voltage in the 5KNN-2BNNO vibrational energy harvester. In the presence of illumination, the electronic polarisation changes the magnitude and direction of the ionic polarisation due to the displacement between Nb^{5+} / Ni^{2+} and O^{2-}; the light

stimulates free charge carriers, altering the displacement current and polarisation. In addition, the light can modify trap levels, fill holes and compensate free charge carriers in piezoelectric elements[376–378]. This probably explains why an ~0.51 V higher open-circuit voltage was obtained under illumination.

The variation of the output voltage and power density when measured using various resistance loads are shown in figures 8.10 and 8.11, respectively. Similar to the comparison of the open-circuit voltage, the 5KNN-2BNNO hybrid energy harvester exhibited the highest peak output voltage and power density at all values of resistive load. From figure 8.10, the peak output voltages of the 5KNN-2BNNO energy harvester (both piezoelectric energy harvesting and hybrid energy harvesting) and the 5KNN piezoelectric energy harvester increased with increasing load resistance. It can be observed in figure 8.11 that the 5KNN-2BNNO hybrid energy harvester also demonstrated higher output power densities than those of the 5KNN or 5KNN-2BNNO piezoelectric-only energy harvesters. Based on impedance matching theory[379], the maximum output power will be achieved when the loaded resistor matches the impedance of the devices. The maximum values were observed at 330 kΩ and 540 kΩ for the 5KNN-2BNNO and 5KNN energy harvesters, respectively, indicating the lower impedance of the 5KNN-2BNNO piezoelectric elements. This fits with the argument used in previous chapters that doping with BNNO introduces oxygen vacancies and results in an increase in conductivity and decrease in impedance. In terms of the comparable open-circuit voltage for the 5KNN-2BNNO hybrid energy harvester and 5KNN piezoelectric energy harvester, the enhancement in the energy density may be due to less dissipation by the 5KNN-2BNNO element.

Thus, it can be concluded that 5KNN-2BNNO is a good potential candidate for use as a hybrid energy harvester with increased open-circuit voltage and power density, however the 5KNN ceramic shows better performance when used in a single-vibration energy harvester.

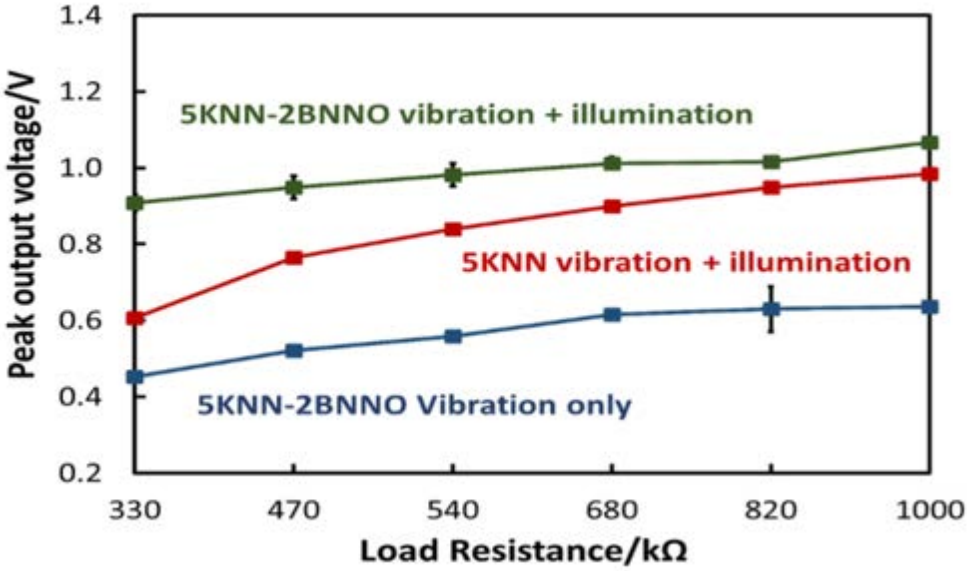

Figure 8.10 Dependence of RMS peak output voltage with various load resistances for the 5KNN and 5KNN-2BNNO energy harvesters induced by vibration and illumination

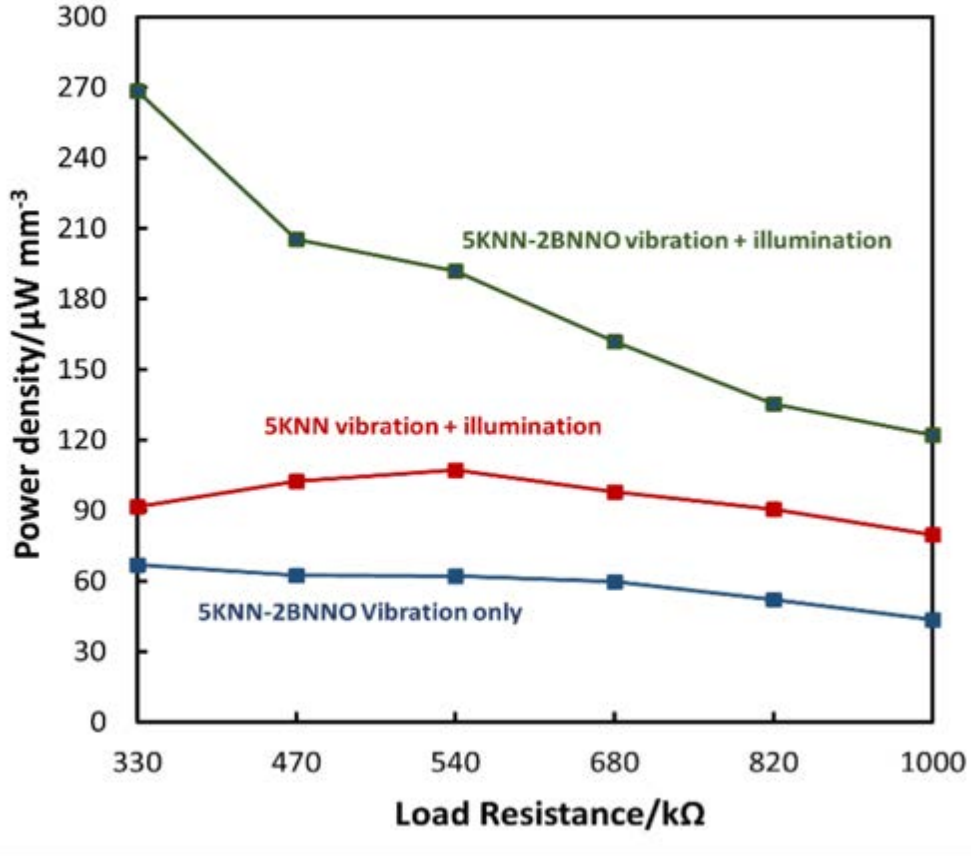

Figure 8.11 Dependence of output power density on various resistances for the 5KNN and 5KNN-2BNNO energy harvesters induced by vibration and illumination

8.4 Summary

In this chapter, the energy harvesting performance of 5KNN ceramics densified by both SSS and TSS approaches and 5KNN-2BNNO ceramics densified using SSS have been evaluated by assembling them into energy harvesters. The findings of this chapter can be summarised as:

1. With a higher energy conversion efficiency and energy density, the undoped 5KNN ceramics fabricated by TSS yielded an energy harvester with an open-circuit voltage of 1.68 V and power density of 107.3 $\mu W\,cm^{-3}$. These results suggest that TSS could be an effective approach to solving the difficulties in achieving high density 5KNN ceramics and hence facilitating the fabrication of high-performance KNN-based devices.
2. A 5KNN-2BNNO-based hybrid energy harvester can deliver a higher output under joint vibration and illumination conditions. The leakage current induced by the oxygen vacancies generated by the doping hindered the performance of the 5KNN-2BNNO as a vibrational energy harvester, however when illumination was also used it could effectively modify the trap level, fill holes and compensate for free charge carriers in the piezoelectric elements to enhance the performance of the HEHer. In addition, the lower impedance of the 5KNN-2BNNO boosted the higher power density.
3. Based on the results, 5KNN-2BNNO ceramics have good potential be used in hybrid energy harvesters with improved performance. However, the 5KNN-based piezoelectric energy harvester showed better performance as a single, vibration-only device.

Chapter 9. Conclusions and future work

9.1 Conclusions

Chapter 4 saw the main aims and objectives for the thesis set out, the central focus being the processing and characterisation of KNN-based multifunctional ceramics and their subsequent use in energy harvesting devices. This resulted in an intensive study of the sintering required, the phase transitions that occur, the electrical and optical characterisation of the 5KNN and doped 5KNN as well as the performance of the subsequent energy harvesters made. The results yield more detailed understanding of sintering in the 5KNN system, as well as the effect of BNNO doping, and the correlation between the doping amount and the resulting piezoelectric (ferroelectric) and optical properties.

To start, the 5KNN composition was used to study the impact of sintering conditions on the microstructure and functional properties. The 5KNN calcined powders demonstrated the perovskite orthorhombic phase at room temperature as expected and the mean crystallite size range of the powder was 300 nm – 500 nm, although the overall particle size was about 1 – 2 μm. Two solid-state sintering processes were used to fabricate the 5KNN ceramics, single-step sintering (SSS) and two-stage sintering (TSS). Samples fabricated by using SSS had a maximum sintered density of 89 – 91%. The microstructures of the 5KNN ceramics fabricated by SSS were largely homogenous with a slightly finer average grain size of ~10 μm when the sintering temperature was below the formation temperature of the K-rich liquid phase (*i.e.* <1110°C). However, when the sintering temperature was higher than this, the mean grain size increased to ~16 μm and ~21 μm at 1120°C and 1140°C, respectively, revealing that fast abnormal grain growth occurred when a large amount of K-rich liquid-phase is generated. Therefore, it was shown that the K-rich liquid phase can demonstrate a significant impact upon the densification of 5KNN ceramics. From the observation of the microstructure and information found in the literature it was concluded that the low sintering density, and hence high porosity, were mainly caused by the rapid abnormal grain growth and the resulting oriented grain growth together with the evaporation of sodium and potassium, all of which restrict densification in 5KNN. Therefore, it was concluded that the strategy for improving the sintering of KNN required: i) avoiding the occurrence of elongated grains, ii) controlling the amount of K-rich liquid phase, and iii) reducing the evaporation of sodium and potassium.

The two-step sintering process utilises a short dwelling time at a high sintering temperature, immediately followed by a longer soak at a lower temperature to control the amount of K-rich liquid

phase and avoid the evaporation of Na and K, these then suppress the grain growth, to increase the sintering density. From the investigation of the first sintering step for 5KNN ceramics, the requirements can be summarised as needing: i) a high density (>75%), ii) a fine grain size and iii) suitable liquid phase (K-rich liquid phase) amount. On this basis, the first step sintering temperature was selected as 1120°C. From the shrinkage results for 5KNN (figure 6.4), a rapid increase in shrinkage into a largely linear shrinkage rate occurred over the temperature range 1000 – 1070°C. Thus 1030, 1050 and 1070°C were investigated as second-step sintering temperatures, with 10, 15 and 20 h soaking times. It was shown that 1070°C provided sufficient energy for diffusion, and hence densification, whilst longer soaking times of 15 h and 20 h at 1070°C caused higher evaporation of the alkali elements rather than further improvements in density. Thus, the best sintering procedure for the 5KNN ceramics was determined to be 1120°C for 10 min followed by 1070°C for 10 h, which lead to a relative density of 95% and a mean grain size of ~7 μm.

The perovskite orthorhombic phase in the calcined power was maintained in both the SSS and TSS fabricated ceramics and the phase transition temperatures were found to occur in the range 190 – 210°C for the orthorhombic to tetragonal phase transition and 400 – 430°C for the Curie temperature (ferroelectric to paraelectric change), both of which are consistent with other reports.

The improvement in sintered density and microstructure lead to improved functional properties in 5KNN piezoelectric ceramics, boosting higher measured values of relative permittivity *(ε_r)*, lower dielectric loss *(tan δ)*, and higher piezoelectric charge coefficient (*d_{33}),* planar coupling factor *(k_p)* and mechanical quality factor (Q_m). The best functional properties were achieved in 5KNN fabricated by SSS at 1120°C for 2 h; the piezoelectric charge coefficient (*d_{33})*, relative permittivity *(ε_r)* and mechanical quality factor (Q_m), being 101 pC N^{-1}, 294 and 32, respectively. The values were enhanced to a maximum of 122 pC N^{-1}, 337 and 76, respectively, for the KNN ceramics densified by optimum two-step sintering procedure (1120°C/10 min/1070°C/10 h). The higher $d_{33} \times g_{33}$ values (4985 $\times$ 10^{-15} m^2 N^{-1}) and energy conversion efficiency (80%) were also obtained by the KNN ceramics densified optimum TSS sintering procedure, compared with the values (3925 $\times$ 10^{-15} m^2 N^{-1} and 58%, respectively) obtained by KNN ceramics densified by SSS. Therefore, it can be concluded that 5KNN ceramics sintered by two-step sintering should be more suitable for piezoelectric energy harvesting applications, benefiting from the generation of higher output than the same ceramics fabricated by single-step sintering.

To prepare 5KNN ceramics with narrow bandgap, BNNO was selected as a dopant. The influence of BNNO addition upon the sinterability of ceramics, phase transition, the resulting functional properties (dielectric, piezoelectric, ferroelectric and optical) and the performance of the subsequent hybrid energy harvester were investigated for a range of different BNNO doping levels, from y=0.02 – 0.10 composition. All the calcined BNNO-doped powders exhibited a mean crystallite size range of about 100 – 200 nm and an overall particle size of about 3 – 5 µm. It was shown that BNNO doped 5KNN compositions require a higher sintering temperature to densify, but the addition of Ba and Ni was helpful in improving the final sintered density and suppressing grain growth, thought to be due to an impurity segregation mechanism. The Ba^{2+} tended to segregate along the grain boundaries and inhibit the grain growth, allowing subsequent densification rather than grain growth in the final sintering stage. However, the sintering temperature was also limited to $\leq$1180°C by the occurrence of a Ni ex-solution process that occurred at higher temperatures, thought to be driven by the raise in concentration of oxygen-vacancy in the doped materials. The generation of oxygen vacancies due the addition of BNNO destabilizes the perovskite lattice stoichiometry, leading to the segregation and ex-solution of Ni^{2+} cations from the B-site to maintain structural stability. Thus, the sintering temperature of doped KNN ceramics needs to be carefully controlled.

SSS and TSS route were also utilised to fabricate the BNNO doped 5KNN ceramics. Comparison of the sintered density, grain size and microstructure allowed the best sintering conditions for SSS and TSS of the 5KNN-2BNNO composition to be identified; they were observed to be 1175°C for 2 h and 1180°C for 10 min and 1150°C for 10 h, respectively. After comparing the functional properties of the 5KNN-2BNNO ceramics sintered by SSS and TSS, it was observed that for the doped composition there was no need for the technically more demanding (and much slower) TSS route. Although TSS contributes to extending the sintering window, the long soaking time at the higher temperature of 1150°C appeared to cause significant sodium and potassium evaporation. Thus, a single-step sintering (SSS) schedule involving 2 h at 1175°C was selected as the basis of the sintering method for the doped 5KNN.

The addition of Ni^{2+} and Ba^{2+} in the KNN structure expands the unit cell of 5KNN and generates oxygen vacancies that change the local distortion of the perovskite structure, resulting in phase transitions. Room temperature XRD, temperature dependent Raman measurements of (1-y) 5KNN – (y) BNNO (y=0-0.10) compositions were investigated to identify the phase transition behaviour with respect to the BNNO addition. A composition-temperature-structural phase diagram of (1-y) 5KNN – (y) BNNO (y=0-0.10) was constructed. The primary phases at room temperature in BNNO-doped 5KNN ceramics were identified as being orthorhombic in the 5KNN-2BNNO & 5KNN-4BNNO compositions and the

tetragonal phase in the 5KNN-6BNNO to 5KNN-10BNNO compositions which agree well with other literature. The BNNO doping decreases the phase transition temperatures for the orthorhombic to tetragonal phase ($T_{O\text{-}T}$) and the tetragonal to cubic transition (T_c), meaning a narrower working temperature range for these materials.

Overall, the improved piezoelectric and ferroelectric properties only occurred in the low BNNO doping level (5KNN-2BNNO, y=0.02). With further BNNO additions (y=0.4-0.10), the ceramics demonstrated increased relative permittivity and dielectric loss, and decreased piezoelectric and ferroelectric properties, which may correlate with the consequent phase transition and formation of oxygen vacancies. As the BNNO doping level increased, 5KNN gradually transformed from an orthorhombic phase to a tetragonal phase, which can be interpreted as causing a first-order dielectric relaxation phenomena thus increasing the relative permittivity. Moreover, the addition of Ni^{2+} generates oxygen vacancies to keep neutrality and the $(Ni_{Nb}''' - V_{\ddot{O}})'$ defect dipoles would tend to pull towards the direction of the depolarisation field, degrading the macro polarisation. Furthermore, accumulated oxygen vacancies may tend to segregate along the 90°-domain boundaries and pin the re-orientation of the 90°-domains. It was observed that the maximum remanent polarisation was obtained in the 5KNN-2BNNO composition (13.62 μC/cm^2), which was higher than that of the undoped 5KNN composition (12.42 μC/cm^2). However, on further increasing the level of BNNO dopant, the polarisation decreased to just 0.007 μC/cm^2 in the 5KNN-10BNNO composition. Although BNNO doping helped to narrow the bandgap, from 3.13 eV in 5KNN ceramics to 1.60 eV in 5KNN-2BNNO and 1.47 eV in 5KNN-10BNNO, the degradation of the piezoelectric and ferroelectric properties was too severe to be accepted.

Compared with the 5KNN ceramics, 5KNN-2BNNO possessed a higher energy conversion efficiency, but a lower $g_{33} \times d_{33}$ value. The higher energy density value indicated that the undoped 5KNN exhibited an obvious advantage for vibration energy harvesting applications in anti-resonance. The photo-ferroelectric cell made from 5KNN-2BNNO exhibited a high open-circuit voltage (0.25 V) and short-circuit current (7.5 μA), demonstrating that it has the capability to be used as a photovoltaic-ferroelectric material.

Cantilever-type energy harvesters were prepared using the undoped 5KNN ceramics single stage sintered (SSS) at 1120°C for 2 h and two-stage sintered (TSS) at 1120°C for 10 min and 1070°C for 10 h and then tested as vibrational energy harvesters. Under 10 Hz vibration, the TSS-sintered 5KNN energy harvester with a 3.0 g tip mass generated a larger open-circuit voltage (1.68 V) and a higher

output power density (107.3 μW/cm^3) than the SSS-fabricated 5KNN energy harvester (1.03 V and 56.5 μW/cm^3 respectively).

5KNN-2BNNO ceramics made using a single-stage sintering routes were also used to fabricate cantilever-type energy harvesters. Both doped 5KNN (SSS) energy harvesters and pure 5KNN (TSS) energy harvesters were tested under both vibration-only and vibration plus illumination. The pure 5KNN energy harvester demonstrated superior performance as a piezoelectric-only energy harvester, exhibiting a higher open-circuit voltage (1.68 V) and power density (107.3 μW cm^{-3}), whilst the 5KNN-2BNNO-based piezoelectric energy harvester delivered a lower output (open-circuit voltage: 1.26 V and power density: 66.8 μW cm^{-3}) due to large leakage current. However, after illumination, the light stimulates the free charge carriers, modifies trap levels, fill holes and compensates free charge carriers in the piezoelectric elements, resulting in a higher open-circuit voltage (1.77 V) and power density (268.3 μW cm^{-3}) being obtained. This shows the potential for using the 5KNN-2BNNO composition as a photovoltaic-ferroelectric multifunctional material to harvest vibration and light energy simultaneously.

9.2 Future work

This thesis has demonstrated that BNNO-doped, KNN-based ceramics are good candidates to work as next-generation hybrid energy harvesters provided the doping level is kept low. However, further work on the fabrication methods and device structure optimisation needs to be carried out in order to further enhance the output of the devices made.

Two-step sintering has been shown to be a good method to fabricate 5KNN ceramics with a high sintered density and a fine microstructure. However, it only improves the density by controlling grain boundary movement and lowering the evaporation of sodium and potassium; it doesn't help to solve the orientated grain growth problems. Thus, it is still very difficult to eliminate pores aligned along the grain boundaries, which occur due to the faceted nature of the KNN grains. However, it might be possible to enhance the densification further if the KNN powder particles were to be spherical, which may achieve closer packed particle configurations. Therefore, it would be good to consider optimising the powder synthesis route, for example, by the use of hydrothermal/solvothermal methods, which have the known ability to control particles shape in the synthesis process.

The development of ferroelectric semiconductors may be a way introduce more energy conversion mechanisms in a single energy harvester and could be investigated further. However, most ferroelectric semiconductors exhibit poor ferroelectric properties and a high conductivity (such as 5KNN with high BNNO doping amount). Therefore, further optimisation of the composition and doping strategy needs to be undertaken to both narrow the bandgap and maintain good ferroelectric properties at the same time.

In terms of the hybrid energy harvester, whilst the 5KNN-2BNNO hybrid energy harvester showed a better performance than the 5KNN piezoelectric-only energy harvester, the output of the 5KNN-2BNNO ceramic was still low, which may be due to the device structure. The short diffusion path of light-induced carriers requires that the piezo elements are thin, however this would lead to surface charges and cause a low piezoelectric response. However, a thinner piezoelectric layer with larger area may help to improve the output of energy harvesters. This could utilise more advanced ceramic processing routes such as tape casting or screen printing to fabricate ceramic materials in the appropriate form, and/or the use the thin film processes such as pulsed laser deposition or RF sputtering.

Reference

1. Chorsi, M. T. *et al.* Piezoelectric Biomaterials for Sensors and Actuators. *Adv. Mater.* **31**, 1802084 (2019).

2. Kim, H. H. S., Kim, J. H. J. J., Kim, J. H. J. J. & and, J. K. A review of piezoelectric energy harvesting based on vibration. **12**, 1129–1141 (2011).

3. Sodano, H. A., Inman, D. J. & Park, G. A review of power harvesting from vibration using piezoelectric materials. *Shock and Vibration Digest* vol. 36 197–205 (2004).

4. Bowen, C. R., Kim, H. A., Weaver, P. M. & Dunn, S. Piezoelectric and ferroelectric materials and structures for energy harvesting applications. *Energy and Environmental Science* vol. 7 25–44 (2014).

5. Priya, S. *et al.* A Review on Piezoelectric Energy Harvesting: Materials, Methods, and Circuits. *Energy Harvest. Syst.* **4**, 3–39 (2017).

6. Roundy, S., Wright, P. K. & Rabaey, J. A study of low level vibrations as a power source for wireless sensor nodes. *Comput. Commun.* **26**, 1131–1144 (2003).

7. Todaro, M. T. *et al.* Piezoelectric MEMS vibrational energy harvesters: Advances and outlook. *Microelectron. Eng.* **183**–**184**, 23–36 (2017).

8. Lopez-Varo P, B. L. B. J. A. M. C. M. H. J. J.-T. J. K. T. N. R. R. F. Y. Y. Physical aspects of ferroelectric semiconductors for photovoltaic solar energy conversion. *Phys. Rep.* **653**, 1–40 (2016).

9. Andosca, R., McDonald, T. & Genova, V. Experimental and theoretical studies on MEMS piezoelectric vibrational energy harvesters with mass loading. *Sensors Actuators A Phys.* **178**, 76–87 (2012).

10. Wani, A., Ara, A. & JA, U. Lead toxicity: a review. *Interdiscip. Toxicol. vol. 8,2* **8**, 55–64 (2015).

11. Renaud, M., Fiorini, P., Van Schaijk, R. & Van Hoof, C. Harvesting energy from the motion of human limbs: The design and analysis of an impact-based piezoelectric generator. *Smart Mater. Struct.* **18**, (2009).

12. Nia, E., Zawawi, N. & Singh, B. A review of walking energy harvesting using piezoelectric materials. *IOP Conf. Ser. Mater. Sci. Eng.* **291**, (2018).

13. Bai, Y., Jantunen, H. & Juuti, J. Energy harvesting research: The road from single source to multisource. *Adv. Mater.* **30**, 1–41 (2018).

14. Grinberg, I. *et al.* Perovskite oxides for visible-light-absorbing ferroelectric and photovoltaic materials. *Nature* **503**, 509 (2013).

15. Bennett, J. W., Grinberg, L. & Rappe, A. M. New highly polar semiconductor ferroelectrics through d 8 cation-0 vacancy substitution into PbTi0 3: A theoretical study. *J. Am. Chem. Soc.* **130**, 17409–17412 (2008).

16. Pal, P., Rudrapal, K., Maji, P., Chaudhuri, A. R. & Choudhury, D. Toward an Enhanced Room-Temperature Photovoltaic Effect in Ferroelectric Bismuth and Iron Codoped BaTiO 3 . *J. Phys. Chem. C* **125**, 5315–5326 (2021).

17. Li, J. F., Wang, K., Zhu, F. Y., Cheng, L. Q. & Yao, F. Z. (K, Na) NbO3-based lead-free piezoceramics: Fundamental aspects, processing technologies, and remaining challenges. *J. Am. Ceram. Soc.* **96**, 3677–3696 (2013).

18. Bai, Y., Tofel, P., Palosaari, J., Jantunen, H. & Juuti, J. A Game Changer: A Multifunctional Perovskite Exhibiting Giant Ferroelectricity and Narrow Bandgap with Potential Application in a Truly Monolithic Multienergy Harvester or Sensor. *Adv. Mater.* **29**, 1–7 (2017).

19. Stübinger, S., Stricker, A. & Berg, B. I. Piezosurgery in implant dentistry. *Clinical, Cosmetic and Investigational Dentistry* vol. 7 115–124 (2015).

20. KATZIR, S. THE DISCOVERY OF THE PIEZOELECTRIC EFFECT. in *THE BEGINNINGS OF PIEZOELECTRICITY* 15–64 (Springer Netherlands, 2007). doi:10.1007/978-1-4020-4670-4_2.

21. Trainer, M. Kelvin and piezoelectricity. *Eur. J. Phys.* **24**, 535 (2003).

22. Rosen, C., Hiremath, B. & Newnham, R. *Piezoelectricity*. (1992).

23. Elahi, H. *et al.* Response of piezoelectric materials on thermomechanical shocking and electrical shocking for aerospace applications. *Microsyst. Technol.* **24**, 3791–3798 (2018).

24. Gareh, S., Kok, B. C., Uttraphan, C., Thong, K. T. & Borhana, A. A. Evaluation of piezoelectric energy harvester outcomes in road traffic applications. in *IET Conference Publications* vol. 2016 (Institution of Engineering and Technology, 2016).

25. Manbachi, A. & Cobbold, R. S. C. Development and Application of Piezoelectric Materials for Ultrasound Generation and Detection. *Ultrasound* **19**, 187–196 (2011).

26. Xiang, H. J., Wang, J. J., Shi, Z. F. & Zhang, Z. W. Theoretical analysis of piezoelectric energy harvesting from traffic induced deformation of pavements. *Smart Mater. Struct.* **22**, 095024 (2013).

27. Cohen, R. E. Origin of ferroelectricity in perovskite oxides. *Nature* **358**, 136–138 (1992).

28. Whatmore, R. W. Piezoelectric and Pyroelectric Materials and Their Applications. *Electron. Mater.* 283–290 (1991) doi:10.1007/978-1-4615-3818-9_19.

29. Heiland, G. and I. H. . Pyroelectricity of zinc oxide. *Solid State Commun.* **4**, 353–356 (1966).

30. Davaasambuu, J. . P. A. . K. V. and P. U. . Atomistic origin of the inverse piezoelectric effect in α-SiO 2 and α-GaPO4 . *Europhys. Lett.* **62**, 834 (2003).

31. Jiang, Y. FABRICATION AND CHARACTERISATION OF NOVEL ULTRASOUND TRANSDUCERS. (University of Birmingham, 2013).

32. Shrout, T. R. & Zhang, S. J. Lead-free piezoelectric ceramics: Alternatives for PZT? *J. Electroceramics* **19**, 111–124 (2007).

33. Jaffe, B. *Piezoelectric ceramics*. (2012).

34. Shrout, T. R. & Zhang, S. J. Lead-free piezoelectric ceramics: Alternatives for PZT? *Journal of Electroceramics* vol. 19 111–124 (2007).

35. Bartel, C. J. *et al.* New tolerance factor to predict the stability of perovskite oxides and halides. *Sci. Adv.* **5**, eaav0693 (2019).

36. Li, C., Soh, K. C. K. & Wu, P. Formability of ABO3 perovskites. *J. Alloys Compd.* **372**, 40–48 (2004).

37. Rödel, J. *et al.* Perspective on the development of lead-free piezoceramics. *J. Am. Ceram. Soc.* **92**, 1153–1177 (2009).

38. Burfoot, J. C. . Ferroelectrics: an introduction to the physical principles. *van Nostrand* (1967).

39. Hoffmann, M. J., Hammer, M., Endriss, A. & Lupascu, D. C. Correlation between microstructure, strain behavior, and acoustic emission of soft PZT ceramics. *Acta Mater.* **49**, 1301–1310 (2001).

40. Pozdnyak, S. I. & Anikeenko, G. N. Measurement of the permittivity of dielectrics. *Meas. Tech.* **11**, 1683–1685 (1968).

41. Meng, K., Li, W., Tang, X.-G., Liu, Q.-X. & Jiang, Y.-P. A Review of a Good Binary Ferroelectric Ceramic: BaTiO3 −BiFeO3. *ACS Appl. Electron. Mater.* (2021) doi:10.1021/acsaelm.1c00109.

42. Acosta, M. *et al.* BaTiO3-based piezoelectrics: Fundamentals, current status, and perspectives. *Applied Physics Reviews* vol. 4 041305 (2017).

43. Morel, A. *et al.* Dielectric Losses Considerations for Piezoelectric Energy Harvesting. *J. Low Power Electron.* **14**, 244–254 (2018).

44. Moulson, A. J. & Hall, J. H. *Electroceramics: materials, properties, and applications*. (John Wiley & Sons, Ltd, 2003).

45. Mason, W. P. and J. H. . Methods for measuring piezoelectric, elastic, and dielectric coefficients of crystals and ceramics. *Proc. IRE* **42**, 921–930 (1954).

46. Fialka, J. & Beneš, P. Measurement of piezoelectric ceramic parameters: A characterization of the elastic, dielectric and piezoelectric properties of NCE51 PZT. in *Proceedings of the 2012 13th International Carpathian Control Conference, ICCC 2012* 147–152 (2012). doi:10.1109/CarpathianCC.2012.6228632.

47. Standard, B. *Piezoelectric properties of ceramic materials and components-Part 2: Methods of measurement–Low power*. *BS EN* (2002).

48. Jackson, R. *Novel sensors and sensing*. (CRC Press, 2004). doi:10.1201/9780429138348.

49. Kim, T. Y., Kim, S. K. & Kim, S. W. Application of ferroelectric materials for improving output power of energy harvesters. *Nano Convergence* vol. 5 30 (2018).

50. Hysteresis Loop. https://www.nde-ed.org/EducationResources/CommunityCollege/MagParticle/Physics/HysteresisLoop.htm.

51. Zhang, Y. Dielectric and Piezoelectric Properties of Reduced-Graphite- Oxide / Poly (vinylidene fluoride) Nanocomposite and its Related Devices. (University of Birmingham, 2018).

52. Jin, L., Li, F. & Zhang, S. Decoding the Fingerprint of Ferroelectric Loops: Comprehension of the Material Properties and Structures. *J. Am. Ceram. Soc.* **97**, 1–27 (2014).

53. Rappaport, P. The photovoltaic effect and its utilization. *Solar Energy* vol. 3 8–18 (1959).

54. Institute, O. M.-N. S. P. R. & 1998, U. Fundamentals of photovoltaic materials.

55. Dixon, A. & Leslie, J. *Solar energy conversion: an introductory course*. (Technology & Engineering, 1979).

56. Hersch, P. & Zweibel, K. *Basic photovoltaic principles and methods*. (Solar Energy Research Inst., Golden, CO (USA), 1982).

57. Chalmers, B. The Photovoltaic Generation of Electricity. *Sci. Am.* **235**, 34–43 (1976).

58. McKee, R. A., Walker, F. J., Nardelli, M. B., Shelton, W. A. & Stocks, G. M. The interface phase and the Schottky barrier for a crystalline dielectric on silicon. *Science (80-.).* **300**, 1726–1730 (2003).

59. Jiao, Y., Hellman, A., Fang, Y., Gao, S. & Käll, M. Schottky barrier formation and band bending revealed by first-principles calculations OPEN. (2015) doi:10.1038/srep11374.

60. Largent UNSW Photovoltaics Centre of Excellence Syndney Australia, R. *Understanding the p-n Junction*. http://www.bookshop.unsw.edu.au.

61. Li, Z. *et al.* Photovoltaic Effect Induced by Self-Polarization in BiFeO 3 Films. *J. Phys. Chem. C* **125**, 9411–9418 (2021).

62. Rühle, S. Tabulated values of the Shockley-Queisser limit for single junction solar cells. *Sol. Energy* **130**, 139–147 (2016).

63. Chynoweth, A. G. Surface space-charge layers in barium titanate. *Phys. Rev.* **102**, 705–714 (1956).

64. Glass, A. M., von der Linde, D., Auston, D. H. & Negran, T. J. Excited state polarization, bulk photovoltaic effect and the photorefractive effect in electrically polarized media. *J. Electron. Mater.* **4**, 915–943 (1975).

65. Fan, Z., Sun, K. & Wang, J. Perovskites for photovoltaics: a combined review of organic-inorganic halide perovskites and ferroelectric oxide perovskites. *J. Mater. Chem. A* **3**, 18809–18828 (2015).

66. Yeh, P., Gu, C., Glass, A. M., Linde, D. von der & Negran, T. J. High-voltage bulk photovoltaic effect and the photorefractive process in LiNbO3. in *Landmark Papers on Photorefractive Nonlinear Optics* 371–373 (WORLD SCIENTIFIC, 1995). doi:10.1142/9789812832047_0047.

67. Nayak, P. K. . G.-B. G. . K. A. . B. J. and C. D. . Photovoltaic efficiency limits and material disorder. *Energy Environ. Sci.* **5**, 6022–6039 (2012).

68. Wang, X. . K. M. R. . G. J. L. . A. M. A. and L. M. S. . Design of GaAs solar cells operating close to the Shockley–Queisser limit. *IEEE J. Photovolt.* **3**, 737–744 (2013).

69. Rühle, S. . Tabulated values of the Shockley–Queisser limit for single junction solar cells. *Sol. Energy* **130**, 139–147 (2016).

70. Yang, S. Y. *et al.* Above-bandgap voltages from ferroelectric photovoltaic devices. *Nat. Nanotechnol.* **5**, 143–147 (2010).

71. Spanier, J. E. *et al.* Power conversion efficiency exceeding the Shockley-Queisser limit in a ferroelectric insulator. *Nat. Photonics* **10**, 611 (2016).

72. Yuan, Y., Xiao, Z., Yang, B. & Huang, J. Arising applications of ferroelectric materials in photovoltaic devices. *J. Mater. Chem. A* **2**, 6027–6041 (2014).

73. Butler, K. T., Frost, J. M. & Walsh, A. Ferroelectric materials for solar energy conversion: Photoferroics revisited. *Energy Environ. Sci.* **8**, 838–848 (2015).

74. Liu, Z., Yu, X. & Li, L. Piezopotential augmented photo- and photoelectro-catalysis with a built-in electric field. *Chinese J. Catal.* **41**, 534–549 (2020).

75. Pandey, R. *et al.* Mutual Insight on Ferroelectrics and Hybrid Halide Perovskites: A Platform for Future Multifunctional Energy Conversion. *Adv. Mater.* **31**, 1807376 (2019).

76. Fridkin, V. M. Bulk photovoltaic effect in noncentrosymmetric crystals. *Crystallogr. Reports* **46**, 654–658 (2001).

77. Brody, P. S. Semiconductor-ferroelectric nonvolatile memory using anomalous high photovoltages in ferroelectric ceramics. *Appl. Phys. Lett.* **38**, 153–155 (1981).

78. Pintilie, L., Vrejoiu, I., Le Rhun, G. & Alexe, M. Short-circuit photocurrent in epitaxial lead zirconate-titanate thin films. *J. Appl. Phys.* **101**, (2007).

79. Seidel, J. *et al.* Efficient photovoltaic current generation at ferroelectric domain walls. *Phys. Rev. Lett.* **107**, (2011).

80. Ji, W., Yao, K. & Liang, Y. C. Bulk Photovoltaic Effect at Visible Wavelength in Epitaxial Ferroelectric $BiFeO_3$ Thin Films. *Adv. Mater.* **22**, 1763–1766 (2010).

81. Chen, F. S. Optically induced change of refractive indices in LiNbO3 and litao3. *J. Appl. Phys.* **40**, 3389–3396 (1969).

82. Nonaka, K. *et al.* Enhanced photovoltaic response in lead lanthanum zirconate-titanate ceramics with a-site deficient composition for photostrictor application. *Japanese J. Appl. Physics, Part 1 Regul. Pap. Short Notes Rev. Pap.* **39**, 5144–5145 (2000).

83. Qin, M., Yao, K. & Liang, Y. C. Photovoltaic mechanisms in ferroelectric thin films with the effects of the electrodes and interfaces. *Appl. Phys. Lett.* **95**, (2009).

84. Qin, M., Yao, K., Liang, Y. C. & Shannigrahi, S. Thickness effects on photoinduced current in ferroelectric thin films. *J. Appl. Phys* **101**, 14104 (2007).

85. Wurfel, P., Batra, I. P. & Jacobs, J. T. Polarization instability in thin ferroelectric films. *Phys. Rev. Lett.* **30**, 1218–1221 (1973).

86. Fan, Z., Xiao, J., Yao, K., Zeng, K. & Wang, J. Ferroelectric polarization relaxation in Au/Cu2O/ZnO/BiFeO3/Pt heterostructure. *Appl. Phys. Lett.* **106**, (2015).

87. Junquera, J. and G. P. . Critical thickness for ferroelectricity in perovskite ultrathin films. *nature.com* **422**, 506–509 (2003).

88. Sturman, B. & Fridkin, V. *Photovoltaic and Photo-refractive Effects in Noncentrosymmetric Materials*. vol. 8 (CRC Press, 1992).

89. Zenkevich, A. *et al.* Giant bulk photovoltaic effect in thin ferroelectric BaTiO3 films. *Phys. Rev. B - Condens. Matter Mater. Phys.* **90**, (2014).

90. Pal, S. *et al.* Giant photovoltaic response in band engineered ferroelectric perovskite. *Sci. Rep.* **8**, 1–7 (2018).

91. Young, S. M. & Rappe, A. M. First principles calculation of the shift current photovoltaic effect in ferroelectrics. *Phys. Rev. Lett.* **109**, (2012).

92. Tan, L. Z. *et al.* Shift current bulk photovoltaic effect in polar materials-hybrid and oxide perovskites and beyond. *npj Comput. Mater.* **2**, (2016).

93. Von Baltz, R. & Kraut, W. Theory of the bulk photovoltaic effect in pure crystals. *Phys. Rev. B* **23**, 5590–5596 (1981).

94. Young, S. M., Zheng, F. & Rappe, A. M. First-principles calculation of the bulk photovoltaic effect in bismuth ferrite. *Phys. Rev. Lett.* **109**, (2012).

95. Nakashima, S. *et al.* Bulk photovoltaic effect in a BiFeO3thin film on a SrTiO3substrate. *Jpn. J. Appl. Phys.* **53**, 09PA16 (2014).

96. Alexe, M. Local mapping of generation and recombination lifetime in BiFeO 3 single crystals by scanning probe photoinduced transient spectroscopy. *Nano Lett.* **12**, 2193–2198 (2012).

97. Alexe, M. & Hesse, D. Tip-enhanced photovoltaic effects in bismuth ferrite. *Nat. Commun.* **2**, 255–256 (2011).

98. Bhatnagar, A., Chaudhuri, A., Kim, Y., Hesse, D. & Alexe, M. Role of domain walls in the abnormal photovoltaic effect in BiFeO3. *Nat. Commun.* **4**, (2013).

99. Zhang, J. *et al.* Enlarging photovoltaic effect: combination of classic photoelectric and ferroelectric photovoltaic effects. *Sci. Rep.* **3**, (2019).

100. Seifert, K. T. P. . Lead-Free Piezoelectric Ceramics. (Diss. Technische Universität, 2010).

101. Egerton, L. & Dillon, D. M. Properties of Ceramics in the System Potassium-Sodium Niobate. *J. Am. Ceram. Soc.* **42**, 223–450 (1959).

102. Dai, Y. J., Zhang, X. W. & Chen, K. P. Morphotropic phase boundary and electrical properties of K1-x Nax NbO3 lead-free ceramics. *Appl. Phys. Lett.* **94**, (2009).

103. Zuo, R., Fu, J. & Lv, D. Phase transformation and tunable piezoelectric properties of lead-free (Na0.52K0.48-xLix)(Nb1-x-ySb yTax)O3 system. *J. Am. Ceram. Soc.* **92**, 283–285 (2009).

104. Kakimoto, K., Masuda, I. & Ohsato, H. Ferroelectric and Piezoelectric Properties of KNbO3 Ceramics Containing Small Amounts of LaFeO3. *Jpn. J. Appl. Phys.* **42**, 6102 (2003).

105. Matsumoto, K., Hiruma, Y., Nagata, H. & Takenaka, T. Piezoelectric properties of KNbO3 ceramics prepared by ordinary sintering. *Ferroelectrics* **358**, 169–174 (2007).

106. Mishra, P., Prasad, U. & Kumar, S. Structural, dielectric and piezoelectric properties of NaNbO3-BaTiO3 ceramic system. *Int. J. Curr. Eng. Technol.* **7**, 362–367 (2017).

107. Xie, S., Zhu, K., Qiu, J. & Guo, H. Microstructure and electrical properties of NaNbO 3-BaTiO 3 lead-free piezoelectric ceramics. *Front Mech Eng Chin* **4**, 345–349 (2009).

108. Shirane, G., Danner, H., Pavlovic, A. & Pepinsky, R. Phase transitions in ferroelectric KNbO3. *Phys. Rev.* **93**, 672–673 (1954).

109. TENNERY, V. J. High-Temperature Phase Transitions in Na Nb O3. *J. Am. Ceram. Soc.* **48**, 537–539 (1965).

110. Trodahl, H. J. *et al.* Raman spectroscopy of (K,Na) NbO3 and (K,Na) 1-xLixNbO3. *Appl. Phys. Lett.* **93**, 1–4 (2008).

111. Wang, K. & Li, J. F. (K, Na)NbO3-based lead-free piezoceramics: Phase transition, sintering and property enhancement. *J. Adv. Ceram.* **1**, 24–37 (2012).

112. Tellier, J., Malic, B., Dkhil, B. & Jenko, D. Crystal structure and phase transitions of sodium potassium niobate perovskites. *Solid State Sci.* **11**, 320–324 (2009).

113. Wang, K. & Li, J. F. Analysis of crystallographic evolution in (Na,K) Nb O3 -based lead-free piezoceramics by x-ray diffraction. *Appl. Phys. Lett.* **91**, 10–13 (2007).

114. Jaffe, B., Cook, W. & Jaffe, H. Piezoelectric Ceramics, Academic Press, London and New York, 1971.

115. Akdoğan, E. K., Kerman, K., Abazari, M. & Safari, A. Origin of high piezoelectric activity in ferroelectric (K0.44 Na0.52 Li0.04) - (Nb0.84 Ta0.1 Sb0.06) O3 ceramics. *Appl. Phys. Lett.* **92**, (2008).

116. Zhang, S., Xia, R. & Shrout, T. R. Modified (K0.5 Na0.5) Nb O3 based lead-free piezoelectrics with broad temperature usage range. *Appl. Phys. Lett.* **91**, (2007).

117. Ahtee, M. & Hewat, A. W. Structural Phase Transitions in Sodium-Potassium Niobate Solid Solutions by Neutron Powder Diffraction. *Acta Cryst* **34**, 309–317 (1978).

118. Saito, Y. *et al.* Lead-free piezoceramics. *Nature* **432**, 84–87 (2004).

119. wu, J. *et al.* Effects ofK/Na ratio on the phase structure and electrical properties of (KxNa0.96-xLi0.04)(Nb0.91Ta0.05Sb0.04)O3 lead-free ceramics. *Appl. Phys. Lett.* **91**, 14103 (2007).

120. Damjanovic, D. Contributions to the piezoelectric effect in ferroelectric single crystals and ceramics. *J. Am. Ceram. Soc.* **88**, 2663–2676 (2005).

121. Hreščak, J. *et al.* Donor doping of K0.5Na0.5NbO3 ceramics with strontium and its implications to grain size, phase composition and crystal structure. *J. Eur. Ceram. Soc.* **37**, 2073–2082 (2017).

122. Vendrell, X. *et al.* Effect of lanthanide doping on structural, microstructural and functional properties of K0.5Na0.5NbO3 lead-free piezoceramics. *Ceram. Int.* **42**, 17530–17538 (2016).

123. Abazari, M. & Safari, A. Effects of doping on ferroelectric properties and leakage current behavior of KNN-LT-LS thin films on substrate. *J. Appl. Phys* **105**, 94101 (2009).

124. Chen, K. *et al.* Acceptor doping effects in (K0.5Na0.5)NbO3 lead-free piezoelectric ceramics. *Ceram. Int.* **42**, 2899–2903 (2016).

125. Hussain, F., Khesro, A., Muhammad, R. & Wang, D. Effect of Ta-doping on functional properties of K0.51Na0.49NbO3. *Mater. Res. Express* **6**, 106309 (2019).

126. Xiao, D. & Zhu, J. Effect of Doping Ions on the Properties of KNN-Based Lead-Free Piezoelectric Ceramics. *Ferroelectrics* **404**, 10–18 (2010).

127. Vendrell, X. *et al.* Improving the functional properties of (K0.5Na0.5)NbO3 piezoceramics by acceptor doping. *J. Eur. Ceram. Soc.* **35**, 125–130 (2015).

128. Zhao, Y. *et al.* Improved piezoelectricity and luminescence behavior in Er2O3 doped (K,Na)NbO3 ceramics. *Mater. Lett.* **162**, 226–229 (2016).

129. Damjanovic, D. & Demartin, M. Contribution of the irreversible displacement of domain walls to the piezoelectric effect in barium titanate and lead zirconate titanate ceramics. *J. Phys. Condens. Matter* **9**, 4943–4953 (1997).

130. Guo, Y., Kakimoto, K. I. & Ohsato, H. Phase transitional behavior and piezoelectric properties of (Na 0.5K0.5)NbO3-LiNbO3 ceramics. *Appl. Phys. Lett.* **85**, 4121–4123 (2004).

131. Lin, D., Kwok, K. W., Tian, H. & Chan, H. W. L. W. Phase transitions and electrical properties of (Na1-xK x)(Nb1-ySby)O3 lead-free piezoelectric ceramics with a MnO2 sintering aid. *J. Am. Ceram. Soc.* **90**, 1458–1462 (2007).

132. Zhou, J. J. *et al.* High and frequency-insensitive converse piezoelectric coefficient obtained in AgSbO3-modified (Li, K, Na)(Nb, Ta) O3 lead-free piezoceramics. *J. Am. Ceram. Soc.* **96**, 519–523 (2013).

133. Priya, S. & Nahm, S. *Lead-free piezoelectrics*. (2011).

134. Wu, J. *et al.* Improved temperature stability of CaTiO3-modified [(K 0.5Na0.5)0.96Li0.04] (Nb 0.91Sb0.05Ta0.04)O3 lead-free piezoelectric ceramics. *J. Appl. Phys.* **104**, (2008).

135. Malič, B. *et al.* Linear thermal expansion of lead-free piezoelectric K0.5Na 0.5NbO3 ceramics in a wide temperature range. *J. Am. Ceram. Soc.* **94**, 2273–2275 (2011).

136. Chang, Y., Poterala, S., Yang, Z. & Messing, G. L. Enhanced electromechanical properties and temperature stability of textured (K0.5Na0.5)NbO3-based piezoelectric ceramics. *J. Am. Ceram. Soc.* **94**, 2494–2498 (2011).

137. Solutions Masafumi Kobune, S., Teraoka, K. & Nishioka, H. Thermal Reliability of Alkaline Niobate-Based Lead-Free Piezoelectric Ceramics. *Japanese J. Appl. Phys. To* **48**, 9–17 (2009).

138. Skidmore, T. A., Comyn, T. P. & Milne, S. J. Temperature stability of ([Na0.5K0.5NbO3] 0.93-[LiTaO3]0.07) lead-free piezoelectric ceramics. *Appl. Phys. Lett.* **94**, (2009).

139. Wu J *et al.* CaTiO3-modified [(K0. 5Na0. 5) 0.94 Li0. 06](Nb0. 94Sb0. 06) O3 lead-free piezoelectric ceramics with improved temperature stability. *Scr. Mater.* **59**, 750–752 (2008).

140. Zhang, S., Xia, R., Shrout, T. R., Zang, G. & Wang, J. Piezoelectric properties in perovskite 0.948(K0.5Na 0.5)NbO3-0.052LiSbO3 lead-free ceramics. *J. Appl. Phys.* **100**, 1–7 (2006).

141. Ahn, C. W., Park, C. S., Dittmer, R., Hong, S. H. & Priya, S. Effect of elemental diffusion on temperature coefficient of piezoelectric properties in KNN-based lead-free composites. *J. Mater. Sci.* **45**, 3961–3965 (2010).

142. Zhang, G. *et al.* New high Tc multiferroics KBiFe2O5 with narrow band gap and promising photovoltaic effect. *Sci. Rep.* **3**, (2013).

143. Basu, S. R. *et al.* Photoconductivity in BiFeO3 thin films. *Appl. Phys. Lett.* **92**, (2008).

144. Nechache, R. *et al.* Bandgap tuning of multiferroic oxide solar cells. *Nat. Photonics* **9**, (2015).

145. Choi, W. S. *et al.* Wide bandgap tunability in complex transition metal oxides by site-specific substitution. *Nat. Commun.* **3**, 686–689 (2012).

146. Bomlai, P., Wichianrat, P., Muensit, S. & Milne, S. J. Effect of calcination conditions and excess alkali carbonate on the phase formation and particle morphology of Na0.5K0.5NbO 3 powders. *J. Am. Ceram. Soc.* **90**, 1650–1655 (2007).

147. Rice, R. *Ceramic fabrication technology*. (2002).

148. Richerson, D. *Modern ceramic engineering: properties, processing, and use in design*. (2005).

149. Barsoum, M. *Fundamentals of ceramics*. (2019).

150. Malič, B. *et al.* Sintering of lead-free piezoelectric sodium potassium niobate ceramics. *Materials (Basel).* **8**, 8117–8146 (2015).

151. Huan, Y., Wang, X., Fang, J. & Li, L. Grain size effects on piezoelectric properties and domain structure of BaTiO 3 ceramics prepared by two-step sintering. *J. Am. Ceram. Soc.* **96**, 3369–3371 (2013).

152. Hiruma, Y. *et al.* Grain-Size Effect on Electrical Properties of (Bi_{1/2}K_{1/2})TiO_{3} Ceramics. *Japanese J. Appl. Phys.* **46**, 1081 (2007).

153. Huan, Y., Wang, X., Fang, J. & Li, L. Grain size effect on piezoelectric and ferroelectric properties of BaTiO3 ceramics. *J. Eur. Ceram. Soc.* **34**, 1445–1448 (2014).

154. Ahn, C. W. *et al.* Sintering behavior of lead-free (K,Na)NbO3-basedpiezoelectric ceramics. *J. Am. Ceram. Soc.* **92**, 2033–2038 (2009).

155. Ahn, C. W. ., Park, H. Y. ., Nahm, S. ., Uchino, K. . & Lee, H. G. and L. H. J. . Structural variation and piezoelectric properties of 0.95 (Na0. 5K0. 5) NbO3–0.05 BaTiO3 ceramics. *Sensors Actuators A* **136**, 255–260 (2007).

156. Svoboda, J., Riedel, H. & materialia, R. G. A model for liquid phase sintering. *Acta Mater.* **44**, 3215–3226 (1996).

157. Pang, X., Qiu, J., Zhu, K. & Luo, J. Study on the sintering mechanism of KNN-based lead-free piezoelectric ceramics. *J. Mater. Sci.* **46**, 2345–2349 (2011).

158. Rollett, A. D., Srolovitz, D. J. & Anderson, M. P. Simulation and theory of abnormal grain growth-anisotropic grain boundary energies and mobilities. *Acta Metall.* **37**, 1227–1240 (1989).

159. Fang, J. *et al.* Two-step sintering: An approach to broaden the sintering temperature range of alkaline niobate-based lead-free piezoceramics. *J. Am. Ceram. Soc.* **93**, 3552–3555 (2010).

160. Jiang, N., Fang, B., Wu, J. & Du, Q. Effects of the co-addition of LiSbO3–LiTaO3 on the densification of (Na1/2K1/2) NbO3 lead free ceramics by atmosphere sintering. *J. Alloys Compd.* **509**, 2420–2424 (2011).

161. Yang, D. Y., Yoon, D. Y. & Kang, S. J. L. Abnormal grain growth enhanced densification of liquid phase-sintered WC-Co in support of the pore filling theory. *J. Mater. Sci.* **47**, 7056–7063 (2012).

162. Zhen, Y. & Li, J. F. Normal sintering of (K,Na)NbO3-based ceramics: Influence of sintering temperature on densification, microstructure, and electrical properties. *J. Am. Ceram. Soc.* **89**, 3669–3675 (2006).

163. Liu, L. *et al.* Effects of Na/K evaporation on electrical properties and intrinsic defects in Na0. 5K0. 5NbO3 ceramics. *Mater. Chem. Phys.* (2009).

164. Popovič, A., Bencze, L., Koruza, J. & Advances, B. M. Vapour pressure and mixing thermodynamic properties of the KNbO 3–NaNbO 3 system. *RSC Adv.* **5**, 76249 (2015).

165. Yang, Z., Chang, Y., Liu, B. & A, L. W. Effects of composition on phase structure, microstructure and electrical properties of (K0. 5Na0. 5) NbO3–LiSbO3 ceramics. *Mater. Sci. Eng. A* **432**, 292–298 (2006).

166. Lin, D., Kwok, K. W., Lam, K. H. & Chan, H. L. W. Structure and electrical properties of K0.5Na 0.5NbO3-LiSbO3 lead-free piezoelectric ceramics. *J. Appl. Phys.* **101**, 074111 (2007).

167. Zang, G. Z. *et al.* Perovskite (Na 0.5 K 0.5) 1-x (LiSb)x Nb1-x O 3 lead-free piezoceramics. *Appl. Phys. Lett.* **88**, (2006).

168. Acker, J., Kungl, H. & Hoffmann, M. J. Influence of alkaline and niobium excess on sintering and microstructure of sodium-potassium niobate (K0.5 Na0.5)NbO3. *J. Am. Ceram. Soc.* **93**, 1270–1281 (2010).

169. Chen, I. W. . & W. X. H. Sintering dense nanocrystalline ceramics without final-stage grain growth. *Nature* **404**, 168–171 (2000).

170. Kawada, S., Kimura, M., Higuchi, Y. & Takagi, H. (KNa)NbO3-Based multilayer piezoelectric ceramics with nickel inner electrodes. *Appl. Phys. Express* **2**, 111401 (2009).

171. Kholkin, A., Taylor, D. & Setter, N. Poling effect on the piezoelectric properties of lead zirconate titanate thin films. *Proc. Elev. IEEE Int. Symp. Appl. Ferroelectr.* 69–72 (1998).

172. Du, H. *et al.* Effect of poling condition on piezoelectric properties of (K0. 5Na0. 5) NbO3 ceramics. *Trans. Nonferrous Met. Soc. China* **16**, s462–s465 (2006).

173. Chandrakala, E., Praveen, J. P. & Das, D. Effect of poling process on piezoelectric properties of sol–gel derived BZT–BCT ceramics. *AIP Conf. Proc.* **1728**, (2016).

174. Zhang, L. *et al.* The effect of poling condition on the piezoelectric properties of 0.3 PNN-0.7 PZT ceramics in the vicinity of MPB. *Springer*.

175. Li, Q. *et al.* Poling engineering of (K,Na)NbO3-based lead-free piezoceramics with orthorhombic-tetragonal coexisting phases. *J. Mater. Chem. C* **5**, 549–556 (2017).

176. Zhang, N., Zheng, T. & Wu, J. Lead-Free (K,Na)NbO3-Based Materials: Preparation Techniques and Piezoelectricity. *ACS Omega* **5**, 3099–3107 (2020).

177. Singh, R., Kambale, K., Kulkarni, A. R. & Harendranath, C. S. Structure composition correlation in KNN-BT ceramics-An X-ray diffraction and Raman spectroscopic investigation. *Mater. Chem. Phys.* **138**, 905–908 (2013).

178. Karapuzha, A. S. *et al.* Structure, dielectric and piezoelectric properties of donor doped PZT ceramics across the phase diagram. (2016) doi:10.1080/00150193.2016.1240571.

179. Smil, V. *Energy transitions: global and national perspectives*. (ABC-CLIO, 2016).

180. McLaren, P. G. *Elementary electric power and machines*. (Halsted Press, 1984).

181. Perera, F. Pollution from fossil-fuel combustion is the leading environmental threat to global pediatric health and equity: Solutions exist. *Int. J. Environ. Res. Public Health* **15**, 16 (2018).

182. Barbir, F., Veziroğlu, T. N. & Plass Jr, H. J. Environmental damage due to fossil fuels use. *Int. J. Hydrogen Energy* **15**, 739–749 (1990).

183. Akyildiz, I. F. & Vuran, M. C. *Wireless sensor networks*. vol. 4 (John Wiley & Sons, 2010).

184. Tree, S. Wireless sensor networks. *Self* **1**, C0 (2014).

185. Đurišić, M. P., Tafa, Z., Dimić, G. & Milutinović, V. A survey of military applications of wireless sensor networks. in *2012 Mediterranean conference on embedded computing (MECO)* 196–199 (IEEE, 2012).

186. Winkler, M., Street, M., Tuchs, K.-D. & Wrona, K. Wireless sensor networks for military purposes. in *Autonomous Sensor Networks* 365–394 (Springer, 2012).

187. Bokareva, T. *et al.* Wireless sensor networks for battlefield surveillance. in *Proceedings of the land warfare conference* 1–8 (2006).

188. Sundararajan, V., Redfern, A., Schneider, M., Wright, P. & Evans, J. Wireless sensor networks for machinery monitoring. in *ASME 2005 International Mechanical Engineering Congress and Exposition* 425–433 (American Society of Mechanical Engineers Digital Collection, 2005).

189. Hou, L. & Bergmann, N. W. Novel industrial wireless sensor networks for machine condition monitoring and fault diagnosis. *IEEE Trans. Instrum. Meas.* **61**, 2787–2798 (2012).

190. Güngör, V. Ç. & Hancke, G. P. *Industrial wireless sensor networks: Applications, protocols, and standards*. (Crc Press, 2013).

191. Shen, X., Wang, Z. & Sun, Y. Wireless sensor networks for industrial applications. in *Fifth World Congress on Intelligent Control and Automation (IEEE Cat. No. 04EX788)* vol. 4 3636–3640 (IEEE, 2004).

192. Flammini, A., Ferrari, P., Marioli, D., Sisinni, E. & Taroni, A. Wired and wireless sensor networks for industrial applications. *Microelectronics J.* **40**, 1322–1336 (2009).

193. Gungor, V. C. & Hancke, G. P. Industrial wireless sensor networks: Challenges, design principles, and technical approaches. *IEEE Trans. Ind. Electron.* **56**, 4258–4265 (2009).

194. Anandarajah, A., Moore, K., Terzis, A. & Wang, I.-J. Sensor networks for landslide detection. in *Proceedings of the 3rd international conference on Embedded networked sensor systems* 268–269 (2005).

195. Ochoa, S. F. & Santos, R. Human-centric wireless sensor networks to improve information availability during urban search and rescue activities. *Inf. Fusion* **22**, 71–84 (2015).

196. Zhang, J., Li, W., Yin, Z., Liu, S. & Guo, X. Forest fire detection system based on wireless sensor network. in *2009 4th IEEE conference on industrial electronics and applications* 520–523 (IEEE, 2009).

197. Bernardo, L., Oliveira, R., Tiago, R. & Pinto, P. A fire monitoring application for scattered wireless sensor networks. in *Proceedings of the international conference on wireless information networks and systems, Barcelona, Spain* vol. 2831 2831 (2007).

198. NagaЎama, T., Ruiz-Sandoval, M., Spencer Jr, B. F., Mechitov, K. A. & Agha, G. Wireless strain sensor development for civil infrastructure. *Present. INSS* (2004).

199. Bocca, M., Cosar, E. I., Salminen, J. & Eriksson, L. M. A reconfigurable wireless sensor network for structural health monitoring. in *Proceedings of the 4th international conference on structural health monitoring of intelligent infrastructure* 22–24 (2009).

200. Yedavalli, R. K. & Belapurkar, R. K. Application of wireless sensor networks to aircraft control and health management systems. *J. Control Theory Appl.* **9**, 28–33 (2011).

201. Arslan, T. *et al.* ESPACENET: A framework of evolvable and reconfigurable sensor networks for aerospace–based monitoring and diagnostics. in *First NASA/ESA Conference on Adaptive Hardware and Systems (AHS'06)* 323–329 (IEEE, 2006).

202. Cao, S. & Li, J. A survey on ambient energy sources and harvesting methods for structural health monitoring applications. *Adv. Mech. Eng.* **9**, 1687814017696210 (2017).

203. Blokhina, E., El Aroudi, A., Alarcon, E. & Galayko, D. Nonlinearity in Energy Harvesting Systems. *Micro-and Nanoscale Appl.* (2016).

204. Wikander, Ö. *Handbook of ancient water technology*. (Brill Leiden, 2000).

205. Drachmann, A. G. *Heron's windmill*. (1961).

206. Guler, U., Sendi, M. S. E. & Ghovanloo, M. A dual-mode passive rectifier for wide-range input power flow. in *2017 IEEE 60th International Midwest Symposium on Circuits and Systems (MWSCAS)* 1376–1379 (IEEE, 2017).

207. Sharma, S., Panwar, V. & Yadav, S. C. Different sources of energy harvesting: A survey. in *2017 International Conference on Computing, Communication and Automation (ICCCA)* 1370–1373 (IEEE, 2017).

208. Wu, W. J., Lee, B. S. & Lallart, M. Piezoelectric MEMS power generators for vibration energy harvesting. in *Small-Scale Energy Harvesting* 156–157 (InTech, 2012).

209. Kazmierski, T. J. & Beeby, S. *Energy harvesting systems*. (Springer, 2014).

210. Caliò, R. *et al.* Piezoelectric Energy Harvesting Solutions. *Sensors* **14**, 4755–4790 (2014).

211. Horowitz, S. B., Sheplak, M., Cattafesta III, L. N. & Nishida, T. A MEMS acoustic energy harvester. *J. Micromechanics Microengineering* **16**, S174 (2006).

212. Kanesaka, T. Development of a thermal energy watch. *Soci été Suisse Chronométrie* (1999).

213. Roundy, S. J. Energy scavenging for wireless sensor nodes with a focus on vibration to electricity conversion. (University of California, Berkeley Berkeley, CA, 2003).

214. Priya, S. & Inman, D. J. *Energy harvesting technologies*. *Energy Harvesting Technologies* (2009). doi:10.1007/978-0-387-76464-1.

215. Mitcheson, P. D., Green, T. C., Yeatman, E. M. & Holmes, A. S. Architectures for vibration-driven micropower generators. *J. microelectromechanical Syst.* **13**, 429–440 (2004).

216. Roundy, S., Wright, P. K. & Pister, K. S. J. Micro-electrostatic vibration-to-electricity converters. in *ASME 2002 International Mechanical Engineering Congress and Exposition* 487–496 (American Society of Mechanical Engineers Digital Collection, 2002).

217. Wang, Z. L. Towards self-powered nanosystems: From nanogenerators to nanopiezotronics. *Adv. Funct. Mater.* **18**, 3553–3567 (2008).

218. Visser, H. J., Reniers, A. C. F. & Theeuwes, J. A. C. Ambient RF energy scavenging: GSM and WLAN power density measurements. in *2008 38th European Microwave Conference* 721–724 (IEEE, 2008).

219. Liu, V. *et al.* Ambient backscatter: Wireless communication out of thin air. *ACM SIGCOMM Comput. Commun. Rev.* **43**, 39–50 (2013).

220. Gudan, K., Chemishkian, S., Hull, J. J., Reynolds, M. S. & Thomas, S. Feasibility of wireless sensors using ambient 2.4 GHz RF energy. in *SENSORS, 2012 IEEE* 1–4 (IEEE, 2012).

221. Bouchouicha, D., Latrach, M., Dupont, F. & Ventura, L. An experimental evaluation of surrounding RF energy harvesting devices. in *The 40th European Microwave Conference* 1381–1384 (IEEE, 2010).

222. Ajmal, T., Dyo, V., Allen, B., Jazani, D. & Ivanov, I. Design and optimisation of compact RF energy harvesting device for smart applications. *Electron. Lett.* **50**, 111–113 (2014).

223. Muramatsu, M. & Koizumi, H. An experimental result using RF energy harvesting circuit with Dickson charge pump. in *2010 IEEE International Conference on Sustainable Energy Technologies (ICSET)* 1–4 (IEEE, 2010).

224. Chemistry, R. S. of. Energy. (2014).

225. Perspectives, S. E. Executive Summary, International Energy Agency, 2011. *Achieved from Orig.* **3**, (2011).

226. Panwar, N. L., Kaushik, S. C. & Kothari, S. Role of renewable energy sources in environmental protection: A review. *Renew. Sustain. energy Rev.* **15**, 1513–1524 (2011).

227. Hermann, W. A. Quantifying global exergy resources. *Energy* **31**, 1685–1702 (2006).

228. Fei, L. *et al.* Electrospun Bismuth Ferrite Nanofibers for Potential Applications in Ferroelectric Photovoltaic Devices. *ACS Appl. Mater. Interfaces* **7**, (2015).

229. Ji, W., Yao, K. & Liang, Y. C. Bulk photovoltaic effect at visible wavelength in epitaxial ferroelectric BiFeO3 thin films. *Adv. Mater.* **22**, 1763–1766 (2010).

230. Zhang, Y., Jie, W., Chen, P., Liu, W. & Hao, J. Ferroelectric and piezoelectric effects on the optical process in advanced materials and devices. *Adv. Mater.* **30**, 1–35 (2018).

231. Zorlu, Ö., Topal, E. T. & Külah, H. A vibration-based electromagnetic energy harvester using mechanical frequency up-conversion method. *IEEE Sens. J.* **11**, 481–488 (2011).

232. Zhang, Y. *et al.* Micro electrostatic energy harvester with both broad bandwidth and high normalized power density. *Appl. Energy* **212**, 362–371 (2018).

233. Zhao, J. & You, Z. A Shoe-Embedded Piezoelectric Energy Harvester for Wearable Sensors. *Sensors* **14**, 12497–12510 (2014).

234. Jeon, Y. B., Sood, R., Jeong, J. H. & Kim, S. G. MEMS power generator with transverse mode thin film PZT. *Sensors Actuators, A Phys.* **122**, 16–22 (2005).

235. Safari, A. & Hejazi, M. Lead-free KNN-based piezoelectric materials. in *Lead-Free Piezoelectrics* 139–175 (Springer, 2013). doi:10.1007/978-1-4419-9598-8_5.

236. Ueberschlag, P. PVDF piezoelectric polymer. *Sensor Review* vol. 21 118–125 (2001).

237. Saadon, S. & Sidek, O. A review of vibration-based MEMS piezoelectric energy harvesters. *Energy Convers. Manag.* **52**, 500–504 (2011).

238. Li, L., Xu, J., Liu, J. & Gao, F. Recent progress on piezoelectric energy harvesting: structures and materials. *Adv. Compos. Hybrid Mater.* **1**, 478–505 (2018).

239. Zhao, J. & You, Z. Models for 31-Mode PVDF Energy Harvester for Wearable Applications. *Sci. World J.* (2014) doi:10.1155/2014/893496.

240. Yang, Z., Zhou, S., Zu, J. & and Inman, D. High-performance piezoelectric energy harvesters and their applications. *Joule* **2**, 642–697 (2018).

241. Kim, S. B. *et al.* Comparison of MEMS PZT cantilevers based on d31 and d 33 modes for vibration energy harvesting. *J. Microelectromechanical Syst.* **22**, 26–33 (2013).

242. Hagood, N. W. . R. K. K. G. and P. G. Improving transverse actuation of piezoceramics using interdigitated surface electrodes. *Int. Soc. Opt. Photonics* **1917**, 341–352 (1993).

243. Wilkie, W. K. *et al.* Low-cost piezocomposite actuator for structural control applications. *Int. Soc. Opt. Photonics* **3991**, 323–334 (2000).

244. Baker, J., Roundy, S. & Wright, P. Alternative geometries for increasing power density in vibration energy scavenging for wireless sensor networks. in *Collection of Technical Papers - 3rd International Energy Conversion Engineering Conference* vol. 2 959–970 (American Institute of Aeronautics and Astronautics, 2005).

245. Roundy, S. & Wright, P. K. A piezoelectric vibration based generator for wireless electronics. *Smart Mater. Struct.* **13**, 1131 (2004).

246. Erturk, A. & Inman, D. J. On Mechanical Modeling of Cantilevered Piezoelectric Vibration Energy Harvesters. *J. Intell. Mater. Syst. Struct.* **19**, 1311–1325 (2008).

247. Erturk, A. & and, D. J. I. A distributed parameter electromechanical model for cantilevered piezoelectric energy harvesters. *J. Vib. Acoust.* **130**, (2008).

248. Liu, H., Zhong, J., Lee, C., Lee, S.-W. & Lin, L. A comprehensive review on piezoelectric energy harvesting technology: Materials, mechanisms, and applications. *Appl. Phys. Rev* **5**, 41306 (2018).

249. Ryu, H., Yoon, H. J. & Kim, S. W. Hybrid Energy Harvesters: Toward Sustainable Energy Harvesting. *Adv. Mater.* **31**, 1–19 (2019).

250. Li, P., Gao, S. & Cong, B. Theoretical modeling, simulation and experimental study of hybrid piezoelectric and electromagnetic energy harvester. *AIP Adv.* **8**, (2018).

251. Yoon, G., Shin, K., Gupta, M. & Lee, K. High-performance hybrid cell based on an organic photovoltaic device and a direct current piezoelectric nanogenerator. *Nano Energy* **12**, 547–555 (2015).

252. Bai, Y., Jantunen, H. & Juuti, J. Energy Harvesting Research: The Road from Single Source to Multisource. *Adv. Mater.* **30**, 1707271 (2018).

253. Yang, B. Hybrid energy harvester based on piezoelectric and electromagnetic mechanisms. *J. Micro/Nanolithography, MEMS, MOEMS* **9**, 023002 (2010).

254. Sang, Y., Huang, X., Liu, H. & Jin, P. A vibration-based hybrid energy harvester for wireless sensor systems. *IEEE Trans. Magn.* **48**, 4495–4498 (2012).

255. Fan, K. *et al.* Scavenging energy from ultra-low frequency mechanical excitations through a bi-directional hybrid energy harvester. *Appl. Energy* **216**, 8–20 (2018).

256. Yu, H., Zhou, J., Yi, X., Wu, H. & Wang, W. A hybrid micro vibration energy harvester with power management circuit. *Microelectron. Eng.* **131**, 36–42 (2015).

257. Wang, H. yan, Tang, L. hua, Guo, Y., Shan, X. biao & Xie, T. A 2DOF hybrid energy harvester based on combined piezoelectric and electromagnetic conversion mechanisms. *J. Zhejiang Univ. Sci. A* **15**, 711–722 (2014).

258. Toyabur, R. M., Salauddin, M., Cho, H. & Park, J. Y. A multimodal hybrid energy harvester based on piezoelectric-electromagnetic mechanisms for low-frequency ambient vibrations. *Energy Convers. Manag.* **168**, 454–466 (2018).

259. Salauddin, M., Toyabur, R. M., Maharjan, P. & Park, J. Y. High performance human-induced vibration driven hybrid energy harvester for powering portable electronics. *Nano Energy* **45**, 236–246 (2018).

260. Jeon, S. B., Kim, D., Yoon, G. W., Yoon, J. B. & Choi, Y. K. Self-cleaning hybrid energy harvester to generate power from raindrop and sunlight. *Nano Energy* **12**, 636–645 (2015).

261. MengDi, H. *et al.* SCIENCE CHINA Low-frequency wide-band hybrid energy harvester based on pie-zoelectric and triboelectric mechanism. *Sci China Tech Sci* **56**, 1835–1841 (2013).

262. Eun, Y. *et al.* A flexible hybrid strain energy harvester using piezoelectric and electrostatic conversion. *Smart Mater. Struct.* **23**, 045040 (2014).

263. Lee, D.-Y. *et al.* Hybrid energy harvester based on nanopillar solar cells and PVDF nanogenerator. *Nanotechnology* **24**, 175402 (2013).

264. Xu, C. & Wang, Z. L. Compact Hybrid Cell Based on a Convoluted Nanowire Structure for Harvesting Solar and Mechanical Energy. *Adv. Mater.* **23**, 873–877 (2011).

265. Tan, Y. K. & Panda, S. K. Energy harvesting from hybrid indoor ambient light and thermal energy sources for enhanced performance of wireless sensor nodes. *IEEE Trans. Ind. Electron.* **58**, 4424–4435 (2011).

266. Wu, Y., Zhong, X., Wang, X., Yang, Y. & Wang, Z. L. Hybrid energy cell for simultaneously harvesting wind, solar, and chemical energies. *Nano Res.* **7**, 1631–1639 (2014).

267. Rahman, M. S., Sarker, P. & Chakravarty, U. K. A hybrid energy harvester based on solar radiation and mechanical vibration. *Appl. Phys. Lett.* **2121**, 130002 (2019).

268. Park, T. *et al.* Photothermally Activated Pyroelectric Polymer Films for Harvesting of Solar Heat with a Hybrid Energy Cell Structure. *ACS Nano* **9**, 11830–11839 (2015).

269. Williams, C. B. & Yates, R. B. Analysis of a micro-electric generator for microsystems. *Sensors Actuators, A Phys.* **52**, 8–11 (1996).

270. Beeby, S. P., Cao, Z. & Almussallam, A. Kinetic, thermoelectric and solar energy harvesting technologies for smart textiles. *Multidiscip. Know-How Smart-Textiles Dev.* 306–328 (2013) doi:10.1533/9780857093530.2.306.

271. Yu, D., Liu, Y., Zhao, H., Wang, G. & Qiu, J. Flexural vibration band gaps in Euler-Bernoulli beams with locally resonant structures with two degrees of freedom. *Phys. Rev. B* **73**, 064301 (2006).

272. Kok, S. L., White, N. M. & Harris, N. R. Fabrication and characterization of free-standing thick-film piezoelectric cantilevers for energy harvesting. *Meas. Sci. Technol.* **20**, (2009).

273. Bai, Y. Vibrational energy harvesting using piezoelectric ceramics and free-standing thick-film structures. *Univ. Birmingham, Ph.D. Thesis* 19–20 (2015).

274. Twiefel, J. & Westermann, H. Survey on broadband techniques for vibration energy harvesting. *Artic. J. Intell. Mater. Syst. Struct.* **24**, 1291–1302 (2013).

275. Ahmad, M. Al, Elshurafa, A. M., Salama, K. N. & Alshareef, H. N. Determination of maximum power transfer conditions of bimorph piezoelectric energy harvesters. *J. Appl. Phys.* **111**, 102812 (2012).

276. Zhu, D., Tudor, M. J. & Beeby, S. P. Strategies for increasing the operating frequency range of vibration energy harvesters: a review. *Meas. Sci. Technol.* **21**, 22001 (2009).

277. Liu, W. *et al.* Bandwidth increasing mechanism by introducing a curve fixture to the cantilever generator . *Appl. Phys. Lett* **109**, 43905 (2016).

278. Gieras, J., Oh, J., Huzmezan, M. & Number, H. S. Electromechanical energy harvesting system. (2007).

279. Wu, X. *et al.* A FREQUENCY ADJUSTABLE VIBRATION ENERGY HARVESTER. *Proc. PowerMEMS* 245–248 (2008).

280. Moon, K., Choe, J., Kim, H., Ahn, D. & Jeong, J. A method of broadening the bandwidth by tuning the proof mass in a piezoelectric energy harvesting cantilever. *Sensors Actuators, A Phys.* **276**, 17–25 (2018).

281. Xiao, Z. *et al.* Giant switchable photovoltaic effect in organometal trihalide perovskite devices. *Nat. Mater.* **14**, 193–198 (2015).

282. Yuan, Y. *et al.* Photovoltaic Switching Mechanism in Lateral Structure Hybrid Perovskite Solar Cells. *Adv. Energy Mater.* **5**, 1500615 (2015).

283. Priya, S. Criterion for material selection in design of bulk piezoelectric energy harvesters. *IEEE Trans. Ultrason. Ferroelectr. Freq. Control* **57**, 2610–2612 (2010).

284. Gao, X. *et al.* Giant Piezoelectric Coefficients in Relaxor Piezoelectric Ceramic PNN-PZT for Vibration Energy Harvesting. *Adv. Funct. Mater.* **28**, (2018).

285. Daniels, A., Zhu, M. & ultrasonics, A. T. Evaluation of piezoelectric material properties for a higher power output from energy harvesters with insight into material selection using a

coupled piezoelectric-circuit. *IEEE Trans. Ultrason. Ferroelectr. Freq. Control* **60**, 2626–2633 (2013).

286. Richards, C. D., Anderson, M. J., Bahr, D. F. & Richards, R. F. Efficiency of energy conversion for devices containing a piezoelectric component. *J. Micromechanics Microengineering* **14**, 717 (2004).

287. Yan, X., Zheng, M., Hou, Y. & Zhu, M. Composition-driven phase boundary and its energy harvesting performance of BCZT lead–free piezoelectric ceramic. *J. Eur. Ceram. Soc.* **37**, 2583–2589 (2017).

288. Wang, F., Grinberg, I. & Rappe, A. M. Band gap engineering strategy via polarization rotation in perovskite ferroelectrics. *Appl. Phys. Lett.* **104**, (2014).

289. Ngo, D. *et al.* Band gap modification and ferroelectric properties of Bi 0.5 (Na,K) 0.5 TiO 3-based by Li substitution. *AIP Adv.* **4**, 17122 (2014).

290. Standard, A. Standard test methods for determining average grain size. *ASTM Int. West Chonshohocke, PA* (2013).

291. Standard, A. E112: Standard test methods for determining average grain size. *West Conshocken* **112**, 4–20 (1996).

292. Mccusker, L. B., Von Dreele, R. B., Cox, D. E., Louër, D. & Scardi, P. Rietveld refinement guidelines. *J. Appl. Crystallogr.* **32**, 36–50 (1999).

293. Rietveld, H. M. The Rietveld method. *Physica Scripta* vol. 89 (2014).

294. Bish, D., Crystallography, S. H.-J. of A. & 1988, undefined. Quantitative phase analysis using the Rietveld method. *scripts.iucr.org*.

295. Tu, C.-S. *et al.* Enhancing Photovoltaic and Photosensing Performances in Bismuth Ferrite via Polar Order Engineering. *ACS Appl. Electron. Mater.* **2**, 3773–3782 (2020).

296. Fialka, J. & Beneš, P. Comparison of methods for the measurement of piezoelectric coefficients. *IEEE Trans. Instrum.* **62**, (2013).

297. Kozuka, H. *et al.* Improvement of (K,Na)NbO3-based lead-free piezoelectric ceramics by asymmetric octahedra. *J. Mater. Chem. C* **4**, 9756–9761 (2016).

298. Pascual-González, C. Processing-composition-structure effects on the optical band gap of KNbO 3-based ceramics. (Sheffield Hallam University, 2017).

299. Sharma, K., Sharma, V. & Sharma, S. S. Dye-Sensitized Solar Cells: Fundamentals and Current Status. doi:10.1186/s11671-018-2760-6.

300. Rubio-Marcos, F., Romero, J. J., Martín-Gonzalez, M. S. & Fernández, J. F. Effect of stoichiometry and milling processes in the synthesis and the piezoelectric properties of modified KNN nanoparticles by solid state reaction. *J. Eur. Ceram. Soc.* **30**, 2763–2771 (2010).

301. Beltrami, R. *et al.* Synthesis of KNN powders: Scaling effect of the milling step. *Powder Technol.* **375**, 101–108 (2020).

302. Okuyama, Y., Ymaguchi, T., Matsunaga, N. & Sakai, G. Proton Conduction and Incorporation into La1−xBaxYb0.5In0.5O3−δ. *MATERIALS TRANSACTIONS* vol. 59 14–18 (2018).

303. Jaffe, B. *Piezoelectric ceramics*. (2012).

304. Darja, J., Bencan, A., Malic, B., Holc, J. & Marija kose. Electron Microscopy Studies of Potassium Sodium Niobate Ceramics. *Microsc. Microanal.* **11**, 572–580 (2005).

305. Standard Test Methods for Determining Average Grain Size 1. doi:10.1520/E0112-10.

306. Zheng, P., Zhang, J. L., Tan, Y. Q. & Wang, C. L. Grain-size effects on dielectric and piezoelectric properties of poled BaTiO 3 ceramics. *Acta Mater.* **60**, 5022–5030 (2012).

307. Bakarič, T. *et al.* Effect of pore size and porosity on piezoelectric and acoustic properties of Pb(Zr0.53Ti0.47)O3 ceramics. *Adv. Appl. Ceram.* **115**, 66–71 (2016).

308. Liu, W. & Ren, X. Large piezoelectric effect in Pb-free ceramics. *Phys. Rev. Lett.* **103**, 1–4 (2009).

309. Tan, Y. *et al.* Unfolding grain size effects in barium titanate ferroelectric ceramics. *Sci. Rep.* **5**, 15–21 (2015).

310. Qin, Y., Zhang, J., Yao, W., Wang, C. & Zhang, S. Domain structure of potassium-sodium niobate ceramics before and after poling. *J. Am. Ceram. Soc.* **98**, 1027–1033 (2015).

311. Cho, J.-H., Lee, Y.-H. & Kim, B.-I. Domain structure of orthorhombic (Li,K,Na)NbO3 ceramics. *J. Ceram. Process. Res.* **11**, 237–240 (2010).

312. López-Juárez, R., Novelo-Peralta, González-García, F., Rubio-Marcos, F. & Villafuerte-Castrejón, M.-E. Ferroelectric domain structure of lead-free potassium-sodium niobate ceramics. *J. Eur. Ceram. Soc.* **31**, 1861–1864 (2011).

313. Cao, W. & Randall, C. A. GRAIN SIZE AND DOMAIN SIZE RELATIONS IN BULK CERAMIC FERROELECTRIC MATERIALS. *Phys. Chem Solie* **57**, 149–1505 (1996).

314. Islam, R. A. & Priya, S. Realization of high-energy density polycrystalline piezoelectric ceramics. *Appl. Phys. Lett.* **88**, 1–3 (2006).

315. Li, Z., Gan, W., He, X., Lu, H. & Zhang, Y. Effect of particle size, transparency and light intensity on the color of powder. *IOP Conf. Ser. Mater. Sci. Eng.* **545**, (2020).

316. Ramana, C. V., Smith, R. J. & Hussain, O. M. Grain size effects on the optical characteristics of pulsed-laser deposited vanadium oxide thin films. *Phys. status solidi* **199**, R4–R6 (2003).

317. Svensson, T., Adolfsson, E., Lewander, M., Xu, C. T. & Svanberg, S. *Disordered, strongly scattering porous materials as miniature multipass gas cells*. (2010).

318. Gupta, K., Lin, T., Wang, R. C. & Liu, C. P. Porosity-induced full-range visible-light photodetection via ultrahigh broadband antireflection in ZnO nanowires. *NPG Asia Mater.* **8**, 314 (2016).

319. Oh, T. S. *et al.* Evidence and Model for Strain-Driven Release of Metal Nanocatalysts from Perovskites during Exsolution. *J. Phys. Chem. Lett.* **6**, 5106–5110 (2015).

320. Rani, J., Yadav, · K L & Prakash, S. Modified structure and electrical properties of BSZT doped KNN hybrid ceramic. *Appl Phys A* **108**, 761–764 (2012).

321. Lin, D., Kwok, W., Chan, L. W., Ramam, K. & Lopez, M. Ferroelectric and piezoelectric properties of Ba modified lead zirconium titanate ceramics. *J. Phys. D Appl. Phys* **39**, 4466–4471 (2006).

322. Zhou, W., Deng, H., Yang, P. & Chu, J. Structural phase transition, narrow band gap, and room-temperature ferromagnetism in [KNbO3]1-x[BaNi1/2Nb1/2O3-δ]xferroelectrics. *Appl. Phys. Lett.* **105**, 1–5 (2014).

323. Sato, Y., Kanai, H. & Yamashita, Y. Grain size dependence of dielectric constant for modified (Pb 0.63 Ba 0.37)(Zr0.7 Ti0.3)O3 ceramic material. *Jpn. J. Appl. Phys.* **33**, 1380–1384 (1994).

324. Wendelbo, R. ., D. E. Akporiaye, A. Karlsson, M. Plassen & and A. Olafsen. Combinatorial hydrothermal synthesis and characterisation of perovskites. *J. Eur. Ceram. Soc.* **26**, 849–851 (2006).

325. Rosen, B. A. Progress and Opportunities for Exsolution in Electrochemistry. *Electrochem* **1**, 32–43 (2020).

326. Kwon, O., Joo, S., Choi, S., Sengodan, S. & Kim, G. Review on exsolution and its driving forces in perovskites. *J. Phys. Energy* **2**, 032001 (2020).

327. Kwon, O. *et al.* Exsolution trends and co-segregation aspects of self-grown catalyst nanoparticles in perovskites. *Nat. Commun.* **8**, 1–7 (2017).

328. Nishihata, Y. *et al.* Self-regeneration of a Pd-perovskite catalyst for automotive emissions control. *nature.com*.

329. Neagu, D., Tsekouras, G., Miller, D. N., Ménard, H. & Irvine, J. T. S. In situ growth of nanoparticles through control of non-stoichiometry. *Nat. Chem.* **5**, 916–923 (2013).

330. Agüero, F. N., Beltrán, A. M., Fernández, M. A. & Cadús, L. E. Surface nickel particles generated by exsolution from a perovskite structure. *J. Solid State Chem.* **273**, 75–80 (2019).

331. Patterson, A. L. The scherrer formula for X-ray particle size determination. *Phys. Rev.* **56**, 978–982 (1939).

332. Bindu, P. & Thomas, S. Estimation of lattice strain in ZnO nanoparticles: X-ray peak profile analysis. *J. Theor. Appl. Phys.* **8**, 123–134 (2014).

333. Shannon, R. D. Revised effective ionic radii and systematic studies of interatomic distances in halides and chalcogenides. *Acta Crystallogr. Sect. A* **32**, 751–767 (1976).

334. Goel, R. *et al.* Enhanced room temperature multiferroic behaviour of Ni-doped Na 0.5 Bi 0.5 TiO 3 ceramics. *J. Mater. Sci. Mater. Electron.* (2021) doi:10.1007/s10854-021-05681-4.

335. Gao, J. *et al.* Phase transition sequence in Pb-free 0.96(K0.5Na0.5)0.95Li0.05Nb0.93 Sb0.07O3-0.04BaZrO3 ceramic with large piezoelectric response. *Appl. Phys. Lett.* **107**, (2015).

336. Wang, R., Bando, H. & Itoh, M. Universality in phase diagram of (K,Na) NbO3-MTiO3 solid solutions. *Appl. Phys. Lett.* **95**, 092905 (2009).

337. Mahesh, P. & Pamu, D. Raman and dielectric studies on lead free (K0.5Na0.5) NbO3 piezoelectric ceramics. *IOP Conf. Ser. Mater. Sci. Eng.* **73**, 0–5 (2015).

338. Wang, Y., Hu, L., Zhang, Q. & Yang, H. Phase transition characteristics and associated piezoelectricity of potassium-sodium niobate lead-free ceramics. *Dalt. Trans.* **44**, 13688–13699 (2015).

339. Wang, L. *et al.* Improved electrical properties for Mn-doped lead-free piezoelectric potassium sodium niobate ceramics. *AIP Adv.* **5**, (2015).

340. Peddigari, M. & Dobbidi, P. Raman, dielectric and variable range hopping nature of Gd2O3-doped K0.5N0.5NbO3 piezoelectric ceramics. *AIP Adv.* **5**, 107129 (2015).

341. Liu, L. *et al.* Average vs. local structure and composition-property phase diagram of K0.5Na0.5NbO3-Bi½Na½TiO3 system. *J. Eur. Ceram. Soc.* **37**, 1387–1399 (2017).

342. Reyes-Montero, A. *et al.* Confocal Raman Microscopy, Synchrotron X-ray Diffraction, and Photoacoustic Study of Ba 0.85 Ca 0.15 Ti 0.90 Zr 0.10 O 3 : Understanding Structural and Microstructural Response to the Electric Field. (2021) doi:10.1021/acsaelm.1c00103.

343. Wang, D. *et al.* Composition and temperature dependence of structure and piezoelectricity in (1−x)(K1−yNay)NbO3-x(Bi1/2Na1/2)ZrO3 lead-free ceramics. *J. Am. Ceram. Soc.* **100**, 627–637 (2017).

344. Chai, Q., Zhao, X., Chao, X. & Yang, Z. Enhanced transmittance and piezoelectricity of transparent K0.5Na0.5NbO3 ceramics with Ca(Zn1/3Nb2/3)O3 additives. *RSC Adv.* **7**, 28428–28437 (2017).

345. Zhou, J. S. *et al.* Multi-scale thermal stability of niobate-based lead-free piezoceramics with large piezoelectricity. *J. Mater. Chem. C* **3**, 8780–8787 (2015).

346. Peddigari, M. & Dobbidi, P. Raman, dielectric and variable range hopping nature of Gd 2 O 3-doped K 0.5 N 0.5 NbO 3 piezoelectric ceramics. *AIP Advances* vol. 5 107129 (2015).

347. Singh, R., Kambale, K., Kulkarni, A. R. & Harendranath, C. S. Structure composition correlation in KNN-BT ceramics-An X-ray diffraction and Raman spectroscopic investigation. *Mater. Chem. Phys.* **138**, 905–908 (2013).

348. Kakimoto, K. I., Akao, K., Guo, Y. & Ohsato, H. Raman scattering study of piezoelectric (Na0.5K 0.5)NbO3-LiNbO3 ceramics. *Japanese J. Appl. Physics, Part 1 Regul. Pap. Short Notes Rev. Pap.* **44**, 7064–7067 (2005).

349. Ahn, C. W., Lee, S. Y. & Lee, H. J. Raman Spectra Study of K 0.5 Na 0.5 NbO 3 Ferroelectric Thin Films Related content The effect of K and Na excess on the ferroelectric and piezoelectric properties of K 0.5 Na 0.5 NbO 3 thin films. *Jpn. J. Appl. Phys.* **49**, (2010).

350. Zhu, W. L. *et al.* Structural characteristics of Mg-doped (1-x)(K 0.5Na 0.5)NbO 3xLiSbO 3 lead-free ceramics as revealed by Raman spectroscopy. *J. Phys. D. Appl. Phys.* **44**, (2011).

351. Zhang, M. H. *et al.* Thermally stable piezoelectric properties of (K, Na)NbO3-based lead-free perovskite with rhombohedral-tetragonal coexisting phase. *Acta Mater.* **122**, 344–351 (2017).

352. Wang, Y. U. Diffraction theory of nanotwin superlattices with low symmetry phase: Application to rhombohedral nanotwins and monoclinic MA and MB phases. *Phys. Rev. B - Condens. Matter Mater. Phys.* **76**, 024108 (2007).

353. Wang, Y. U. Diffraction theory of nanotwin superlattices with low symmetry phase. *Phys. Rev. B - Condens. Matter Mater. Phys.* **74**, 104109 (2006).

354. Baker, D. W., Thomas, P. A., Zhang, N. & Glazer, A. M. Structural study of Kx Na1 - X NbO3 (KNN) for compositions in the range x = 0.24-0.36. *Acta Crystallogr. Sect. B Struct. Sci.* **65**, 22–28 (2009).

355. Liang, X., Meng, Z. & Wu, W. Effect of Acceptor and Donor Dopants on the Dielectric and Tunable Properties of Barium Strontium. *J. Am. Ceram. Soc* **87**, 2218–2222 (2004).

356. Perumal, R. N. & Marimuthu, A. Temperature dependence on dielectric and ferroelectric properties of rubidium titanyl phosphate single crystal. *Journal of Materials Science: Materials in Electronics* vol. 31 6385–6393 (2020).

357. Sun, Y., Liu, H., Hao, H. & Zhang, S. Effect of Oxygen Vacancy on Electrical Property of Acceptor Doped BaTiO3–Na0.5Bi0.5TiO3–Nb2O5 X8R Systems. *J. Am. Ceram. Soc.* **99**, 3067–3073 (2016).

358. Fei Liu, S., Wu, Y. J., Li, J. & Ming Chen, X. Effects of oxygen vacancies on dielectric, electrical, and ferroelectric properties of Ba4Nd2Fe2Nb8O 30 ceramics. *Appl. Phys. Lett.* **104**, 082912 (2014).

359. Li, M. D. *et al.* Oxygen-vacancy-related dielectric relaxation behaviours and impedance spectroscopy of Bi(Mg1/2Ti1/2)O3 modified BaTiO3 ferroelectric ceramics. *J. Mater.* **4**, 194–201 (2018).

360. Xiao, H. *et al.* Understanding the Role of Oxygen Vacancy in Visible–Near-Infrared-Light-Absorbing Ferroelectric Perovskite Oxides Created by Off-Stoichiometry. *Adv. Electron. Mater.* **5**, (2019).

361. Noguchi, Y., Matsuo, H., Kitanaka, Y., Reports, M. M.-S. & 2019, U. Ferroelectrics with a controlled oxygen-vacancy distribution by design. *Sci. Rep.* (2019).

362. Shao, T. *et al.* Potassium-sodium niobate based lead-free ceramics: novel electrical energy storage materials. *J. Mater. Chem. A* **5**, 554–563 (2017).

363. Kitanaka, Y., Noguchi, Y. & Miyayama, M. Oxygen-vacancy-induced 90°-domain clamping in ferroelectric Bi 4 Ti 3 O 12 single crystals. doi:10.1103/PhysRevB.81.094114.

364. López, R. & Gómez, R. Band-gap energy estimation from diffuse reflectance measurements on sol-gel and commercial TiO 2: A comparative study. *J. Sol-Gel Sci. Technol.* **61**, 1–7 (2012).

365. Bai, Y. Counterfeit band gaps caused by microstructural voids in photo-ferroelectric ceramics. *Open Ceram.* 100079 (2021) doi:10.1016/j.oceram.2021.100079.

366. Park, J., Won, S. S., Ahn, C. W. & Kim, I. W. Ferroelectric Photocurrent Effect in Polycrystalline Lead-Free ($K_{0.5}Na_{0.5}$)($Mn_{0.005}Nb_{0.995}$)O_3 Thin Film. *J. Am. Ceram. Soc.* **96**, 146–150 (2013).

367. Tan, Z. *et al.* Thinning ferroelectric films for high-efficiency photovoltaics based on the Schottky barrier effect. *NPG Asia Mater.* **11**, 1–13 (2019).

368. Poosanaas, P., Dogan, A., Thakoor, S. & Uchino, K. Influence of sample thickness on the performance of photostrictive ceramics. *J. Appl. Phys.* **84**, 1508–1512 (1998).

369. Keizer, K. Grain Size Effects on the Ferroelectric-Paraelectric Transition, the Dielectric Constant, and the Lattice Parameters in Lanthana-Substituted Lead Titanate. **561**, 561–569 (1974).

370. Padurariu, L., Lukacs, V.-A., Stoian, G., Nicoleta, L. & Petronela, L. Scale-Dependent Dielectric Properties in BaZr0.05Ti0.95O3 Ceramics. *Materials (Basel).* **13**, 1–9 (2020).

371. Hu, W., Chen, Z., Lu, Z., Wang, X. & Fu, X. Effect of Bi2O3 and Ho2O3 co-doping on the dielectric properties and temperature reliability of X8R BaTiO3-based ceramics. *Ceram. Int.* **47**, 24982–24987 (2021).

372. Zhu, F. *et al.* Diffuse dielectric behaviour in Na0.5K0.5NbO 3-LiTaO3-BiScO3 lead-free ceramics. *Mater. Chem. Phys.* **129**, 411–417 (2011).

373. Long, C. *et al.* High oxide ion conductivity in layer-structured Bi 4 Ti 3 O 12-based ferroelectric ceramics High oxide ion conductivity in layer-structured Bi 4 Ti 3 O 12-based ferroelectric ceramics †. *J. Mater. Chem. C* **7**, 8825 (2019).

374. Gupta, R., Verma, S., Singh, D., Singh, K. & Bamzai, K. K. Effect of Ni/Nb on structure, electrical and ferroelectric properties of 0.5PNN-0.5PZT ceramics. *Processing and Application of Ceramics* vol. 9 1–9 (2015).

375. Batool, S. S. *et al.* Study of electric conduction mechanisms in bismuth silicate nanofibers. *Scientific reports* 2775 (2020) doi:10.1038/s41598-020-59563-6.

376. Borkar, H. & Kumar, A. Effects of light on ferroelectric polarization and leakage current. *Vacuum* **153**, 91–95 (2018).

377. Borkar, H. *et al.* Experimental evidence of electronic polarization in a family of photo-ferroelectrics. *RSC Adv.* **7**, 12842–12855 (2017).

378. Land, C. E. & Smith, W. D. Reflective-mode ferroelectric-photoconductor image storage and display devices. *Appl. Phys. Lett.* **23**, 57–59 (1973).

379. Liang, J. & Liao, W. H. Impedance modeling and analysis for piezoelectric energy harvesting systems. *IEEE/ASME Trans. Mechatronics* **17**, 1145–1157 (2012).

Appendix I. Actual amounts of raw powders added for initial synthesis

1. $(K_{0.5}Na_{0.5})NbO_3$ composition (50g, Unit: g)

Raw material/g	5KNN
K_2CO_3	8.907
Na_2CO_3	6.831
Nb_2O_5	34.262

2. KNN-based composition (50g, Unit: g)

Raw material	5KNN-2BNNO	5KNN-4BNNO	5KNN-6BNNO	5KNN-8BNNO	5KNN-10BNNO
K_2CO_3	8.634	8.366	8.104	7.848	7.597
Na_2CO_3	6.621	6.416	6.215	6.018	5.826
Nb_2O_5	33.548	32.850	32.167	31.499	30.844
$BaCO_3$	1.006	1.991	2.954	3.898	4.821
NiO	0.190	0.377	0.559	0.738	0.912

Appendix II. XRD refinement

1. Basic introduction of XRD refinement using TOPAS-Academic

The user interface (UI) of TOPAS-Academic software is shown in figure II. 1, consisting of main parameter window, fitting window, data window and quantitative analysis results window. The parameters of D8 XRD instrument are also listed in table II.1.

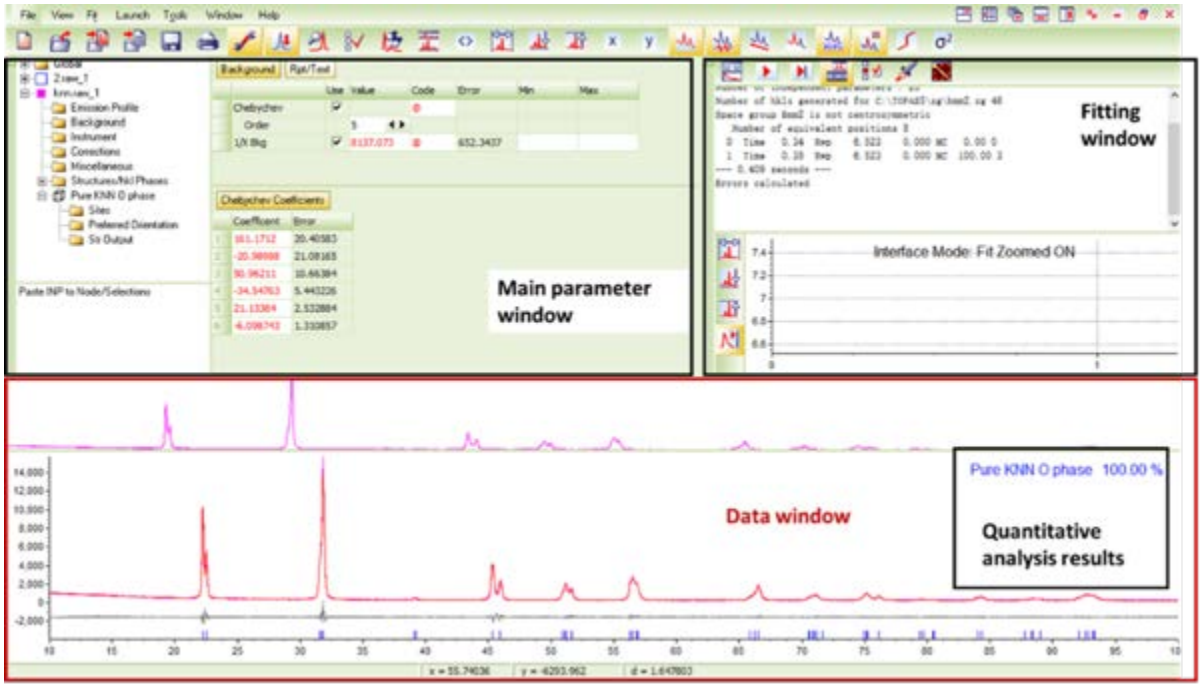

Figure II.1 UI of TOPAS-Academic

Table II.1 Parameter of D8 XRD instrument

Parameter		values
Goniometer radii	Primary radius	280 mm
	Secondary radius	280 mm
Equatorial convolutions Linear PSD	2^{nd} angular range of LPSD	2.91°
	FDS angle	0.3°
	Beam spill, sample length	20 mm
	Prim. Soller	2.5°
	Sec. Soller	2.5°
Lorentz-polarisation factor		0

2. Rietveld refinement

The basic Rietveld refinement analysis procedures by using TOPAS-Academic software is shown in fugue II. 2 and the detailed analysis of 5KNN composition are shown in figure II.3 – figure II. 8.

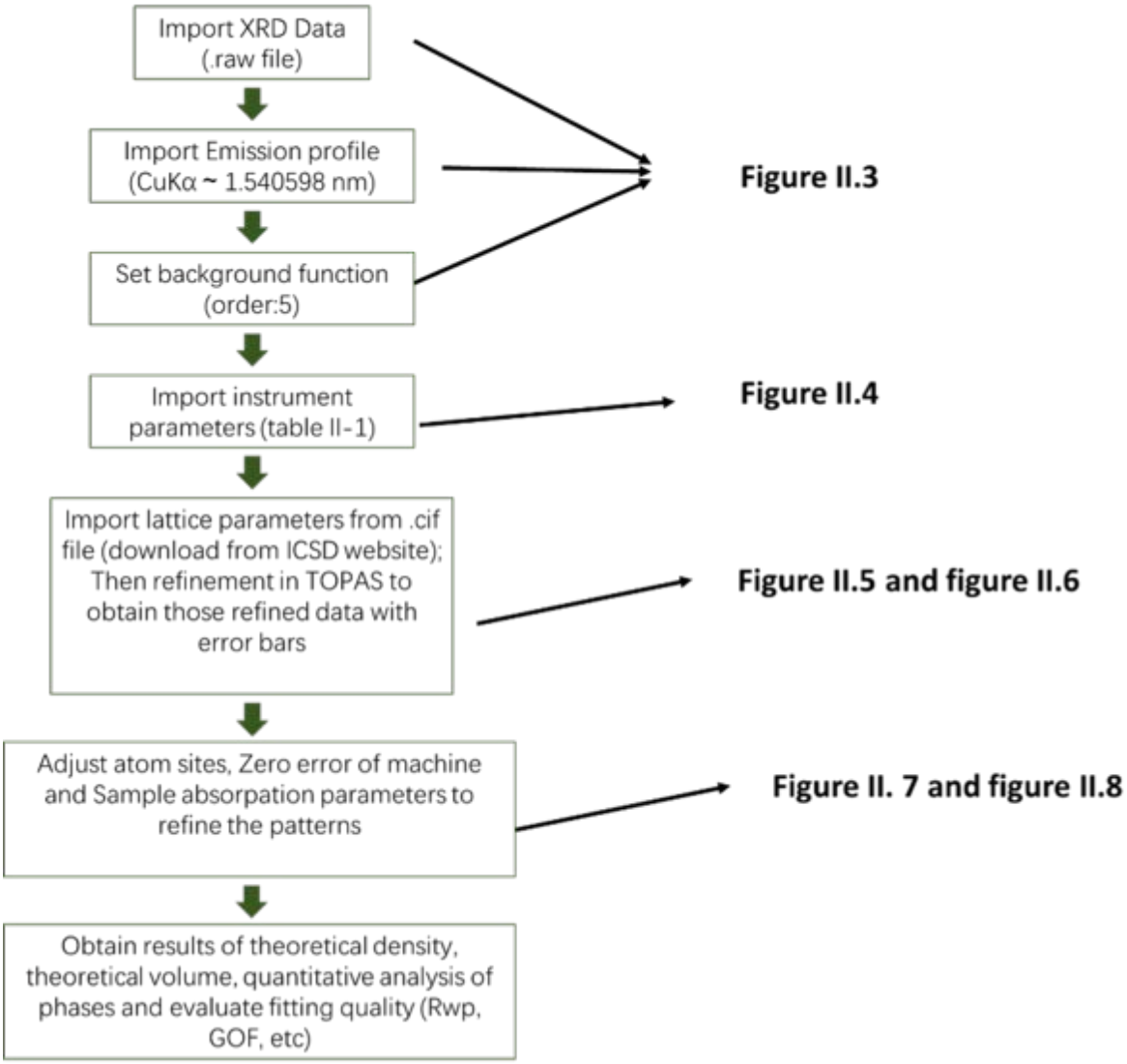

Figure II.2 Rietveld refinement analysis procedures

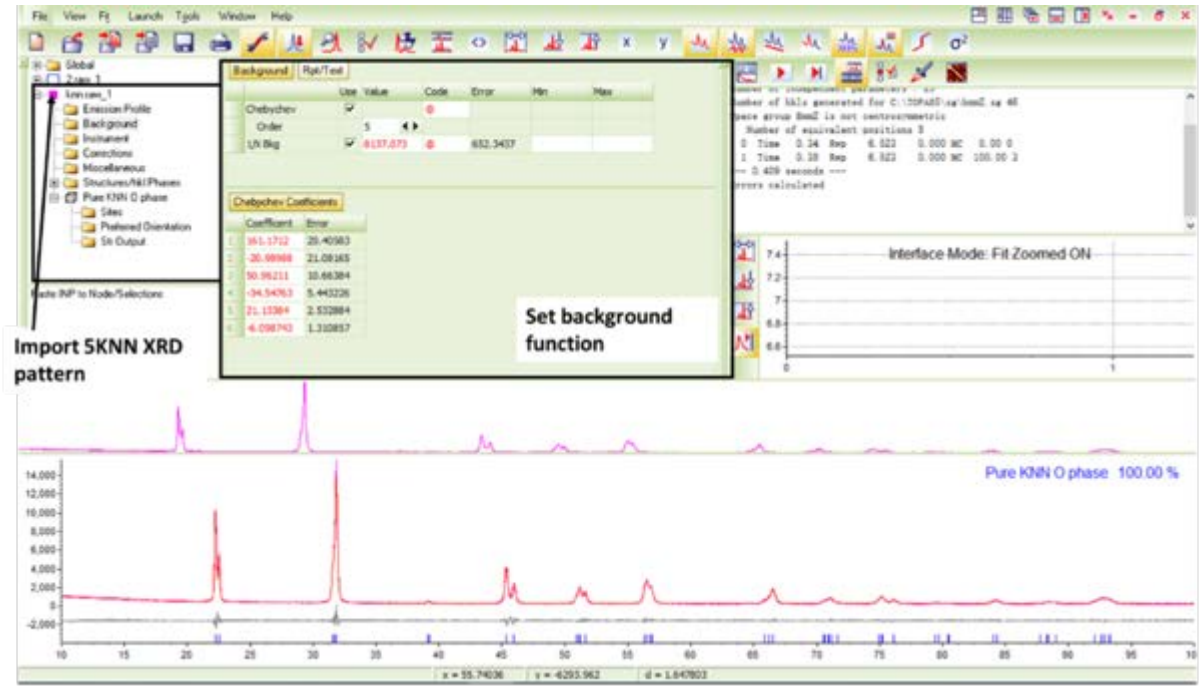

Figure II.3 UI of importing 5KNN XRD pattern and setting background function

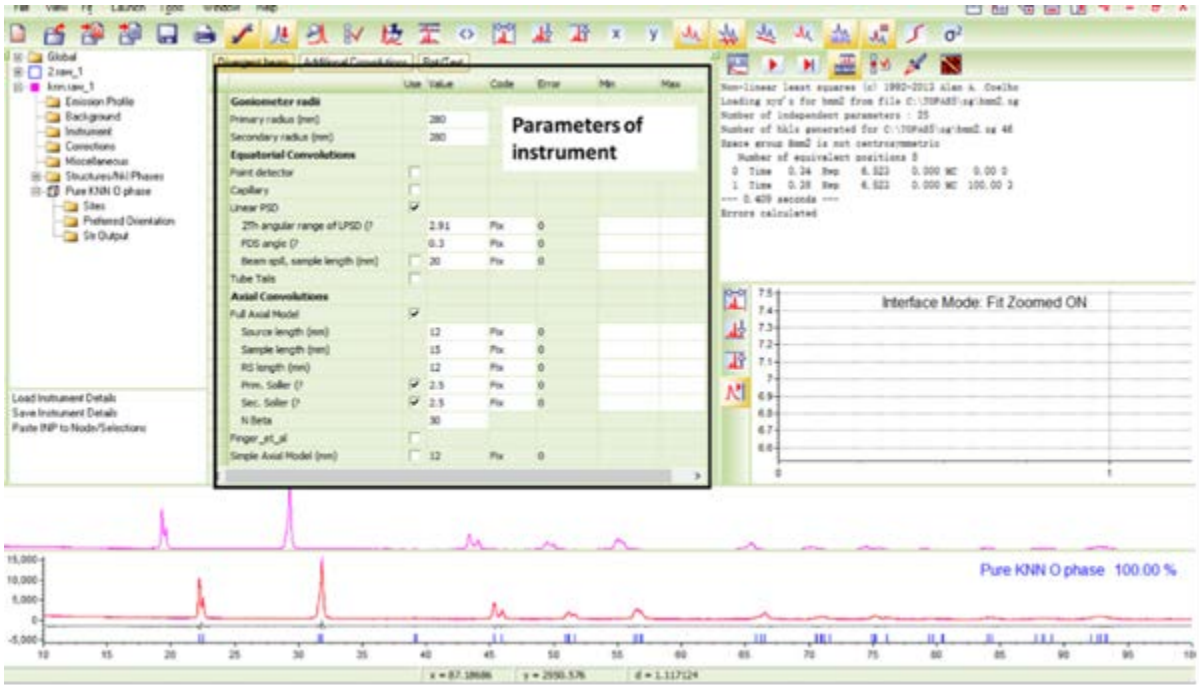

Figure II.4 UI of importing parameters of D8 XRD equipment

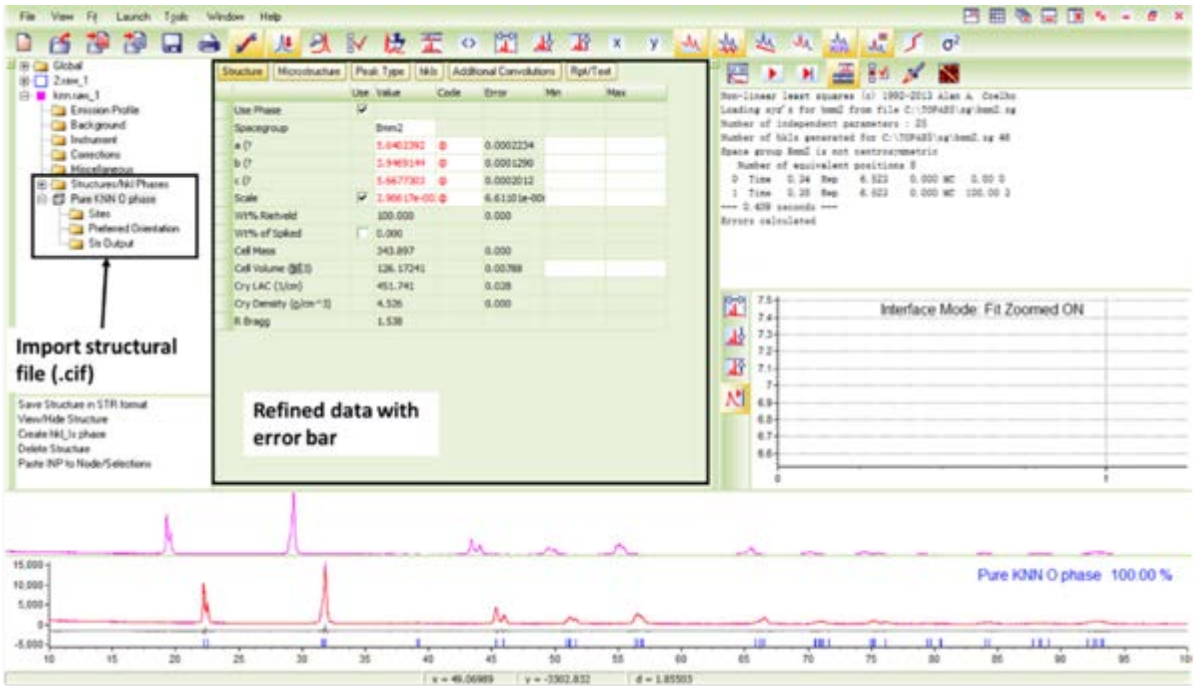

Figure II.5 UI of refinement in TOPAS

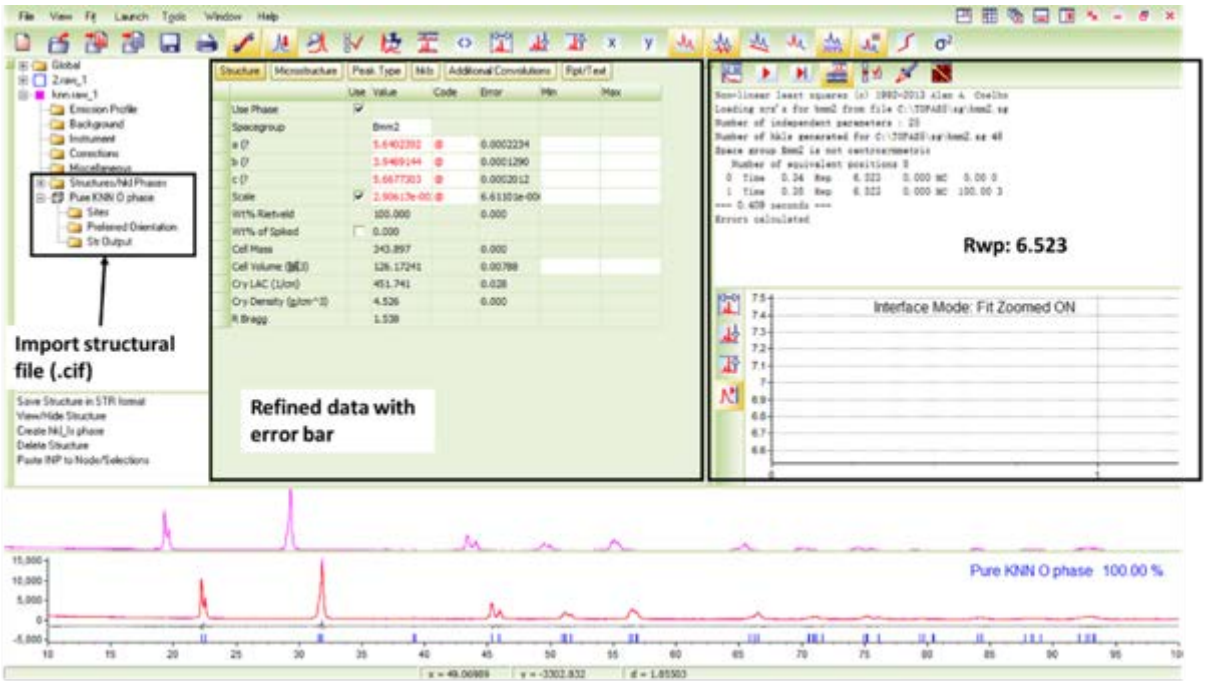

Figure II.6 UI of refinement in TOPAS

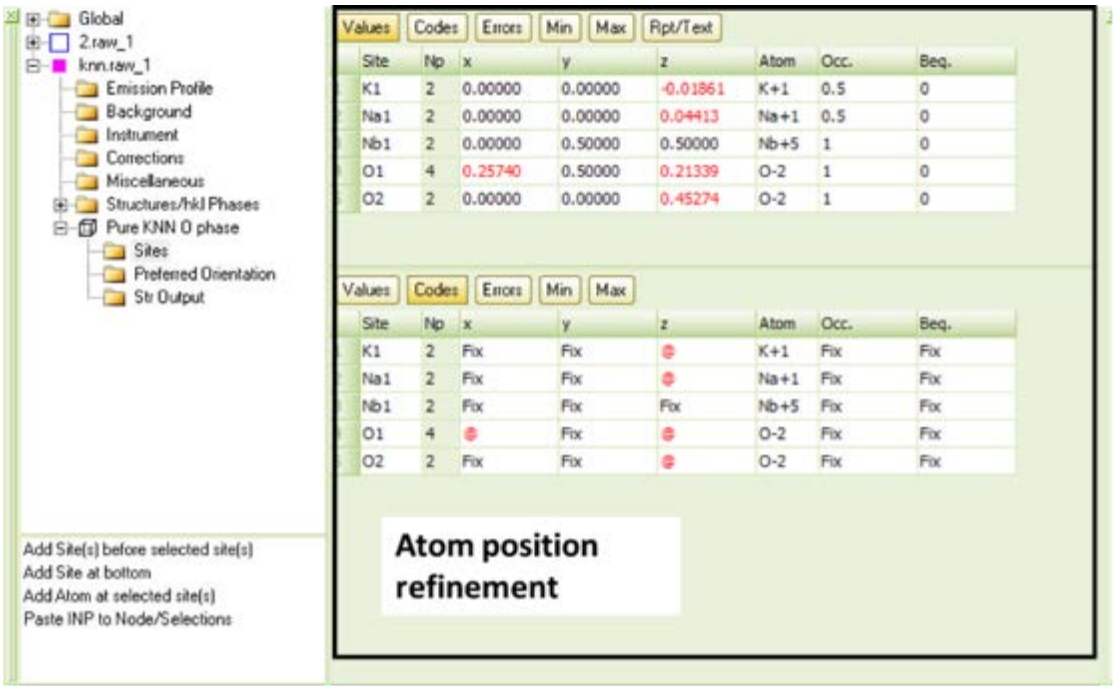

Figure II.7 UI of adjusting atom positions

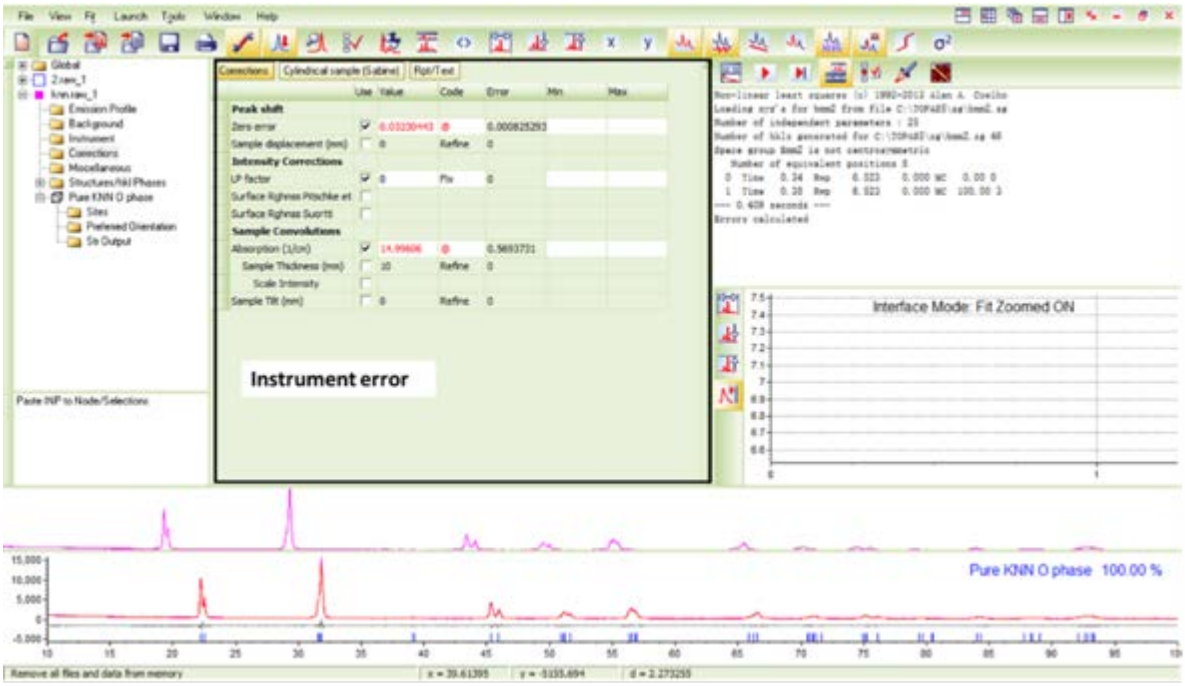

Figure II.8 UI of Zero correction and sample absorption

The XRD refinement of BNNO doped 5KNN composition were using same procedures with 5KNN. Because the .cif file of BNNO doped 5KNN is not available, the Ba, Ni atom were manually added into A-site and B-site of 5KNN. Cif file, respectively, for further refinement (figure II.9).

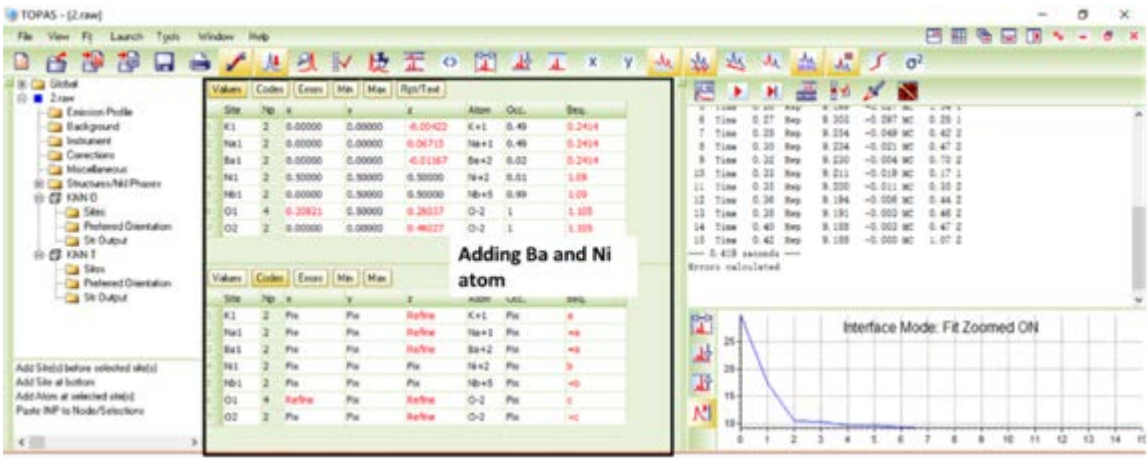

Figure II.9 UI of Ba, Ni atom addition

3. The refined pattern in TOPAS

The refined results of 5KNN and 5KNN-2BNNO composition are shown in figure II.10 – figure II 11, respectively. It can be seen from figure II.10, the purple line represents measured pattern, the red line represents the refined pattern, and the grey line represents the difference between measured data and the refined data.

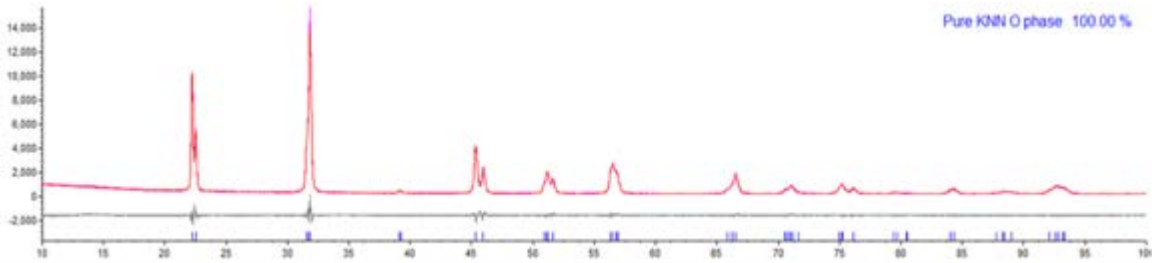

Figure II.10 Refinement of 5KNN sintered at 1120°C/10 min/1070°C/10 h

Similarly with 5KNN refinement results. The blue line in figure II.11 represent measured patterns of 5KNN-2BNNO. Also, the red lines and the grey lines represent the calculated data and the difference. The weight fractions of each phase were exhibited on the right corner.

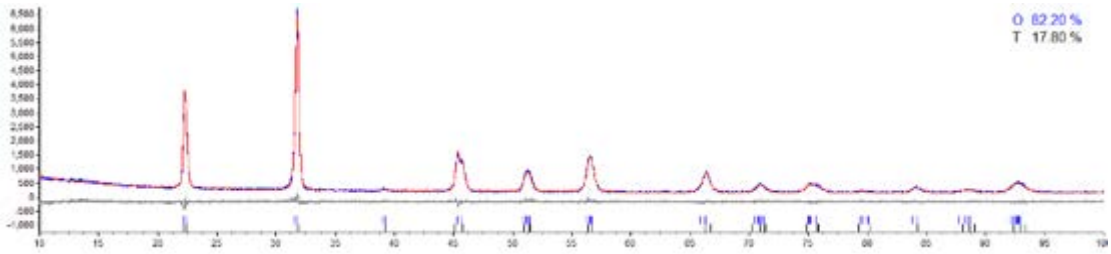

Figure II.11 Refinement of 5KNN-2BNNO sintered at 1175°C/2 h

4. The results obtained from TOPAS

5KNN composition

File 4 : " E:\desktop\Thesis\thesis\5KNN.raw"

File Name

R-Values

Rexp : 5.50 Rwp : 8.55 Rp : 6.58 GOF : 1.55

Rexp`: 6.87 Rwp`: 10.68 Rp` : 8.42 DW : 0.84

Evaluation of fitting

Quantitative Analysis - Rietveld

Phase 1 : Orthorhombic 100.000 %

Calculated weight fraction of KNN orthorhombic phase

Background

One on X 6000(500)

Chebychev polynomial, Coefficient 0 78(17)

1 16(17)

2 17(9)

3 -18(4)

4 12(2)

5 -5.8(11)

Background profile

Instrument

Primary radius (mm) 280

Secondary radius (mm) 280

Linear PSD 2Th angular range (°) 2.91

FDS angle (°) 0.3

Full Axial Convolution

Filament length (mm) 12

Sample length (mm) 15

Receiving Slit length (mm) 12

Primary Sollers (°) 2.5

Secondary Sollers (°) 2.5

D8 XRD instrument profile

Corrections

Zero error 0.0325(8)

LP Factor 0

Absorption (1/cm) 15.0(6)

Corrections of machine and sample absorption

KNN-Orthorhombic

Phase name Orthorhombic

R-Bragg 2.484

Spacegroup Bmm2

Scale 0.001545(4)

Cell Mass 343.897

Cell Volume (Å ^3) 126.396(6)

Wt% - Rietveld 100.000

Double-Voigt|Approach

Cry size Lorentzian 177(11)

k: 1 LVol-IB (nm) 113(7)

k: 0.89 LVol-FWHM (nm) 157(10)

Crystal Linear Absorption Coeff. (1/cm) 450.94(2)

Crystal Density (g/cm^3) 4.518(2)

PV_MOD peak type: a + b Tan(Th) + c / Cos(Th)

FWHM a 0.03(8)

Structural file from .cif file (based on KNN orthorhombic phase) and the refined data with error

Theoretical volume of orthorhombic phase

Theoretical density of orthorhombic phase

b 0.27(4)

c 0.04(9)

Lorentzian mix a 0.1(8)

b 0.8(5)

c 0.2(9)

Lattice parameters

a (Å) 5.64359(18)

b (Å) 3.94702(10)

c (Å) 5.67426(17)

Refined lattice parameters

Site	Np	x	y	z	Atom	Occ	Beq
K1	2	0.00000	0.00000	-0.01770	K+1	0.5	0
Na1	2	0.00000	0.00000	0.00380	Na+1	0.5	0
Nb1	2	0.00000	0.50000	0.50000	Nb+5	1	0
O1	4	0.25740	0.50000	0.22530	O-2	1	0
O2	2	0.00000	0.00000	0.47040	O-2	1	0

Refined atom position

5KNN-2BNNO composition

File 1 : "E:\desktop\Thesis\thesis\5KNN-2BNNO.raw"

File Name

R-Values

Rexp : 5.40 Rwp : 6.81 Rp : 5.33 GOF : 1.26

Rexp`: 5.45 Rwp`: 6.88 Rp` : 5.48 DW : 1.26

Evaluation of fitting

Quantitative Analysis - Rietveld

Phase 1 : "KNN O " 82.2(19) %

Phase 2 : "KNN T" 17.8(19) %

Calculated weight fraction of KNN orthorhombic phase and KNN tetragonal phase

Background

One on X 8900(500)

Chebychev polynomial, Coefficient 0 -1(16)

1 102(16)

2 -29(8)

3 10(4)

4 -1(2)

5 -1.0(10)

Background profile

Instrument

Primary radius (mm) 280

Secondary radius (mm) 280

Linear PSD 2Th angular range (°) 2.91

FDS angle (°) 0.3

D8 XRD instrument profile

Full Axial Convolution

Filament length (mm) 12

Sample length (mm) 15

Receiving Slit length (mm) 12

Primary Sollers (°) 2.5

Secondary Sollers (°) 2.5

Corrections

Zero error 0.0171(18)

LP Factor 0

Absorption (1/cm) 9.3(6)

Corrections of machine and sample absorption

KNN-Orthorhombic

Phase name KNN O

R-Bragg 2.371

Spacegroup Bmm2

Scale 0.00126(3)

Cell Mass 347.464

Cell Volume (Å^3) 126.72(3)

Wt% - Rietveld 82.2(19)

Double-Voigt|Approach

Structural file from .cif file (based on KNN orthorhombic phase) and the refined data with error

Theoretical volume of orthorhombic phase

Cry size Lorentzian 400(200)

k: 1 LVol-IB (nm) 250(150)

k: 0.89 LVol-FWHM (nm) 300(200)

Crystal Linear Absorption Coeff. (1/cm) 468.66(10)

Crystal Density (g/cm^3) 4.5533(10)

Theoretical density of orthorhombic phase

PV_TCHZ peak type

U 0.28(7)

V -0.02(4)

W 0.007(6)

Z 0

X 0.43(5)

Y 0

Lattice parameters

a (Å) 5.6382(7)

b (Å) 3.9656(5)

c (Å) 5.6674(7)

Refined lattice parameters

Site	Np	x	y	z	Atom	Occ	Beq
K1	2	0.00000	0.00000	-0.01770	K+1	0.49	0
Na1	2	0.00000	0.00000	0.00380	Na+1	0.49	0
Ba1	2	0.00000	0.00000	0.00000	Ba+2	0.02	1
Ni1	2	0.50000	0.50000	0.50000	Ni+2	0.01	1
Nb1	2	0.00000	0.50000	0.50000	Nb+5	0.99	0
O1	4	0.26050	0.50000	0.22530	O-2	1	0
O2	2	0.00000	0.00000	0.47040	O-2	1	0

Refined atom position

KNN Tetragonal

Phase name KNN T

R-Bragg 2.216

Spacegroup P4mm

Scale 0.00110(14)

Cell Mass 173.732

Structural file from .cif file (based on KNN tetragonal phase) and the refined data with error

Cell Volume (Å^3) 62.89(3)

Wt% - Rietveld 17.8(19)

Theoretical volume of tetragonal phase

Double-Voigt|Approach

Cry size Lorentzian 0(500000)

k: 1 LVol-IB (nm) 0(300000)

k: 0.89 LVol-FWHM (nm) 0(400000)

Crystal Linear Absorption Coeff. (1/cm) 472.1(3)

Crystal Density (g/cm^3) 4.587(2)

Theoretical density of tetragonal phase

PV_TCHZ peak type

U -0.4(3)

V 1.3(2)

W -0.30(4)

Z 0

X 0.00(18)

Y 0

Lattice parameters

Refined lattice parameters

a (Å) 3.9591(8)

c (Å) 4.0124(14)

Site	Np	x	y	z	Atom	Occ	Beq
O1	1	0.50000	0.50000	-0.03200	O-2	1	0.0198
O2	2	0.50000	0.00000	0.46920	O-2	1	0.0196
Ni1	1	0.50000	0.50000	0.50000	Ni+2	0.01	1
Nb1	1	0.50000	0.50000	0.50000	Nb+5	0.99	0.01114
K1	1	0.00000	0.00000	-0.02180	K+1	0.49	0.0112
Na1	1	0.00000	0.00000	0.00600	Na+1	0.49	0.033
Ba1	1	0.00000	0.00000	0.00000	Ba+2	0.02	1

Refined atom position

Appendix III. In-situ Raman spectra analysis

As mentioned in Chapter 5 (section 5.4.5), In-situ Raman spectra was conducted by Renishaw InVia Reflex Raman spectrometer. During the measurement, the powder samples was heating at 1°C/min, and the Raman spectrum was measured at every 30 seconds (approximate 1°C), the analysis procedures were shown below.

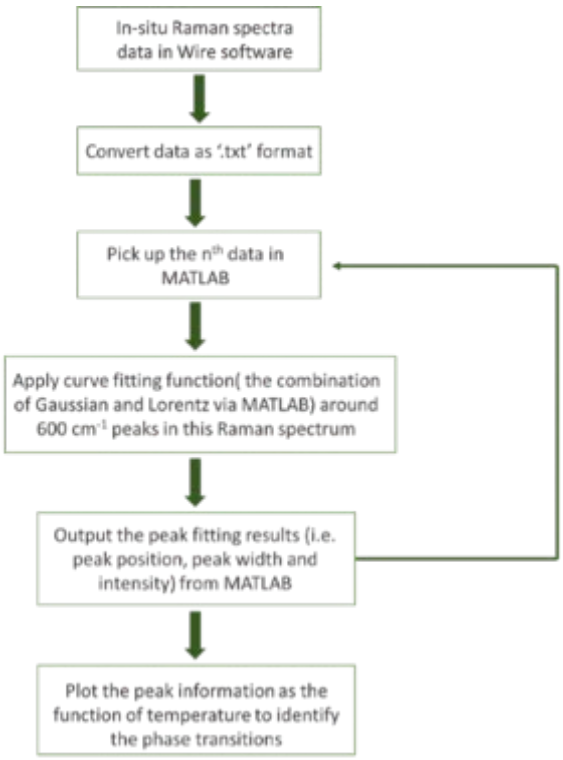

Figure III.1 The analysis procedures of temperature-dependent Raman spectra

There are 470 Raman spectra per composition and 2820 Raman spectra in total (6 compositions). It is better to use computation method (MATLAB) to analyse thousands of data set. In order to ensure the data can be recognized by the computer, the collected data was firstly converted into '.txt' files in the same folder. Each '.txt' file was named with 'composition name temperature range_heating rate_collect temperature_spectrum number_measure temperature_ramprate_1' (*i.e.* 5KNN_2BNNO 25 to 500°C 1kmin every 1k_0__Time_0__Temperature_30__RampRate_1). MATLAB was then used to read the file name and pick up the n^{th} Raman spectrum. A MATLAB peak fitting tool was conducted to analyse the peak position, width and intensity, by utilizing a non-linear optimisation algorithm (combination of Gaussian function and Lorentz function) to decompose a complex, overlapping peak signal into its component peaks. The corresponding peak position, width and intensity of each Raman spectrum were then obtained. After repeating this process for all data set, the peak information was

output and plotted as a function of temperature to observe the discontinuous changes of peak information.

2. Raman peak position and FWHM as the function of temperature

5KNN

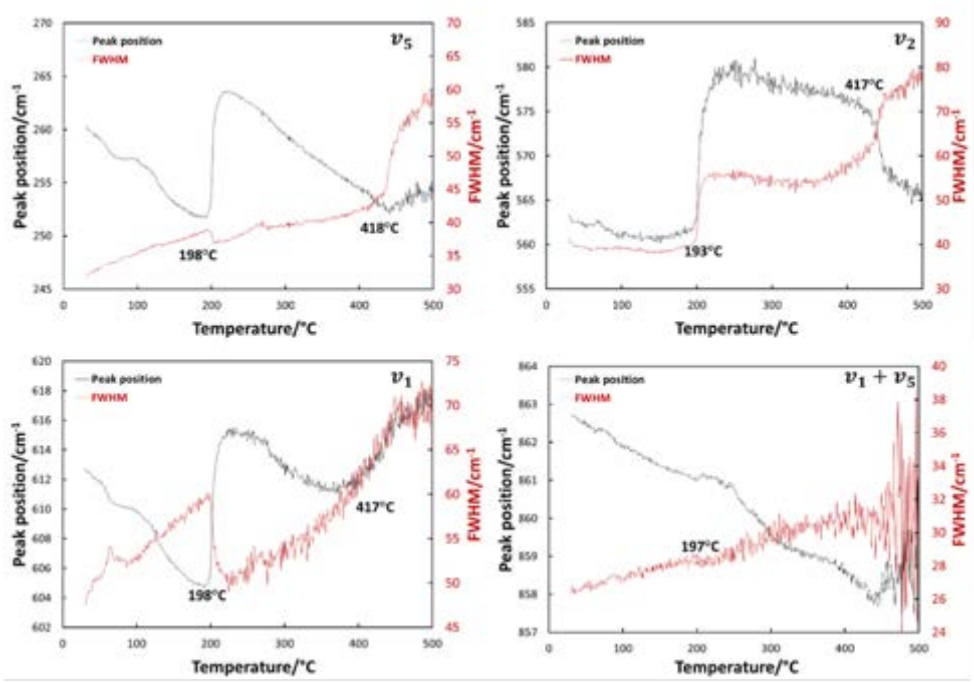

5KNN-4BNNO

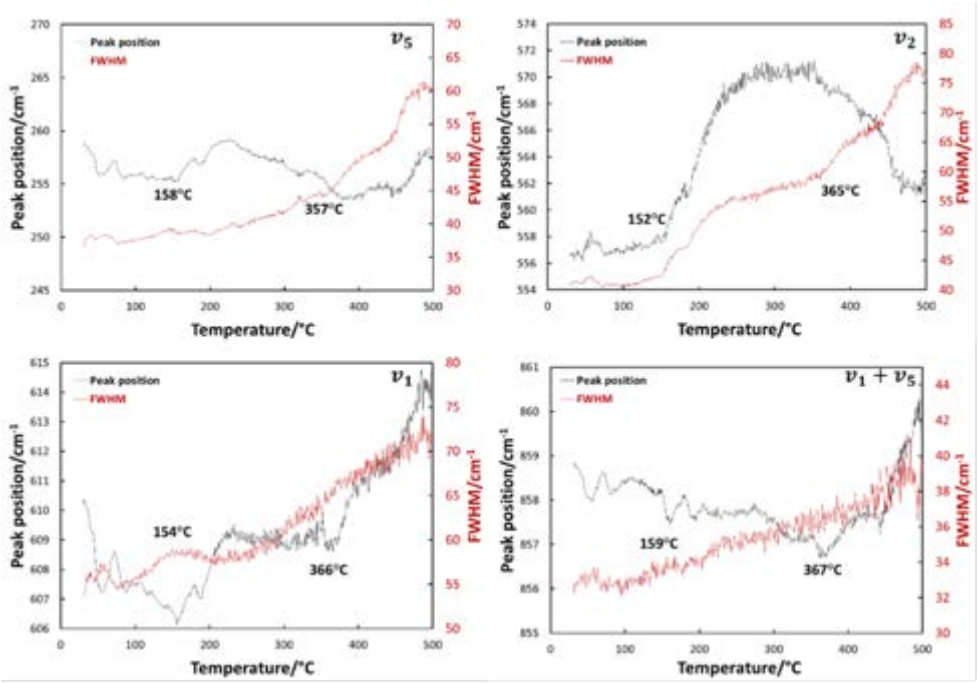

5KNN-6BNNO

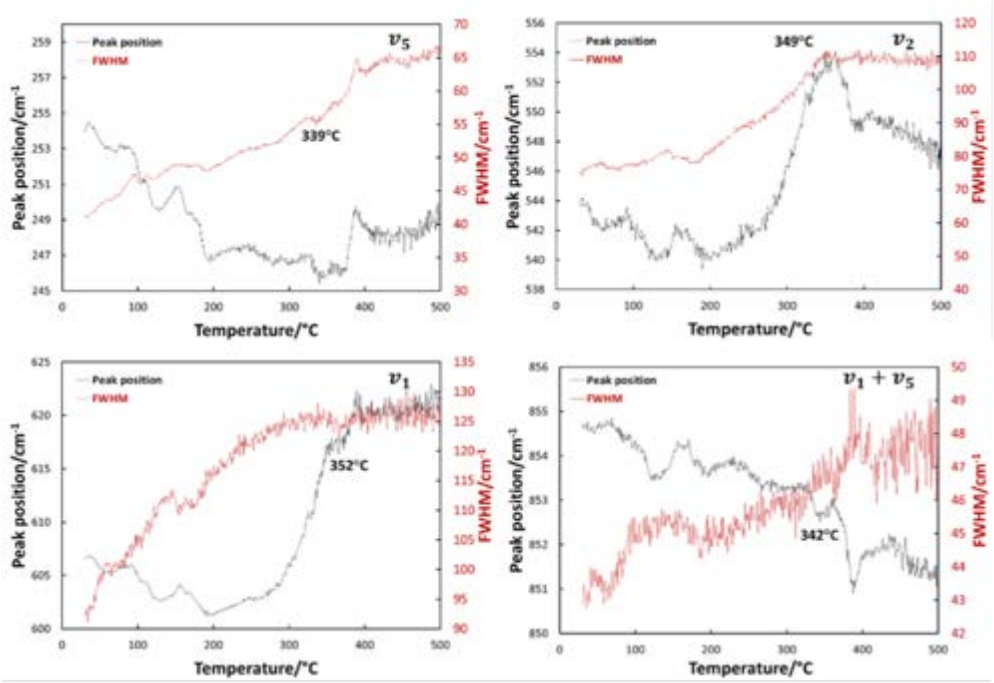

5KNN-8BNNO

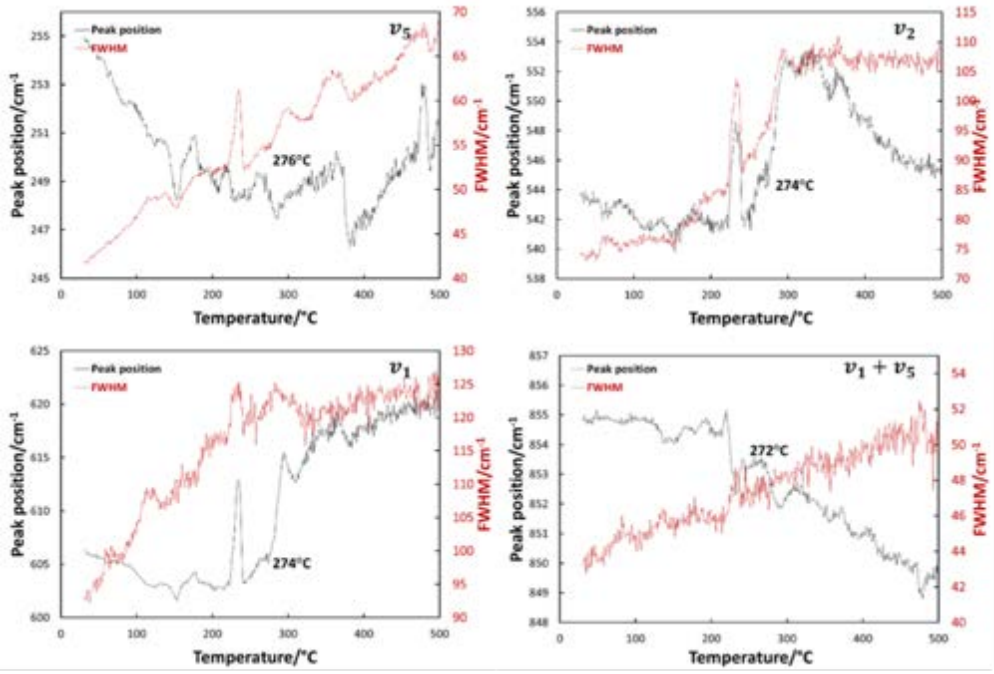

5KNN-10BNNO

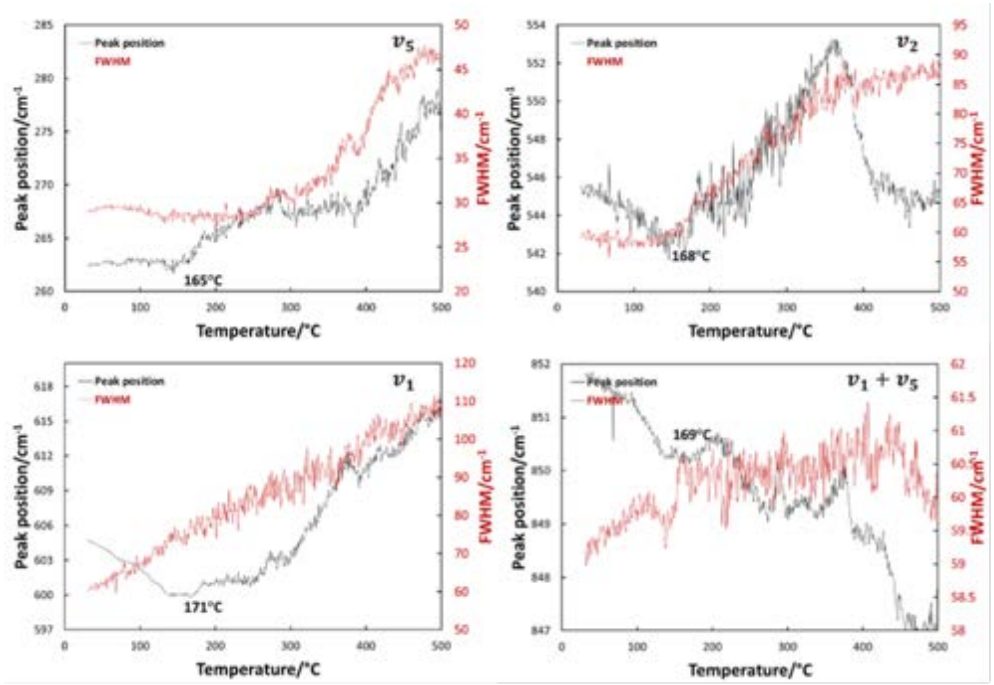
Peak position
FWHM
υ_5
Peak position/cm^{-1}
FWHM/cm^{-1}
165°C
Temperature/°C
υ_2
168°C
υ_1
171°C
$\upsilon_1 + \upsilon_5$
169°C

Appendix IV. Optical properties

1. open-circuit voltage of 5KNN-2BNNO photo-ferroelectric solar cell

In order to confirm the band gap nature of the 5KNN-2BNNO composition, the open-circuit voltage of photo ferroelectric solar cell was measured under the visible light. It can be seen from figure IV.1, ~1.78 eV energy can motivate the photovoltaic response. Therefore, the bang gap of 5KNN-2BNNO should be narrow than 1.78 eV which is consistent with the results of UV-vis-NIR spectrometry.

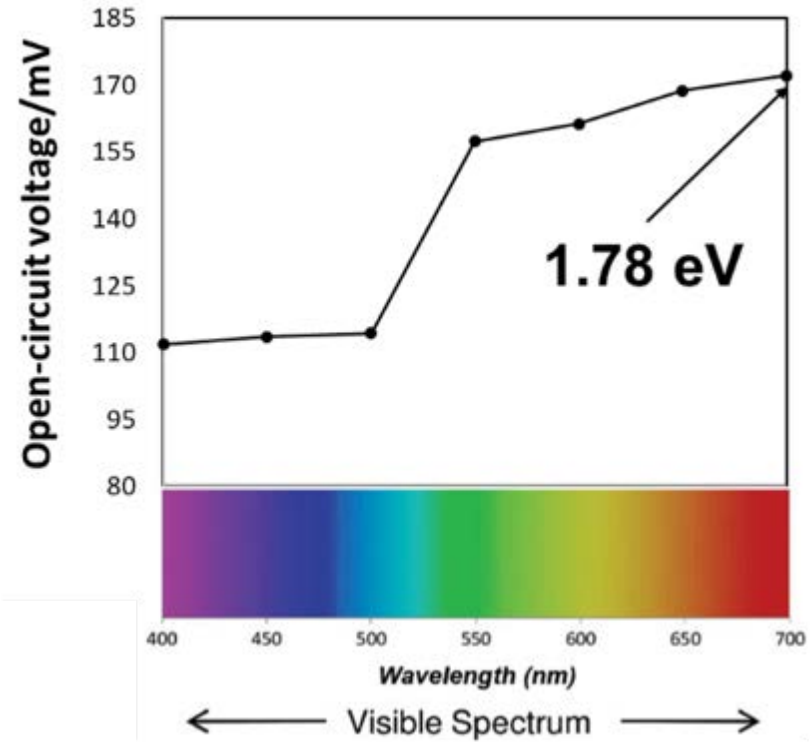

Figure IV.1 Open-circuit voltage of 5KNN-2BNNO photo ferroelectric solar cell induced by visible lights

List of publications

G. Ye., J. Wade-Zhu., J Zou., T Zhang., TW Button., & J Binner., Microstructures, piezoelectric properties and energy harvesting performance of undoped $(K_{0.5}Na_{0.5})NbO_3$ lead-free ceramics fabricated via two-step sintering. *Journal of the European Ceramic Society*, 40.8 (2020), 2977-2988.

G. Ye., D. Reed, J. Wade-Zhu., T Zhang., J Zou., TW Button., & J. Binner., Phase diagram of (1-y) 0.98 $(K_{0.5}Na_{0.5})NbO$ – y $Ba(Nb_{0.5}Ni_{0.5})O_{3-\delta}$ system measured by Raman and X-ray diffraction. *To be submitted.*

G. Ye., J. Wade-Zhu., J Zou., T Zhang., TW Button., & J Binner., The effect of Ni ex-solution for the sintering of 0.98 $(K_{0.5}Na_{0.5})NbO$ – 0.02 $Ba(Nb_{0.5}Ni_{0.5})O_{3-\delta}$. *To be submitted.*

Conference oral and poster presentations

Oral presentation

G. Ye., The fabrication of KNN-based Multifunctional Materials for a Hybrid Energy Harvester. Advanced material network: Multiscale tuning of interfaces for energy applications (MISE) "Energy Materials Interfacing", Gather town (online), UK. 21-22nd June 2020.

G. Ye., The processing of Pure KNN ceramics: two-step sintering V.S. conventional one-step sintering. 16th conference and exhibition of the European Ceramic Society (ECERS 2019), Torino, Italy. 16 – 19th June 2019.

G. Ye., Sintering of KNN ceramics. UK HEAT of the European Student Speaking competition (1DRAC), London, United Kingdom. 26th March 2019.

Poster

G. Ye, J Zou, Tim Button and Jon Binner, Pure KNN piezoelectric ceramics fabricated by two-step sintering for energy harvester. 3rd Annual Energy Harvesting Society Meeting, Virginia, American, 4 – 6th September 2019.

G. Ye, J Zou, Tim Button and Jon Binner, Investigation of KNN-based Materials for Multifunctional Energy Harvesting Applications. Material Science & Technology 2018 of the American Ceramics Society (MS&T18), Columbus, American, 17-19th October 2018.

G. Ye, Y Bai, J Zou, J Binner and T. Button, Investigation of KNN-based Materials for Energy harvesting Devices, 5th energy harvesting workshop, Dublin, Ireland, 23-24th April 2018.

G. Ye, Y Bai, J Zou, J Binner and T. Button. Comparisons of Piezoelectric Ceramics and Investigation of Interface between the Individual Layers, Inaugural workshop, Edinburgh, United Kingdom, 31st October 2017.

Y. Chen, H. Zhang, **G. Ye,** L. Ma, S. Gu. Synthesis and Mechanism of Titanium Carbonate Cermet Powder by Hydrate Gel, Shanghai, 2017 The 13th Annual Symposium on Engineering Ceramics.

UNIVERSITY OF OULU

UNIVERSITY OF BIRMINGHAM

Investigation of KNN-based Materials for Energy Harvesting Devices

Guoyang Ye[1], Yang Bai[2], Ji Zou[1], Jon Binner [1]& Tim Button[1]

[1]School of Metallurgy & Materials, University of Birmingham, Birmingham B15 2TT, United Kingdom

[2]Faculty of Information Technology and Electrical Engineering, University of Oulu, Finland

Email: gxy742@student.bham.ac.uk

Introduction

Lead-based piezoelectric materials are widely used in energy harvesting devices, but due to the highly-toxic nature of lead (Pb), such materials are facing impending legislative restrictions. $(K_{0.5}Na_{0.5})NbO_3$ (KNN) piezoelectric ceramics show comparable properties to conventional lead-based materials and are a promising lead-free replacement. Recently, $(K_{0.5}Na_{0.5})NbO_3$ (KNN) doped with 2 mol% $Ba(Ni_{0.5}Nb_{0.5})O_{3-\delta}$ (BNNO) displayed not only good piezoelectric and pyroelectric properties, but also a narrow photonic band gap[1]. This heralds the possibility of truly multifunctional sensing devices that enable the simultaneous and efficient conversion of solar, thermal, and kinetic energies into electricity in a single material.

Aims and Objectives

Aims: investigate processing and doping strategies for KNN-based materials in order to further optimize the energy harvesting properties.

Objectives:

- ❖ Synthesis of powder with a fine particle size and small size distribution;
- ❖ Fabrication of bulk samples with homogeneous and dense microstructures;
- ❖ Sintering in a manner to minimize grain growth, avoid the evaporation of K and Na, and enable co-processing with electrodes.
- ❖ Investigate the influence of the compositional and processing variables on the functional, optical and electrical properties, with the aim of increasing the energy-conversion effectiveness.

This poster presents early progress in this work.

Experimental Procedures

$(K, Na)NbO_3$ powders are synthesized by conventional solid-state method, as shown below:

$$x\,Na_2CO_3 + (1-x)K_2CO_3 + Nb_2O_5 \rightarrow 2(K_{1-x}Na_x)NbO_3 + CO_2$$

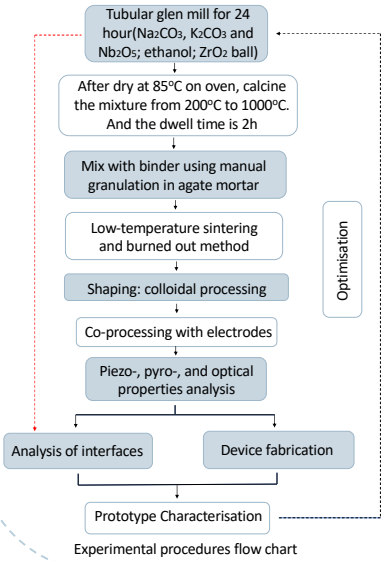

Experimental procedures flow chart

1. Raw powder preparation and compositional design via the conventional solid-state method;
2. KNN bulk samples are fabricated by colloidal processing;
3. The bulk samples are sintered whilst buried in sacrificial powder of the same composition in a covered alumina crucible;
4. Electrodes are deposited on the both sides of the sintered KNN bulk samples, then co-fired.
5. The testing system involves an electrometer, lamp and dryer. Then the data of pyro and photocurrents can be analysed. And the piezoelectric properties can be detected by d33 meter and Impedance analyzer.

Results and Discussion

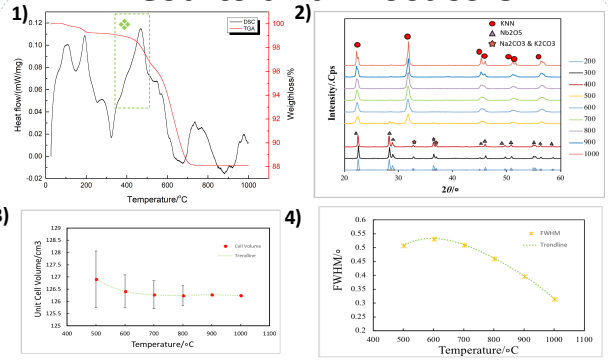

Calcination process from mixed carbonates and oxide to the calcined KNN, showing 1) DTA/DSC curves, 2) XRD pattern from 200°C to 1000°C, 3) and 4) unit cell volume and FWHM curve, calculated from XRD refinement data.

- TG curves show around a 12% decrease in overall mass as the temperature of these mixtures increase up to 700°C. There are two major endothermic peaks in the DTA curve. The endothermic area ❖ is thought to be due to the starting point of the reaction.
- The XRD patterns indicate the reaction started at 400°C and the crystallinity increased with increasing temperature.
- Unit cell volume and FWHM curves show a reduction with increasing temperature, which means solid solution takes time and temperature to form a single homogeneous phase.

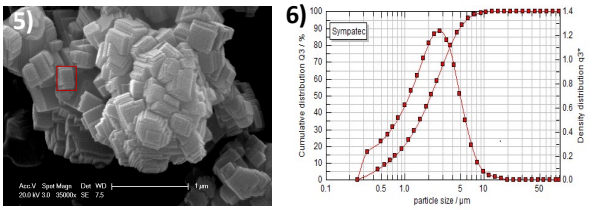

The pure calcined $(Na_{0.5}K_{0.5})NbO_3$ powder at 850°C, showing 5) powder morphology and 6) powder size distribution.

- $(K,Na)\ NbO_3$ powders show the facet morphology, with the range of crystallite size about 300~500 nm. However, the small crystals are inclined to agglomerate, and the size of agglomerated particles is about 1-2µm, as shown by the peak in 6) particle size analysis.

Conclusions

$(K,Na)NbO_3$ powders have been successfully synthesized by a conventional solid-state method. After comparing the XRD patterns (FWHM and unit cell volume data) at different calcination temperatures (200 – 1000°C) and the DTA/TG curves, it can be seen that 900°C is the optimal calcination temperature. The SEM image indicates the as-received KNN powders have a narrow particle size distribution and fine crystallite size (less than 500 nm), while the small particles are easy to form aggregations with broad particle size (1-2µm) based on the particle size analysis.

References

[1] B Yang et al, *ACS. Nano.*. **7** (2010) P. 785-790

Acknowledgements

This work is supported by the project "Multiscale tuning of interfaces and surfaces for energy applications" (EPSRC Reference: EP/P007821/1)" a collaboration between the Universities of St Andrews, Edinburgh, Bath and Birmingham.

EPSRC Engineering and Physical Sciences Research Council

Investigation of $(K_{0.5}Na_{0.5})NbO_3$ ceramics sintered by two-step sintering for Energy Harvesting Devices

Guoyang Ye[1], Ji Zou[1], Yang Bai [2], Jon Binner [1] & Tim Button[1]

[1]School of Metallurgy & Materials, University of Birmingham, Birmingham B15 2TT, United Kingdom

[2]Faculty of Information Technology and Electrical Engineering, University of Oulu, Finland

Email: gxy742@student.bham.ac.uk

Summary

Lead-based piezoelectric materials are widely used in energy harvesting devices, but due to the highly-toxic nature of lead, such materials are facing impending legislative restrictions. $(K_{0.5}Na_{0.5})NbO_3$, KNN, piezoelectric ceramics show comparable properties to conventional lead-based materials and are a promising lead-free replacement. In this work, KNN ceramics have been prepared by two-step sintering, which has yielded homogenous grain sizes and prevented abnormal grain growth. Compared with conventional single-step sintering, KNN samples fabricated using two-step sintering were of higher density, increasing from 91% to 95% of theoretical, and reduced mean grain size, from ~17 µm to <7.5 µm. This translated into an improved piezoelectric performance and higher energy harvesting output. This demonstrates the potential of two-step sintering as a high through-put sintering technique of moderate-performance, pure KNN ceramics.

Aims and Objectives

Aims: Optimization of two-step sintering processing conditions and investigation of energy harvesting performance for pure KNN ceramics.

Objectives:

- Synthesis of $(K_{0.5}Na_{0.5})NbO_3$ ceramic powders with a fine particle size and small size distribution;
- Fabrication of high density $(K_{0.5}Na_{0.5})NbO_3$ ceramics through two-step sintering to minimize grain growth and avoid the evaporation of K and Na;
- Preparation and vibration testing of pure $(K_{0.5}Na_{0.5})NbO_3$ cantilever-energy harvester densified by two-step sintering (TSS) and single step sintering (SSS).

Experimental Procedures

(K, Na)NbO_3 powders were synthesized by conventional solid-state method, as shown below:

$$x\,Na_2CO_3 + (1-x)K_2CO_3 + Nb_2O_5 \rightarrow 2(K_{1-x}Na_x)NbO_3 + CO_2$$

Turbular Glen mill for 24 h (Na_2CO_3, K_2CO_3 and Nb_2O_5; ethanol; ZrO_2 balls)

↓

After drying at 75°C, calcine at 900°C for 2 h

↓

Mix with 0.5 wt % PVA binder using manual granulation in agate mortar

↓

Dry press at 200 MPa

↓

Single-step sintering (SSS) or Two-step sintering (TSS)

↓

Piezoelectric properties analysis and energy harvester preparation

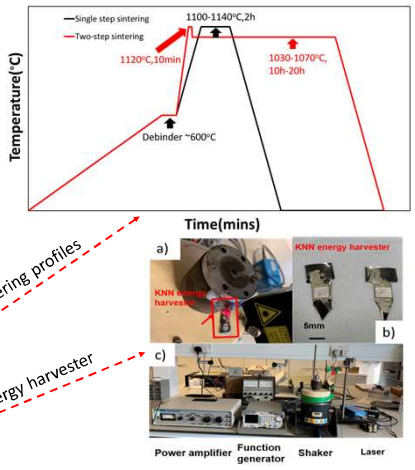

Fig. 1 Experimental procedures flow chart

- For both sintering routes, all samples were buried in a powder bed with a composition equivalent to that of the calcined $(K_{0.5}Na_{0.5})NbO_3$ powders;
- The piezoelectric properties were measured using a d_{33}-meter and an impedance analyser.

Two-step sintering V.S. Single step sintering

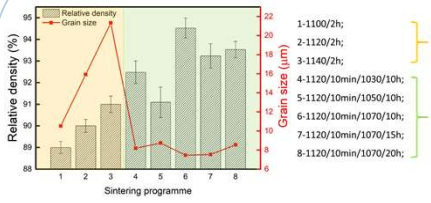

Compared with the samples prepared via SSS, it is clear that the samples fabricated via two-step sintering exhibit both higher densities (93-95%) and finer microstructures.

TSS KNN ceramics show a finer and more homogenous microstructure and less inter- and intra-granular porosity. For TSS, the lower sintering temperatures were used to activate grain boundary diffusion and to slow down the grain boundary migration to obtain higher densities and supress the grain growth. Also, the lower sintering temperature decreased the evaporation of alkali and thus avoided a bimodal grain size developing.

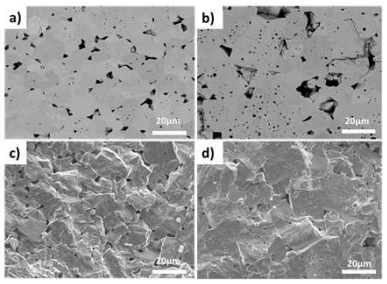

a),c):TSS & b),d): SSS

Piezoelectric properties of KNN fabricated by TSS and SSS

Sample No.	Sintering conditions (T_1 t_1 / T_2 t_2)	Rel. density (%)	Grain size (µm)	d_{33} (pC N^{-1})	$tan\delta$ (%)	ε_r	K_p (%)	Q_m
1	1100°C / 2 h	90	10.52	97	8.9	297	34	17
2	1120°C / 2 h	91	15.92	101	6.1	294	33	32
3	1140°C / 2 h	91	21.33	94	4.8	305	25	22
4	1120°C 10 m / 1030°C 10 h	92	8.18	112	9.3	327	35	34
5	1120°C 10 m / 1050°C 10 h	91	8.74	104	7.4	310	31	42
6	1120°C 10 m / 1070°C 10 h	95	7.46	122	4.8	337	36	76
7	1120°C 10 m / 1070°C 15 h	93	8.23	118	3.9	329	34	45
8	1120°C 10 m / 1070°C 20 h	93	8.55	108	4.4	279	33	39

TSS samples yield better piezoelectric properties due to higher densities, less evaporation of alkali and finer and more homogenous grain size.

The lower evaporation of alkali can reduce compositional deviation from stoichiometry and hence improve the properties; smaller grain sizes tend to have smaller domain walls that can re-orientate more easily and respond more actively to external signals due to higher domain mobility.

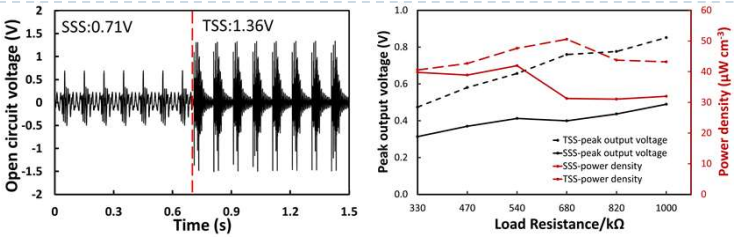

The 1120°C SSS sample and 1120°C/1070°C/10 h TSS samples were chosen to prepare the energy harvester. The values obtained were an open circuit peak voltage value of 1.36 V (TSS) vs 0.71 V (SSS) and a power density at 680 kΩ of 51 µW cm^{-3} (TSS) vs 42 µW cm^{-3} (SSS).

Conclusions

- Compared to the SSS approach, $(K_{0.5}Na_{0.5})NbO_3$ ceramics sintered by TSS demonstrated an improved density (~95%) and smaller grain size (<7.5 µm);
- The lower sintering temperature in TSS is helpful in decreasing the evaporation of alkali and reducing active grain boundary diffusion thus yielding more homogenous microstructures;
- As a result of the points above, TSS $(K_{0.5}Na_{0.5})NbO_3$ ceramics exhibited better piezoelectric properties;
- The energy harvester fabricated using TSS-KNN ceramic showed better performance.

Future Work

- Fabrication of KNN-based multifunctional ceramics materials via co-doping;
- Fabrication of KNN-based multifunctional thin films;
- Structural modelling of a piezoelectric energy harvester;
- Incorporation of multifunctional KNN-based ceramics into energy harvesting devices.

Acknowledgements

This work is supported by the project "Multiscale Tuning Of Interfaces And Surfaces For Energy Applications" (EPSRC Ref: EP/P007821/1)", a collaboration between the Universities of St Andrews, Edinburgh, Bath & Birmingham.

Journal of the European Ceramic Society 40 (2020) 2977–2988

Contents lists available at ScienceDirect

Journal of the European Ceramic Society

journal homepage: www.elsevier.com/locate/jeurceramsoc

Original Article

Microstructures, piezoelectric properties and energy harvesting performance of undoped $(K_{0.5}Na_{0.5})NbO_3$ lead-free ceramics fabricated via two-step sintering

G. Ye*, J. Wade-Zhu, J. Zou, T. Zhang, T.W. Button, J. Binner

School of Metallurgy & Materials, University of Birmingham, Birmingham, B15 2SE, UK

ARTICLE INFO

Keywords:
Potassium sodium niobate ($K_{0.5}Na_{0.5}NbO_3$)
Sintering kinetics
Two-step sintering
Density
Grain size

ABSTRACT

Piezoelectric energy harvesters have become increasingly popular in the field of green energy because of the ability to convert low-frequency environmental vibrations into usable electricity. To fabricate high-performance energy harvesters, the key requirements are piezoelectric ceramics with a small grain size, of near-full density, the intended stoichiometric ratio and a high transduction coefficient. In this work, the effects of two-step sintering on the sinterability, microstructure, piezoelectric properties and energy harvesting performance of $(K_{0.5}Na_{0.5})NbO_3$ were systematically investigated. Compared with conventional single-step sintering, two-step sintering samples were of higher density, increasing from 91 % to 95 % of theoretical, reduced mean grain size, down from 17 μm to 7.5 μm, and decreased evaporation of the alkali metals. This translated into an improved piezoelectric performance (d_{33} ~122 pC/N, k_p ~36 % and Q_m ~76), a higher transduction coefficient and energy conversion efficiency as well as a higher open-circuit voltage and power density. This demonstrates the potential of two-step sintering as a high through-put sintering technique for moderate-performance, pure KNN ceramics.

1. Introduction

Piezoelectric ceramic materials have been a core topic of research in recent years due to their widespread application, allowing them to be used as actuators, sensors, transducers and energy harvesting devices [1]. In the past several decades, the majority of research has been concentrated on lead zirconate titanate (PZT) based ceramic materials due to their high piezoelectric response [1]. However, because of the highly-toxic nature of lead (Pb), the current demand is for the development of lead-free piezoelectric materials [2].

Compared with other lead-free piezoelectric ceramics, sodium potassium niobate-based piezoelectric materials (KNN) are one of the most promising choices to replace the lead-based ceramics, offering a high Curie Temperature (415 °C) and moderate piezoelectric and dielectric constants (e.g. d_{33} ~160 pC/N and ε_r ~586) [3–6]. However, because of the low sinterability and high volatility of KNN, caused by presence of the alkali metals, the use of conventional single-step sintering (SSS) in the fabrication of undoped KNN ceramics often leads to piezoelectric ceramics of low density and stoichiometry different to that intended. This translates into piezoelectric properties that are poor (d_{33} ~ 80 pC/N) [7–9]. The extremely narrow sintering window for KNN also means that obtaining high-density KNN piezoelectric ceramics via SSS presents a significant challenge [10]. To date, approaches to improve the sinterability of KNN-based piezoelectric ceramics have been focused on using dopants [11–20], sintering aids [21,22], compositional modifications [23,24], and/or the adoption of pressure-based sintering techniques such as hot pressing [25] or spark plasma sintering [26,27]. When using dopants such as $LiNbO_3$ [28] and Li (Nb, Ta, Sb)O_3 [14,12,12,13,14,15,16,17,18,19,20], it has been reported that KNN-based ceramics may be produced with improved densities and enhanced electrical properties. However, the use of dopants also lowers the temperature stability of these improved electrical properties, limiting their practical application as functional materials [29]. Moreover, the use of pressure-based sintering results in increased manufacture costs and low production output rates, making KNN unsuitable for widespread adoption [25–27]. Given the aforementioned shortcomings of the solutions explored to date, the sintering of KNN requires a new and innovative method, capable of producing dopant-free, piezoelectric ceramics of high density and a fine microstructure.

The sintering of KNN can be divided into three primary stages of densification and growth [30]. The initial stage involves the fusing of the characteristically faceted powder particles of KNN to form stacks of

* Corresponding author.
E-mail address: GXY742@student.bham.ac.uk (G. Ye).

https://doi.org/10.1016/j.jeurceramsoc.2020.02.035
Received 14 November 2019; Received in revised form 25 January 2020; Accepted 14 February 2020
Available online 22 February 2020

plate-type particles [31]. This is achieved through interparticle neck growth via mechanisms of diffusion, vapour transport or viscous flow. At the intermediate stage, high temperatures lead to the evaporation of Na (as well as some K) at the grain boundary and the creation of a K-rich liquid phase that bridges residual pores present at grain boundary junctions [32]. This liquid phase provides a transport path for the rearrangement of particles resulting in reduced surface area and improved packing [33]. The final stage is dominated by liquid phase-induced rapid and abnormal grain growth via diffusion-controlled coarsening mechanisms [31,34]. Here, limited densification occurs. As demonstrated above, the grain boundary liquid phase of KNN plays a critical role in its densification, owing to the non-uniform and cubical shape of its particles. Thus, higher densities may be achieved by retaining a higher fraction of the liquid phase through the suppression of alkali metal loss via evaporation [31]. Moreover, further improvements in overall density may be achieved by delaying the onset of rapid grain growth during the final sintering stage.

In 2000, Chen and Wang [35] introduced a new, low cost and relatively easy to use sintering technique, known as two-step sintering (TSS), which aimed at improving the properties of ceramics by increasing the density whilst suppressing grain growth. The intention of TSS is to limit the accelerated grain growth that typically occurs in the final stages of SSS. This is achieved by first densifying the ceramic to an intermediate density at a high initial temperature, T_1, over a short period of time. The ceramic is then cooled rapidly to a lower temperature, T_2, typically 50–100 °C below T_1 and densified over a much longer period of time. The TSS method exploits the higher activation energy of grain boundary migration at triple-points, which form during the first stage of sintering and are immobilised by the rapid cooling of the ceramic. Subsequent densification to final density occurs by grain boundary diffusion [35]. For the sintering of KNN specifically, the use of a lower dwelling temperature in TSS has the added benefit of reducing the evaporation of Na and K, enabling better stoichiometric control, the retention of a higher liquid content during sintering and improved piezoelectric performance [30–32]. Since the work was first published, TSS has been successfully used to fabricate a range of different ceramics, including Al_2O_3 [36,37], Y_2O_3 [38], AlN [39], $BaTiO_3$ (BTO) [40] and nanostructured ZrO_2 [41]. With respect to KNN, TSS has been used to broaden the sintering temperature range and improve the density of doped KNN, including $0.9625(Na_{0.5}K_{0.5}NbO_3)–0.0375Li(Ta_{0.4}Sb_{0.6})O_3$ [42], $(K_xNa_{1-x})_{0.94}Li_{0.06}NbO_3$ [43], $0.89Bi_{0.5}Na_{0.5}TiO_3–0.06BaTiO_3–0.05K_{0.5}Na_{0.5}NbO_3$ [44] and $(K_{0.4425}Na_{0.52}Li_{0.0375}) – (Nb_{0.8925}Sb_{0.07}Ta_{0.0375})O_3$ [45]. Wang *et al.* has also shown that the density and electrical properties of pure KNN may be significantly improved via the adoption of TSS [46]. However, while the benefit of TSS on the performance of pure KNN has been well-demonstrated, a detailed analysis of the mechanisms involved at the different stages and their influence on the resultant microstructure and performance is more limited.

In this paper, the processing conditions of SSS and TSS have been optimised to fabricate piezoelectric ceramics of pure KNN with as high a density and as fine a grain size as possible. In accordance with fundamental sintering theory and the principal mechanisms of SSS and TSS, the densification and resultant evolution of the KNN microstructure has been systematically analysed at each stage of the sintering process. Based on the functional properties and energy harvesting performance of the pure KNN piezoelectric ceramics produced, a discussion is presented on the comparative benefits of TSS over conventional SSS and the potential of TSS as a means of delivering fine grain size, dense, lead-free $(K_{0.5}Na_{0.5})NbO_3$ ceramics.

2. Experimental procedure

2.1. Material preparation

KNN samples were prepared by conventional powder processing. The first step involved drying as-received powders of Na_2CO_3 (≥ 99.50 %, Sigma-Aldrich, UK), K_2CO_3 (≥ 99.0 %, Sigma, UK) and Nb_2O_5 (≥ 99.90 %, Aldrich, UK) at 150 °C for 24 h to remove any residual moisture. After cooling back to room temperature in a desiccator to avoid reabsorption of moisture, the powders were then weighed out in stoichiometric quantities according to the molar ratio of $(K_{0.5}Na_{0.5})NbO_3$. Mixing of the powders was completed in ethanol using a tubular mill for 24 h with zirconia balls as the milling media. After removing the ethanol in an oven at 75 °C for 12 h, the powders were calcined at 900 °C for 2 h in a closed alumina crucible. The powders were then put back into ethanol and vibro-milled for 24 h to break up the agglomerates. The calcined $(K_{0.5}Na_{0.5})NbO_3$ powders were dried again and mixed with 1 wt% polyvinyl alcohol solution (5 wt% concentration, Polyvinyl alcohol 100000, Fluka Chemika) before being uniaxially pressed into pellets with a diameter of 13 mm and 1 mm thickness under a pressure of 200 MPa.

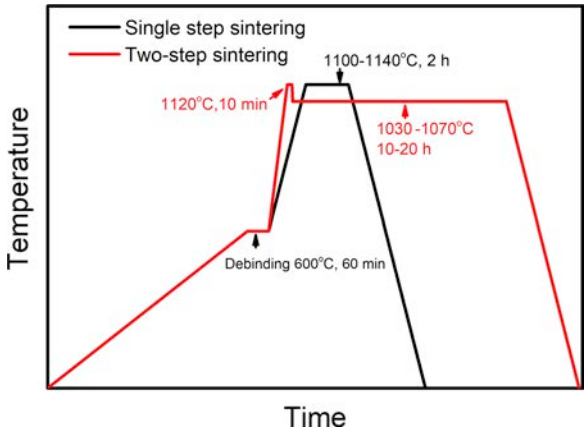

Fig. 1. Schematic diagram of the conventional SSS and TSS profiles. Binder removal was carried out at $T = 600$ °C and was identical for both sintering methods.

Densification was achieved using both SSS and TSS; the heating profiles are shown in Fig. 1. Binder removal was completed for all samples at a heating rate of 1 °C/min to a final temperature of 600 °C for 1 h. Samples sintered using SSS were heated at 5 °C/min to a peak temperature in the range of between 1080–1140 °C and held for 2 h. The samples were then allowed to cool naturally. For samples sintered using TSS, the first step involved heating to an initial temperature, T_1, in the range 1040–1140 °C using a heating rate of 10 °C/min and a very short dwell of 10 min. The samples were then cooled rapidly at 30 °C/min to a lower temperature, T_2, in the range of 1030 − 1070 °C and held for a further 10 − 20 h. The sintering conditions of SSS and TSS are summarized in Table 1. All samples for both sintering routes (6 samples for each sintering condition) were buried in a powder bed with a composition equivalent to that of the calcined $(K_{0.5}Na_{0.5})NbO_3$ powders. The density of the samples was measured using the Archimedes method and the relative density calculated using a theoretical density value of 4.506 g/cm [4,47].

Table 1
Sintering conditions for SSS and TSS.

Sample No.	Heating rate/°C min^{-1}	T_1/°C	t_1/h	T_2/°C	t_2/h
1	5	1100	2		
2	5	1120	2		
3	5	1140	2		
4	10	1120	0.16 (10 min)	1030	10h
5	10	1120	0.16 (10 min)	1050	10h
6	10	1120	0.16 (10 min)	1070	10h
7	10	1120	0.16 (10 min)	1070	15h
8	10	1120	0.16 (10 min)	1070	20h

2.2. Chemical and microstructural characterisation

The phase purity and crystal structure of the calcined $(K_{0.5}Na_{0.5})NbO_3$ powders and as-sintered KNN pellets were assessed by XRD (Bruker D8 Advanced X-ray Diffractometer, CuKα = 0.15405 nm, accelerating voltage 40 kV, current 40 mA) across a 2θ range of 10° to 90° with a step size of 0.0142°. All XRD data were refined using Topas-Academic and jEdit software. Representative shrinkage rates of green bodies were measured using dilatometry (NETZSCH 402E-1600 °C) across a temperature range of 30 − 1130 °C and using a heating rate of 5 °C/min. Scanning electron microscopy was used to analyse the morphology of the calcined powder produced as well as the fracture and polished surfaces of the as-sintered KNN ceramics (Phillips XL30 ESEM-FEG, accelerating voltage 20 kV). Backscattered images were used to measure the average grain size, the analyses of which were performed using the linear intercept method [48]. Meanwhile, the maximum Feret diameter (the longest line that can fit within the boundaries of the grain) was measured using Nano Measurement software (Nano measurer 1.2, Department of Chemistry, Fudan University) to obtain the grain size distribution.

2.3. Piezoelectric property measurements

Prior to performing any electrical measurements, the planar faces of all samples were first polished to a smooth surface finish using 20 µm silicon carbide paper. A sputter coater (K575X, Emitech) was then used to coat polished surfaces with a 40 nm chromium layer followed by two 200 nm gold layers. The samples were then poled in a silicone oil bath by applying an electric field of 3.5 kV mm^{-1} for 30 min at 120 °C. The piezoelectric charge coefficients (d_{33}) were measured by a quasi-static piezoelectric coefficient testing meter (YE2730A, SINOCERA, China) 24 h after poling. Dielectric properties were measured at room temperature using wide frequency range impedance spectroscopy (Agilent 4294 A Precision Impedance Analyser, USA).

2.4. Energy harvesting performance measurements

For the purpose of fabricating piezoelectric energy harvesters [49,50], sintered KNN pellets, with a diameter of 10 mm and a thickness of 0.8 mm, were first polished into squares of 5 mm length and width and 0.3 mm thickness. The KNN squares were coated on both sides with approximately 0.5 µm silver electrodes by brush (Silver Top Coat Paste C2060217P3, SunChemical) and annealed in a furnace at 550 °C for 1 h at a heating rate of 1 °C/min. After cooling, two copper wires were connected to the samples via soldering, one on either side. The final KNN component was then fixed onto a stainless-steel substrate (thickness 0.35 mm) using silver epoxy paste (Conductive Adhesive Epoxy, RS Components Ltd). A schematic representation of the final energy harvester is presented in Fig. 2 and is a reproduction of a design reported elsewhere [51]. An external vibration was then applied to the energy harvesting device using an electromagnetic shaker head (Gearing & Watson Electronics, UK) with integrated power amplifier (Model K2007E01; The Modal Shop Inc, Cincinnati, USA). Both the bending signal and electrode signal were recorded by an oscilloscope (Pico 4424, Pico -Technologies, UK) and monitored by the PicoScope software.

3. Results and discussion

3.1. Chemical analysis and morphology

The XRD patterns of both the calcined KNN powder and ceramics sintered by SSS and TSS are presented in Fig. 3. The major Bragg peaks detected corresponded to the pure KNN perovskite orthorhombic structure. Note, no new reflections were observed. Therefore, the calcined powder and sintered samples may be considered reasonably pure

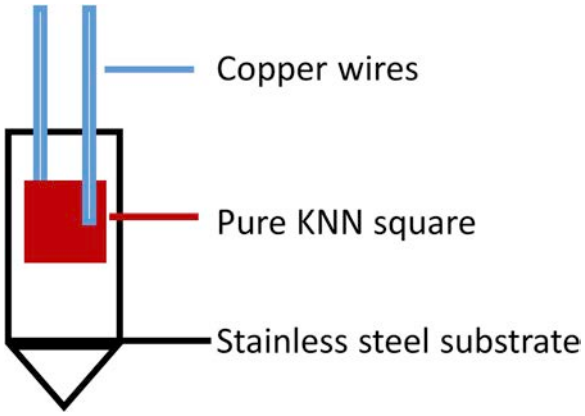

Fig. 2. Schematic diagram of energy harvester.

with no impurity phases inside the detection limit of XRD (~2%). As expected, the peaks of the sintered KNN specimens were narrower than those of the calcined powder; this is associated with the larger crystal size in the ceramics after sintering. Milling of the calcined powder is likely to have introduced defect structures into the lattice, the resultant micro-strain causing significant distortion in the crystals and broadening of the XRD peaks. Such defect structures anneal out during sintering at high temperatures, resulting in a narrowing of the XRD peaks. The consistency of the results from sample-to-sample is a strong indication that the calcined powder synthesised for this work offer excellent chemical homogeneity.

SEM analysis of the calcined powder is shown in Fig. 4 and reveals a highly-faceted surface morphology. The overall granule shape is highly irregular with multiple cubic domains growing outwards in a concertina structure. The mean crystallite size range of the particles was ~300 – 500 nm, whilst the overall particle size was closer to 1–2 µm.

3.2. Sinterability of KNN ceramics using SSS and TSS

3.2.1. Single-step sintering of pure KNN

The dynamic shrinkage curve of the KNN powder compacts heated at temperatures ranging from 600 °C to 1130 °C are presented in Fig. 5. The compacts began shrinking at ~875 °C, where a steep slope in the shrinkage curve may be observed. A rapid increase in shrinkage into a largely linear shrinkage rate occurred at 1000–1070 °C; beyond 1080 °C, the shrinkage rate decreased as the curve begins to level off, with the KNN powder compacts reaching their highest level of shrinkage at ~1120 °C. As confirmed by the smooth solid-liquid line of the $KNbO_3$-$NaNbO_3$ phase diagram [10,52], this densification limit corresponds with the generation of a K-rich liquid phase at ~1110 °C. Although the presence of such a liquid phase provides a faster medium for diffusion, it also reduces the energy for grain boundary migration. This promotes rapid grain growth, reducing the amount of free energy available and the driving force for the further densification [30] such that no further shrinkage occurs beyond 1120 °C. Gas phase release associated with the volatilisation of Na and K at above 1000 °C [30] is also likely to be a contributing factor. From these results, the sintering window of pure KNN is considered to be 1080 − 1120 °C.

Based on the results in Fig. 5, four KNN ceramics were produced by SSS, each one sintered at different peak temperatures of 1080 °C, 1100 °C, 1120 °C and 1140 °C[a] for 2 h. The relative density and corresponding grain sizes of these materials are shown in Fig. 6(a). As can be observed, higher relative densities were achieved when the ceramics were sintered at higher temperatures as expected. The peak density achieved was 91 % at both 1120 °C and 1140 °C.

[a] Note that above 1138°C the sample will start to soften slightly as the first liquid starts to form.

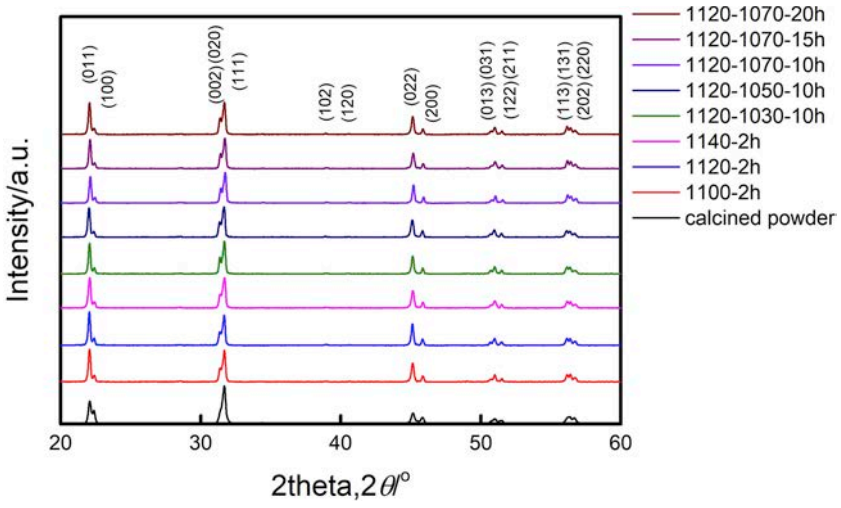

Fig. 3. XRD patterns across a 2θ range of 20–60° for the calcined KNN powder and ceramics sintered at various temperatures and times (t) using conventional single-step and two-step sintering (T_1-T_2-t_2 for TSS; T_1-t_1 for SSS).

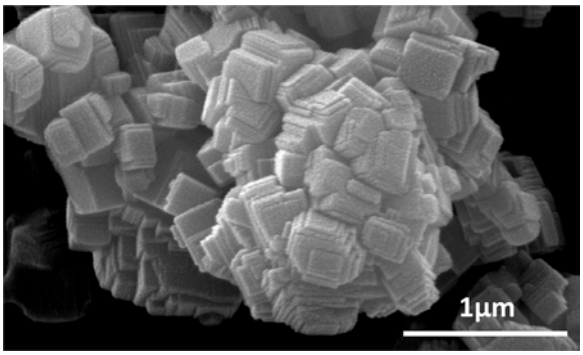

Fig. 4. A representative SEM image of the $(K_{0.5}Na_{0.5})NbO_3$ powder calcined at 900 °C for 2 h.

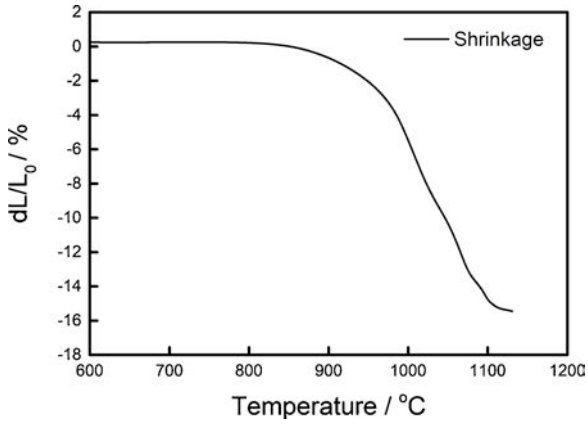

Fig. 5. Sample density as a function of temperature for calcined KNN powder sintered at temperatures up to 1130 °C at 5 °C min^{-1}.

Micrographs of the microstructures of the KNN ceramics sintered using SSS are presented in Fig. 6(b–d). As shown in Fig. 6(b), after sintering at 1100 °C, a largely homogenous microstructure was achieved with a relatively fine average grain size of ~10 μm. Fig. 6(c–d) shows that, along with marginal improvements in density, increases in temperature promote appreciable amounts of grain growth, the mean grain size increasing to ~16 μm at 1120 °C and ~21 μm at 1140 °C. This result is in agreement with the idea that rapid grain growth, due to the generation of the K-rich liquid phase at ~1110 °C [10,30,52], is the principal cause of the limited densification observed at temperatures beyond 1120 °C. While the grains in the 1120 °C and 1140 °C specimens remain primarily equiaxial in form, the wide size distribution of the grains would indicate that the grain growth experienced is abnormal. This is confirmed in Fig. 7, where the grain size distribution of all three microstructures exhibits significant variability. The abnormal nature of grain growth is governed by multiple affects. Firstly, oriented grain boundaries move faster than disoriented ones; the faceted structure of the KNN powder particles, see Fig. 4, leads to discontinuities in terms of particle orientation. As a result, some particles will be well-oriented and have a grain boundary of high mobility, whilst others will be disoriented and have a grain boundary of low mobility. Secondly, the grain boundary energies of pure KNN are intrinsically anisotropic, leading to local differences in the mobility of the grain boundary during sintering [30,53]. Lastly, in an oxidising environment, the evaporation of Na will lead to K and Nb segregation, generating sites that are K-rich and Nb-rich at the grain boundary. At the K-rich sites, a K-rich liquid-solid phase mixture forms preferentially, which, as described above, reduces the energy for grain boundary migration, causing it to expand rapidly [42,54,55]. Meanwhile, Nb-rich grain boundaries remain in a state of solid-phase sintering and, thus, continue to grow at a normal rate. Differences in the migration rate of the grain boundaries leads to abnormal grain growth [6] and contribute significantly to the wide grain size distributions in Fig. 7. It is important to note that the higher vapour pressure of K means that, as a whole, it evaporates more than Na during sintering [11–13,56,57]. However, K-rich sites have been shown to form in local areas [52], especially grain boundaries. From the KNN phase diagram, Na_2O evaporation will cause a compositional shift to the K-rich side to form a Na-deficient liquid phase during the sintering and a K-rich secondary phase ($K_2Nb_4O_{11}$) during cooling. This has been well-reported by Ahn et al. [31,32].

The low density of all the KNN ceramics sintered using SSS corresponds with considerable amounts of both inter- and intra-granular porosity retained within the microstructures. There are three different kinds of pores that exist in KNN ceramics: (1) small, thin inter-granular pores with a straight line edge, mostly located at triple-junctions – residual pores due to incomplete densification; (2) intra-granular closed pores of an irregular morphology – caused by rapid grain growth trapping such pores inside grains; and (3) intra-granular pores of a cubic morphology – associated with gas phase release that results from the volatilisation of Na and K at ~1000 °C [30]. Pores with a similar structure can be found during the sintering of NaCl, where the {100} surface have the lowest activation energies for vapourization [58]. In addition, a fourth type of 'porosity' can be observed as a result of

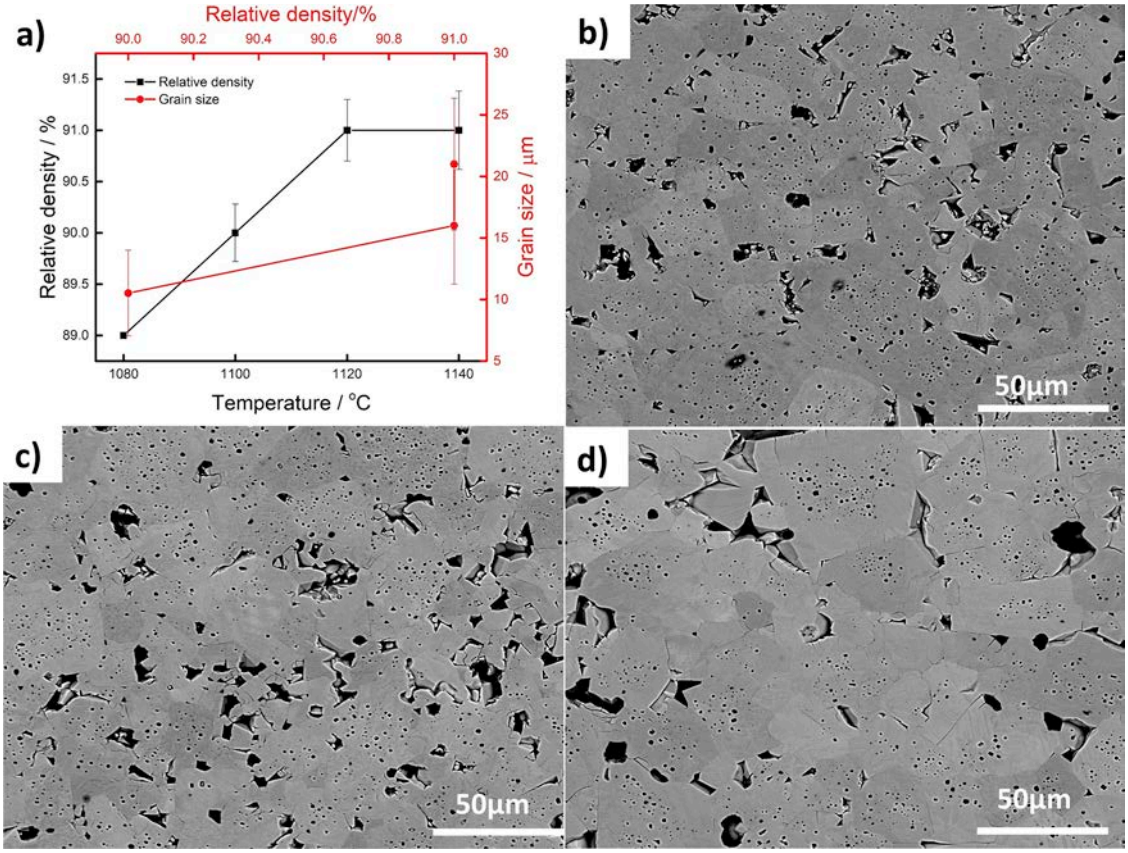

Fig. 6. Single-step sintering of pure KNN ceramics: (a) relative density and grain size as a function of sintering temperature (sintering time 2 h) and their resultant microstructures after sintering at: (b) 1100 °C, (c) 1120 °C, and (d) 1140 °C.

sample preparation; large inter-granular pores with a smooth, irregular shape generated by grain pull-out are forming during grinding and polishing.

As shown in Table 2, the loss of the alkali elements results in moderate mass loss. Without a significant decrease in volume, this negatively influences the final density of the KNN ceramics. Based on Fig. 5, the maximum shrinkage of KNN via SSS was achieved at 1120 °C. This would suggest that samples sintered at > 1120 °C will not achieve higher densities, a result that is confirmed by the fact that the 1140 °C specimen had a density equivalent to that of the 1120 °C samples.

3.2.2. Two-step sintering

In order to achieve high density ceramics with a fine microstructure using TSS, a sufficiently high intermediate density must be obtained during the first sintering step. This is required to ensure that any residual pores that are subjected to second step sintering are of a sub-critical size and unstable to shrinkage. The critical relative density that must be achieved during first step sintering is material dependent and requires careful optimisation of the T_1 temperature [35]. Fig. 8 shows the relative density of KNN pellets partially sintered at different T_1 temperatures and demonstrates that T > 1060 °C provides the minimum level of densification required within the short dwell period of 10 min. The relative density then exhibits a plateau at 1100 °C and 1120 °C before decreasing at 1140 °C, the latter being consistent with the results in section 3.2.1 and reductions in sample mass due to the loss of Na and K. Fig. 8 also shows that higher T_1 temperatures lead to significant increases in grain size, from ~0.7 μm at T_1 = 1080 °C to 9.5 μm at T_1 = 1140 °C. This clearly demonstrates that, within the 10 min dwell period, the KNN ceramics sintered at temperatures > 1080 °C have transitioned from the initial and intermediate sintering stages, dominated by bulk diffusion and sample shrinkage, into the final sintering stage dominated by grain growth [48]. The samples sintered at T_1 = 1120 °C for 10 min obtained the highest density and lowest grain size and, thus, this was chosen as T_1 sintering temperature. Note, whilst T_1 = 1100 °C for 10 min also achieved similar density and grain size values as that of T_1 = 1120 °C, second step sintering yielded almost no change in density. This is believed to be due to the lack of a K-rich liquid phase that forms at ~1100 °C.

Fig. 9(a–f) shows the fracture morphologies of KNN samples sintered at different T_1. At 1040 °C, limited densification has occurred, the morphology of the $(K_{0.5}Na_{0.5})NbO_3$ powder is still clearly visible. There are some signs of the fusing of particles, but significant inter-granular porosity remains. This suggests that only the particles with the lowest activation energy have been activated at this T_1 temperature; most probably the smaller particles with the highest surface free energy. At T_1 temperatures > 1040 °C, it is apparent that significant densification has occurred and that triple-points have formed. Below 1100 °C, the microstructure remains homogenous and exhibits no intra-granular porosity. However, above 1100 °C, grain growth clearly has an increased contribution on the evolution of the microstructure and intra-granular porosity begins to develop. At 1120 °C and 1140 °C, samples are found to contain fewer pores and are smoother in terms of their grain morphology. This is associated with the formation of K-rich liquid-phase at 1110 °C, which has coated the particle surfaces and partially-filled intra-granular pores, see Fig. 9(f). As discussed above, it is the formation of K-rich liquid phase that inhibits densification beyond T_1 = 1120 °C.

Given that the aim of T_2 and t_2 is to achieve a maximum density without significant grain growth and to minimise the evaporation of Na and K, the optimum temperature T_2 and dwelling time t_2 needed to facilitate the maximum amount of densification. Recalling the dynamic sintering curve in Fig. 5, the highest densification rates were achieved at temperatures between 1030 − 1070 °C. As such, this is the temperature range that was exploited for use as T_2. Fig. 10(a) shows the relative

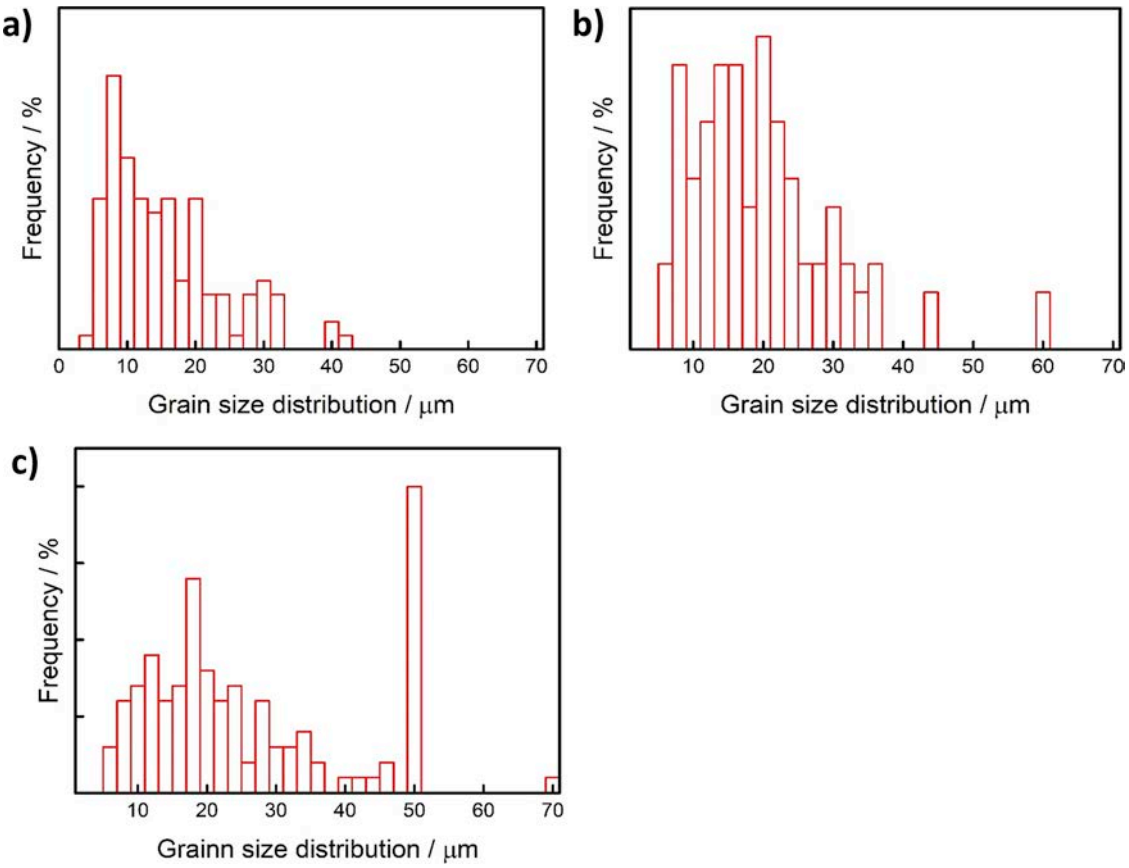

Fig. 7. Grain size distribution of pure KNN ceramics in SSS: a) 1100 °C, b) 1120 °C, and c) 1140 °C.

Table 2
Mass loss of KNN ceramics sintered using SSS (sintering time 2 h).

Samples	Mass loss/%	Δ /%
1100 °C/2 h	1.76	0.040
1120 °C/2 h	1.95	0.018
1140 °C/2 h	2.47	0.110

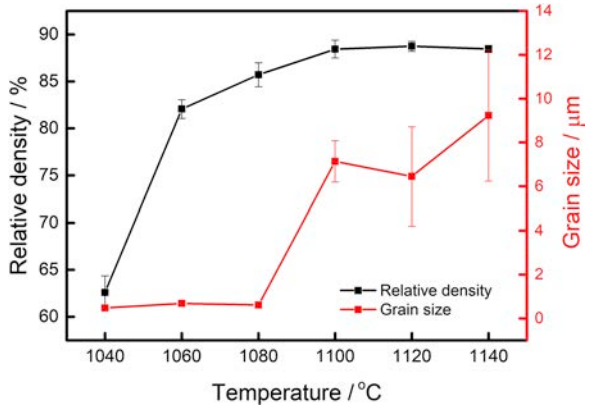

Fig. 8. Relative density of KNN specimens sintered for 10 min. as a function of first step temperature (black line) and the grain size of KNN specimens sintered for 10 min. as a function of first step temperature (red line) (For interpretation of the references to colour in this figure legend, the reader is referred to the web version of this article).

densities and grain size of samples sintered at a T_1 of 1120 °C for 10 min and then a T_2 temperature of 1030/1050/1070 °C for 10 h. From the results, a T_2 of 1070 °C was able to achieve the highest density and the finest grain size. In order to explore whether the density could be further improved by increasing the dwell time at the T_2 stage, additional samples were sintered at 1070 °C for extended dwell periods of 15 h and 20 h. The results are shown in Fig. 10(b) and revealed that longer dwell times lead to a decrease in sample density, associated with increased amounts of alkali evaporation, a view supported by the mass loss data in Table 3, and subsequent gaseous phase release. Based on the findings, a T_2 of 1070 °C for 10 h yielded pure KNN ceramics with the highest relative density via TSS, which was measured to be ~95 % of theoretical.

Fig. 11 presents the representative microstructures of the TSS and SSS sintered KNN ceramics; polished surfaces in a) and b), and fracture surfaces in c) and d). The relative densities and grain size are shown in e). It is clear that the samples fabricated via TSS exhibit both higher densities and finer and more homogenous microstructures. Through a systematic study, the morphologies of KNN ceramics fabricated by SSS and TSS confirm the porosity due to incomplete densification (small inter-granular pores at triple-junctions) is an unavoidable event, and even remains a prevalent feature in high density samples sintered by TSS, see Fig. 11(c). These pores are caused by the intrinsically low sinterability of KNN. The improved density of KNN sintered by TSS is thus achieved by supressing grain boundary migration such that fewer pores are trapped insides grains. Moreover, by comparing Table 2 and 3, the inhibition of mass loss via Na and K evaporation also plays a significant role in the TSS methods ability to produce higher density specimens. Fig. 11(e) summarises the grain sizes and densities of the different KNN ceramics made. As mentioned before, the mean grain size of SSS samples increased from 10.5 μm to 21.3 μm with the increase in sintering temperature from 1100 °C to 1140 °C. For the TSS, the grain size is approximately 50 % less than SSS. The finest grain size and highest density pure KNN sample in this work was obtained at optimum TSS conditions of T_1 = 1120 °C for 10 min, T_2 = 1070 °C for 10 h.

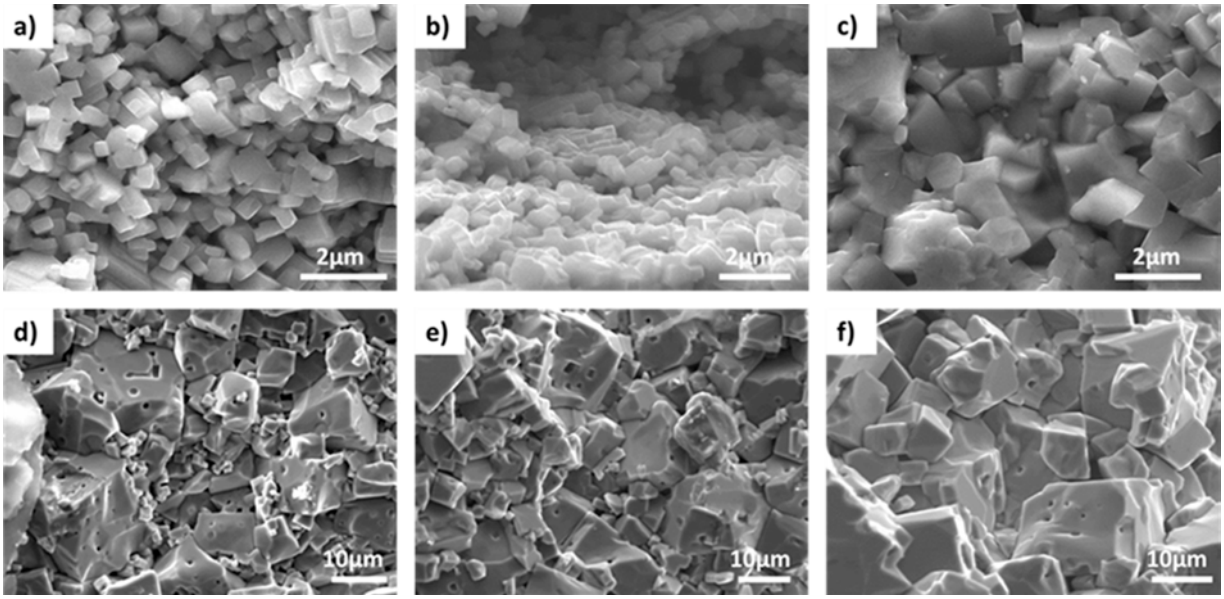

Fig. 9. Fracture morphologies of KNN specimens sintered for 10 min. at: (a) 1040 °C, (b) 1060 °C, (c) 1080 °C, (d) 1100 °C, (e) 1120 °C, and (f) 1140 °C.

3.3. Piezoelectric properties of SSS and TSS samples

The piezoelectric charge coefficient (d_{33}), relative permittivity (ε_r), dielectric loss ($tan\delta$) and mechanical quality factor (Q_m) of the KNN ceramics fabricated using SSS and TSS are summarised in Table 4. Based on these properties, it is clear that KNN samples fabricated via TSS provided better piezoelectric performance, boasting higher measured values of d_{33}, k_p, ε_r and lower $tan\delta$. Such improvements are attributed to the denser microstructures, the improved stoichiometry and the finer grain sizes achieved in the TSS samples. Denser microstructures yield superior piezoelectric properties by retaining lower amounts of porosity, the presence of which impedes the negative/positive charge transfer path [59]. Whilst porosity will always lead to a reduction in dielectric and piezoelectric constants, studies have demonstrated a preference for fewer, larger pores over a greater number of smaller pores [59]. As such, the ability for TSS to inhibit the amount of mass lost due to the evaporation of Na and K compared to SSS will have contributed to the improved properties of the KNN ceramics fabricated by TSS by limiting the generation of porosity, as shown by Fig. 11(a–b). In addition, the retention of Na and K will reduce shifts in the composition of KNN from stoichiometry, which is associated with improved piezoelectric properties [59]. It is well known that the piezoelectric properties can be significantly enhanced along the MPBs (morphotropic phase boundaries) and any deviation from stoichiometry will degrade the properties due to the deviation from the MPB [60]. In addition, the generation of fewer A-site defects results in lower evaporation of alkali via two-step sintering, which can help prevent domain wall pinning to improve the properties [61]. In terms of the grain size, this affects performance by reducing the contribution of the domain wall to the piezoelectric properties [62]. The domain wall contribution is determined by the domain wall density and mobility. The former is the number of domain walls per unit volume and is typically estimated by measuring the average domain width exhibited by piezoelectric ceramics after poling. Unlike PZT and BTO, which have a tetragonal structure and hence mainly exist in 90°- and 180°- domain patterns, pure KNN is an orthorhombic structure at room temperature and, thus, has a very complicated domain pattern with 60°-, 90°-, 120°-, and 180°- domain walls all co-existing [63]. As a result, it is difficult to accurately measure the exact domain size of KNN because it exhibits

Table 3
Mass loss of KNN ceramics sintered using TSS (different dwelling time).

Samples	Mass loss/%	Δ/%
1120°C/10 min./1070°C/10 h	1.51	0.061
1120°C/10 min./1070°C/15 h	1.77	0.052
1120°C/10 min./1070°C/20 h	1.86	0.071

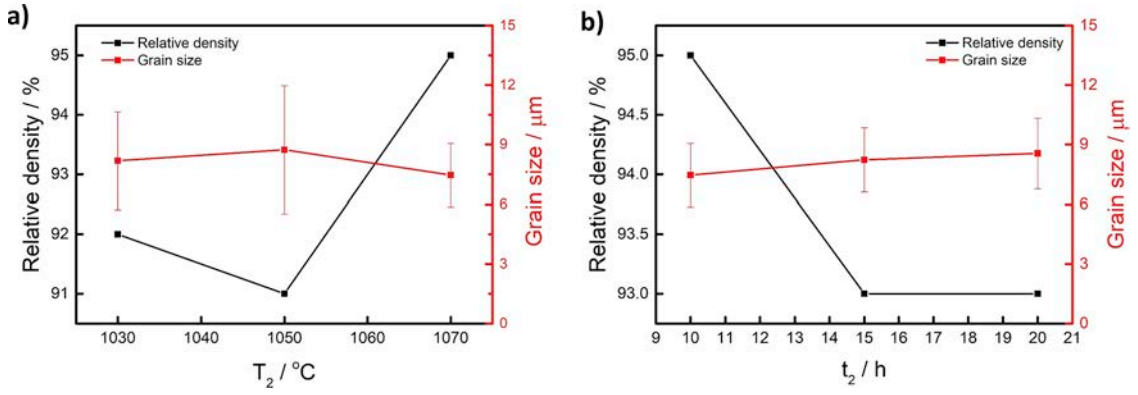

Fig. 10. Relative density and the grain size of KNN specimens sintered at T_1 = 1120 °C for 10 min: (a) held for 10 h at different T_2, and (b) held for different dwell periods at a T_2 of 1070 °C.

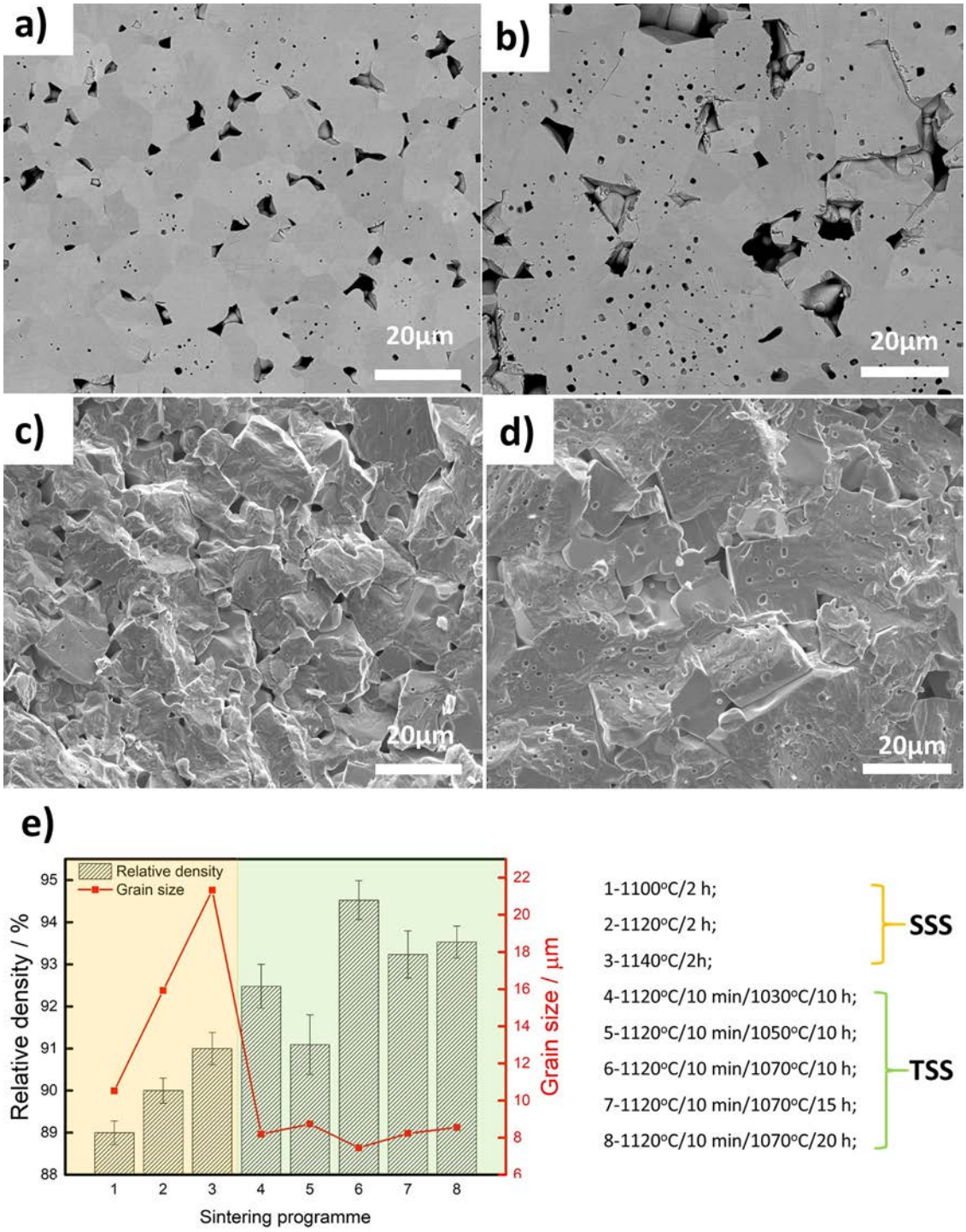

Fig. 11. Pure KNN produced using the best processing conditions determined in this work, polished surfaces: (a) TSS, and (b) SSS, and fracture morphologies: (c) TSS and (d) SSS; (e) relative densities and grain sizes of representative KNN ceramics densified by both sintering approaches.

such significant variance from grain-to-grain [64]. Nevertheless, it is generally acknowledged that smaller domain widths exist within smaller grains [65,66]. This translates into a higher domain wall density, increasing the domain wall contribution by increasing the total domain wall activity [62,66]. Further contributions are made by the relaxation of grain boundary pinning effects at smaller grain sizes, which enable the smaller domain walls to re-orient more easily and respond more actively to an external signal due to higher domain wall mobility [62,67]. Furthermore, an inhomogeneous microstructure, particularly a bimodal grain size distribution, such as that seen in the SSS samples in the present work, will diminish the electrical properties as well.

The data shown in Fig. 12(a–c) depicts the relationships between different piezoelectric properties of the KNN ceramics produced as a function of their relative density at equivalent grain size. In general, all three plots confirm the benefit of a higher density. The slope exhibited by the trend lines of d_{33}, ε_r and k_p would suggest that the elimination of porosity should be prioritised in order to maximise piezoelectric performance; only a 1% reduction in relative density culminated in a significant loss in piezoelectric performance. With respect to the dissimilar

Table 4
Piezoelectric properties of KNN ceramics fabricated using SSS and TSS sintering routes. A comparison with typical literature values reported4 = = is included.

Sample No.	Sintering conditions (T_1 t_1 / T_2 t_2)	Rel. density /%	Grain size /μm	d_{33} /pC N^{-1}	$tan\delta$ /%	ε_r	k_p /%	Q_m
1	1100 °C / 2 h	90	10.52	97	8.9	297	34	17
2	1120 °C / 2 h	91	15.92	101	6.1	294	33	32
3	1140 °C / 2 h	91	21.33	94	4.8	305	25	22
4	1120 °C 10 m / 1030 °C 10 h	92	8.18	112	9.3	327	35	34
5	1120 °C 10 m / 1050 °C 10 h	91	8.74	104	7.4	310	31	42
6	1120 °C 10 m / 1070 °C 10 h	95	7.46	122	4.8	337	36	76
7	1120 °C 10 m / 1070 °C 15 h	93	8.23	118	3.9	329	34	45
8	1120 °C 10 m / 1070 °C 20 h	93	8.55	108	4.4	279	33	39
	Literature KNN[3]	94	–	80	4	290	36	130

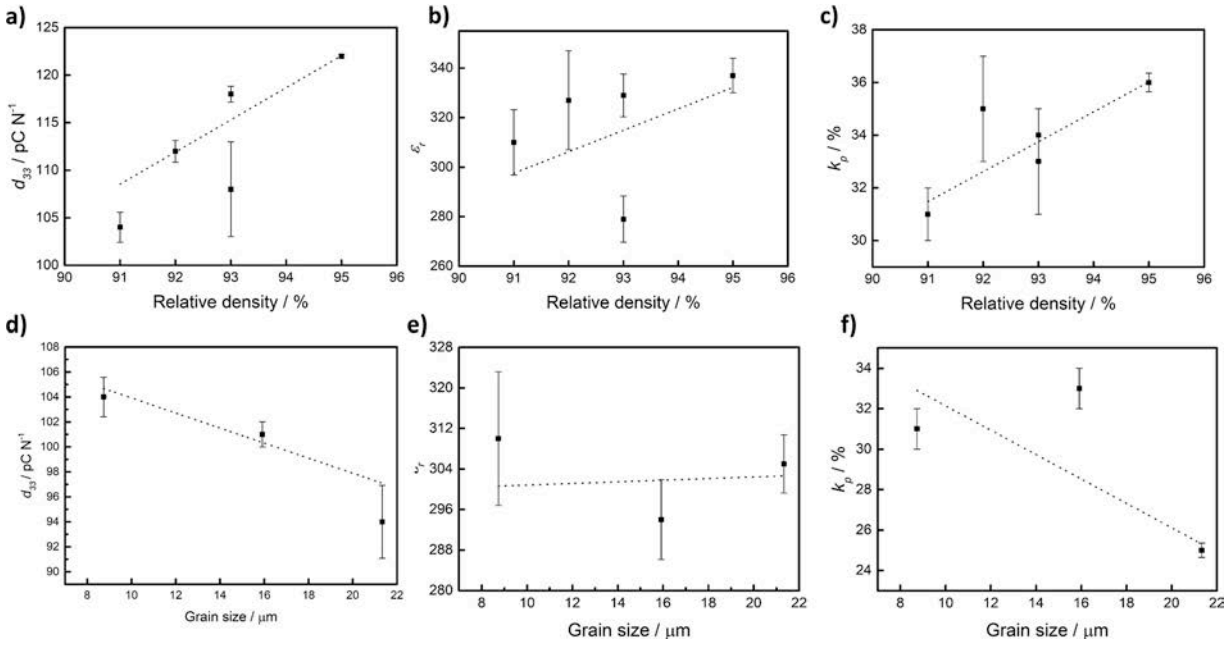

Fig. 12. Relationship between piezoelectric properties and relative density (for similar grain sizes): (a) d_{33}, (b) ε_r, and (c) k_p; relationship between piezoelectric properties and grain size (for similar relative densities): (d) d_{33}, (e) ε_r, and (f) k_p.

properties displayed by the two samples of equivalent grain size (~8.5 μm) and density (93 %) in Fig. 12(a–c), this may be associated with differences in the stoichiometry of the samples. The two samples in question were held at the same T_2 temperature (1070 °C) over different periods of time, one for 15 h and the other for 20 h. The sample that had a longer dwell period exhibited a reduced performance, which may correspond with an increased amount of alkali metal loss via evaporation during long hold times. It is the difference in the evaporation rate of K and Na that can cause the stoichiometry of the pure KNN samples to change if they experience significantly greater weight loss over extended dwell periods.

Fig.12(d–f) show the relationship between the properties and grain size at similar relative densities. Whilst there is a general trend of reduction in d_{33} and k_p with increasing grain size, the dependence of relative permittivity on grain size is less clear. This may be due to the limited data available for these comparisons (i.e. samples with similar relative densities), and the fairly large errors involved in the measurements, but may also be influenced by the range of grain sizes in these particular samples. As discussed above, grain size will affect the piezoelectric properties by changing the corresponding domain wall structure. A critical value exists, when the grain size is larger than this the properties will improve with decreasing grain size. When the grain size is smaller than the critical value the properties decrease due to a domain pinning effect. For example, when the grain size of BTO [62,67] is > 1 μm a smaller grain size can yield better properties, but the opposite result can be obtained if the grain size is < 1 μm. In the present work, whilst two-step sintering is an effective and simple method for reducing the grain size of KNN ceramics, it is still difficult to control the final grain size via this method. Thus, the critical grain size of KNN ceramics may be missed as the grain sizes in the samples reported here ranged from 7.5–21 μm, much larger then the critical grain size reported for BTO. Also, there is no literature available that has systematically investigated the effect grain size has on the piezoelectric properties and domain structure of pure KNN ceramics. As such, further study is required.

3.4. Energy harvesting performance of SSS and TSS samples

As well as the piezoelectric properties listed in Table 4, there are two important parameters to evaluate piezoelectric materials for energy harvesting applications [50]. The first is the energy conversion efficiency, η, which can be calculated using the piezoelectric electromechanical coupling factor, k, and Q_m based on the following equation [68]:

$$\eta = \frac{\frac{1}{2}\frac{k^2}{1-k^2}}{\frac{1}{Q_m} + \frac{1}{2}\frac{k^2}{1-k^2}} \quad (1)$$

In addition, piezoelectric energy harvesting devices usually work at anti-resonance, which means piezoelectric materials need to generate a

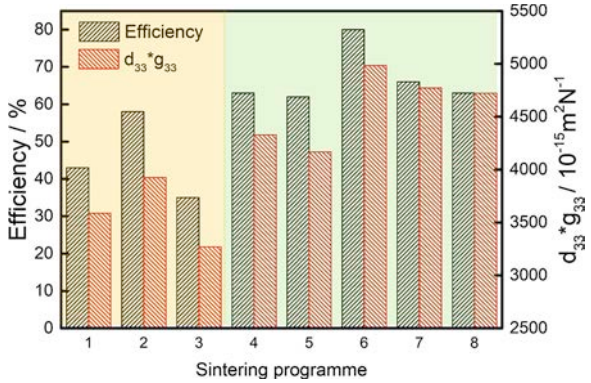

Fig. 13. Influence of different sintering conditions on the efficiency of energy conversion and d_{33}*g_{33} values of KNN ceramics (processing condition number are given in Table 3).

high energy density, u, which is calculated by [69]:

$$u = \frac{1}{2}(d \times g)(\frac{F}{A})^2 \quad (2)$$

where d is the piezoelectric strain constant, g is the piezoelectric voltage constant, $g = d/\varepsilon$, F is the applied force and A is the working area of piezoelectric ceramics. From eq. (2), at equivalent F and A, u is proportional to the product of d and g (transduction coefficient), thus the values of d x g are commonly used to represent the energy density.

Fig. 13 compares the efficiency of energy conversion, η, and transduction coefficient, d_{33} x g_{33}, of the KNN ceramics produced via SSS and TSS under different sintering conditions. The data shows that, in general, the KNN ceramics sintered using TSS exhibited superior piezoelectric properties, due to the higher densities and finer microstructures achieved; this has translated into improved energy harvesting characteristics. The highest values of η and d_{33} x g_{33} for SSS and TSS are 58 % and 3925 $*10^{-15}$ m^2 N^{-1} (for 1120 °C/2 h) and 80 % and 4985 $*10^{-15}$ m^2 N^{-1} (for 1120 °C/10 min./1070 °C/10 h), respectively. In order to evaluate the power generation characteristics directly, these two sets of sintering conditions were selected to fabricate ceramics for use in prototype piezoelectric energy harvesters.

Fig. 14(a) shows the variation of the open circuit voltage with time for the prototype energy harvesters fabricated using KNN ceramics produced by TSS and SSS. It is clear that the highest value for the open circuit peak voltage, 1.36 V, was obtained using the TSS-densified ceramic within the energy harvester. Therefore, this system is expected to demonstrate a superior energy generation performance. Fig. 14(b) shows the peak output voltage and output power as a function of load resistance for the two energy harvesters. It can be seen that with increasing load resistance, the output voltages of both show a slowly increasing trend, with the TSS-based energy harvester displaying a higher value. With both energy harvesters, the relationship between power density and load resistance shows a trend of increasing first and then decreasing. The maximum power density was obtained at 680 kΩ (50.1 μW cm^{-3}) and at 540 kΩ (42 μW cm^{-3}) for TSS- and SSS-based harvesters, respectively. Thus, the results reveal that the energy harvester made of the lead-free KNN ceramic using TSS for densification of the ceramic demonstrates a promising but still not perfect performance.

Normally, better piezoelectric properties yield superior energy harvesting performance, however, the performance of an energy harvester not only depends on the piezoelectric properties, but the structure of energy harvester also has an influence. Thin film structures can yield better harvesting performance because they are easily integrated into a cantilever structure [70]. Table 5 compares the harvesting results generated by the energy harvester made using SSS and TSS in this work with the reported values in the literatures. Although the power density of TSS bulk KNN energy harvester is still lower than these made of KNN thin films and other materials, the KNN-based devices are still promising. An improved energy harvester structure will be developed in the future to improve the energy generation performance further.

4. Conclusions

$(K_{0.5}Na_{0.5})NbO_3$ ceramics were fabricated using both SSS and TSS. The effects of different sintering methods on the sintering mechanism, densification, microstructure, piezoelectric properties, energy performance and the relationship between properties and density as well as grain size were systematically investigated. Compared to the SSS approach, the use of a lower T_2 sintering temperature of the TSS approach improves the density and decreases the grain size of pure KNN ceramics by a reduction in both the amount of grain boundary migration and reducing evaporation of the alkali elements. The low sinterability of pure KNN meant that pores located at triple-points remain difficult to eliminate, even using the TSS method. Thus, the maximum density achieved via TSS was 95 % of theoretical. This compared favourably, however, to the 91 % achieved by SSS. When the best TSS conditions were used, viz. T_1 = 1120 °C for 10 min and T_2 = 1070 °C for 10 h, the samples exhibited improved piezoelectric and dielectric characteristics, the piezoelectric charge coefficient and relative permittivity being 122 pC N^{-1} and 337, respectively. The TSS samples displayed a ~58 % higher mechanical quality factor and a 21 % lower dielectric loss compared to the SSS sintered samples. With a higher energy conversion efficiency and energy density, the pure KNN ceramics fabricated by TSS were used to produce a good-performance energy harvester showing characteristics of 1.36 V open circuit voltage and 50.1 μW cm^{-3} power density. The results suggest that TSS could be an effective approach to

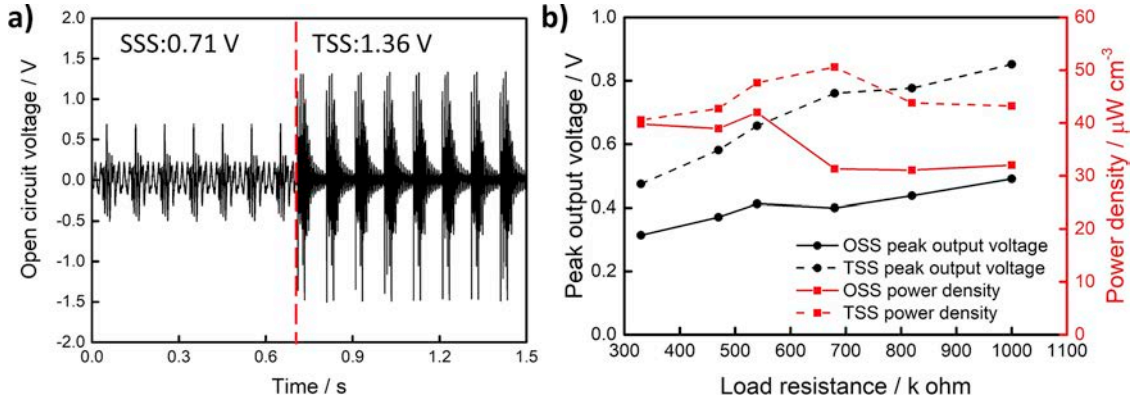

Fig. 14. Measured performance of KNN energy harvester devices fabricated via SSS and TSS: (a) variation of the open circuit voltage with time and (b) variation of the open circuit voltage and power density with load resistance.

Table 5
Comparison of the power generation characteristics of piezoelectric energy harvesters.

Materials	Size: L*W*T / mm	Frequency / Hz	Open circuit voltage / V	Power density / μW mm^{-3}	Ref.
KNN bulk	5 × 5 × 0.3	10	0.71	0.042	SSS
KNN bulk	5 × 5 × 0.3	10	1.36	0.05	TSS
KNNS bulk	35 × 10 × 0.3	70	24.6	0.008	[[71]]
Mn-KNN bulk	10 × 10 × 0.5	90	7	0.32	[[72]]
KNN thin film	–	1036	0.1	6.5	[[73]]
PZT	4.8 × 0.4 × 0.036	462.5	–	3.272	[[74]]
(1-x)BCZT-xBCT	10 × 10 × 0.5	90	8	1.4	[[50]]

solving the difficulties in achieving fully-dense pure KNN ceramics and hence facilitate the fabrication of high-performance KNN-based devices.

Declaration of Competing Interest

The authors declare that there are no conflicts of interest.

Acknowledgements

The work was supported by grants from the UK's Engineering and Physical Science Research Council 'Multi scale tuning of interfaces and surfaces for energy applications', grant number EP/P007821/1 and School of Metallurgy and Materials, University of Birmingham. The authors also appreciate the contributions from Dr. Daniel Reed, Dr. Vinothini Venkatachalam, Mr. Carl Meggs and Mr. Paul Stanley from the University of Birmingham, also Prof. Mike Reece from the Queen Mary University of London for assistance.

References

[1] Jing-Feng Li, et al., (K,Na)NbO_3-based lead-free piezoceramics: fundamental aspects, processing technologies, and remaining challenges, J. Am. Ceram. Soc. 96.12 (2013) 3677–3696.
[2] E.U. Directive, 96/EC of the European Parliament and of the Council of 27 January 2003 on waste electrical and electronic equipment (WEEE), Off. J. Eur. Union L 37 (2002) 24–38.
[3] Ye-Jing Dai, Xiao-Wen Zhang, Ke-Pi Chen, Morphotropic phase boundary and electrical properties of $K_{1-x}Na_xNbO_3$ lead-free ceramics, Appl. Phys. Lett. 94 (2009) 042905.
[4] Thomas R. Shrout, Shujun J. Zhang, Lead-free piezoelectric ceramics: alternatives for PZT, J. Electroceram. 19 (1) (2007) 113–126.
[5] Ruzhong Zuo, Jian Fu, Danya Lv, Phase transformation and tunable piezoelectric properties of lead-free $(Na_{0.52}K_{0.48-x}Li_x)(Nb_{1-x-y}Sb_yTa_x)$ O_3 system, J. Am. Ceram. Soc. 92 (1) (2009) 283–285.
[6] Yuhua Zhen, Jing-Feng Li, Normal sintering of (K,Na) NbO_3-based ceramics: influence of sintering temperature on densification, microstructure, and electrical properties, J. Am. Ceram. Soc. 89.12 (2006) 3669–3675.
[7] Tadashi Takenaka, Hajime Nagata, Yuji Hiruma, Current developments and prospective of lead-free piezoelectric ceramics, J. Appl. Phys. 47 (5S) (2008) 3787.
[8] L. Egerton, Dolores M. Dillon, Piezoelectric and dielectric properties of ceramics in the system potassium—sodium niobate, J. Am. Ceram. Soc. 42.9 (1959) 438–442.
[9] Yiping Guo, Ken-ichi Kakimoto, Hitoshi Ohsato, Phase transitional behavior and piezoelectric properties of $(Na_{0.5}K_{0.5})NbO_3$–$LiNbO_3$ ceramics, Appl. Phys. Lett. 85 (18) (2004) 4121–4123.
[10] B. Jaffe, W.R. Cook, H. Jaffe, Piezoelectric Ceram. (1971) 135–183.
[11] Zupei Yang, et al., Effects of composition on phase structure, microstructure and electrical properties of $(Na_{0.5}K_{0.5})NbO_3$–$LiSbO_3$ ceramics, Mater. Sci. Eng. A 432.1-2 (2006) 292–298.
[12] Guo-Zhong Zang, et al., Perovskite $(Na_{0.5}K_{0.5})_{1-x}(Li,Sb)_xNb_{1-x}O_3$ lead-free piezoceramics, Appl. Phys. Lett. 88 (21) (2006) 212908.
[13] Dunmin Lin, et al., Structure and electrical properties of $(Na_{0.5}K_{0.5})NbO_3$–$LiSbO_3$ lead-free piezoelectric ceramics, J. Appl. Phys. 101 (7) (2007) 074111.
[14] Shujun Zhang, et al., Piezoelectric properties in perovskite 0.948$(Na_{0.5}K_{0.5})NbO_3$–0.052$LiSbO_3$ lead-free ceramics, J. Appl. Phys. 100 (10) (2006) 104108.
[15] Yasuyoshi Saito, et al., Lead-free piezoceramics, Nature 432 (7013) (2004) 84.
[16] Zupei Yang, Yunfei Chang, Lingling Wei, Phase transitional behavior and electrical properties of lead-free $(K_{0.44}Na_{0.52}Li_{0.04})(Nb_{0.96-x}Ta_xSb_{0.04})O_3$ piezoelectric ceramics, Appl. Phys. Lett. 90 (4) (2007) 042911.
[17] Bao-Quan Ming, et al., Piezoelectric properties of (Li, Sb, Ta) modified (Na,K)NbO_3 lead-free ceramics, J. Appl. Phys. 101 (5) (2007) 054103.
[18] Yunfei Chang, et al., Effects of Li content on the phase structure and electrical properties of lead-free $(K_{0.46-x/2}Na_{0.54-x/2}Lix)(Nb_{0.76}Ta_{0.20}Sb_{0.04})O_3$ ceramics, Appl. Phys. Lett. 90 (23) (2007) 232905.
[19] Jiagang Wu, et al., Effects of Ag content on the phase structure and piezoelectric properties of $(K_{0.44-x}Na_{0.52}Li_{0.04}Ag_x)(Nb_{0.91}Ta_{0.05}Sb_{0.04})O_3$ lead-free ceramics, Appl. Phys. Lett. 91.13 (2007) 132914.
[20] Hongliang Du, et al., Perovskite lithium and bismuth modified potassium-sodium niobium lead-free ceramics for high temperature applications, Appl. Phys. Lett. 91 (18) (2007) 182909.
[21] Hongliang Du, et al., Microstructure, piezoelectric, and ferroelectric properties of Bi_2O_3-added $(Na_{0.5}K_{0.5})$ NbO_3lead-free ceramics, J. Am. Ceram. Soc. 90.9 (2007) 2824–2829.
[22] Masato Matsubara, et al., Synthesis and characterization of $(K_{0.5}Na_{0.5})(Nb_{0.7}Ta_{0.3})$ O_3 piezoelectric ceramics sintered with sintering aid $K_{5.4}Cu_{1.3}Ta_{10}O_{29}$, J. Appl. Phys. 44 (9R) (2005) 6618.
[23] Yiping Guo, Ken-ichi Kakimoto, Hitoshi Ohsato, $(Na_{0.5}K_{0.5})NbO_3$–$LiTaO_3$ lead-free piezoelectric ceramics, Mater. Lett. 59 (2-3) (2005) 241–244.
[24] R. Wang, et al., Enhanced piezoelectricity around the tetragonal/orthorhombic morphotropic phase boundary in (Na,K)NbO_3–$ATiO_3$ solid solutions, J. Electroceramics 21 (1-4) (2008) 263–266.
[25] R.E. Jaeger, L. Egerton, Hot pressing of potassium-sodium niobates, J. Am. Ceram. Soc. 45 (5) (1962) 209–213.
[26] Bo-Ping Zhang, et al., Compositional dependence of piezoelectric properties in $Na_xK_{1-x}NbO_3$ lead-free ceramics prepared by spark plasma sintering, J. Am. Ceram. Soc. 89.5 (2006) 1605–1609.
[27] Jing-Feng Li, et al., Ferroelectric and piezoelectric properties of fine-grained $(Na_{0.5}K_{0.5})$ NbO_3 lead-free piezoelectric ceramics prepared by spark plasma sintering, J. Am. Ceram. Soc. 89 (2) (2006) 706–709.
[28] Evelyn Hollenstein, Dragan Damjanovic, Nava Setter, Temperature stability of the piezoelectric properties of Li-modified KNN ceramics, J. Eur. Ceram. Soc. 27 (13-15) (2007) 4093–4097.
[29] Lang Wu, et al., Good temperature stability of $(Na_{0.5}K_{0.5})NbO_3$ based lead-free ceramics and their applications in buzzers, J. Eur. Ceram. Soc. 28 (15) (2008) 2963–2968.
[30] Barbara Malič, et al., Sintering of lead-free piezoelectric sodium potassium niobate ceramics, Materials 8 (12) (2015) 8117–8146.
[31] Cheol-Woo Ahn, et al., Sintering behavior of lead-free (K, Na) NbO_3-based piezoelectric ceramics, J. Am. Ceram. Soc. 92 (9) (2009) 2033–2038.
[32] Cheol-Woo Ahn, et al., Structural variation and piezoelectric properties of 0.95 $(Na_{0.5}K_{0.5})NbO_3$–0.05 $BaTiO_3$ ceramics, Sens. Actuators A Phys. 136 (1) (2007) 255–260.
[33] J. Svoboda, H. Riedel, R. Gaebel, A model for liquid phase sintering, Acta Mater. 44 (8) (1996) 3215–3226.
[34] Xuming Pang, et al., Study on the sintering mechanism of KNN-based lead-free piezoelectric ceramics, J. Mater. Sci. 46 (7) (2011) 2345–2349.
[35] I.-Wei Chen, X.-H. Wang, Sintering dense nanocrystalline ceramics without final-stage grain growth, Nature 404 (6774) (2000) 168.
[36] Dong-Suk Kim, et al., Improvement of translucency in Al_2O_3 ceramics by two-step sintering technique, J. Eur. Ceram. Soc. 27 (13-15) (2007) 3629–3632.
[37] Katarína Bodišová, et al., Two-stage sintering of alumina with submicrometer grain size, J. Am. Ceram. Soc. 90 (1) (2007) 330–332.
[38] Xiao-Hui Wang, Pei-Lin Chen, I.-Wei Chen, Two-step sintering of ceramics with constant grain-size, I. $Y2O_3$, J. Am. Ceram. Soc. 89 (2) (2006) 431–437.
[39] Hai Jiang, et al., Effects of two-step sintering on thermal and mechanical properties of aluminum nitride ceramics by impedance spectroscopy analysis, J. Eur. Ceram. Soc. 39 (2-3) (2019) 249–254.
[40] Seok-Young Ko, Suk-Joong L. Kang, Growth behavior of faceted $Na_{1/2}Bi_{1/2}TiO_3$-$BaTiO_3$ grains in single and two-step sintering, J. Eur. Ceram. Soc. 36 (5) (2016) 1159–1165.
[41] Jon Binner, et al., Dense nanostructured zirconia by two stage conventional/hybrid microwave sintering, J. Eur. Ceram. Soc. 28 (5) (2008) 973–977.
[42] Jian Fang, et al., Two-step sintering: an approach to broaden the sintering temperature range of alkaline niobate-based lead-free piezoceramics, J. Am. Ceram. Soc. 93 (11) (2010) 3552–3555.
[43] Jigong Hao, et al., Improved piezoelectric properties of $(K_xNa_{1-x})_{0.94}Li_{0.06}NbO_3$ lead-free ceramics fabricated by combining two-step sintering, J. Alloys Compd. 534 (2012) 13–19.
[44] Jianxiang Ding, et al., Enhanced energy-storage properties of 0.89 $Bi_{0.5}Na_{0.5}TiO_3$–0.06$BaTiO_3$–0.05$K_{0.5}Na_{0.5}NbO_3$ lead-free anti-ferroelectric ceramics by two-step sintering method, Mater. Lett. 114 (2014) 107–110.
[45] Xuming Pang, et al., (K, Na) NbO_3-based lead-free piezoelectric ceramics manufactured by two-step sintering, Ceram. Int. 38 (3) (2012) 2521–2527.

[46] Daoli Wang, et al., Two-step sintering of the pure $K_{0.5}Na_{0.5}NbO_3$ lead-free piezoceramics and its piezoelectric properties, Ferroelectrics 392 (1) (2009) 120–126.
[47] Chunyu Jiang, Xiaoxiao Tian, Guodong Shi, $K_{0.5}Na_{0.5}NbO_3$ Piezoelectric Ceramics and Its Composites Fabricated From Hydrothermal Powders." 2016 4th International Conference on Sensors, Mechatronics and Automation (ICSMA 2016), Atlantis Press, 2016.
[48] A.S.T.M. Standard, E112, "Standard Test Method for Determining Average Grain Size, ASTM International, West Conshohocken, PA, 2010, https://doi.org/10.1520/E0112-10.".
[49] Yunge Yue, et al., Submicron crystalline buildup and size-dependent energy harvesting characteristic in PZN–PZT ternary ferroelectrics, J. Am. Ceram. Soc. 100 (11) (2017) 5211–5219.
[50] Xiaodong Yan, et al., Composition-driven phase boundary and its energy harvesting performance of BCZT lead–free piezoelectric ceramic, J. Eur. Ceram. Soc. 37 (7) (2017) 2583–2589.
[51] Ye. Zhang, Dielectric and Piezoelectric Properties of reduced-graphite-oxide/poly (vinylidene Fluoride) Nanocomposite and Its Related Devices, Diss. University of Birmingham, 2019.
[52] J.érôme Acker, Hans Kungl, Michael J. Hoffmann, Influence of alkaline and niobium excess on sintering and microstructure of sodium-potassium niobate $(K_{0.5}Na_{0.5})NbO_3$, J. Am. Ceram. Soc. 93 (5) (2010) 1270–1281.
[53] A.D. Rollett, David J. Srolovitz, M.P. Anderson, Simulation and theory of abnormal grain growth—anisotropic grain boundary energies and mobilities, Acta Metall. 37 (4) (1989) 1227–1240.
[54] Na Jiang, et al., Effects of the co-addition of $LiSbO_3$–$LiTaO_3$ on the densification of $(Na_{1/2}K_{1/2})NbO_3$ lead free ceramics by atmosphere sintering, J. Alloys Compd. 509 (5) (2011) 2420–2424.
[55] Dong-Yeol Yang, Duk Yong Yoon, Suk-Joong L. Kang, Abnormal grain growth enhanced densification of liquid phase-sintered WC–Co in support of the pore filling theory, J. Mater. Sci. 47 (20) (2012) 7056–7063.
[56] Laijun Liu, et al., Effects of Na/K evaporation on electrical properties and intrinsic defects in $Na_{0.5}K_{0.5}NbO_3$ ceramics, Mater. Chem. Phys. 117 (1) (2009) 138–141.
[57] A. Popovič, et al., Vapour pressure and mixing thermodynamic properties of the KNbO 3–NaNbO 3 system, RSC Adv. 5.93 (2015) 76249–76256.
[58] Darja Jenko, et al., Electron microscopy studies of potassium sodium niobate ceramics, Microsc. Microanal. 11 (6) (2005) 572–580.
[59] T. Bakarič, et al., Effect of pore size and porosity on piezoelectric and acoustic properties of $Pb(Zr_{0.53}Ti_{0.47})O_3$ ceramics, Adv. Appl. Ceram. 115 (2) (2016) 66–71.
[60] Wenfeng Liu, Xiaobing Ren, Large piezoelectric effect in Pb-free ceramics, Phys. Rev. Lett. 103 (25) (2009) 257602.
[61] Hyunwook NAM, et al., Effect of A-site off-stoichiometry on ferroelectric and piezoelectric properties of $BaTiO_3$–Bi $(Mg_{1/2}Ti_{1/2})$ O_3–$BiFeO_3$ ceramics, J. Ceram. Soc. Jpn. 127 (6) (2019) 369–373.
[62] Yongqiang Tan, et al., Unfolding grain size effects in barium titanate ferroelectric ceramics, Sci. Rep. 5 (2015) 9953.
[63] Yalin Qin, et al., Domain structure of potassium-sodium niobate ceramics before and after poling, J. Am. Ceram. Soc. 98 (3) (2015) 1027–1033.
[64] Jeong-Ho Cho, Yong-Hyun Lee, Byung-Ik Kim, Domain structure of orthorhombic $(Li,K,Na)NbO_3$ ceramics, J. Ceram. Process. Res. 11 (2) (2010) 237–240.
[65] Wenwu Cao, Clive A. Randall, Grain size and domain size relations in bulk ceramic ferroelectric materials, J. Phys. Chem. Solids 57 (10) (1996) 1499–1505.
[66] Rigoberto López-Juárez, et al., Ferroelectric domain structure of lead-free potassium-sodium niobate ceramics, J. Eur. Ceram. Soc. 31 (9) (2011) 1861–1864.
[67] Yu Huan, et al., Grain size effects on piezoelectric properties and domain structure of $BaTiO_3$ ceramics prepared by two-step sintering, J. Am. Ceram. Soc. 96 (11) (2013) 3369–3371.
[68] Cecilia D. Richards, et al., Efficiency of energy conversion for devices containing a piezoelectric component, J. Micromech. Microeng. 14 (5) (2004) 717.
[69] Rashed Adnan Islam, Shashank Priya, Realization of high-energy density polycrystalline piezoelectric ceramics, Appl. Phys. Lett. 88 (3) (2006) 032903.
[70] Huidong Li, Chuan Tian, Z. Daniel Deng, Energy harvesting from low frequency applications using piezoelectric materials, Appl. Phys. Rev. 1 (4) (2014) 041301.
[71] Youngkwang Oh, et al., Dielectric and piezoelectric properties of CeO_2-added Nonstoichiometric $(Na_{0.5}K_{0.5})_{0.97}(Nb_{0.96}Sb_{0.04})O_3$ ceramics for piezoelectric energy harvesting device applications, IEEE Trans. Ultrason. Ferroelectr. Freq. Control 58.9 (2011) 1860–1866.
[72] Mupeng Zheng, et al., A highly dense structure boosts energy harvesting and cycling reliabilities of a high-performance lead-free energy harvester, J. Mater. Chem. C 5.31 (2017) 7862–7870.
[73] Isaku Kanno, et al., Power-generation performance of lead-free (K, Na)NbO_3 piezoelectric thin-film energy harvesters, Sens. Actuators A Phys. 179 (2012) 132–136.
[74] Dongna Shen, et al., The design, fabrication and evaluation of a MEMS PZT cantilever with an integrated Si proof mass for vibration energy harvesting, J. Micromech. Microeng. 18 (5) (2008) 055017.